

2015

Synthesis of nanostructured metal chalcogenides used for energy conversion and storage

Chao Han
University of Wollongong, ch861@uowmail.edu.au

Follow this and additional works at: <https://ro.uow.edu.au/theses>

University of Wollongong

Copyright Warning

You may print or download ONE copy of this document for the purpose of your own research or study. The University does not authorise you to copy, communicate or otherwise make available electronically to any other person any copyright material contained on this site.

You are reminded of the following: This work is copyright. Apart from any use permitted under the Copyright Act 1968, no part of this work may be reproduced by any process, nor may any other exclusive right be exercised, without the permission of the author. Copyright owners are entitled to take legal action against persons who infringe their copyright. A reproduction of material that is protected by copyright may be a copyright infringement. A court may impose penalties and award damages in relation to offences and infringements relating to copyright material.

Higher penalties may apply, and higher damages may be awarded, for offences and infringements involving the conversion of material into digital or electronic form.

Unless otherwise indicated, the views expressed in this thesis are those of the author and do not necessarily represent the views of the University of Wollongong.

Recommended Citation

Han, Chao, Synthesis of nanostructured metal chalcogenides used for energy conversion and storage, Doctor of Philosophy thesis, Institute for Superconducting and Electronic Materials, University of Wollongong, 2015. <https://ro.uow.edu.au/theses/4602>

Research Online is the open access institutional repository for the University of Wollongong. For further information contact the UOW Library: research-pubs@uow.edu.au

**UNIVERSITY OF
WOLLONGONG**



**Synthesis of Nanostructured Metal Chalcogenides Used for Energy Conversion and
Storage**

This thesis is presented as part of the requirements for the

Award of the Degree of

Doctor Philosophy

from

University of Wollongong

by

Chao Han, B. Sc., M. Sc.

Institute for Superconducting and Electronic Materials (ISEM)

Faculty of Engineering

September 2015

Dedication

To my parents, sister, and my girlfriend Weijie Li, who have always been there when I need them.

Acknowledgements

I would like to express my utmost gratitude to my supervisors, A/Prof. Shixue Dou, A/ Prof. Huakun Liu, Dr. Zhen Li for their encouragement, understanding, invaluable advice, and constructive expert supervision of my PhD career during my study at University of Wollongong (UOW). Special Thanks to Dr. Tania Silver, who always critically read every manuscript during my PhD study.

I would also like to thank the UOW and China Scholarship Council (CSC) for the international postgraduate tuition award (IPTA) and the scholarship support, respectively.

I am grateful to the collaborators, like Prof. Zhenxiang Cheng, Dr. Jianli Wang, Prof. Qiao Sun (Suzhou University), Dr Yang Bai (University of Queensland), Prof. Lianzhou Wang (University of Queensland), and Prof. Gaoqing (Max) Lu (University of Queensland), who provided important contribution in the collaborated publications during my PhD study.

Technical assistance from people at UOW, such as Dr. Kosta Konstantinov (TGA, BET), Dr. Germanas Peleckis (XRD), Dr. Dongqi Shi (XPS), Dr. Tony Romeo (FESEM), Dr. Gilberto Casillas-Garcia (TEM), Dr. David Mitchell (TEM) is also highly appreciated. I also want to thank the university staff, especially at ISEM, like Ms. Crystal Mahfouz (Administrative Assistant), Ms. Narelle Badger (Administrative Assistant), Ms. Joanne George (Laboratory and Safety Operations Officer), Ms. Candace Gabelish (Laboratory and Safety Operations Officer), who gave me a great deal of administrative and safety education assistance.

I also would like to thank my good friends and colleagues during my PhD study at ISEM, who have contributed in different ways throughout my doctoral degree. Many thanks to Ms. Jinyan Xiong, Ms. Lijuan Zhang, Ms. Xinqi Chen, Mr. Shaohua Zhang, Dr. Tomas Katkus, Mr. Xavier Reales Ferreres, Dr. Sima Aminorroaya-Yamini, Mr. Rafael Santos, for their

readiness to share their knowledge and valuable suggestion. It is really appreciate that we can stay together to have a lot of fun and build up strong friendship.

Finally, I would like to thank my parents, my sisters for their love and support. My special thanks go to my girlfriend, Weijie Li, who is always there and give me a lot of support during my PhD study.

Table of Contents

Declaration.....	i
Dedication.....	ii
Acknowledgements.....	iii
Abstract.....	viii
Nomenclature.....	xii
List of Figures.....	xxii
List of Tables.....	xxxv
Chapter 1. Introduction.....	1
1.1 General Background.....	1
1.2 Statement of the Problem.....	1
1.3 Objectives and Outlines of Research.....	2
Chapter 2. Literature Review.....	5
2.1 Metal Chalcogenides.....	5
2.1.1 Properties of Chalcogen Elements.....	5
2.1.2 Category and Properties of Metal Chalcogenides.....	7
2.2 Synthetic of Nanostructured Metal Chalcogenides Materials via Wet Chemical Method.....	29
2.2.1 Hydrothermal/Solvothermal method.....	32
2.2.2 Hot-injection Method.....	39
2.2.3 Single Precursor Method.....	43
2.2.4 Mixed Solvents Method.....	44
2.2.5 Liquid Exfoliation Method.....	47
2.2.6 Ion-exchange and Kirkendall-effect-induced Method.....	49
2.2.7 Electro-depositing Method.....	56
2.2.8 Electrospinning Method.....	57
2.3 Application on Energy Storage and Conversion.....	58
2.3.1 Heat-electricity Conversion.....	59
2.3.2 Quantum dot Solar Cells.....	64
2.3.3 Lithium/Sodium Ion Batteries.....	69
Chapter 3 Experiment.....	74
3.1 Chemicals and Materials.....	74
3.2 Experimental Outline.....	77
3.3 Synthesis Method.....	78
3.3.1 Reduction-Precipitate Reaction.....	79
3.3.2 Anion Exchange Reaction.....	80
3.3.3 Hot-injection Method.....	81
3.4 Composition and Morphology Characterization.....	82
3.4.1 X-Ray Diffraction.....	83
3.4.2 Field Emission Scanning Electronic Microscopy.....	83

3.4.3 Transmission Electronic Microscopy.....	83
3.4.4 Brunauer Emmett Teller Surface Area Analysis.....	84
3.4.5 Thermal Analysis.....	84
3.4.6 Physical Property Measurement System.....	85
3.4.7 Atomic Force Microscopy (AFM).....	85
3.4.8 Inductively Coupled Plasma Atomic Emission Spectroscopy (ICP-AES).....	85
3.4.9 X-ray Photoelectron Spectroscopy (XPS).....	85
Chapter 4. Robust Scalable Synthesis of Surfactant-free Binary Thermoelectric Metal Chalcogenide Nanostructures.....	88
4.1 Introduction.....	88
4.2 Experimental.....	90
4.2.1 Chemicals.....	90
4.2.2 Synthesis of Metal Chalcogenide Nanostructures.....	90
4.3 Results and Discussion.....	94
4.3.1 Fabricating of the Nanostructured MCs.....	94
4.3.2 Size and Composition Control.....	108
4.3.3 Thermoelectric Performance of Binary Selenides.....	112
4.4 Conclusion.....	118
Chapter 5. Ambient Scalable Synthesis of Promising Surfactant-free Thermoelectric CuAgSe Nanoparticles with Reversible Metallic-n-p Conductivity Transition.....	119
5.1 Introduction.....	119
5.2 Experimental Section.....	121
5.2.1 Synthesis of CuAgSe Nanoparticles.....	121
5.2.2 Characterization.....	121
5.2.3 Thermoelectric Properties Test.....	122
5.2.4 Theoretical Calculations.....	123
5.3 Results and Discussion.....	123
5.3.1 Preparation of CuAgSe Nanoparticles.....	123
5.3.2 Low Temperature TE for CuAgSe Nanobulk.....	130
5.3.3 High Temperature TE of CuAgSe Nanobulk.....	136
5.3.4 Calculation on Band Structure of Low and High temperature phase of CuAgSe nanobulk.....	139
5.3.5 Cycle Stability on TE Performance of CuAgSe Nanobulk.....	141
5.4. Conclusion.....	144
Chapter 6. Ambient Aqueous Growth of Cu ₂ Te Nanostructures with Excellent Electrocatalytic Activity towards Sulfide Redox Shuttles.....	145
6.1 Introduction.....	145
6.2 Experiment Section.....	147
6.2.1 Synthesis of Cu ₂ Te nanotubes and nanosheets.....	147
6.2.2 Characterization.....	148
6.2.3 Fabrication and Testing of CdS/CdSe Co-sensitized Solar Cell.....	149
6.3 Results and Discussion.....	151
6.3.1 Reaction Mechanism.....	151

6.3.2 Morphology Control by Adjusting Reaction Parameters	161
6.3.3 Performance of Different Cu ₂ Te nanostructures as Counter Electrodes of QDSSCs.....	168
6.4. Conclusion	173
Chapter 7. Graphite-Nanoplate-Coated Bi ₂ S ₃ Composite with High-Volume Energy Density and Excellent Cycle Life for Room-Temperature Sodium Ion Batteries	174
7.1 Introduction.....	174
7.2 Experimental Section.....	176
7.2.1 Synthesis of Bi ₂ S ₃ Nanoparticles and Bi ₂ S ₃ @C Composite	176
7.2.2 Characterization of the Bi ₂ S ₃ @C Composite.....	177
7.2.3 Electrochemical Measurements	178
7.3 Results and Discussion	178
7.3.1 Characterization of Bi ₂ S ₃ and Bi ₂ S ₃ @C Composite	178
7.3.2 Electrochemical Performance of Bi ₂ S ₃ @C Composite.....	182
7.3.3 Investigation of the Sodium Storage Mechanism of Bi ₂ S ₃	190
7.4 Conclusions.....	193
Chapter 8. Controlled Synthesis of Copper Telluride Nanostructures for Long-cycling Anode in Lithium Ion Batteries	195
8.1 Introduction.....	195
8.2 Experiment.....	196
8.2.1 Materials	196
8.2.2 Synthesis.....	197
8.2.3 Characterization	199
8.2.4 Battery Performance Testing	200
8.3 Results and Discussion	201
8.3.1 Synthesis of Copper Telluride Nanocubes	201
8.3.2 Synthesis of Cu _{2-x} Te nanosheets	214
8.3.3 Battery Performance of Cu _{2-x} Te As Anodes for the Lithium Ion Batteries	218
8.4 Conclusions.....	222
Chapter 9. General Conclusions and Outlook.....	223
9.1 General Conclusions	223
9.2 Future work.....	227
9.2.1 Future Work on Synthesis of Nanostructured Metal Chalcogenides.....	227
9.2.2 Future Work on Applications of Nanostructured Metal Chalcogenides.....	229
Reference	231
Appendix.....	248

Abstract

Despite that now most of our energy is still originated from burning of fossil fuels which are non-renewable in short period and may cause serious pollution to the environment; it has become a common sense that human being is facing with more and more serious energy crisis as well as environmental problems including global warming and pollutions. To save our future, now the developing and utilization of green renewable energy, such as solar energy, waste heat recovery, fuel cells, and so on, has been one of the hottest topics all around the world's scientists.

Metal chalcogenides (MCs) have many energy related applications ranging from energy storage to catalysts, from solar cells to thermoelectric, etc.. Especially nanostructured MCs usually possess better performance than bulk due to the ultra-high specific area, unique quantum effect, and high reactivity. However, the wide application of nanostructured MCs is strongly hindered by lacking of a low cost, high yield fabricating method with excellent control over morphology, size and compositions of the final product.

Thereby in this doctoral work, a robust low-cost ambient aqueous method for the scalable synthesis of surfactant-free nanostructured metal chalcogenides (M_aX_b , $M = \text{Cu, Ag, Sn, Pb, Bi}$; $X = \text{S, Se, Te}$; $a = 1 \text{ or } 2$; and $b = 1 \text{ or } 3$) is developed in this work. The effects of reaction parameters, such as precursor concentration, ratio of precursors, and amount of reducing agent, on the composition, size, and shape of the resultant nanostructures have been comprehensively investigated. This environmentally friendly approach is capable of producing metal chalcogenide nanostructures in a one-pot reaction on a large scale, which were investigated for their thermoelectric properties towards conversion of waste heat into electricity. The results demonstrate that the thermoelectric properties of these metal chalcogenide nanostructures are strongly dependent on the types of metal chalcogenides, and

their figure of merits are comparable with previously reported figures for their bulk or nanostructured counterparts.

Based on this method, surfactant-free CuAgSe nanoparticles were also successfully synthesized on a large scale within a short reaction time via a simple environmentally friendly aqueous approach. The nanopowders obtained were consolidated into pellets for investigation of their thermoelectric properties between 3 K and 623 K. The pellets show strong metallic characteristics below 60 K and turn into an n-type semiconductor with increasing temperature, accompanied by changes in the crystal structure (i.e. from the pure tetragonal phase into a mixture of tetragonal and orthorhombic phases), the electrical conductivity, the Seebeck coefficient, and the thermal conductivity, which leads to a figure of merit (ZT) of 0.42 at 323 K. The pellets show further interesting temperature-dependent transition from n-type into p-type in electrical conductivity arising from phase transition (i.e. from the mixture phases into cubic phase), evidenced by the change of the Seebeck coefficient from $-28 \mu\text{V/K}$ into $226 \mu\text{V/K}$ at 467 K. The ZT value increased with increasing temperature after the phase transition and reached 0.9 at 623 K. The sintered CuAgSe pellets also display excellent stability, and there is no obvious change observed in 5 cycles of consecutive measurements. Our results demonstrate the potential of CuAgSe to simultaneously serve (at different temperatures) as both a promising n-type and a promising p-type thermoelectric material.

Using Cu_2E (E = O, S, Se) nanoparticles synthesized by this low cost aqueous method as precursor, surfactant-free Cu_2Te nanotubes and nanosheets are fabricated in aqueous solution at room temperature. Cu_2E (E = O, S, Se) nanoparticles can be easily transformed into Cu_2Te nanosheets and nanotubes via a simple anion exchange reaction under ambient conditions. The formation of Cu_2Te nanosheets is ascribed to a novel exchange-peeling growth mechanism instead of simple Kirkendall effect; and the resultant nanosheets can be further

rolled into nanotubes with assistance of stirring. The morphologies of Cu₂Te nanosheets and nanotubes could be easily controlled by changing the synthesis parameters, such as the concentration of precursors, the size of nanoparticle precursor, and the amount of NaBH₄, as well as the stirring speed. Thus-formed Cu₂Te nanostructures exhibited excellent catalytic activity towards sulfide redox shuttles and were exploited as counter electrodes catalysts for quantum dot sensitized solar cells. The performance of Cu₂Te nanostructures strongly depends on their morphology, and the solar cells made with counter electrodes from Cu₂Te nanosheets show the maximum power conversion efficiency of 5.35 %.

Graphite-nanoplate coated Bi₂S₃ composite (Bi₂S₃@C) was fabricated by ball milling of graphite and the Bi₂S₃ nanorods prepared from the low cost aqueous method. And this composite can be used as either the cathode material for room temperature sodium-sulfide batteries or anode of sodium ion batteries. It delivered an initial capacity of 550 mAh.g⁻¹ and high stable specific energy in the range of 275-300 Wh.kg⁻¹ at a rate of 0.1 C, with enhanced capacity retention of 69% over 100 cycles. The unique structure demonstrated superior cycling stability, with a capacity drop of 0.3% per cycle over 100 cycles, compared with that of bare Bi₂S₃. The sodium storage mechanism of Bi₂S₃ was assigned to the substitution and insertion reaction of Bi₂S₃, in which Bi₂S₃ reacts with Na to form Bi and Na₂S; then Na is inserted into Bi layers to form 3 NaBi molecules. The low polarization, high density, and excellent cycling performance make Bi₂S₃@C a promising cathode candidate for room-temperature sodium–Sulphur batteries.

Although good control over size and compositions can be achieved by the low cost aqueous method, the control of morphology of final product is poor because no surfactants are used. Thereby to get good control over morphology of nanostructured MCs, a hot injection method in organic solvent and different surfactants is also studied. Copper telluride nanocubes, nanosheets, and nanoparticles were prepared by a novel hot injection method under the

protection of inert atmosphere. The influence of reaction parameters, including precursor concentration, precursor ratio, precursor type, reaction time, reaction temperature, solvent, and organic ligands, on the size, morphology, crystalline structure, and composition of the resultant copper telluride nanostructures was comprehensively investigated. The results show that the crystal structure and composition of the resultant nanostructures varied case by case, demonstrating the complexity of copper tellurides, despite their simple molecular formula. The obtained copper telluride nanostructures were tested as anodes in lithium ion batteries. The assembled Li/LiPF₆/Cu_xTe cells exhibit extremely high cycling stability (up to 5000 cycles), and their highest specific capacity is 280 mAh/g. The results also show better performance of the Cu_{2-x}Te nanosheet electrodes than those of electrodes made from nanoparticles and nanocubes, demonstrating the importance of controlling the morphology of copper telluride during preparation.

Nomenclature**List of Abbreviations**

Abbreviation	Full name
3 D	Three dimensional
2 D	Two dimensional
1 D	One dimensional
0 D	Zero dimensional
AAO	Aluminum oxide template
AFM	Atomic force microscopy
AM	Air mass
atm	Standard atmosphere
a.u.	Arbitrary unit
BET	Brunauer Emmett Teller
cm	Centimeter
CE	Counter electrode

CQD	Colloidal quantum dot solar cells
CV	Cyclic voltammetry
DOS	Density of states
DSC	Differential scanning calorimetry
DSSCs	Dye sensitized solar cells
EDS	Energy dispersive x-ray spectroscopy
EIS	Electrochemical impedance spectroscopy
FESEM	Field emission scanning electron microscopy
FFT	Fast Fourier transform
ZT	Figure of merits
ICP-AES	Induced couple plasma atomic emission microscopy
IFFT	Inversed fast Fourier transform
IPCE	Incident photon to current efficiency
JCPDS	Joint committee on powder diffraction standards

HT	High temperature
HRTEM	High-resolution transmission electron microscopy
LIBs	Lithium-ion battery
MCs	Metal chalcogenides
mm	Millimeter
nm	Nanometer
NP	Nanoparticles
NS	Nanosheets
NT	Nanotubes
ORR	Oxygen reduction reaction
PBE	Perdew-Burke-Ernzerh method
PCE	Power conversion efficiency
PGEC	Phonon-glass electron-crystal
PLEC	Phonon-liquid electron-crystal

PPMS	Physical property measurement system
QD	Quantum dot
QDSSC	Quantum dot sensitized solar cells
RS	Rock salt type structure
RT	Room temperature
SAED	Selected area electron diffraction
SEI	Solid electrolyte interphase
SEM	Scanning electron microscopy
SIBs	Sodium-ion battery
SPS	Spark plasma sinter
STEM	Scanning tunneling electron microscopy
TE	Thermoelectric
TEG	Thermoelectric generator
TER	Thermoelectric refrigerator

TEM	Transmission electron microscopy
TGA	Thermogravimetric analysis
W	Wurtzite type structure
XPS	X-ray photoelectron spectroscopy
XRD	X-ray diffraction
ZB	Zinc blende type structure

List of Symbols

Symbol	Name	Unit
2θ	Detection angle in XRD	Degree
B	Magnetic field	T
C-rate	Charged or discharged rate	mA.g^{-1}
C_p	Specific heat of sample	$\text{J.g}^{-1}.\text{K}^{-1}$
C_R	Specific heat of reference material	$\text{J.g}^{-1}.\text{K}^{-1}$
d	Lattice spacing	\AA
D	Thermal diffuse coefficient	$\text{cm}^2.\text{s}^{-1}$
e	Charge of electron	C
E_g	Band gap	eV
f	Frequency in the EIS test	Hz
F	Faradic constant = 96485	C
FF	Fill factor	-

ΔG	Free Gibbs energy	KJ.mol^{-1}
h	Planck constant	J.s
I	Current density	A.cm^{-2}
I_{sc}	Short circuit current density	A.cm^{-2}
k_B	Boltzmann constant	J.K^{-1}
K_{sp}	Solubility product	-
L	Lorenz number	$\text{W}\cdot\Omega\cdot\text{K}^{-2}$
m	Active material weight	g
m^*	Effective mass	-
n	Carrier concentration	cm^{-3}
N	Avogadro's number = 6.022×10^{23}	mol^{-1}
P	Relative pressure	Pa
P_0	Saturation pressure	Pa
P_F	Power factor	$\text{W.m}^{-1}\cdot\text{K}^{-2}$

Q	Specific capacity	mAh. g^{-1}
Q_{TSC}	Theoretical specific capacity	mAh. g^{-1}
R	Gas constant = 8.319	$\text{J.K}^{-1}.\text{mol}^{-1}$
R_s	Series resistance	Ω
R_{ct}	Charge transfer resistance	Ω
S	Seebeck coefficient	$\mu\text{V.K}^{-1}$
S_{BET}	Specific BET surface area	$\text{m}^2.\text{g}^{-1}$
T	Temperature	$\text{K or } ^\circ\text{C}$
T_1	Temperature at hot side	$\text{K or } ^\circ\text{C}$
T_2	Temperature at cold side	$\text{K or } ^\circ\text{C}$
V_{oc}	Open circuit voltage	Volt
t	Time	h or s
σ	Electrical conductivity	S cm^{-1}
η	Energy conversion efficiency	%

η_c	Hot engine efficiency	%
η_e	Coulombic efficiency	%
λ	X-ray wavelength	Å
κ	Thermal conductivity	W.m ⁻¹ .K ⁻¹
κ_e	Carrier thermal conductivity	W.m ⁻¹ .K ⁻¹
κ_L	Lattice thermal conductivity	W.m ⁻¹ .K ⁻¹
μ	Carrier mobility	cm ² .V ⁻¹ .s ⁻¹
ρ	Density	g.cm ⁻³
χ	Electronegativity	-
φ	Standard redox potential	Volt
ν	Frequency of wave	Hz

List of Organizations

Abbreviation	Full name
---------------------	------------------

AIIM	Australian Institute for Innovative Materials
------	---

CSC	China Scholarship Council
-----	---------------------------

EMC	Electron Microscopy Center
-----	----------------------------

ISEM	Institute for Superconducting and Electronic Materials
------	--

UOW	University of Wollongong
-----	--------------------------

List of Figures

Figure 2.1. Image of (a) α -Sulphur, (b) gray Selenium and (c) Tellurium powder.

Figure 2.2. Main group MCs and transition group MCs, the electronegativity of different elements are also labeled.

Figure 2.3. Atom arrangement for (a) RS, (b) ZB and (c) W type.

Figure 2.4. Crystal structure of (a) Na_2S ; (b) Cs_2S ; (c) CaTe ; and (d) BeS .

Figure 2.5. Crystal structure of (a) Al_2S_3 ; (b) Ga_2Te_3 , white part means vacant; (c) InSe ; (d) TlTe .

Figure 2.6 Crystal structures of (a) GeS , (b) SnS , (c) PbS , (d) GeTe , (e) SnS_2 .

Figure 2.7. Crystal structure of (a) Sb_2S_3 , and (b) Bi_2Te_3 .

Figure 2.8. Layered transition metal sulfides or selenides with the metal in octahedral or trigonal prismatic coordination (Nb and Ta are found in both).

Figure 2.9. (a) top view and side view of 1T and 2H type structure; (b) stable structure for MX_2 .

Figure 2.10. Crystal structure of FeS_2 with (a) pyrite structure, and (b) marcasite.

Figure 2.11. Crystal structure of (a) Ce_2S_3 and (b) Ce_3S_4 .

Figure 2.12. (a) High temperature structure of Cu_2Se ; (b) crystal structure of CuS .

Figure 2.13. Crystal structure of (a) α - HgS and (b) β - HgS .

Figure 2.14. SEM images of the Ni-Se system fabricated by hydrothermal method under different conditions: (a, b) Ni_{1-x}Se microspheres obtained at 140 °C; (c) hexagonal NiSe

microspheres obtained at 180 °C; d) rhombohedral NiSe nanowires obtained at 180 °C (65 h); (e, f) Ni₃Se₂ microspheres obtained at 180 °C; (g) octahedral-shaped NiSe₂ microcrystals (140 °C, pH 10).

Figure 2.15. A schematic illustration of the fabrication of ZnO nanotube and nanorod array films on the top and bottom surfaces of the same zinc foil substrate by a vapour-phase hydrothermal method.

Figure 2.16. Fe₃S₄ and FeS₂ fabricated under magnetic field with different Sulphur source.

Figure 2.17. SEM images of (a) dodecahedron-like NiS₂ synthesized with 0.5 mmol NiCl₂.6H₂O and 2 mmol S at 200 °C for 6 h in a solvothermal of mixed solvent (EN:Glycol=3:1); and (b) NiS₂ microspheres synthesized with 0.5 mmol NiCl₂.6H₂O and 2 mmol S at 200 °C for 6 h in a solvothermal of mixed solvent (EN:Glycol=1:3). (c) SEM of truncated Fe₇Se₈ synthesized with solvothermal of DETA:H₂O=1:2 at 140 °C for 12 h; (d) Fe₇Se₈ nanorods synthesized with DETA:H₂O=1:4 at 140 °C for 12 h.

Figure 2.18. TEM image of (a) nanoparticles and (b) nanorods of Bi₂S₃. (c) TEM image of FeTe nanosheets. (d) SEM image of FeSe₂ nanoflower.

Figure 2.19. (a) TEM of the SnSe nanosheets; (b) SEM of the SnS nanoflowers fabricated by one step colloid method.

Figure 2.20. (a) TEM image of Fe₃S₄ nanoparticles; (b) SEM image of Fe₇S₈ nanoplates; (c) TEM of Fe₇S₈ nanobelts.

Figure 2.21. Nanosheets fabricated from electrochemical insertion of Li⁺ ions. (a) MoS₂; (b) WS₂; (c) TiS₂; (d) TaS₂.

Figure 2.22. (a) SEM images of Cu_{2-x}Se and (b) Cu_{2-x}S within the mixed ethanol/2-

mercaptoethanol/NaOH solution. (c) Energy profiles for reactions of $\text{HOCH}_2\text{CH}_2\text{SSe}^-$ ions. (d) SEM image of the Cu_{2-x}Se synthesized within the mixed ethanol/3-mercaptopropionic acid/NaOH solution.

Figure 2.23. (a) Scheme of LSS phase transfer synthetic strategy. (b) TEM images of as-synthesized MC nanocrystals: PbS, Ag_2S , and ZnSe. Insets show cyclohexane solutions of corresponding MC nanocrystals.

Figure 2.24. The relative order in the solubility product of various metal chalcogenides.

Figure 2.25. (a) Scheme of the forward cation exchange reaction and reverse cation exchange reaction between CdSe and Ag_2Se . (b) Initial CdSe, (c) Ag_2Se transformed from the forward cation exchange reaction, and (d) recovered CdSe nanocrystals from the reverse cation exchange reaction. Scale bars all present 40 nm.

Figure 2.26. Some typical hollowed structures obtained from ion exchange reaction. (a-b) SEM image of hollowed PbS and CuS microspheres synthesized from ZnS microballs via cation exchange reaction. (c) SEM of CdSe nanotubes fabricated from anion exchange of $\text{Cd}(\text{OH})_2$ nanowires. (d) SEM image of the hollowed CuS nanocubes prepared from anion exchange of Cu_2O nanocubes. (e) Schematic of Kirkendall effect.

Figure 2.27. (a) TEM of Ag_2Te nanowires synthesized from Te nanowires. (b) TEM of Bi_2Te_3 nanotubes prepared from Te nanowires. (c) TEM of Bi_2Te_3 nanowires prepared from Te nanowires. (d) TEM of the ultrathin Bi_2Te_3 nanowires fabricated from ultrathin Te nanowires.

Figure 2.28. (a) Schematic of electrospinning method. (b) $\text{Cu}_2\text{FeSnS}_4$ nanowires; (c) Bi_2Te_3 nanotubes; and (d) CdS@ZnO core-shell nanowires prepared by electro-spinning method.

Figure 2.29. Working principle and structure of a thermoelectric generator (TEG) module.

Figure 2.30. Working principle and structure of Quantum Dot Sensitized Solar Cells.

Figure 2.31. Schematic of working mechanism in a rechargeable LIB.

Figure 3.1. Outline of my research procedures.

Figure 3.2. Design of the reduction-precipitation method.

Figure 3.3. Standard Schlenk Line used for hot injection synthesis route. (a) Working part of Schlenk line; (b) temperature and stirring control part. (c) Landt Battery Testing System. (d) PANalytical diffractometer.

Figure 3.4. Pictures of (a) GBC-MMA X ray diffraction meter; (b) JOEL-7500F field emission scanning electronic microscopy; (c) JOEL-2010 transmission scanning electronic microscopy; (d) ARM200F scanning tunnel electronic microscopy; (e) Quanta Chrome Nova 1000 system; (f) Mettler-Toledo TGA/DSC 1 thermal analyze system; (g) physical property measurement system; (h) Ayslum AFM machine; (i) VISTA MPX axial simultaneous ICP-AE spectrometer; (j) PHOIBOS 100 hemispherical XPS system.

Figure 4.1. Schematic illustration of synthesis route; inset picture shows the weight of 40 mmol (theoretical yield) synthesized Cu_2Se powder.

Figure 4.2. Pictures of the (a) SP 10-4, spark plasma sintering machine, inset at left down corner is the chamber and graphite die; (b) Ozawa RZ200li instrument, inset at left up corner shows the connection of samples onto electrodes; (c) Linseis LFA 1000 system; (d) Netzsch 204 F1 DSC machine.

Figure 4.3. (a-i) SEM images and (j) XRD patterns of the as-prepared metal chalcogenide nanostructures, with the black vertical lines marking the lines of the standard.

Figure 4.4. (a) XRD of the annealed Bi_2Se_3 ; (b) XRD of Bi_2Te_3 sample, the standard peaks

Figure 4.5. (a) EDS spectra and (b) HRTEM of Bi_2Te_3 sample.

Figure 4.6. (a) XPS survey spectra for different metal chalcogenides; (b) peaks of Cu and the chalcogens in copper chalcogenides; (c) peaks of Pb and the chalcogens in lead chalcogenides; (d) peaks of Bi and the chalcogens in bismuth chalcogenides.

Figure 4.7. (a-i) TEM images of Cu-, Pb-, and Bi-based chalcogenide nanostructures.

Figure 4.8. (a-i) Particle size distributions for different metal chalcogenides, counted from 200 particles in TEM images, with the values in (g) referring to the diameters of the nanorods.

Figure 4.9. (a) Calculated formation energies of different kinds of metal chalcogenides; (b) average particle sizes of the Cu-, Pb- and Bi-chalcogenides, with the shuttle-like Bi_2S_3 nanorods excluded.

Figure 4.10. (a) Set up for measuring released H_2 ; and time-dependence of the release of H_2 and the change of temperature during reduction of (b) Se and (c) Te with NaBH_4 .

Figure 4.11. The changes in temperature in the (a-b) Bi-Se and (c-d) Bi-S systems before and after precipitation.

Figure 4.12. (a) TEM of Bi_2S_3 nanorod, the end of which are marked by red circle; (b) XRD of the Bi_2S_3 nanoparticles obtained by decreasing the amount of HCl and of the amorphous Sb_2Se_3 nanoparticles; XRD patterns of (c) tin and (d) silver chalcogenide nanostructures prepared by our method. The red vertical lines mark the line positions of the standard.

Figure 4.13. (a). XRD patterns of copper selenides synthesized with a ratio of NaBH_4 to Se increasing from 2:1 to 8:1; (b) XRD patterns of Cu_2Se nanoparticles prepared from different concentrations of Se precursors and with different reduction times.

Figure 4.14. TEM images of Cu₂Se nanoparticles prepared from (a) 0.01 M; (b) 0.05 M; (c) 0.4 M NaHSe; (d) dependence of particle size on concentration of NaHSe.

Figure 4.15. TEM images of Cu₂Se nanoparticles prepared by using different reduction times: (a) 15 min; (b) 45 min, and (c) 60 min. (d) dependence of particle size on reduction time.

Figure 4.16. (a) TEM of the SnSe nanoparticles, inset is the size distribution; (b) XPS results of Sn 3d and Se 3d core level; (c) SEM image of prepared Ag₂Se nanoparticles; (d) XPS result.

Figure 4.18. Morphology of cross-sections of (a) Cu₂Se pellet; (b) Bi₂Se₃ pellet; (c) SnSe pellet; and (d) Ag₂Se pellet. (e) XRD patterns of the sintered pellets, with the red vertical lines showing the line positions of the standard.

Figure 4.17. TGA and Cp curves for (a, e) Cu₂Se; (b, f) Bi₂Se₃; (c, g) SnSe and (d, h) Ag₂Se pellets.

Figure 4.19. Temperature dependence of the thermoelectric properties, the electrical conductivity (left column), the thermal conductivity (middle column), and the ZT (right column), of (a-c) Cu₂Se pellet, (d-f) Bi₂Se₃ pellet, (g-i) SnSe pellet, and (j-l) Ag₂Se pellet in comparison with previous reports.

Figure 5.1. Schematic of the synthesis procedure of CuAgSe nanoparticles.

Figure 5.2. Schematic crystal structures of CuAgSe: (a) low temperature tetragonal CuAgSe; (b) low temperature orthorhombic CuAgSe; (c) high temperature cubic CuAgSe. The mixed gray and red mean randomly occupied by Ag or Cu atoms.

Figure 5.3. (a) X-Ray diffraction pattern, (b) SEM image of the prepared nanoparticles; (c)

TEM and (d) HRTEM images of as-synthesized CuAgSe nanoparticles, inset picture is Fast Fourier Transform pattern from HRTEM image.

Figure 5.4. XPS results of the prepared CuAgSe nanoparticles.

Figure 5.5. (a) XRD patterns and (b) SEM images of the precipitate before and (c) after the addition of CuCl solution.

Figure 5.6. XRD patterns and SEM images of the precipitate obtained by mixing Cu₂Se and Ag₂Se in the aqueous system for different times, in comparison with that of nanoparticle precursors: (a) XRD patterns, (b) SEM image of the precipitate after stirring for 30 hours, and (c) SEM image of the Cu₂Se nanoparticle precursor.

Figure 5.7. (a) X-ray diffraction patterns of samples synthesized with different Cu²⁺:Ag⁺:Se²⁻ ratios (R) and (b) different NaBH₄/Se ratios (r).

Figure 5.8. (a) SEM image of the consolidated pellet from the prepared CuAgSe nanoparticles, inset is the coin-like pellet; (b) XRD pattern of the pellet; (c-f) TE performance of the sintered CuAgSe nanoparticles from 3 K to room temperature. The black dot in (f) presents the data from reference.

Figure 5.9. Temperature dependent XRD result for the sintered CuAgSe pallet from 20 K to 300 K.

Figure 5.10. (a) Sample connections and dimensions for the measurement, inset is the assembled device for testing; (b) Hall resistivity as a function of magnetic field; (c) calculated n and (d) calculated μ as functions of temperature.

Figure 5.11. TE performance of sintered CuAgSe nanoparticles from 323 K to 623 K: (a) electrical conductivity; (b) Seebeck coefficient; (c) power factor; (d) thermal conductivity; (e)

specific heat capacity; (f) ZT value, the black triangle represents the data from reference.

Figure 5.12. (a) DSC and (b) TGA curve of CuAgSe pellet.

Figure 5.13. Calculated band structure for (a) tetragonal CuAgSe; (b) α -phase cubic CuAgSe; and (c-d) magnified part of Γ point. Total density of states for (e) low temperature β -tetragonal phase and (f) high temperature α -cubic phase CuAgSe.

Figure 5.14. TE properties of sintered CuAgSe nanoparticles tested over 5 cycles (heating and cooling): (a) micromorphology after 5 cycles; right side is the macromorphology before and after 5 cycles; (b) XRD pattern after 5 cycles; (c) electrical conductivity; (d) Seebeck coefficient. (e) XPS spectra of CuAgSe pellet before and after 5 cycles.

Figure 6.1. Schematic illustration of the synthesis of Cu₂Te nanosheets and nanotubes from Cu₂Se nanoparticles.

Figure 6.2. Pictures of (a) solar simulator (Oriel); (b) Keithley model 2420 digital source meter; (c) Solartron 1260 Frequency Response Analyzer (upper) in combination with a Solartron 1480 Potentiostat (lower); (d) CHI660d electrochemical workstation.

Figure 6.3. (a) SEM, (b) TEM, and (c) HRTEM images of Cu₂Se nanoparticle precursor; (d) SEM, (f) TEM, and (c) HRTEM images of the as-prepared Cu₂Te nanosheets; (g) SEM, (h) TEM, and (i) HRTEM images of Cu₂Te nanotubes. The insets to (c) and (f) are the corresponding FFT patterns; the inset in (i) is the IFFT image of the part marked by red rectangle.

Figure 6.4. XRD patterns for Cu₂Se nanoparticle precursor, and Cu₂Te nanosheets and nanotubes.

Figure 6.5. XRD patterns of Cu₂Te transferred from (a) Cu₂O and (b) Cu₂S in comparison

with that of precursors. SEM images of the Cu₂Te nanosheets transferred from (c) Cu₂O and (d) Cu₂S.

Figure 6.6. (a-c) SEM and TEM images of the precipitate after reaction of 2 min (d) EDS mapping of the precipitate after reaction of 2 min; (e) XRD patterns of the precipitates obtained from different reaction times; right side shows crystal structures of hexagonal Cu₂Te (top) and fcc Cu₂Se (bottom), respectively.

Figure 6.7. XPS spectra of Cu₂Se nanoparticle precursor and the precipitates taken out after reaction of 2 min and 30 min, respectively.

Figure 6.8. HRTEM images of the samples obtained from different mole ratios of Cu₂Se:Te equal to (a) 20:1; (b) 10:1; (c) 5:1; and (d) 2:1. (e) Hybrid structure consisting of sheets and nanoparticles in the sample obtained from a ratio of 10:1. (f) Statistical thickness of Cu₂Te layers in (a-d).

Figure 6.9. Schematic illustration of the transfer reaction from Cu₂Se nanoparticles to Cu₂Te nanosheets.

Figure 6.10. SEM images of Cu₂Te nanosheets prepared from different concentrations of Na₂Te: (a) 0.1 M; (b) 0.05 M; (c) 0.02 M; (d) 0.01 M.

Figure 6.11. TEM images of different sized Cu₂Se nanoparticle precursors used in the experiments: (a) E4-1; (b) E4-2; (c) E4-3; (d) E4-4. (e) XRD results of E4-1 to E4-4.

Figure 6.12. Size distributions of Cu₂Se nanoparticles used in the experiments: (a) E4-1; (b) E4-2; (c) E4-3; (d) E4-4.

Figure 6.13. SEM images of Cu₂Te nanosheets fabricated from different sized Cu₂Se precursors. (a) E4-1; (b) E4-2; (c) E4-3; (d) E4-4.

Figure 6.14. 3D AFM images of Cu_2Te nanosheets fabricated from different sized Cu_2Se precursors. (a) E4-1; (b) E4-2; (c) E4-3; (d) E4-4. (e) The effect of Cu_2Se nanoparticle size on the specific surface area and thickness of E4-1, E4-2, E4-3 and E4-4 Cu_2Te nanosheets.

Figure 6.15. Cu_2Te nanosheets prepared with different mole ratios of NaBH_4 to Te. (a) 9:1; (b) 18:1; (c) 36:1; (d) 80:1.

Figure 6.16. SEM images of Cu_2Te nanotubes synthesized with different stirring speeds: (a) 100 rpm; (b) 300 rpm; (c) 800 rpm; (d) 1000 rpm.

Figure 6.17. (a) Photograph of the assembled Cu_2Te CEs; (b) J-V curves for the different CEs; (c) electrochemical impedance spectra for the CEs, with the inset showing the equivalent circuit; (d) Tafel-polarization curves for the CEs.

Figure 6.18. (a) BET results of Cu_2Te nanoparticles, nanosheets, and nanotubes; (b) Schematic illustration of different Cu_2Te CEs.

Figure 7.1. Preparation process for the $\text{Bi}_2\text{S}_3@\text{C}$ composite.

Figure 7.2. (a) PULVERISETTE-7 planetary ball milling machine and (b) HR800 Raman spectrometer.

Figure 7.3. (a) XRD patterns and (b) Raman spectra of Bi_2S_3 and the $\text{Bi}_2\text{S}_3@\text{C}$ composite. XPS spectra of the $\text{Bi}_2\text{S}_3@\text{C}$ composite: (c) survey spectrum; (d) S 2s; (e) Bi 4f ; (f) C 1s.

Figure 7.4. Morphologies of (a–d) the as-prepared Bi_2S_3 and (e–f) the $\text{Bi}_2\text{S}_3@\text{C}$ composite: (a), (b), and (e) SEM images; (f) EDS mapping; (c) and (g) low-magnification TEM images; (d) and (h) are high-magnification TEM images; inset of (h) is SAED pattern.

Figure 7.5. Electrochemical performance of the $\text{Bi}_2\text{S}_3@\text{C}$ composite electrode tested in the voltage range of 0–2.5 V. (a) Charge–discharge curves for selected cycles for the $\text{Bi}_2\text{S}_3@\text{C}$

composite charged at 60 mA.g^{-1} in $1 \text{ m NaClO}_4/(\text{EC}:\text{DEC})$ electrolyte a) with and (b) without FEC additive; energy density of the electrode in the electrolyte (c) with and (d) without FEC additive; (e) dQ/dV curves of the $\text{Bi}_2\text{S}_3@\text{C}$ composite with and without FEC additive at the first cycle; (f) rate capability tested at different current densities; (g) cycling performance of the $\text{Bi}_2\text{S}_3@\text{C}$ composite.

Figure 7.6. Electrochemical impedance spectroscopy (EIS) of the $\text{Bi}_2\text{S}_3@\text{C}$ electrodes after 5 cycles. Inset is the equivalent circuit.

Figure 7.7. Low and high magnification SEM images of the $\text{Bi}_2\text{S}_3@\text{C}$ electrodes (a, b) before and (c-f) after cycling in the electrolyte (c, d) without FEC and (e, f) with FEC.

Figure 7.8. (a) The cycling performance of the milled graphite; (b) EDS spectrum of the separator in the cell cycled for 100 cycles (inset: photograph of the separator).

Figure 7.9. TEM of the $\text{Bi}_2\text{S}_3@\text{C}$ electrode after 100 cycles. (a) Low magnification; (b) high magnification.

Figure 7.10. Ex-situ XRD patterns of the Bi_2S_3 electrodes charged or discharged to different states.

Figure 7.11. STEM characterization of the Bi_2S_3 electrodes (a-b) discharged to 0 V and (c-d) charged to 2.5 V. (a) and (c) are EDS mapping; (b) and (d) are SAED patterns.

Figure 8.1. (a) SEM image of copper telluride nanocubes; insets are the size distribution of the nanocubes, and a nanocube model; (b) HRTEM image with the FFT pattern (inset) of a selected area (marked by red rectangle); (c) X-ray diffraction pattern of copper telluride nanocubes; (d) XPS spectrum of Cu 2p from copper telluride nanocubes, with the satellite peak marked by “*” indicating the presence of Cu^{2+} arising from oxidation.

Figure 8.2. XPS spectra of Te 3d from (a) copper telluride nanocubes and (b) copper telluride nanosheets.

Figure 8.3. SEM images and size distributions of copper telluride nanocubes prepared from different reaction times: (a, d) 5min, (b, e) 6min, and (c, f) 8min.

Figure 8.4. SEM images and size distribution of nanostructures prepared using different CuCl concentrations at 250 °C: (a, d) 0.2 M, (b, e) 0.05 M, and (c, f) 0.01M.

Figure 8.5. (a-b) SEM images of samples prepared at 230 °C and 270 °C using 0.02 M CuCl; (c) size distribution of sample prepared at 230 °C; (d) XRD pattern of sample prepared at 270 °C.

Figure 8.6. SEM images and XRD patterns of copper telluride nanostructures prepared from different Cu/Te ratios (R) by using 0.02 M CuCl reacted with 1 M TOPTe at 250 °C for 10 min: (a) R=2; (b) R=1; (c) R=0.5; (d) XRD patterns of the 3 samples.

Figure 8.7. (a) SEM image, (b) size distribution and (c) X-ray diffraction pattern of copper telluride nanocubes synthesized with a ratio of 10 (CuCl/TOPTe).

Figure 8.8. XRD patterns of samples prepared in oleic acid, TOPO and oleylamine.

Figure 8.9. SEM images and XRD patterns of nanocubes prepared by adding small amount of ligands into TOP: (a) oleylamine; (b) TOPO; (c) oleic acid.

Figure 8.10. XRD and SEM images of samples prepared with different copper precursors. (a) XRD patterns; (b) CuBr; (c) CuCl₂; (d) CuF₂; (e) Cu(CH₃COO)₂; (f) Cu(acac)₂. All scale bars are 200 nm.

Figure 8.11. (a-b) XRD and SEM image of precipitate obtained by heating CuF₂ in TOP at 250 °C for 10 min. (c-d) XRD and SEM image of product obtained by heating CuCl in

oleylamine at 250 °C for 10 min.

Figure 8.12. (a) SEM image of copper telluride nanosheets synthesized at 250 °C for 10 min with 0.02 M CuCl; (b) SEM image of nanosheets synthesized at 230 °C for 10 min with 0.02 M CuCl; (c) XRD pattern of nanosheets synthesized at 250 °C for 10 min with 0.05 M CuCl; (d) Cu 2p spectrum of copper telluride nanosheets synthesized at 250 °C for 10 min with 0.05 M CuCl.

Figure 8.13. Different Cu_{2-x}Te sheet structure synthesized under different temperatures and CuCl concentrations. (a) TEM of sample synthesized with 0.02 M CuCl at 230 °C; (b) sample obtained from 0.02 M CuCl at 270 °C; (c) sample synthesized with 0.05 M CuCl at 250 °C; (d) sample synthesized with 0.005 M CuCl at 250 °C.

Figure 8.14. XRD patterns and SEM images of copper telluride nanostructures synthesized in pure oleylamine at 250°C for 10 min with different CuCl/TOPTe ratios (R): (a) XRD patterns; SEM images: (b) R = 3; (c) R = 2; (d) R = 0.5.

Figure 8.15. (a) SEM image, (b) XRD pattern, and (c-d) TEM images of hollow Cu_{2-x}Te nanoparticles synthesized by thermal decomposition of $\text{Cu}(\text{acac})_2$ in HDA. The scale bars in (d) are 10 nm.

Figure 8.16. (a-c) Typical charge-discharge voltage profiles of the initial 100 cycles of the Li/LiPF₆/Cu_{2-x}Te batteries cycled at a current density of 0.5 C from 0 to 2 V. The anode electrodes are made from (a) nanosheets, (b) hollow nanoparticles, and (c) nanocubes, respectively; (d) cycling performance of cells from 0 to 2 V at the rate of 0.5 C; (e) charge-discharge curves of three cells at various current densities; (f) cycling performance of the Li/LiPF₆/Cu_{2-x}Te (nanosheet) battery between 0 and 2 V.

List of Tables

Table 2.1. Some physical-chemical properties of S, Se and Te.

Table 2.2. Crystal structures of monochalcogenides of Group 12 metal.

Table 2.3. Comparison of some fabricating method for nanostructure.

Table 2.4. Experimental conditions used in preparation of PbSe nanocrystals and nanowires with different morphologies.

Table 3.1. Chemicals and materials used in this thesis.

Table 4.1. Water solubility (K_{sp}) of different metal chalcogenides.

Table 4.2. Reaction parameters applied in the preparation of metal chalcogenide nanostructures.

Table 4.3. Elemental analysis (EDS) results for Bi_2Se_3 nanoparticles.

Table 4.4. EDS result of Bi_2Te_3 sample.

Table 4.5. XPS spectra of individual elements in different metal chalcogenides

Table 4.6. SPS parameters used for sintering Cu_2Se , Bi_2Se_3 , SnSe, and Ag_2Se nanopowders, and the density of the resultant pellets.

Table 5.2. Calculated n and μ at different temperatures.

Table 5.1. Calculated lattice parameters at different temperature for the orthorhombic CuAgSe .

Table 6.1. Some physical-chemical parameters of cuprous chalcogenides.

Table 6.2. Reaction parameters for preparation of Cu_2Te nanostructures.

Table 6.3. Photovoltaic performance of QDSSCs with different CEs and EIS parameters in cells assembled with the same CdS/CdSe QD working electrodes.

Table 8.1. Reaction parameters for synthesising nanocubes and nanosheets.

Table 8.2. Inductively coupled plasma atomic emission spectrometry (ICP-AES) measurements of Cu_xTe nanocubes.

Table 8.3. Copper deficiency (i.e. x values) and theoretical capacity of the three copper tellurides used as anodes of LIB.

Chapter 1. Introduction

1.1 General Background.

With the explosive growth of population and the threat of global warming, as well as severe pollution problems, human beings have been pushed to develop cost-effective, high-efficiency solutions to meet the ever increasing demand for clean energy. Advanced functional nanomaterials and relevant nanotechnologies are playing a crucial role in resolving energy issues.¹⁻⁸ Especially, nanostructured metal chalcogenides (MCs), including sulphides, selenides, and tellurides, is a kind of materials including at least one metal cation and one chalcogen anion. Nanostructured MCs have been widely used in a variety of energy conversion and storage devices,⁹⁻¹³ such as fuel cells,^{9, 11-15} solar cells,^{5, 11, 16-19} light-emitting diodes,²⁰⁻²² Li/Na-ion batteries,²³⁻²⁶ supercapacitors,²⁶⁻²⁸ and thermoelectric devices,²⁹⁻³³ etc., because the chalcogenides elements are easy to form compounds with different kinds of structures, compositions and physical-chemical properties.

For example, as very promising non-precious metal catalysts for the oxygen reduction reaction (ORR), transition MCs are expected to serve as effective substitutes for the Pt-based electrocatalysts in fuel cell systems, such as Co_{1-x}S .^{3, 12-15} Many MCs have become popular choices for solar absorber materials and device architectures, such as CdSe, Cu_2S .^{5, 17-19, 22} Recently, layered metal di-chalcogenides (for example, MoS_2) have been actively investigated as electrode materials in Li-ion batteries and electrochemical supercapacitors.²³ Bi_2Te_3 and PbTe have long been thermoelectric materials possess the best performance.³⁴

1.2 Statement of the Problem.

The wide applications of nanostructured MCs are based on the progress in the synthesis of new nanostructured materials of different sizes and new morphologies.^{2, 20, 21, 23, 35} For one

thing, once the size of the MCs is reduced to the nanometer scale, new physical and chemical properties emerge owing to the quantum size effect.³⁶ In addition, the small size of nanostructured MCs provide a much higher specific surface area compared with their bulk counterparts, thus the activity of nanostructured MCs is significantly higher than corresponding bulk.^{35, 37} For another, the morphologies of nanostructured MCs may affect their specific area directly and the other properties, such as mechanical properties, transport properties of nanostructures.

Thereby the first important problem is that how to achieve precisely control over nanostructured metal chalcogenides. Besides, although now significant progress has been made in the technique of fabricating nanostructured materials, how to get high quality nanostructures in large scale with minimum cost is still a big challenge, and this also hinders the wide applications of nanostructured metal chalcogenides. For example, nanostructured metal chalcogenides have been proved to be effective thermoelectric materials, but to fabricate a thermoelectric module, at least grams of high purity nanopowders are needed. Although ball milling could achieve low cost and high yield to produce nanopowders, their drawbacks are also obvious, such as, the morphologies of the final product can't be controlled, there is a limit for reducing size of the product by ball milling, lots of impurities would be introduced into the product, as well as the long processing time needed.

In general, there are two big problems that wide application of metal chalcogenides as energy storage and conversion materials. The first is how to accurately tailor the properties of the nanostructures, while increasing the yield and minimizing the fabricating cost. The other is how will the nanostructures affect the performance of energy storage and conversion.

1.3 Objectives and Outlines of Research.

The overall objective of this doctoral work is divided into two parts: (i) Synthesis of

nanostructured metal chalcogenides materials with large yield, and well control over quality of final product. (ii) Application of these nanostructures in energy conversion and storage, the influences of morphologies, compositions of the nanostructures on the performance are well investigated.

The scope of the research that is carried out in this doctoral thesis is briefly outlined below as follows:

In chapter 1, the general background, and some major problems for fabricating of metal chalcogenides nanostructures, as well as their applications on energy conversion and storage are simply introduced. The objectives and outlines of the doctoral study are also presented.

Chapter 2 presents a comprehensive literature review on nanostructured metal chalcogenides, especially with respect to the structures of different metal chalcogenides; fabricating method; and some important applications of nanostructured metal chalcogenides based materials on energy conversion and storage including quantum dot solar cells, thermoelectric, and Lithium/Sodium ion batteries.

Chapter 3 presents the chemicals, methods, as well as general used characterizations and facilities used in the thesis, such as including X-ray diffraction (XRD), thermogravimetric analysis (TGA), differential scanning calorimetry (DSC), scanning electron microscopy (SEM), transmission electron microscopy (TEM), energy dispersive X-ray spectroscopy (EDS), Brunauer-Emmet-Teller (BET) surface area measurements, atomic force microscopy (AFM), physical property measuring system (PPMS), inductively coupled plasma atomic emission spectroscopy (ICP-AES), and X-ray Photoelectron Spectroscopy (XPS).

Chapter 4 exploits a large scale, low cost, aqueous synthesis route for different kinds of binary nanostructured metal chalcogenides, as well as the series control over the size,

compositions, and structures. Both surfactant free binary and ternary metal chalcogenides are fabricated. Four selenides prepared by this method are consolidated and tested their thermoelectric performance and thermal stability.

Chapter 5 presents the fabricating of ternary CuAgSe nanoparticles based on the method developed in Chapter 4. Reaction mechanism, thermoelectric properties of CuAgSe from 5 K to 623 K, band structure, and thermal stability are well investigated.

Chapter 6 describes synthesis of Cu₂Te nanosheets and nanotubes based on an anion exchange reaction in aqueous solutions. A new anion exchange mechanism, different from the Kirkendall effect is proposed. The effect of different synthesis parameters on the morphology, size and composition is also well demonstrated. Electrocatalytic activity properties of different Cu₂Te nanostructures as counter electrodes of CdS/CdSe co-sensitized quantum dot solar cells are reported.

In Chapter 7, nanorod like Bi₂S₃ is prepared in large scale from the method developed in Chapter 4. Their performance as anode of sodium ion batteries is tested and further improved by formation of composite with carbon. The effect of additives, composite; as well as sodium ion storage mechanisms are investigated using different characterizations.

Chapter 8 investigates the controlled synthesis of nanostructured Cu-Te system via a novel hot injection method, and the influence of synthetic parameters on their compositions, crystal structures, and morphologies. Electrochemical performance of these nanostructures as anode of LIBs is also well investigated.

Chapter 9 summarizes the conclusions we obtained from this doctoral work and providing some suggestions for further research work related to both the synthetic and applications of nanostructured metal chalcogenides materials.

Chapter 2. Literature Review

2.1 Metal Chalcogenides.

Metal chalcogenide (MC), is a group of inorganic chemical compound consisting of at least one chalcogen anion and at least one more electropositive metal element. Although elements from group VI_A are all called chalcogens, the term metal chalcogenide is more commonly reserved for sulfides, selenides, and tellurides, rather than oxides and polonium compounds. This is because with descending the group VI_A of Periodical Table, the metallic character of elements increases. Thus the extremely strong nonmetallic properties of Oxygen and strong metallic properties of Polonium (Po) made them totally different from the other three chalcogens (S, Se, Te). For example, elementary substance of O₂ is a gas while the others are solid, and the temperature coefficient of electrical resistivity for S, Se, Te is negative while Po has resistivity typical of metal. There are many kinds of metal chalcogenides with different structures and compositions, such as binary Na₂S, CaTe, Ti₂S, Cu₂Se; ternary CuFeS₂, CsBi₄Te₆, AgBiSe₂; quaternary Cu₂ZnSnS₄, AgPb_mSbTe_{m+2}, etc.. Diversity of metal chalcogenides is related with the d orbit of the transition metals, and more important, the properties of chalcogen elements, which are listed in Table 2.1.

2.1.1 Properties of Chalcogen Elements.

Table 2.1. Some physical-chemical properties of S, Se and Te.

	Sulphur (S)	Selenium (Se)	Tellurium (Te)
Atomic Mass	32.07	78.96	127.60
Atomic Number	16	34	52

Abundance in Earth Crust (ppm)	420	0.05	0.001
Toxicity	LD50 Oral - rat - > 2,000 mg/kg	LD50 Oral - rat - 6,700 mg/kg	LD50 Oral - rat - 83 mg/kg
Electronic Structure	[Ne]3s ² 3p ⁴	[Ar]3d ¹⁰ 4s ² 4p ⁴	[Kr]4d ¹⁰ 5s ² 5p ⁴
Melting Point (°C)	119.0	220.5	449.8
Boiling Point (°C)	444.6	694.8	989.8
Density (g/cm ³)	2.03	4.82	6.25
Atomic Radius (10 ⁻¹⁰ m)	1.00	1.20	1.40
X ²⁻ Ion Radius (10 ⁻¹⁰ m)	1.03	1.16	1.37
Electronegativity (Pauling's data)	2.58	2.55	2.10
Standard Redox Potential (V)	-0.48	-0.92	-1.14
(X + 2e ⁻ → X ²⁻)			

Some physical-chemical properties of chalcogens are listed in Table 2.1 and the elemental

substance powders are shown in Figure 2.1. The abundance of S [Figure 2.1(a)] is 420 ppm in the Earth's crust, numbered 16th in all the elements.³⁸ It exists in the form of both elemental and compounds of sulfides or sulfates. On the contrary, Se and Te, with a gray or dark appearance for powder [Figure 2.1(b) and (c)], are very rare in the crust, being 66th and 73rd.³⁸ The toxicity of S varies with the form, and Te possesses the highest toxicity (LD50 Oral - rat - 83 mg/kg), as presented in Table 2.1.

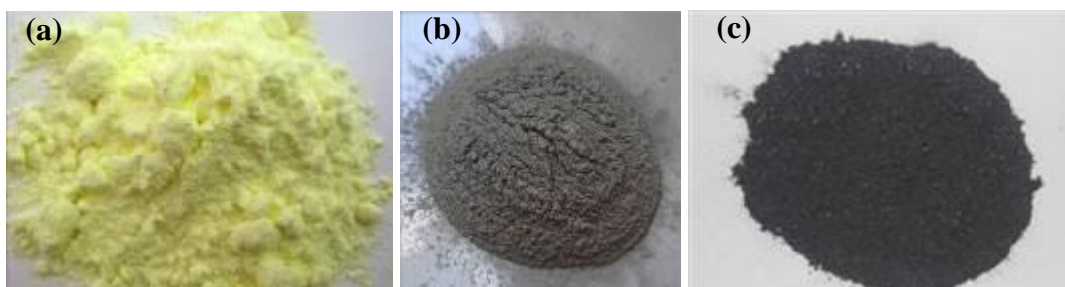


Figure 2.1. Image of (a) α -Sulphur, (b) gray Selenium and (c) Tellurium powder.

It is also easy to know from table 1 that with the increasing of atomic number (i.e., from S to Te), the atomic radius, as well as ion radius, increases from 1 to 1.4 Å and from 1.03 to 1.37 Å, respectively. Simultaneously the electronegativity of S to Te also decreased from 2.58 to 2.10, indicating the metallic character increases. The small atom radius and large electronegativity of S makes it has the tendency of catenation via sharing of electron pairs.

2.1.2 Category and Properties of Metal Chalcogenides.

Due to the non-metallic properties of chalcogens, plenty of metal chalcogenides can be formed; in addition the variety of polychalcogenide ions, the family of metal chalcogenides is further enriched. Moreover, for some metal elements, especially transition metals, which possesses unfilled d orbit, may lead to formation of off stoichiometry compounds, such as InSe, In₃Se₂, In₄Se₃; Cu_{1.97}S, Cu₂S; Ta₂S, Ta₃S; etc.. Thereby family of metal chalcogenides is extremely huge and diversity and could be categorized in many different ways.

For example, simply by chalcogen elements, they could be divided into sulfides, selenides, tellurides, and multi-chalcogen chalcogenides; while according to the number of elements-binary, ternary, quaternary and multi chalcogenides are defined. From the point of metal elements, main group metal chalcogenides, transition metal chalcogenides, as well as multi-metal chalcogenides can be defined. Most of main group metal chalcogenides are stoichiometry compounds, but for transitional metal, ascribed to the unfilled d orbit of transition (Group 3 to Group 12), it is easy to form off-stoichiometric MCs. The literature review of this doctoral work is limited to the binary metal chalcogenides, i.e., consisting only one kind metal cation and one kind chalcogen element. We categorized the binary MCs by the kind of metal elements, e.g., main group MCs, including metal elements from group 1, 2, 13, 14, and the transition metal MCs with metal elements from Group 3-12, as shown in Figure 2.2. The polychalcogenides are ruled out in these two group MCs since the polychalcognide ions have been discussed.

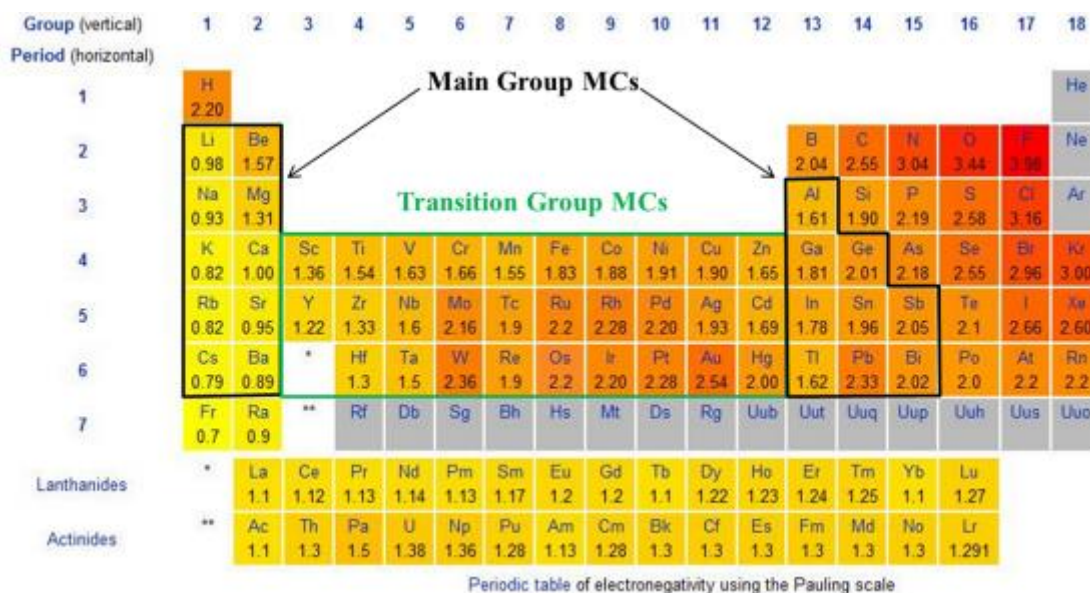


Figure 2.2. Main group MCs and transition group MCs, the electronegativity of different elements are also labeled.

To statement the crystal structures of MCs, atom arrangements and crystal information about

three basic type structures: NaCl type (RS), Zinc blende type (ZB), and wurtzite type (W), are respectively shown in Figure 2.3. For the zinc blende structure, the S atoms show a cubic symmetry and the Zn occupy half of the tetrahedral holes, which leads to a diamond like framework; while the atom connectivity in the wurtzite structure are similar (tetrahedral), but shows different crystal symmetry.

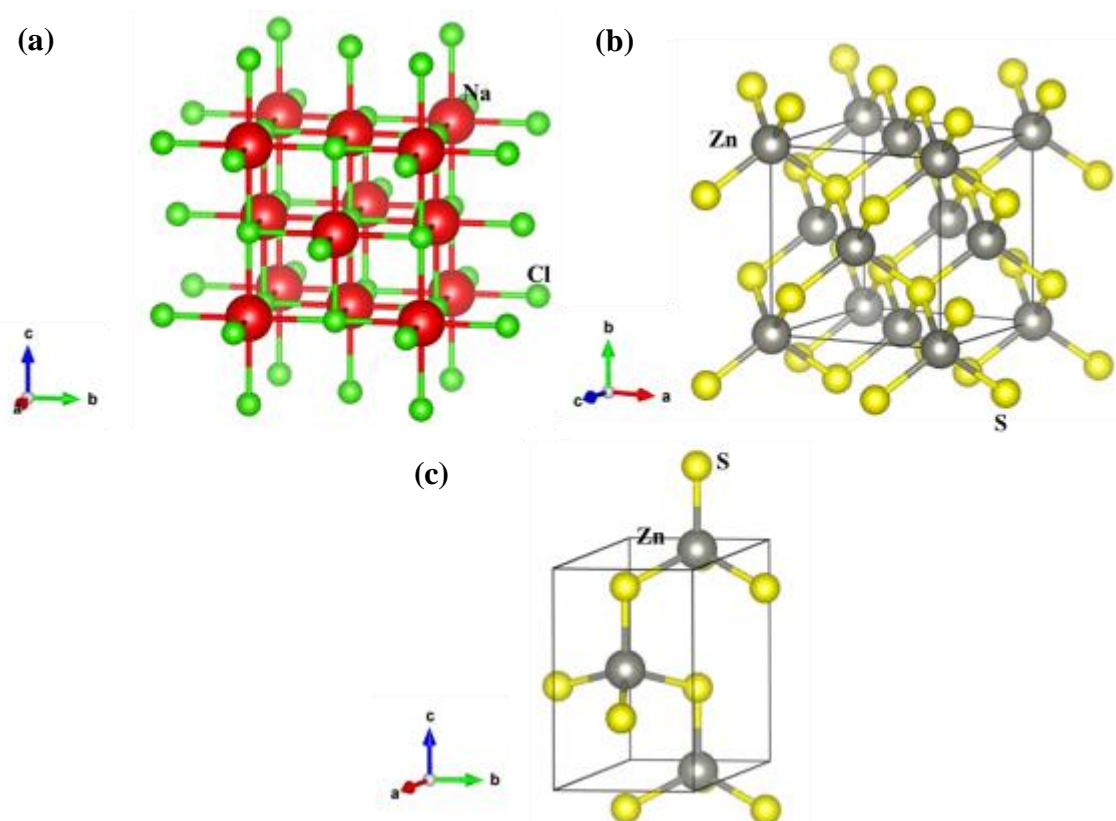
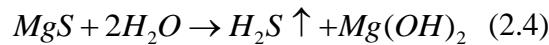
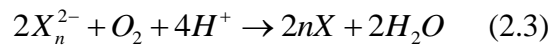
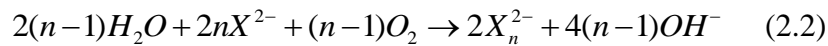


Figure 2.3. Atom arrangement for (a) RS, (b) ZB and (c) W type.

2.1.2.1 Structures and Properties of Main Group MCs.

(1) As shown by Figure 2.4(a), the alkali metal di-chalcogenides M_2X ($M=Li, Na, K, Rb$; $X=S, Se, Te$) often crystallize with the anti-fluorite structure, in which the alkali metal ions and chalcogen ions occupy the positions of F and Ca, respectively. The bonding of M-X is ionic bonding due to the big $\Delta\chi$ (Figure 2.2). Cs_2X ($X=S, Se, Te$) are an exception and crystallize in an anti- $PbCl_2$ type structure due to the big size of Cs [Figure 2.4(b)].

Alkali metal di- and poly- chalcogenides are both water soluble but di-chalcogenides usually tends to undergo hydrolysis to form derivatives containing HX^- anions according to Equation (2.1). They are soluble in water, but the solutions are easily oxidized to polychalcogenides, which makes the turbid red or purple black [Equation (2.2)]. Then the polyselenides and polytellurides are easy to react with O_2 like strong reducing agents, which reduce X_n^{2-} ions to X [Equation (2.3)].



(2) Alkaline earth metal monochalcogenides, MX (M=Mg, Ca, Sr, Ba; X=S, Se, Te) have a crystal structure of NaCl type (Fm-3m), as presented in Figure 2.4(c). BeX possesses zinc blende type structure [Figure 2.4(d)] due to the covalent bonding between Be and X, which is caused by small electronegativity difference ($\Delta\chi \leq 1.0$) with X. MgTe possess wurtzite type structure. Benefit from its covalent bonding, BeX is broad band gap semiconductors with band gap of 2.7-5.5 eV.³⁹ They are primarily used in luminescent devices.^{39, 40} It has been reported that the structures of MX (M=Mg, Ca, Sr, Ba; X=S, Se, Te) can be transferred from NaCl type (B1) to CsCl type (B2) under high pressure.⁴¹

Except insoluble BaS, other MX can partially or totally (for MgS) hydrolyze in warm water to form HX^- ions or H_2S , as shown in Equation (2.4). They could also react with oxygen to form the corresponding sulfate.

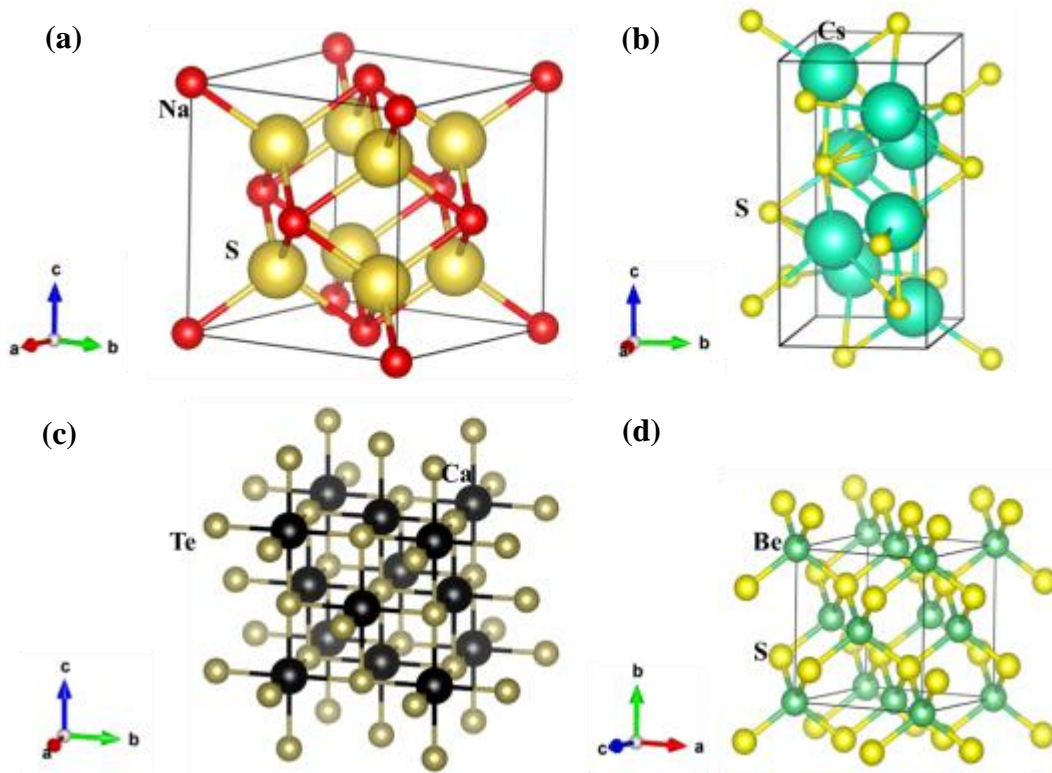


Figure 2.4. Crystal structure of (a) Na_2S ; (b) Cs_2S ; (c) CaTe ; and (d) BeS .

(3) Because the moderate electronegative difference with chalcogen elements ($0.29 \leq \Delta\chi \leq 0.97$), the chalcogenides composed by metal element from Group 13 (Al, Ga, In, and Tl) are extremely complex and diversity like transition Group MCs. Intrinsic, they possess vacancy structures possessing semiconductor properties because the smaller electronegativity (Figure 2.2). There is no off stoichiometry compounds for Al and Al_2X_3 ($\text{X} = \text{S}, \text{Se}, \text{or Te}$) is the only stable form. Due to the small size of Al compared with the X atoms, they usually form a wurtzite structure with tetrahedral coordination; two-thirds of the metal sites are occupied [Figure 2.5(a)]. On the contrary, chalcogenides of Ga, In, and Tl are much more complex with various atom ratio, e.g., several off stoichiometric phases exist.

Similar to Al, the M_2X_3 crystals ($\text{M} = \text{Ga}, \text{In}, \text{Tl}; \text{X} = \text{S}, \text{Se}, \text{Te}$) are mostly wurtzite (Ga_2S_3 , In_2Se_3) or zinc blende (Ga_2Se_3 , Ga_2Te_3 , In_2Te_3) structure. Because of the unequal atomic concentrations of the components, some lattice sites which are occupied in zinc blende and

wurtzite are vacant in these compounds, as shown in Figure 2.5(b). Moreover, a vacancy plane can be formed, such as in Ga_2Te_3 , which shows ultralow thermal conductivity due to the vacancy plane.⁴² Thereby it is a candidate of high performance thermoelectric materials.⁴² Despite their simple stoichiometric composition, M_2X_3 may show different possible structures. For example, In_2S_3 have three possible structures- α , β , and γ . α - In_2S_3 has a defect cubic structure and yellow color; red β - In_2S_3 has a defect spinel like tetragonal structure; and γ - In_2S_3 is layered hexagonal structure. Under ambient, the red β phase is most stable. In_2S_3 is insoluble in all solvents. No hydrolyze phenomena was observed. While In_2Se_3 and In_2Te_3 also have several polymorphs and wide applications through optical, thermoelectric to phase change memory materials.⁴³⁻⁴⁵

The monochalcogenides of MX (M=Ga, In, Tl; X= S, Se, Te) compounds, such as InSe, are known as layered structures with regular stacking of X–M–M–X layers [Figure 2.5(c)],⁴⁶ whereas InTe, TlS, and TlSe consist of chains of edge-shared tetrahedral.⁴⁷ These systems do not mean formation of M^{2+} cations; instead, the mixed valence has to be considered. For example, in TlSe, half of the metal atoms (Tl) are present as Tl^+ and half as Tl^{3+} ; Tl^{3+} ions are surrounded tetrahedral by four Se^{2-} ions, while Tl^+ is localized between long negatively charged chains of $(\text{Tl}^{3+}\text{Se}^{2-}_2)^-$; therefore the compound should be formulated as an $\text{Tl}^+\text{Tl}^{3+}\text{Se}_2$.⁴⁷ This is owing to the relativistic downshift in energy of the 6s orbital, thallium does indeed favor the oxidation state +1 over +3.⁴⁸ Another notable thing is that TlTe possesses a complex W_5Si_3 -type structure, which is different with TlSe [Figure 2.5(d)].⁴⁹ Besides MX type and polychalcogenides, there are several other off stoichiometric MCs for Group 13 element, such as Tl_2S , which possesses a distorted CdI_2 layer structure, i.e., Tl^+ ion is in trigonal coordination;^{50, 51} In_4X_3 , which is found to be a zinc blende structure semiconductor showing zigzag In-Se bonding,^{52, 53} etc..

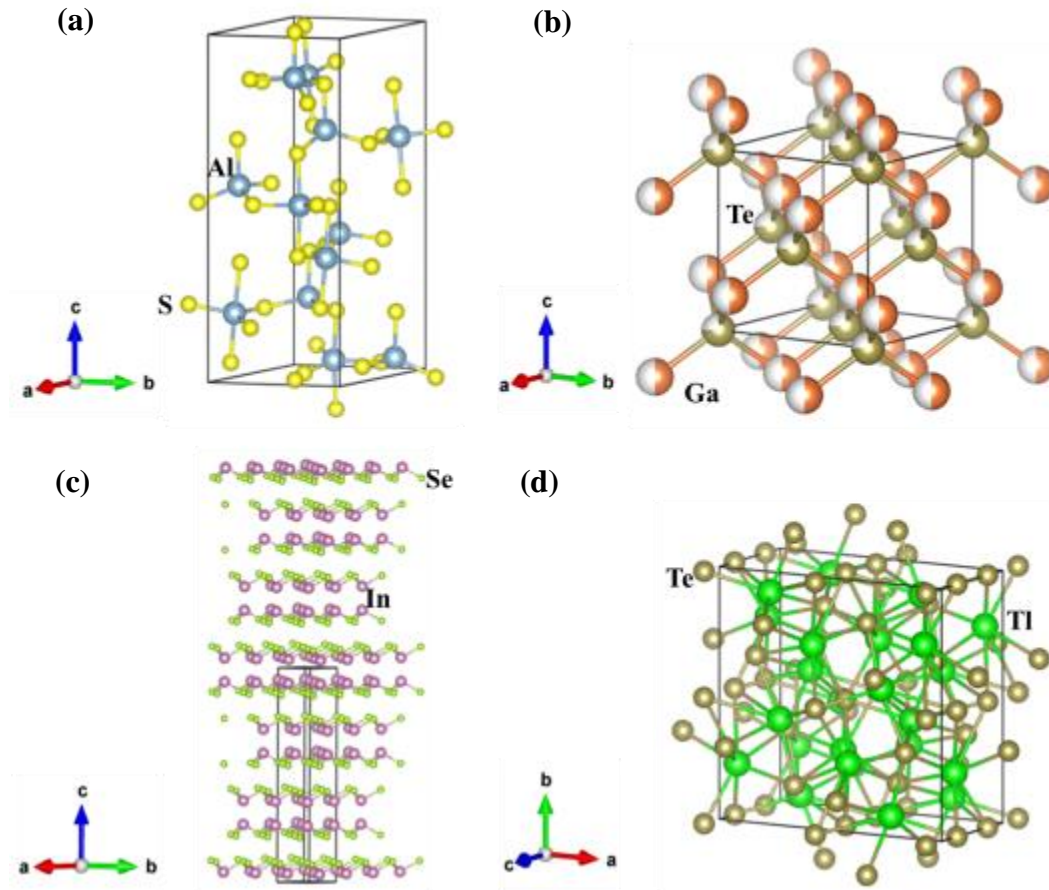


Figure 2.5. Crystal structure of (a) Al_2S_3 ; (b) Ga_2Te_3 , white part means vacant; (c) InSe ; (d) TlTe .

Most of binary MCs composed by Al, Ga, In, and Tl are wide band gap semiconductors and are widely used as optical materials, solar cells, and thermoelectric materials. For example, Al_2Se_3 , ($E_g=3.1$ eV), as well as Ga_2Se_3 , ($E_g=1.9\text{--}2.6$ eV) exhibit the advantage of having a small lattice mismatch compared with silicon (0.1 and 1.3% mismatch, respectively); therefore, they can be widely used in silicon-based technologies and other optical devices.⁵⁴ ⁵⁵ Ga_2Te_3 shows ultra-low thermal conductivity because the vacancy plane and thus is a good thermoelectric materials.⁴² $\text{In}_4\text{Se}_{3-x}$ has been proved to be high performance N type thermoelectric materials.^{53, 56, 57} Benefit from its various colors and the band gap of 2.1 eV,⁵⁸ In_2S_3 has the potential of application in solar cells, either as electrode or a buffer layer to replace hazardous cadmium chalcogenides.⁵⁸⁻⁶⁰ InSe (band gap 1.0 eV) could be also used in

silicon based solar cells.⁶¹ In_2Te_3 ($E_g=1$ eV) has a suitable match with the solar spectrum, and presents good radiation stability. Besides, its electrical conductivity is insensitive to impurities.⁶²

(4) With the metallic elements of Group 14, two kinds of MCs could be formed, monochalcogenides, MX and dichalcogenides of MX_2 (M=Ge, Sn, Pb; X=S, Se, Te). The crystalline structure of MX can be viewed as distortion of the NaCl type (or zinc blende type) depending on the components, the lighter the atoms, and the larger distortion. There is big distortion in GeS and SnS, while structure of GeTe, SnTe and PbS is the NaCl type without distortion, as presented in Figure 2.6(a-d). Instead of showing NaCl type structure, MX (M=Ge, Sn; X=S, Sn) exhibit layer structures and a semiconductor conductivity. However, recently a new cubic phase consisting of 64 atoms in each unit cell for SnS is reported, which was deduced to be associated with the NaCl-type structure.⁶³

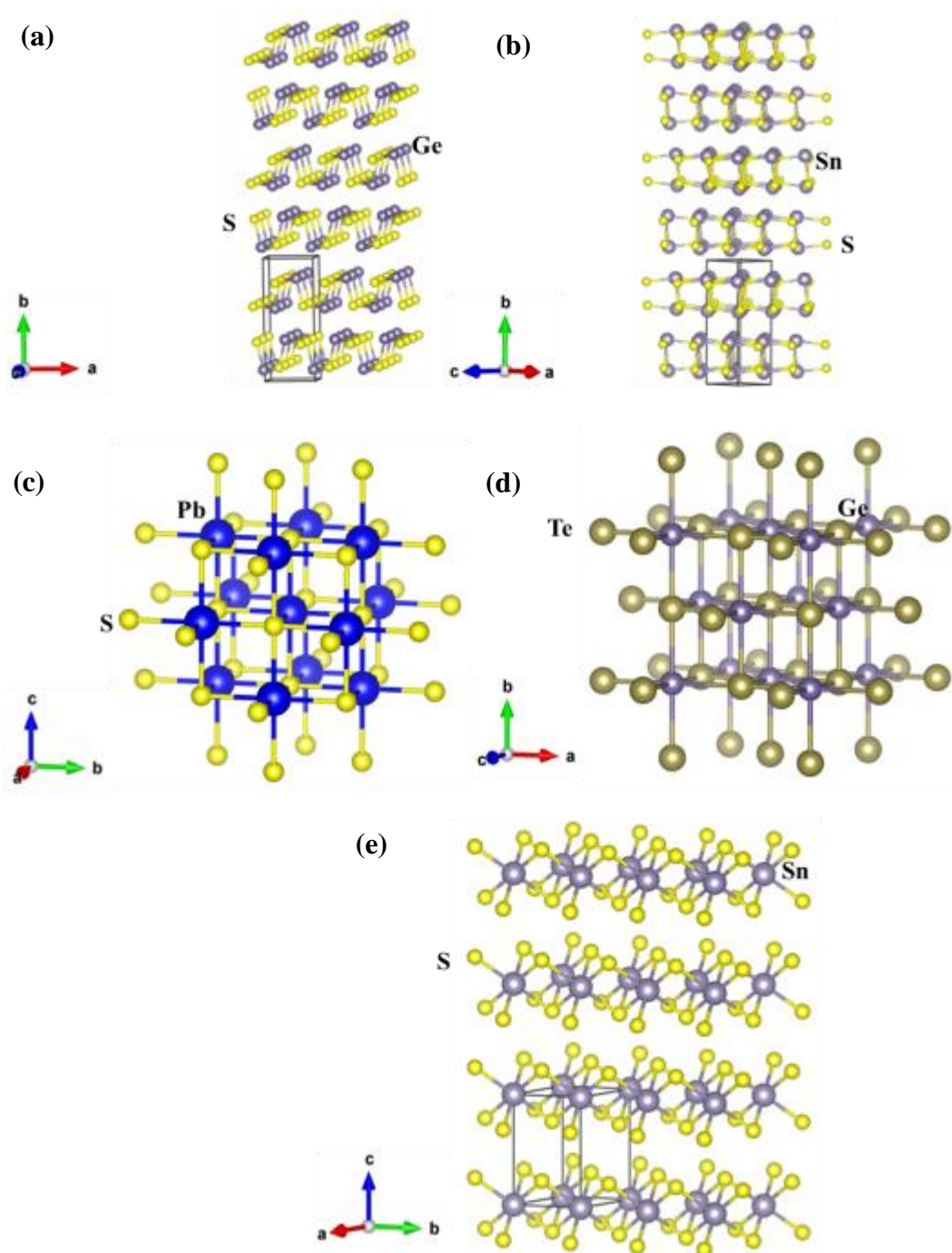


Figure 2.6. Crystal structures of (a) GeS, (b) SnS, (c) PbS, (d) GeTe, (e) SnS₂.

Other binary metal compounds in this group, such as MX_2 ($\text{M}=\text{Sn, Ge}$; $\text{X}=\text{S, Se}$), Sn_2S_3 , and Sn_3S_4 . GeS₂ is reported to present a layered structure consisting of a 3D framework of GeS₄ tetrahedra;⁶⁴ while SnS₂ has a CdI₂-type layered structure and weakly bound S atoms between the layers, which allows a cleavage in [001] direction [Figure 2.6(e)]. Nominally it is an n-

type semiconductor. The MCs composition ranges from SnS_2 to SnSe_2 also comprise CdI_2 -type layered structures. Sn_2S_3 (orthorhombic structure) is also a semiconductor ($E_g=0.95$ eV).⁶⁵

The layered MX (M=Ge, Sn; X=S, Se) are non-centrosymmetric, allowing them to be good piezoelectric materials.⁶⁶ And due to the zigzag arrangement of Sn-Se bonding, single crystal SnSe has been proved to be the most effective P type thermoelectric materials with $ZT=2.6$.⁶⁷ PbX (X=S, Se, Te) are narrow band gap semiconductors and also traditional thermoelectric materials with high performance due to their special band structure and low thermal conductivity.^{29, 32, 68} Besides, MCs composed by Ge, Sn, Pb (such as PbS_2 , SnS_2 , SnS , etc.) has also been used on energy storage and solar cells.⁶⁹⁻⁷⁴ Ge-X system is easy to form amorphous (or chalcogenides glass) structures. They are promising infrared optical materials, xerography, switching and memory devices, photolithography and in the fabrication of inexpensive solar cells, as well as for reversible phase-change optical recording.⁷⁵⁻⁷⁸

(5) Metal elements M from Group 15 (Bi and Sb) possess almost the same electronegativity with chalcogens from Group 16 ($0.05 \leq \Delta\chi \leq 0.56$). Thereby strong covalent bonding between M-X is formed and almost no off stoichiometry phase can be formed, e.g., they are all in the form of M_2X_3 (M = Sb, Bi; X= S, Se, Te) and show semiconductor properties. The intrinsic band gap of sesquichalcogenides M_2X_3 decreases from Sb to Bi for a given chalcogen and in the sequence $\text{S} > \text{Se} > \text{Te}$ for a given metal. Stibnite Sb_2S_3 , has an orthorhombic structure, as shown in Figure 2.7(a). Sb_2S_3 and Sb_2Se_3 are regarded as a promising material for solar cells because of their direct band gap of 1.8–2.5 eV and other various optical devices.⁷⁹⁻⁸¹ Bismuth sulfide, Bi_2S_3 (stibnite structure), with its direct band gap of 1.3 eV has a large potential in optoelectronics and thermoelectric materials.⁸²⁻⁸⁴ The selenide and telluride semiconductors Bi_2Se_3 , Sb_2Se_3 , Bi_2Te_3 , and Sb_2Te_3 show a layered structure. For example in Bi_2Te_3 , Bi-Te layers are arranged in the order -Te(1)-Bi-Te(2)-Bi-Te(1)- along the c-axis direction, where

the Bi-X(2) bond is covalent while the Bi-Te(1) bond is a covalent–ionic bond. The interaction between two adjacent Te(1) layers is via weak van der Waals forces [Figure 2.7(b)]. The layered M_2X_3 ($M=Sb, Bi, X=Se, Te$) system, along with their solid solutions, are well-known as excellent thermoelectric materials and topological insulator.^{29, 30, 34, 85-88}

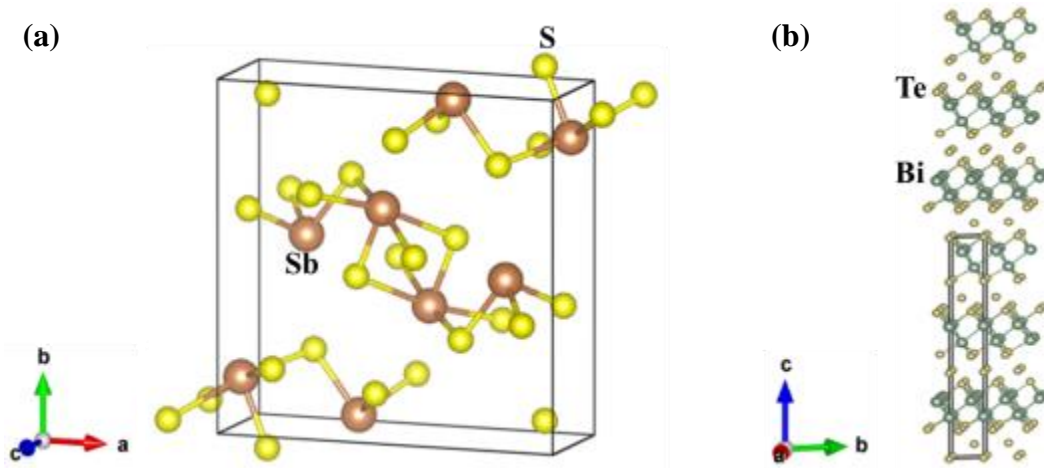


Figure 2.7. Crystal structure of (a) Sb_2S_3 , and (b) Bi_2Te_3 .

2.1.2.2 Structures and Properties of Transition Group MCs.

Although composed only by one metal and one chalcogen, transition metal chalcogenides occur with various stoichiometry and diversity structures due to the unfilled d orbit and moderate electronegativity. Non-stoichiometry binary MCs could be divided into the “chalcogen rich” and “metal rich” phase, such as TaS_2 and Ta_3S_2 . The complexity of metal-chalcogen bonding, as well as excess chalcogen-chalcogen or metal-metal bonding further increases the diversity of structures for the binary transition chalcogenides. For instance, according to the properties of Sulphur-Sulphur bonding, the transition metal sulfides would be classified as “Sulphur rich” phases including S-S bonding, usually in the form of di-Sulphur units S_2^{2-} (such as FeS_2) or compounds like TaS_3 and TiS_3 containing both di- and single-Sulphur units. While without presence of S-S bonding, series stoichiometry transition metal sulfides including only S^{2-} center, e.g., MoS_2 and FeS , are formed. On the other hand,

metal rich phases (like Ta_3S_2) exhibiting excess metal-metal bonding also exists.

The transition MCs are easy to form low dimension structures because compared with the ionic bonding in 3D network of oxides, transition MCs tend to form covalent structures, thereby the electron pair is prone to form metal-metal bonding. Thus coordination polyhedral structure is easy to form. And the linkage of these polyhedral often ends up with an arrangement of metal clusters, which are usually condensed by sharing common vertices, edges, or faces. Chain (or column) structures are also common, in which the central metal atoms interact to form the one dimension chain like structure while in layered chalcogenides,⁸⁹ enough d-electrons in transition metal could also offer significant M-M bonding to form two dimension structure. Further, in certain cases,⁹⁰ the metal cluster network is best regarded as a 3D framework, i.e., as a metal packing arrangement. It may be emphasized in this connection that the occurrence of M-M bonds in MCs has substantiated the use of classification schemes based on structural elements rather than oxidation numbers, rationalizing thus the coincidental integer values of the oxidation state of transition metals and consequently the apparent stoichiometry.⁹⁰

Atom size, valence electron concentrations, and bonding between elements play key roles in the determination of structure features.⁹¹ Luckily, among the diversity structures of transition MCs, the most common and most important structures, however, are the chalcogenides with simple stoichiometry, such as 1:1 and 1:2, because for a large part the binary compounds belong or related to the very basic structural types and may be approached easily in a descriptive manner. “3D” structures, commonly the cubic NaCl type and Zinc Blende type, or the hexagonal NiAs and Wurtzite types, as well as “2D” layer-lattice varieties related to the CdI_2 type, are the major structure types observed. The simple compounds formed by selenium and tellurium are generally similar with their sulfide analogues, although there are differences.

Structures of most MCs show strong relationship with their electronegativity. For example, the metal elements from Group 1 and 2, which possess a small electronegativity (i.e., a big difference with chalcogens), show anti-fluorite structure; while derived from the 4:8-coordinated anti-fluorite forms of alkali metal chalcogenides structure, monochalcogenides of metal elements with slighter higher electronegativity (such as metal from Ln and Ac series) adopt the 6:6 NaCl type structure. And with further decreasing of electronegativity difference, the ionic RS structure gradually gives way to ZB and W types. Thus the increasing electronegativity of many metals in the later transition-element groups (with higher electronegativity) causes lower coordination numbers in their structures; for example, the monosulfides of Zn, Cd may adopt either the ZB or W structure,⁹²⁻⁹⁵ while those of Hg, and Mn adopt the ZB and W structure, respectively.^{96, 97} When further increasing of electronegativity (i.e., decreasing $\Delta\chi$, increasing metallic property), the 6:6 NiAs structure is observed, where the metal is now of octahedral coordination. This structure can be regarded as intermediate state between the RS structure and the more highly coordinated structures of metals. Most first row (3d) transition metal monochalcogenides MX (M=Ti, V, Cr, Fe, Co, Ni) come under this case.^{98,99} These compounds often contain vacancies at the metal site, so that the crystal becomes distorted owing to vacancy ordering which varies with temperature as well as composition. Their magnetic and electrical properties are generally complex and depend on the vacancy order.

Sc	Ti	V	Cr	Mn	Fe	Co	Ni	Cu	Zn
Y	Zr	Nb	Mo	Tc	Ru	Rh	Pd	Ag	Cd
La	Hf	Ta	W	Re	Os	Ir	Pt	Au	Hg



	Octahedral		Trigonal Prismatic
---	------------	---	--------------------

Figure 2.8. Layered transition metal sulfides or selenides with the metal in octahedral or trigonal prismatic coordination (Nb and Ta are found in both).¹⁰⁰

Many transition metal elements react with chalcogen atoms to give dichalcogenides MX_2 with a precise 1:2 stoichiometry, crystallizing in either 2D or 3D structures, depending on the atom size, valence electron concentrations, and bonding between elements. Two thirds of the MX_2 MCs possess a layered structure formed by one third of the transition metal element from Group 4-6, as shown in Figure 2.8, which can be formulated as $\text{M}^{4+}(\text{X}^{2-})_2$, consist of sandwiched sheets of the X-M-X form, separated by a “van der Waals” gap between the X layers of adjacent sheets.¹⁰¹ As shown in Figure 2.9(a-b), inside the sheets, the coordination of the metal ions is sixfold, either octahedral (as in the 1T poly type, which is more commonly denoted as the CdI_2 structure) or a body-centered trigonal prism (2H poly type).^{101,}¹⁰² Conduction of the MX_2 transition MCs varies from semiconductor to metallic. Note that the layered structures may be derived from vacancy ordering of the basic 3D types, for instance, 1T arrangement can be viewed as a defect NiAs structure in which every other plane of Ni atoms has been removed.¹⁰¹

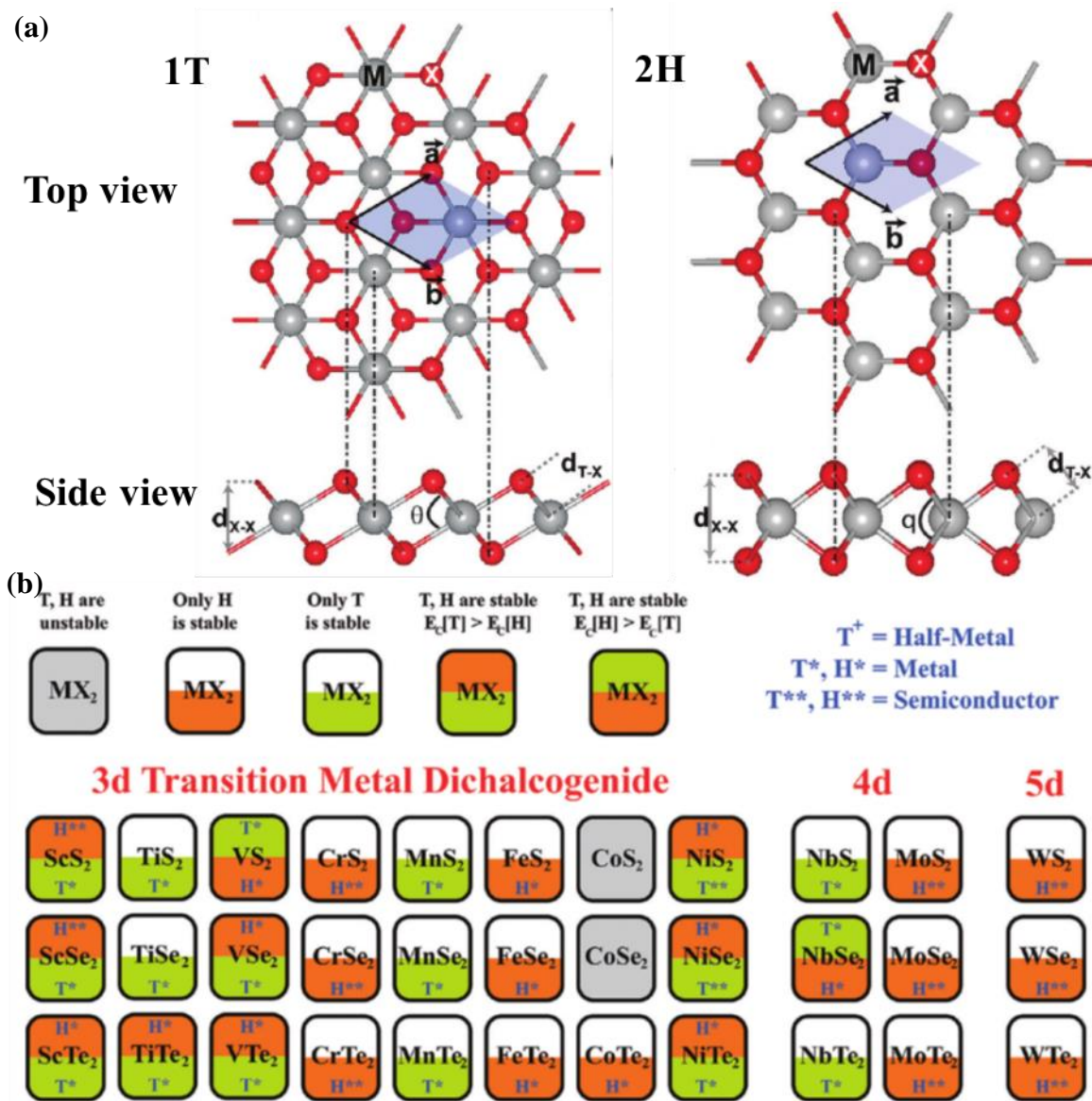
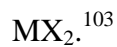


Figure 2.9. (a) top view and side view of 1T and 2H type structure; (b) stable structure for



Although comprising a simple structural and stoichiometry composition, the layered MX_2 (M represents transition metal), displays various properties and applications, such as order-disorder phase transition,¹⁰⁴ strong d-p covalent mixing and fast ionic diffusion.^{105, 106} They cover wide applications on thermoelectric, optical device, energy storage; superconductivity; metal-insulator transistors, etc..¹⁰⁷⁻¹⁰⁹ Besides, now this class compounds has also been the star materials in exploring unusual electronic phenomena such as quantum size effects, and

charge wave density waves (i.e., coupled fluctuations of electronic density and atomic positions along a conducting chain or layer).¹¹⁰⁻¹¹³ Moreover, their layered structure offered good platform for the rich intercalation chemistry with many potential applications.¹⁰⁰ The intercalation process is accompanied by charge transfer, reducing the M^{4+} centers to M^{3+} .

The non-layered MX_2 compounds usually formed by the elements from "late" transition metal disulfides (Mn, Fe, Co, Ni) present quite different infinite "3D" networks composed by metal atoms and X_2 units.¹¹⁴ As shown in Figure 2.10, two structures of close similarity exist in this connection: pyrite (such as MS_2 ; M= Fe, Mn, Co, Ni, Cu, Ru, Os) and marcasite (known only for FeS_2 among the disulfides). Dichalcogenides of this type can be formulated as $M^{2+}(X_2)^{2-}$ or $M^{1+}(X_2)^{1-}$, respectively. Various 3D structure transition MCs will be briefly introduced in the following part.

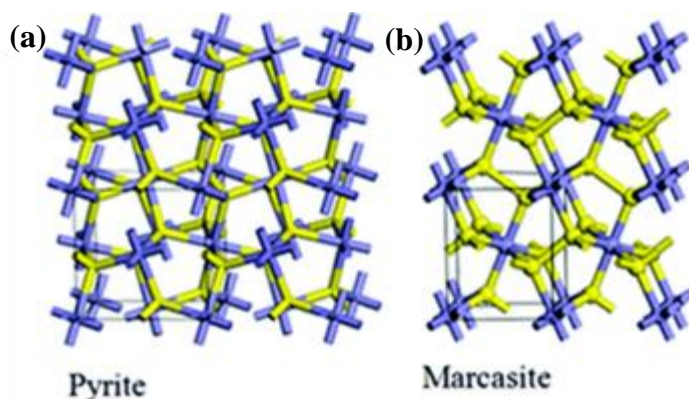


Figure 2.10. Crystal structure of FeS_2 with (a) pyrite structure, and (b) marcasite.¹¹⁵

The rare earth metal elements (La and Ac series), as well as Sc and Y possess similar chemical properties and form a bridge between the highly reactive Cs, Ba and Hf. However, their physical properties varied due to the subtle features of electronic structures. The rare earth elements may form many kinds of stoichiometry chalcogenides including RX_2 , R_2X_3 , R_3X_4 , and RX ($R=Sc, Y, La, Ac$) with many different structures due to mixed valence effects (i.e., different valences exist on one element in one compound).¹¹⁶ Most monochalcogenides

(RX) of the Group 3 metals adopt the Rock Salt (NaCl) structure, while R_2X_3 contains several structures, in which the most common is the cubic Th_3P_4 type structure. As an example, high temperature structure of Ce_2S_3 is shown in Figure 2.11(a), a defect-type Th_3P_4 structure, involving Ce atoms occupied 8-coordinate positions randomly.^{117, 118} Interestingly, with the increasing the metal content from the stoichiometric R_2X_3 to R_3X_4 , the conductivity of materials improved from an insulator or semiconductor to a semimetal and finally to a metallic substance, this is related with the increasing of metallic bonding. For instance, the stoichiometry Ce_2S_3 is insulator, with increasing Ce content to off stoichiometry Ce_3S_4 [Figure 2.11(b)] its electrical conductivity increases and color changed from red to grey.¹¹⁹ Unusual metal rich phase of RX_2 , such as $ScTe_2$, Dy_2Te , Gd_2Te , can be described in terms of 10-atom macro-cluster sequences further condensed into infinite columns that are separated by telluride atoms.¹²⁰ In addition, another metal rich phase, M_8X_3 , contains two types of complex puckered metal sheets separated by chalcogenide anions.¹²⁰

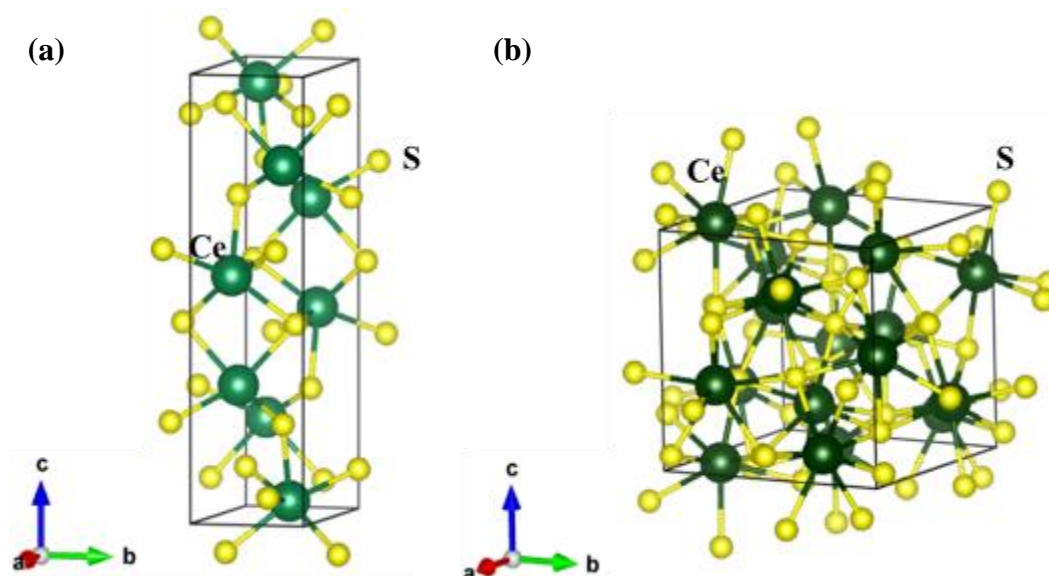


Figure 2.11. Crystal structure of (a) Ce_2S_3 and (b) Ce_3S_4 .

Besides the NiAs type MX and layered MX_2 structure, the chalcogenides of Ti, Zr, Hf are extremely complex because the variety of other stoichiometry compositions,^{121, 122} such as

Ti₂Se, Ti₈S₃, HfTe₅, ZrTe₃, etc.. Zr and Hf own similar chemical properties because they have nearly same atomic and ionic radius, electronegativity, and atom structure, however, the physical of their chalcogenides have a big difference.¹²³ Their applications are mainly derived from corresponding layered MX₂ structures.

The vanadium–chalcogen system comprises metal-rich (V₃S, V₂Se, V₅Te₄) and chalcogen-rich (VS₄, VSe₂, VTe₂) phases, and their structures can be derived from the NiAs or CdI₂ structure.^{124, 125} Low dimension structure is a common feature in many Nb and Ta chalcogenides besides MX₂ (M = Nb, Ta; X = S, Se, Te), such as MX₃ (X = S, Se), MTe₄, Nb₃X₄ (X = S, Se, Te), and Ta₂X (X = S, Se).^{126, 127} Metal-rich compositions, such as the tantalum systems Ta₆S, Ta₂S, Ta₆Te₅, etc., apply unique structures like the sandwich of layered structures. For example, the metal framework of Ta₆S consists of distorted, centered Ta₁₃ icosahedra, which extend along a “fivefold axis of symmetry” to form chains; or Ta₂Se exhibits quasi-2D structure, where the layers of metal and chalcogen atoms are arranged in the same way as in the structure of bcc Ta. Vanadium chalcogenides (such as V-S system) show anomalous magnetic properties;¹²⁸ while Nb and Ta chalcogenides are used to investigate charge wave density and applied in the field of superconductor.^{126, 127, 129, 130}

Cr-X system also possesses complex compositions and provides instances of defect structures intermediate between the NiAs type and the CdI₂ one, containing vacant metal sites; they are widely studied as magnetic and thermoelectric materials.¹³¹⁻¹³⁴ Such as Cr-S system, with two forms of Cr₂S₃ (trigonal and rhombohedral) and several intermediate phases Cr₂S₃ those and CrS, (Cr₇S₈, Cr₅S₆, Cr₃S₄).¹³² Rhombohedral Cr₂S₃ has complex electrical and magnetic properties.¹³⁵ Cr₃S₄ is found to have a wide range of homogeneity; deviations from stoichiometry within this range are due to the existence of point defects.¹³⁴

The layered MX₂ (M=Mo, W; X=S, Se) compounds are layered structures and stable with the

2H type poly type (Figure 2.9). However, another 3R poly type is also possible, as reported by literature.¹³⁶ They have received much attention due to their optical, electrochemical, and mechanical properties, as well as their rich intercalation chemistry. Their applications include solid-state and photo-electrochemical solar cells, rechargeable batteries, and solid lubricants.

As an important magnetic element, Mn can form magnetic material Rock Salt type MnX and pyrite structure MnX₂, which can't form energy bands due to the strong electron correlation except MnTe is a P type semiconductor (direct band gap 1.3 eV) and can be used as diluted magnetic semiconductors, photovoltaic and thermoelectric applications.¹³⁷⁻¹⁴¹

TcX₂ (X=S, Se, Te) and ReX₂ (X=S, Se) are both semiconductors with layered structures, but do not belong to 1T and 2H poly type structures, instead, TcX₂ adopts a stacking similar with Cd(OH)₂ type.¹⁴² TcTe₂ has been found to crystallize in a monoclinic layer structure.¹⁴³ ReX₂ is a CdCl₂ type structure (triclinic symmetry) distorted by Re-Re bonding network with 4 or 8 molecules in each unit cell.^{144, 145} ReTe₂ does not own a layered structure but orthorhombic. Notable that the disulfides in ReX₂ and TcX₂, unlike the pyrite-type Mn²⁺S₂, are two S²⁻ units (i.e. valence of Tc and Re are +4).¹⁴² Tc and Re have other high states chalcogenides, such as M₂X₇ and MX₄ and much stronger metallic bonding than Mn may lead to more M-M bonding in their structures.^{146, 147} Chalcogenides of Re and Tc are mainly applied on photovoltaic and catalysts of hydrogenation.¹⁴⁸⁻¹⁵⁰

FeS is NiAs type structure containing random Fe vacancies, and magnetic and electronic properties of FeS depends on the vacancy order. Pyrite FeS₂ could be regarded as a distorted NaCl type structure, in which Fe occupies position of Na and the S₂²⁻ group are placed with their centers at Cl position. FeSe and FeTe adopt PbO type structure with a layered structure. FeSe₂ is a marcasite structure; FeTe_{1.5} is defect NiAs structure with one third of Fe is missing; however, situation for Fe-Te is complex including both FeTe, FeTe₂, Fe_{1.1}Te, FeTe_{1.4}, etc..¹⁵¹

Co and Ni possess similar sulfides and selenides with Fe. But both CoTe and CoTe₂ possess a NiAs type structure. This structure is stable with Co content decreasing from CoTe to CoTe₂ until every other plane of Co atoms present in CoTe has completely vanished. Similar behaviour is available in other systems (V–Se, Ti–Se, Ti–Te, and Ni–Te). This property leads to the variety of these systems, which can have any composition between those corresponding to MTe and MTe₂ (M=V, Ti, Co, Ni).

Benefit from their low cost, chalcogenides of Fe, Co, Ni have variety applications such as energy storage, magnetic materials, superconductor, photovoltaic, thermoelectric and oxygen reduction.¹⁵²⁻¹⁵⁸

Ru and Os only possess the basic MX₂ (M=Ru, Os; X=S, Se, Te) type with the pyrite structure,^{159, 160} while Rh and Ir owns diverse structure types besides basic MX (NiAs type) and MX₂ (pyrite type), such as M₂X₃ (M=Rh, Ir; X=S, Se) with the metal atoms in octahedral arranged in layers of ABAB stacking; Rh₃X₄ (X=S, Se, Te) with a monoclinic modification of NiAs type structure, and M₃X₈ (M=Rh, Ir; X=Se, Te) in a rhombohedral modification of a pyrite structure.³⁸

Chalcogenides of Pt and Pd are more diverse than Rh and Ir. Besides MX and MX₂ (M=Pt, Pd; X=S, Se, Te), Pd₃X and Pd₄X (X=S, Se, Te) are also found. Detailed structures for different chalcogenides of Pt, Pd, Ir, Os, Ru, Rh, as well as their applications are well presented in a comprehensive review.¹⁶¹

Binary copper chalcogenides are the well-known I_B-VI_A semiconductors adopting various stoichiometry and polymorphs because the existence of many defected structures.¹⁶²⁻¹⁶⁴ For example, in the Cu-S system, Cu₂S, pyrite-type CuS₂, Cu_{2-x}S, Cu_{1.96}S, Cu_{1.94}S, Cu_{1.8}S, Cu₇S₄, Cu₉S₈, CuS etc. exist. Likewise, the Cu-Se and Cu-Te system both include several kinds of chalcogenides, such as Cu_{2-x}Se, Cu₇Se₄, Cu₃Se₂, Cu₅Se₄, Cu₇Te₅, Cu_{2-x}Te, Cu₃Te₄, etc..¹⁶⁵

Usually Cu-X system show variety of crystal structures and phase transitions, such as Cu_2Se and Cu_2Te has a unique hexagonal structure with mean coordination number at low temperature; while with temperature rising, they gradually changed into fcc structure with Se atoms form the lattice and Cu atom highly movable, namely super ionic state,¹⁶⁶ which is extremely good for thermoelectric application due to the enhanced phonon scattering by movable Cu ions.¹⁶⁷ To explain this property, the crystal structure of the high temperature cubic phase of Cu_2Se is presented in Figure 2.12(a), in which the Se atoms are stacked in a close-packed arrangement with the layers in the sequence of ABC. The Cu1 position is located exactly at the center of the tetrahedral interstice, whereas the Cu2 and Cu3 atoms are located close to a triangular face of the tetrahedron. Each tetrahedron is always occupied by a copper atom; however the copper atom can be disordered in static or dynamic manner, which means that Cu^+ can easily drift among the Cu1, Cu2 and Cu3 positions inside the tetrahedron.¹⁶⁸

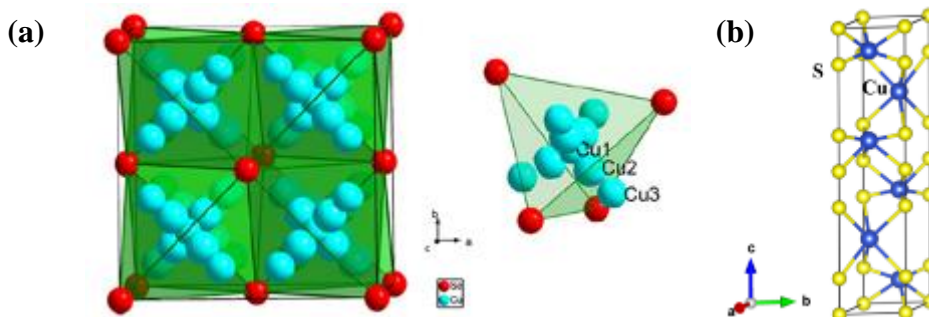


Figure 2.12. (a) High temperature structure of Cu_2Se ;¹⁶⁸ (b) crystal structure of CuS .

Another notable thing is that CuS , instead of NiAs type structure, adopts a very unusual structure, in which the Cu is both partly 3-coordinate and partly 4-coordinate, with two-thirds of the Sulphur atoms existing as S_2 groups like those in pyrites [Figure 2.12(b)]. The low-temperature form of CuSe has also a covellite structure, the high-temperature modification (β - CuSe) being orthorhombic. All CuX_2 ($\text{X}=\text{S}, \text{Se}, \text{Te}$) crystallize in pyrite-type structures.

A few binary chalcogenides of silver and gold are known. Ag_2X is insoluble black substance exhibiting low temperature phase and a high temperature super ionic phase. Au_2S has the cuprite structure and little is known for the Au_2X_3 system, however, Au_2Te_3 , Au_3Te_5 , and AuTe_2 have been reported.

One way to account for the ambiguous valence of the metal and chalcogen atoms in such compounds is by using the concept of mixed valence. For example, formula of CuS would be presented as $(\text{Cu}^+)_4(\text{Cu}^{2+})_2(\text{S}^-)_2(\text{S}^{2-})_2$; while AuX should be $(\text{Au}^+)(\text{Au}^{3+})(\text{X}^{2-})_2$. The chalcogenides of Group 11 (I_B) have long been investigated and remarkable progress has been made, the variety of their compositions and structures span a broad spectrum of electrical and magnetic properties, thereby leads to their wide applications ranging from sensors, energy storages, photovoltaic to thermoelectric, oxygen reduction, localize surface plasma resonance, phototherapy, and so on.¹⁶⁹

All the metal monochalcogenides of the Group 12 metals MX ($\text{M}=\text{Zn}, \text{Cd}, \text{Hg}$; $\text{X}=\text{S}, \text{Se}, \text{Te}$) crystallize in the tetrahedral zinc blende (ZB) or wurtzite (W) structures, as shown in the Table 2.2, with the exception of HgS that exists also in a distorted rock salt (RS) form. They are most important semiconductors widely used in optical devices, luminescence, photovoltaic, sensors, laser and so on.¹⁷⁰⁻¹⁷² For example, as early as in 1956, CdTe , has been theoretically proved as the semiconductor yielding the highest efficiency of photovoltaic solar energy conversion efficiency (24%).¹⁷³

Table 2.2. Crystal structures of monochalcogenides of Group 12 metal.

	S	Se	Te
Zn	W, ZB	ZB	W, ZB

Cd	W, ZB	W, ZB	ZB
Hg	ZB	ZB	ZB

Notable that HgS may have another unique distorted NaCl type type, trigonal structure (red α -HgS) besides zinc blende structure (β -HgS) (Figure 2.13). As shown in Figure 2.13(a), α -HgS is built of helical chains in which Hg has two nearest neighbors at 2.36 Å, two more at 3.10 Å, and two at 3.30 Å.¹⁷⁴ Upon heating, β -HgS can be converted to the stable α -form. The ZB structure of HgS is stabilized when mixed with a few percent of transition metals, which replace Hg ions in the lattice. Another notable thing is that chalcogenides of Hg are zero band gap semiconductors, which possess extremely high thermal and electrical conductivity.^{175, 176}

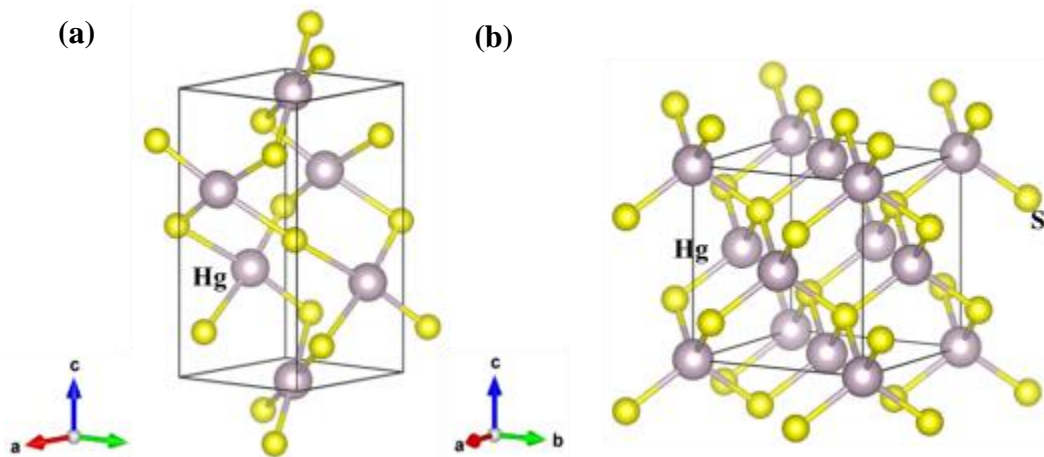


Figure 2.13. Crystal structure of (a) α -HgS and (b) β -HgS.

2.2 Synthetic of nanostructured metal chalcogenides materials via wet chemical method.

As aforementioned, intrinsic diversities of structures and properties are exhibited by metal chalcogenides, which finally result in their wide applications over several fields, such as

catalysts, sensors, bio-field, energy field, optical devices, magnetic materials, etc.. Particularly, nanostructured metal chalcogenides possess much wider applications due to the intriguing properties of nanostructures. For one thing, nanostructures possess ultra-high specific area which can offer more reaction sites compared with bulk counterparts. Adsorption ability, as well as reaction activity could be significantly improved. For another, nanostructures may exhibit quantum effect if the size is sufficient small under which interesting physical and chemical properties may appear. Thirdly, plenty amount of boundaries existed in nanobulk materials may improve their mechanical properties and enhance phonon or charge carrier scattering. Intriguing physical and chemical properties offered by nanostructures have recently emerged as ideal platforms to solve many key challenges in energy [e.g., energy conversion (solar cells, fuel cells, thermoelectric, hydrogen energy) and energy storage (lithium-ion batteries and supercapacitors)] and environment (e.g., green catalysts, sensors, pollution prevention, treatment, and remediation).⁷

Innovative MC nanostructures synthesized on a large scale with controlled morphology, size, composition, and structure lie at the heart of their practical applications.¹⁷⁷ Generally there are two routes for preparing nanostructured materials, the “bottom up” route and “top down” route. Table 2.3 compares several fabricating methods for nanostructures from different aspects, such as yielding, controllability and costs, etc., relevant references are also listed.

Table 2.3. Comparison of some fabricating method for nanostructure

Method	Yielding	Controllability	Cost	Efficiency	Ref.	Comment
Ball milling	High	No	Low	Low	178	Easy to introduce impurities

Deformation	High	No	Medium	Medium	179	Bulk materials should show good mechanical property
Fast quench	High	No	Medium	Low	180	Ultra-fast cooling speed needed
Melt-spinning	Medium	Low	High	Medium	181	Mainly nanoribbons
Molecular beam epitaxy	Low	High	High	Low	182	Mainly thin film or superlattice
Etching	Low	Medium	High	Low	183	Mainly nanoarrays
Physical vapour deposition	Low	Low	Medium	Low	184	Thin film and superlattice
Chemical vapour deposition	Low	Low	Medium	Low	185	Thin film and superlattice
Wet chemical	Low	High	Medium	High	186	Highly controllability

Compare with other listed methods, liquid-based wet chemical method has been intensively investigated to be very powerful for obtaining nanostructured MCs with controlled sizes, compositions and shapes. It has the following merits: (i) the nucleation and growth process of the nanocrystals can be easily controlled by adjusting the thermodynamic and kinetic

parameters of the reaction, such as temperature, kind of surfactants or solvents, addition sequence of reactants, etc.. Thus size, compositions and structures of products are highly controllable. (ii) The wet chemical method conducts under relative facile conditions compared with other method such as melt-spinning, molecule beam epitaxy, etc.. (iii) The cost of wet chemical method is relatively low because it does not need expensive facilities. Moreover, the cost can be further decreased by carefully design and selecting of chemicals. (iv) As the nanocrystals are produced in liquid phase, good uniformity of products could be expected. (v) Usually the wet chemical method can be completed in short time, thus it is time efficient. Thereby in this section, we will selectively summarize the main and general liquid-based methods for the controlled synthesis of MCs nanomaterials.

2.2.1 Hydrothermal/Solvothermal Method.

The hydrothermal/Solvothermal process using water or other solvents as reaction medium in a sealed pressure vessel named autoclave. The autoclave is composed by Teflon linings vessel and outside-steel can; the whole system is security sealed by screwing and rubber O-rings. By heating to a moderate temperature (usually higher than the boiling point of solvent, i.e., >100 °C for hydrothermal), a high pressure condition is simultaneously generated in the sealed system with suitable temperature, therefore the reaction is significantly promoted. Under this extreme (high temperature, high pressure) conditions, even in pure solvent, some quite unexpected reactions will take place, accompanied with the formation of nanoscopic morphologies and new phases, which cannot be achieved by traditional reactions.¹⁸⁷ Such as the ultra-long CdS nanowires and CdS-CdSe core-sheath nanowires.¹⁸⁸ The pressure of the reaction system is strongly affected by the temperature, size of Teflon vessels and amount of liquid; plus the influence of varieties of solution concentrations, solvent kinds and usage of different ligands, which are general control parameters in all the wet chemical method; properties of fabricated nanostructures are diverse and highly controllable by this simple

hydrothermal/solvothermal method. Besides, hydrothermal/solvothermal processes have other advantages such as fast reaction kinetics, short processing times, phase purity, high crystallinity, high yield, homogeneous in composition, narrow particle-size distributions, cost effective, environmentally benign, and easily scalable, etc..^{189, 190} Thereby although this method also shows many problems, such as (i) reproducibility of the product, because many occasional factors such as residual solvent on the wall of surface, situation of vessel sealing, etc., could affect properties of final product; (ii) the black-box like reaction system make the investigation of its mechanisms very difficult; (iii) there is safety issues for using of this technique as presence of high pressure, now various kinds of nanostructured MCs with specific shape and size have been fabricated, to name a few, such as nanoparticles of Ag_2Se ;¹⁹¹ nanowires of CdS , NiSe ;^{188, 192} nanoplates of Bi_2Te_3 ;¹⁹³ nanobelts of Sb_2Te_3 ;¹⁹⁴ nanoflowers of In_2S_3 ;¹⁹⁵ nanotubes of Ag_2Te ;¹⁹⁶ as well as hollowed ZnSe and MoS_2 ,^{197, 198} etc..

For the hydrothermal method, water is used as the main reaction medium, which is low cost and able to dissolve other water soluble coordinating molecules (such as ethylenediamine, hydrazine hydrate, mercaptoethanol, etc.). These “mixed solvents” can either serve as surfactants or as a doping agent to adjust the growth and final composition of final product. For example, Zhao et al.¹⁹⁹ employed CuCl and thiourea as the precursors to fabricate CuS nanostructures with assistant of different amines. Nanostructures including nanowires, nanotubes and nanovesicles can be obtained with the presence of triethylenediamine (TEDA), trimethylethylenediamine (TEMA), and di-n-butylamine (DBA), respectively. They proposed the different interaction between CuCl and amines was the key factor in the structural and morphological control.¹⁹⁹ Notable thing is that even for the same organic molecules with same concentration, it is still possible to affect the properties of product by tuning pH value because an appropriate pH value can affect the hydrolyzation rate of inorganic salts and anion

sources (e.g., thiourea and thioacetamide).^{200, 201} Qian et al.²⁰² fabricated a nitrogen doped TiO₂ using hydrothermal method and the ammonium as N source. Thus tuning of morphologies, compositions and structures could be easily achieved via adjusting fabricating parameters of hydrothermal, such as temperature, pH value, ligands, monomer concentrations etc., as shown by the Ni-Se system in Figure 2.14.

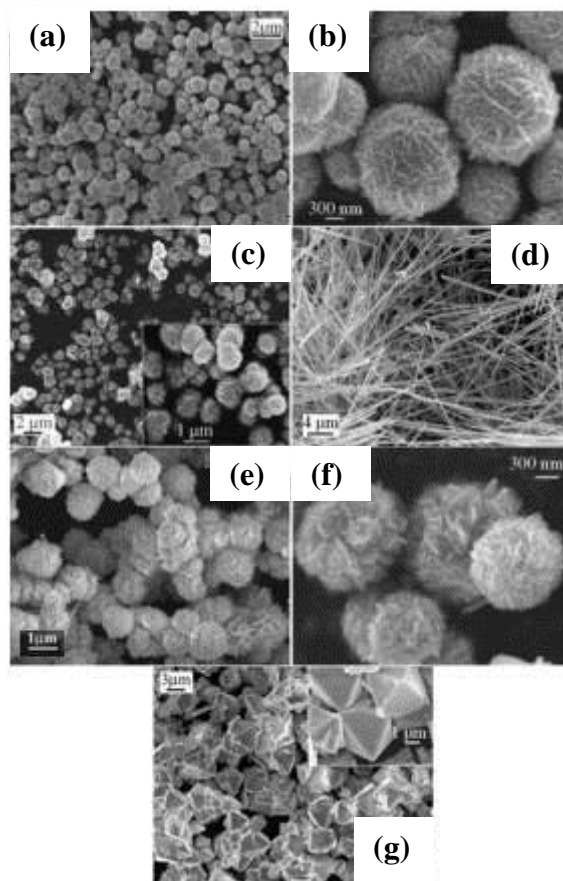


Figure 2.14. SEM images of the Ni-Se system fabricated by hydrothermal method under different conditions: (a, b) Ni_{1-x}Se microspheres obtained at 140 °C; (c) hexagonal NiSe microspheres obtained at 180 °C; (d) rhombohedral NiSe nanowires obtained at 180 °C (65 h); (e, f) Ni₃Se₂ microspheres obtained at 180 °C; (g) octahedral-shaped NiSe₂ microcrystals (140 °C, pH 10).¹⁹²

Based on the liquid phase hydrothermal (LPH) method, vapor phase hydrothermal (VPH) method is developed.²⁰³⁻²⁰⁵ As shown in Figure 2.15, instead of using single liquid

environmental, the VPH process referred to immersing a substrate with vapour either pre-injected or produced by liquid phase. The reaction environment created under VPH conditions differs remarkably from LPH. Under VPH conditions, all reactions take place within a thin liquid layer formed on the substrate surface (the reaction zone) and the dissolved products could rapidly supersaturate in the reaction zone (with very small volume) to facilitate the structure formation.²⁰³ Under such conditions, dissolution and structure formation are highly localized due to the mass transport limitation within the thin liquid-layer reaction zone.²⁰³ As shown in Figure 2.15, Zhang et al. simultaneously synthesized ZnO nanotube arrays and ZnO nanorod arrays on two sides of the same Zn substrate. Under this VPH process, the NH_3 -saturated thin liquid layers are instantly formed on both sides of the zinc foil substrate. Hence a fast growth rate of ZnO nanorod takes place on both sides of the substrate. Simultaneously selective etching takes place on the tip of the formed nanorods on the top surface of the substrate due to the presence of metastable (001) surfaces of ZnO nanorods with larger diameters. The upper surface is easy to accumulate the liquid layer and thus finally lead to a hollow structure. Moreover, such unique reaction environments created under VPH conditions result in not only formation of different nanostructures but also different formation mechanisms. Liu et al.²⁰³ proved that the morphology control mechanism of VPH is also different from LPH using a TiO_2 nanotube as an example. Unlike the TiO_2 obtained from LPH processes, the diameters of the TiO_2 nanotubes obtained from VPH processes are much larger and tuneable. Importantly, a roll-up of nanosheet mechanism, and subsequent crystal reformation processes are experimentally proved to explain the growth of nanotube structures.²⁰³

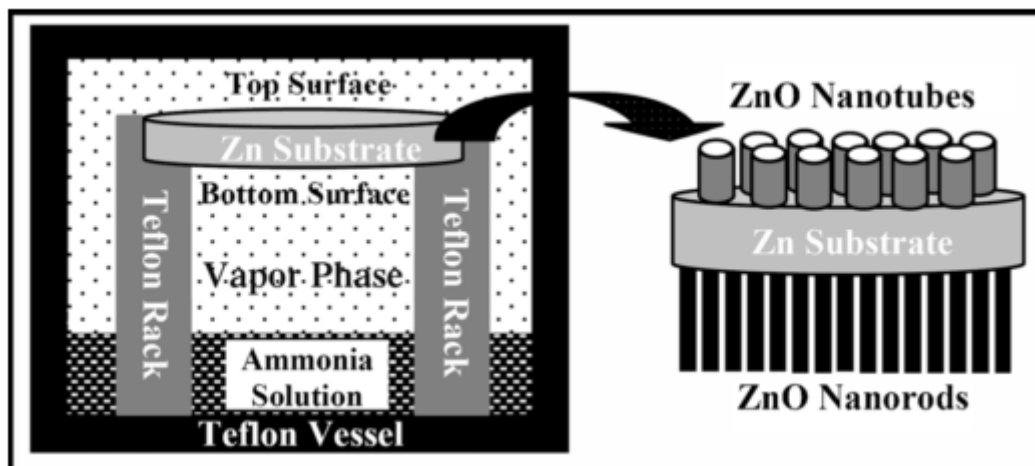


Figure 2.15. A schematic illustration of the fabrication of ZnO nanotube and nanorod array films on the top and bottom surfaces of the same zinc foil substrate by a vapour-phase hydrothermal method.²⁰⁵

Another important progress for hydrothermal method is the assistant of various kinds of field, such as the microwave and magnetic field. Compared with traditional hydrothermal process, microwave assistant can (a) lead to rapid heating to temperature of heat treatment, (b) increase the kinetics of reaction by one to two orders of magnitude, (c) lead to the formation of some novel phases, and (d) lead to selective crystallization of phases in the chemical system used.²⁰⁶ Figure 2.16 shows the morphologies of nanostructured Fe_3S_4 and marcasite (FeS_2), which are prepared under a magnetic-field-assisted (intensity is 0.045 Wb/m^2) hydrothermal route.²⁰⁷ The weak magnetic field can affect the growth and directional aggregation of Fe-S nanocrystallites, resulting in the formation of pearl-chain-like microrods. In contrast, only irregular microspheres are obtained in the absence of a magnetic field. Besides the magnetic field, the shape and fine structure of the building blocks also depend on the Sulphur precursor.²⁰⁷ In addition, other field, such as ultrasonic could also be used to the hydrothermal synthesis of nanostructured metal chalcogenides, they can lead to nanostructures with smaller size and homogeneity morphologies due to accelerated reaction

speed.^{208, 209}

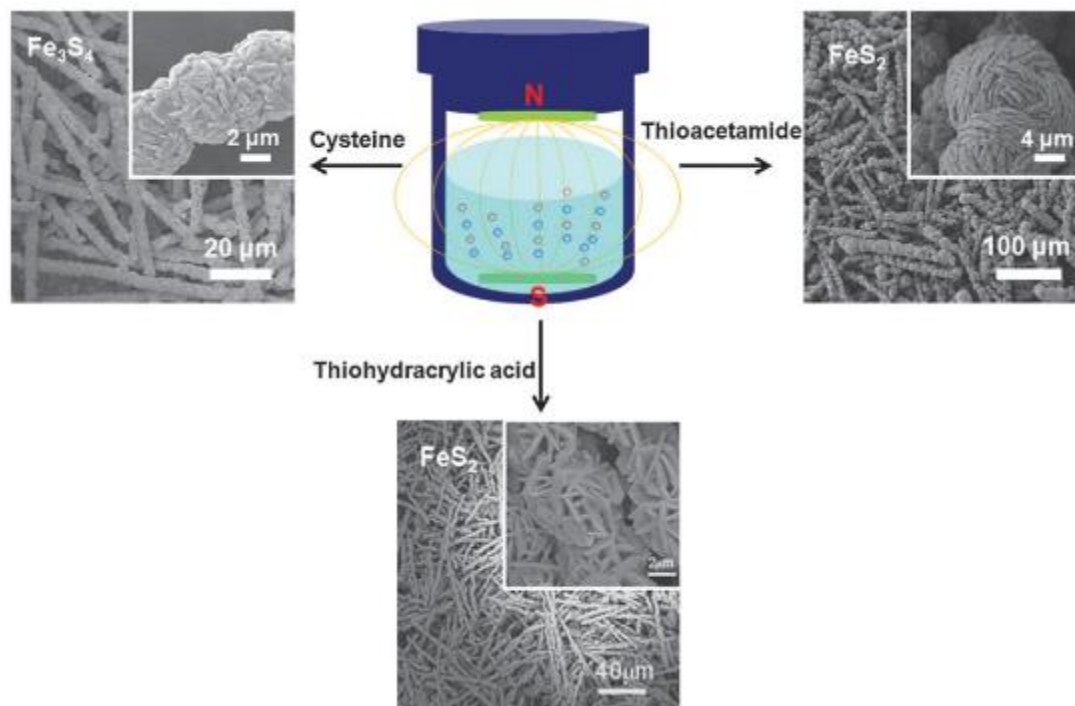


Figure 2.16. Fe_3S_4 and FeS_2 fabricated under magnetic field with different Sulphur source.²⁰⁷

Solvothermal method is much alike the hydrothermal method except using other high boiling point organic solvent, compared with hydrothermal method, their temperature range maybe higher. And the non-water solvents strongly suppress water hydrolyse of some metal salt, such as BiCl_3 and SbCl_3 , thus the selection of both chalcogen source and metal source is enlarged, which means it is possible to further reduce cost and increase diversity of products than hydrothermal. Moreover, the density, viscosity, as well as structure of solvents may strongly influence the properties of final product. For example, in Yu et al.²¹⁰ prepared NiS_2 dodecahedrons at a high temperature (200 °C) in ethylenediamine (EN)-glycol mixed solvent using $\text{NiCl}_2 \cdot 6\text{H}_2\text{O}$ and Sulphur as precursors [Figure 2.17(a)]. The formation of NiS_2 dodecahedrons may be caused by facet-selective modification of EN. EN molecules prefer to coordinate with the Ni^{2+} and selectively bind with the (101) planes and thus stabilize these crystal planes, resulting in the formation of NiS_2 dodecahedron microcrystals.²¹⁰ With

varying reaction conditions, NiS_2 microsphere can be obtained [Figure 2.17(b)]. Another interesting case is the successful synthesis of Fe_7Se_8 polyhedral²¹¹ with exposed high-index facets by solvothermal treatment of $\text{FeSO}_4 \cdot 7\text{H}_2\text{O}$ in diethylenetriamine (DETA)/water mixed solvent with Na_2SeO_3 at 140 °C for 12 h. Most of the obtained Fe_7Se_8 NCs have a truncated dodecahedral morphology with a size from 300 to 390 nm and (012) facets exposed,²¹¹ as presented in Figure 2.17(c). Also, by adjusting reaction parameters, nanorod structure Fe_7Se_8 could be obtained [Figure 2.17(d)].

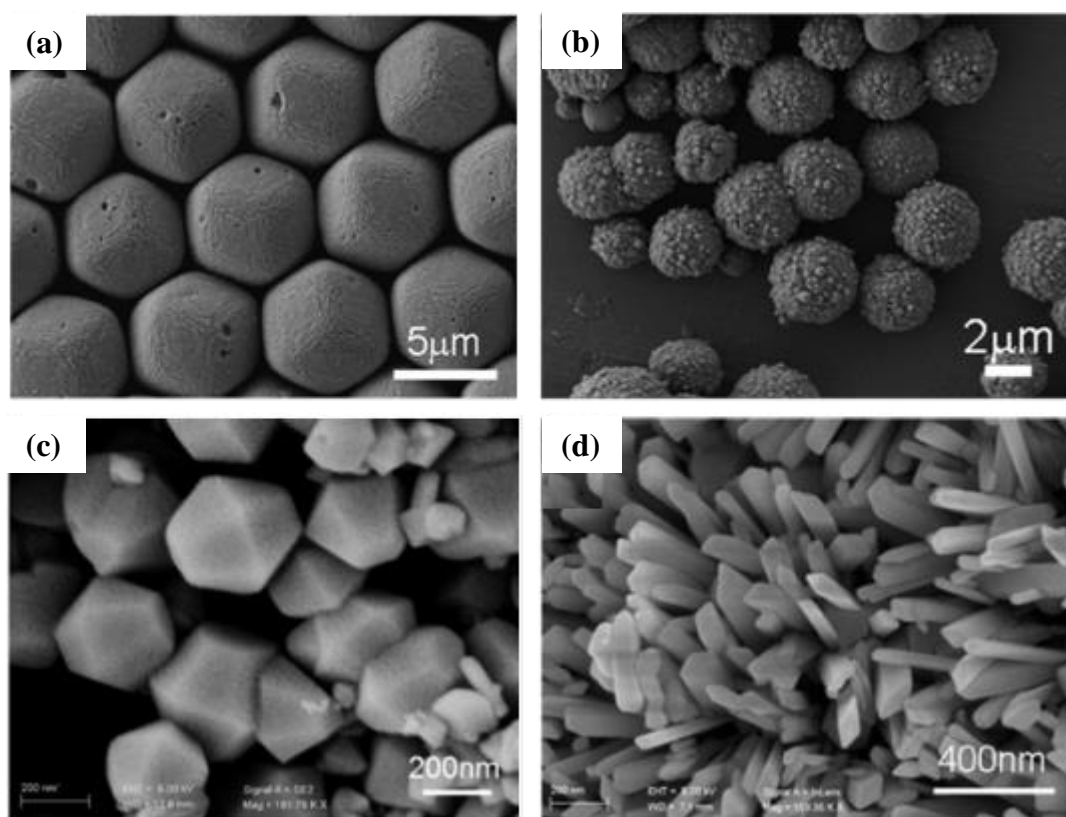


Figure 2.17. SEM images of (a) dodecahedron-like NiS_2 synthesized with 0.5 mmol $\text{NiCl}_2 \cdot 6\text{H}_2\text{O}$ and 2 mmol S at 200 °C for 6 h in a solvothermal of mixed solvent (EN:Glycol=3:1); and (b) NiS_2 microspheres synthesized with 0.5 mmol $\text{NiCl}_2 \cdot 6\text{H}_2\text{O}$ and 2 mmol S at 200 °C for 6 h in a solvothermal of mixed solvent (EN:Glycol=1:3).²¹⁰ (c) SEM of truncated Fe_7Se_8 synthesized with solvothermal of DETA:H₂O=1:2 at 140 °C for 12 h; (d) Fe_7Se_8 nanorods synthesized with DETA:H₂O=1:4 at 140 °C for 12 h.²¹¹

2.2.2 Hot-injection Method.

The hot-injection method, first used by Bawendi et al.²¹² to prepare CdSe nanocrystals, is effective in synthesizing high quality nanocrystals with good crystallinity and narrow size distributions. This simple method only needs a rapid injection of hot, highly reactive precursors into hot organic solvent to trigger a short burst of nucleation, which then subsequent growth into nanocrystals with various morphologies and conditions. The key point of formation of well controlled nanocrystals is separation of the nucleation and growth steps.²¹³ Compared with hydrothermal/solvothermal, this method has similar controllability, but is reproducible, much faster and much safer as it conducts under ambient pressure. Drawbacks of this method lie in the following aspects, however, (i) toxic and expensive organics maybe used, which is do harm to both human/environmental and increase the cost; (ii) there are always capping ligands on the surface of product, which may do harm to their applications; (iii) sometimes in order to get monodispersed nanostructures, low concentration for precursors is needed, meaning the low yield; (iv) to prevent oxidation or absorption of water, purging of protection gas or Schlink line is needed, which leads to the complexity for operation. Nevertheless, size and morphology of a specific MC can be effectively controlled by adjustment of a few experimental parameters, such as the type and ratios of the starting reagents, reaction temperature, reaction time, reaction time, solvent, capping ligands, and so on. To exemplify a typical example, as shown by Table 2.4,²¹⁴ simply by adjusting reaction parameters, PbSe with different morphologies ranging from 0 D nanocrystals to 3 D branched nanowires can be obtained.²¹⁴

Table 2.4. Experimental conditions used in preparation of PbSe nanocrystals and nanowires with different morphologies.²¹⁴

Structure	Stabilizing agents, solvent ^a	OA:Pb ratio (Molar ratio)	Pb:Se ratio (Molar ratio)	Injection/Growth temperature (°C)	Time (min)
Quasi-spherical nanocrystals	OA-TOP, Ph ₂ O or squalane	4:1	1:3	180/140-160	1-10
Cubic nanocrystals	OA-TOP, Ph ₂ O	4:1	1:3	120/110 ^b	5-15
Octahedral nanocrystals	OA-DDA-TOP, Ph ₂ O	4:1	1:3	230/170	1-2
Star-shape nanocrystals	OA-HDA-TOP, Ph ₂ O	4:1	1:3	230/170	2-5
Undulated nanowires	OA-TOP, Ph ₂ O	3.15:1	3:1	250/170	1-5
Zigzag nanowires	OA-HDA-TOP, Ph ₂ O	3.15:1	3:1	250/180	1-5
Straight nanowires	OA-TDPA-TOP, Ph ₂ O	3.15:1	3:1	250/190	0.5-1
Star-shape branched nanowires	OA-TOP, Ph ₂ O or OA-HAD-TOP, Ph ₂ O	3.15:1	3:1	250/170 ^b	1-5

Tapered branched nanowires	OA-HAD-TOP, octyl ether	3.15:1	3:1	250/170	1-3
-------------------------------	----------------------------	--------	-----	---------	-----

- a. OA, oleic acid; HAD, hexadecylamine; TOP, trioctylphosphine; Ph₂O, phenyl ether; TPDA, n-tetradecylphosphonic acid.
b. Additional injections of Pb:Se precursors.

Many other high-quality semiconductor nanocrystals have also been successfully synthesized by this method, such as Ag₂X, GaSe nanoparticles,^{215, 216} Bi₂Te₃ nanoplates,²¹⁷ FeX (X=Se, Te) and FeTe₂ nanosheets,²¹⁸ ZnS nanorods,²¹⁹ FeSe nanoflakes,²²⁰ core@shell structured Pb-X system,²²¹ hollowed Cu₂Te,²²² multi-shell Bi-X system,²²³ etc.. Figure 2.18 represents nanostructured MCs ranging from 0 D to 3 D synthesized by hot injection method.

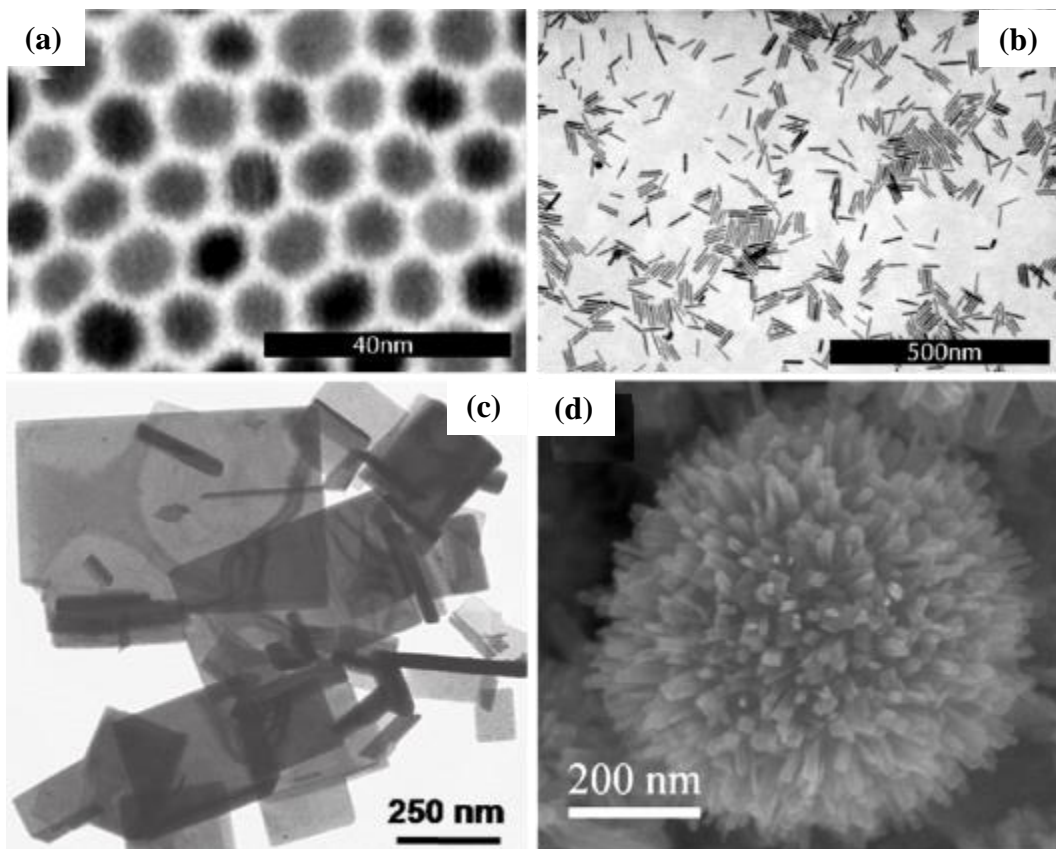


Figure 2.18. TEM image of (a) nanoparticles and (b) nanorods of Bi₂S₃.²²⁴ (c) TEM image of FeTe nanosheets.²¹⁸ (d) SEM image of FeSe₂ nanoflower.¹⁵⁴

An important progress based on the hot injection method is the non-injection or one step colloid method, i.e., without injection of the precursors at high temperature, the precursors are both mixed under room temperature and then heated to the reaction temperature. Compared with conventional hot injection method, the manipulation is simplified while preserving good control over properties of product. Another important notable thing is the selection of precursor, as the precursors are mixed at the first beginning, the reactivity of precursors should be much weaker at room temperature (otherwise the reaction procedure would be out of control), such as the combination of insoluble solid precursors, which are less expensive than high activity precursors; thus it is possible to further decrease the cost than hot injection method. As a typical example, the Schaak group reported the synthesis of wurtzite-type MnSe by directly heating $\text{MnCl}_2 \cdot 4\text{H}_2\text{O}$, Se powder, oleic acid, and tetraethylene glycol (TREG) at 235 °C for 1 h under the protection of Ar.²²⁵ The same group further fabricated SnSe nanosheets,²²⁶ and SnS nanoflowers using similar methods; which are respectively shown in Figure 2.19(a) and (b). Their morphologies, sizes can be simply controlled by reaction parameters, such as the ligands, reaction time, temperature, etc..^{226, 227} Besides the materials aforementioned, other MCs with well control over sizes and morphologies, such as Ag_2S nanowires,²²⁸ Sb_2S_3 nanotubes,²²⁹ In_2S_3 and Fe_3Se_4 nanosheets,^{230, 231} EuSe ,²³² Cu_{2-x}Se ,²³³ ZnS and SnS nanoparticles,^{234, 235} and so on.

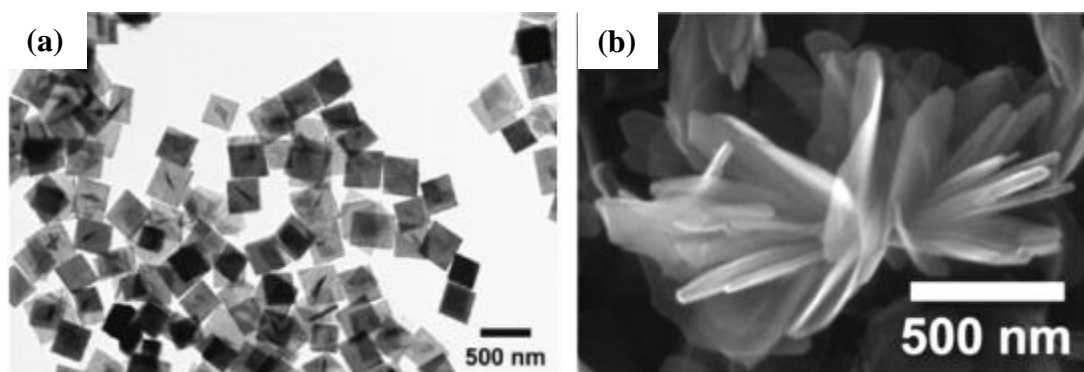


Figure 2.19. (a) TEM of the SnSe nanosheets;²²⁶ (b) SEM of the SnS nanoflowers fabricated

by one step colloid method.²²⁷

If using a single precursor, the one step colloid method is further developed into the single precursor method.

2.2.3 Single Precursor Method.

The key point for single precursor method lies in the selection of a precursor contains both the desired metal and corresponding chalcogen elements, which is able to decompose at a moderate temperature. The properties of fabricated MC nanostructures can be well adjusted by selection of precursor, decomposition temperature, solvents, ligands, concentration of precursors, reaction time. This method has been proved to be highly effective for a facile and reproducible production of colloid NCs with single-crystallinity, purity, and monodispersity. Many different nanostructured MCs with various compositions and shapes can be fabricated by this method, such as nanoparticles of Pd_xSe,²³⁶ EuS,²³⁷ Ag₂S,²³⁸ M_xS (M=Cu, In, Cd, Ag),²³⁹ Fe_xS²⁴⁰ and CoX (X = S, Se)²⁴¹; nanoplates of SnS₂,²⁴² Fe₇S₈,²⁴³ and Sb₂Te₃²⁴⁴; nanosheets of MoS₂ and WS₂²⁴⁵, nanorods and nanoprisms of NiS,²⁴⁶ nanowires of GeS₂ and GeSe₂,²⁴⁷ Sb₂Se₃,²⁴⁸ etc.. A good example of morphology and composition control was reported by Zhang et al. and shown in Figure 2.20.²⁴³ They fabricated Fe₃S₄ nanoparticles from decomposition of single precursor of Fe(diethyldithiocarbamate)₃ in a mixed oleylamine/1-octadecene (volume ratio 1:1) solution at 280 °C; while Fe₇S₈ nanoplates are got by changing the precursor with Fe(Ddtc)₂(Phen) (Phen=1,10-phenanthroline; Ddtc=diethyldithiocarbamate); and with same precursor of Fe(Ddtc)₂(Phen) but different solvents (oleic acid/oleylamine/1-octadecene, volume ratio 1:1:1), amorphous Fe₇S₈ nanobelts are fabricated.

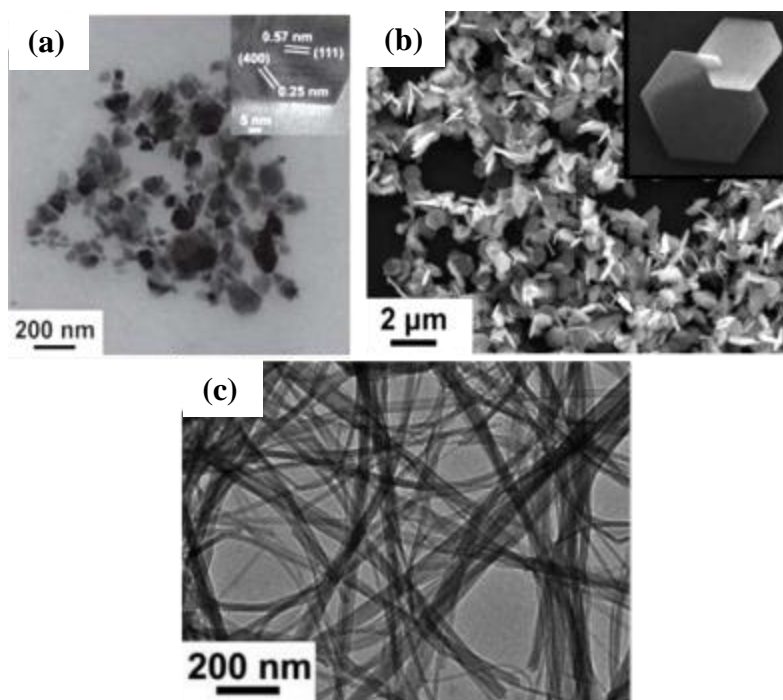


Figure 2.20. (a) TEM image of Fe₃S₄ nanoparticles; (b) SEM image of Fe₇S₈ nanoplates; (c) TEM of Fe₇S₈ nanobelts.²⁴³

Compared with hot injection method, this method is much simpler and easier; however, its applications are hindered by the limited selection of precursor, which are usually expensive and toxic, as well as its low yield.

2.2.4 Mixed Solvents Method.

In the wet chemical method, as a reaction media, the liquid solvent plays pivotal role on shape, size and composition control for the synthesized product. For one thing, the solvent can affect the dispersion of precursors directly, which is related with the reactivity and homogeneity of reaction; typical examples are the micro-emulsion system, which is well explained in several review articles.²⁴⁹⁻²⁵¹ For another, the solvent may modify surface of the monomers to control both the growth direction and the final size of nanocrystals. Thirdly, different solvents may improve reactivity of some reaction systems, either by lowering reaction energy or form a highly reactive precursor. Based on this point, a mixed solvent

method is developed for controlled synthesis of MCs nanostructures. The properties of product can be tuned by changing the components and volume ratios, achieving some appropriate synthetic conditions to the desired nanostructures.¹⁸⁷ Several examples related with effect of mixed solvents on morphology control over MCs nanostructures have been presented in the above three methods, such as Ni-S and Fe-Se system shown in Figure 2.17 and Figure 2.18;^{210, 211} Fe₃S₄ and Fe₇S₈ shown in Figure 2.20.²⁴³ However, the real purpose we emphasized this method lies in that either it is possible to achieve reduction of reaction temperature or its ability of fabricating nanostructures with special morphologies. As a typical example, Chen et al.²⁵² reported an ambient synthesis of Cu_{2-x}X (X=S, Se) nanotube structure [Figure 2.21(a) and (b)] within a mixed ethanol/2-mercaptoethanol/NaOH solution solvent from Cu nanowires and Se/S powder. According to their description, the mixed solvents play important role in its reaction mechanism. In common sense, Cu nanowires can't react with Se powder directly under room temperature, however, Se powder can be dissolved into 2-mercaptoethanol (a small molecule liquid contains thiol group) to form selenothiolate (HOCH₂CH₂SSe⁻), which can absorb onto the surface of Cu nanowire and generate an intermediate complex with low energy [Figure 2.21(c)]. Because the low energy state of this complex, the reaction of Cu and the selenothiolate becomes spontaneous. Then the layered like Cu_{2-x}Se gradually formed and covered the Cu nanowires. After a Kirkendall effect, the Cu nanowires transferred into Cu_{2-x}Se nanotubes gradually. The effect of NaOH solution is to promote the formation of hydroxyethylmercaptide (HOCH₂CH₂S⁻), which is then react with Se or S powder to give selenothiolate. Without presence of NaOH solution, the dissolve of Se or S powder under room temperature is impossible.²⁵² Moreover, replacing 2-mercaptoethanol with 3-mercaptopropionic acid, the nanotube structures are totally broken down into Cu_{2-x}Se nanoplates [Figure 2.21(d)].

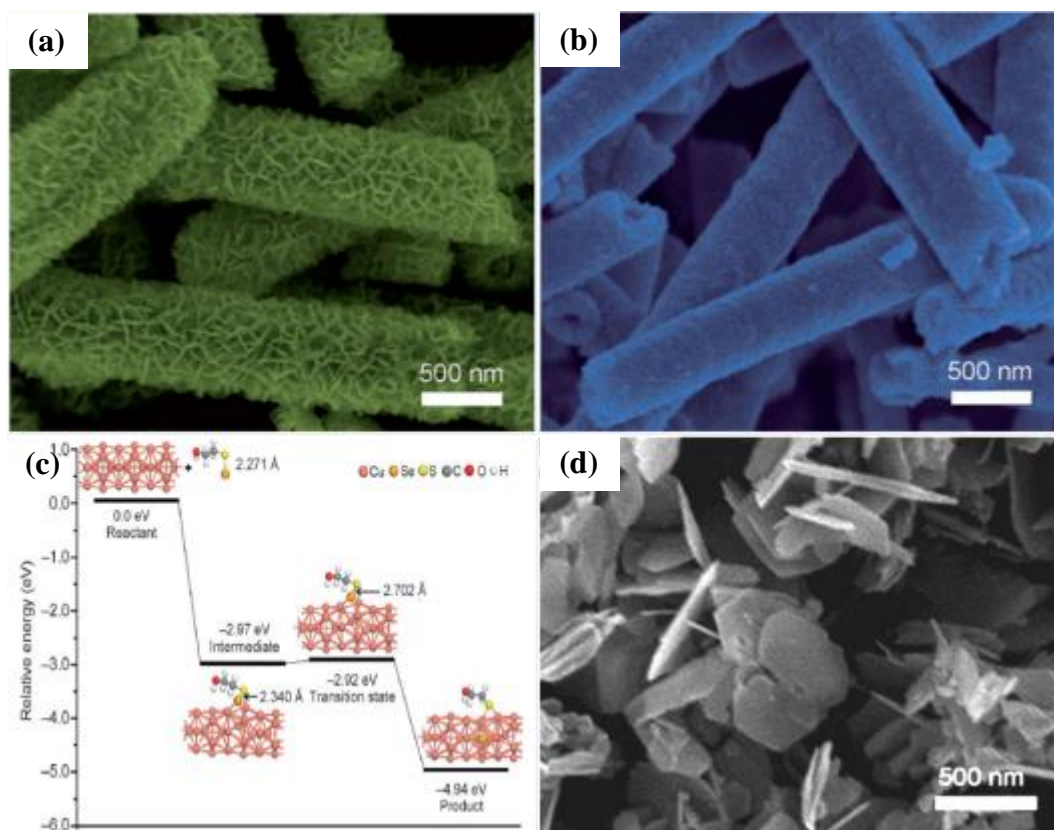


Figure 2.21. (a) SEM images of Cu_{2-x}Se and (b) Cu_{2-x}S within the mixed ethanol/2-mercaptoethanol/NaOH solution. (c) Energy profiles for reactions of HOCH₂CH₂SSe⁻ ions. (d) SEM image of the Cu_{2-x}Se synthesized within the mixed ethanol/3-mercaptopropionic acid/NaOH solution.²⁵²

An improved mixed solvents method has been developed by Li et al.²⁵³ to prepare a broad range of nanocrystals. Using a liquid–solid–solution (LSS) system consisting of an ethanol–linoleic acid liquid phase, metal linoleate (solid), and a water–ethanol solution under hydrothermal conditions [Figure 2.22(a)], monodisperse MC nanocrystals such as PbS, Ag₂S, and ZnSe were successfully synthesized [Figure 2.22(b)]. The product can be easily dispersed in nonpolar solvents to form homogeneous colloidal solutions [insets in Figure 2.22(b)]. This LSS strategy relies on a general phase transfer and separation mechanism happening at the interfaces of the liquid, solid, and solution phase. It is also generalized to prepare a variety of nanocrystals such as noble metal, magnetic/dielectric nanoparticles, and so on.

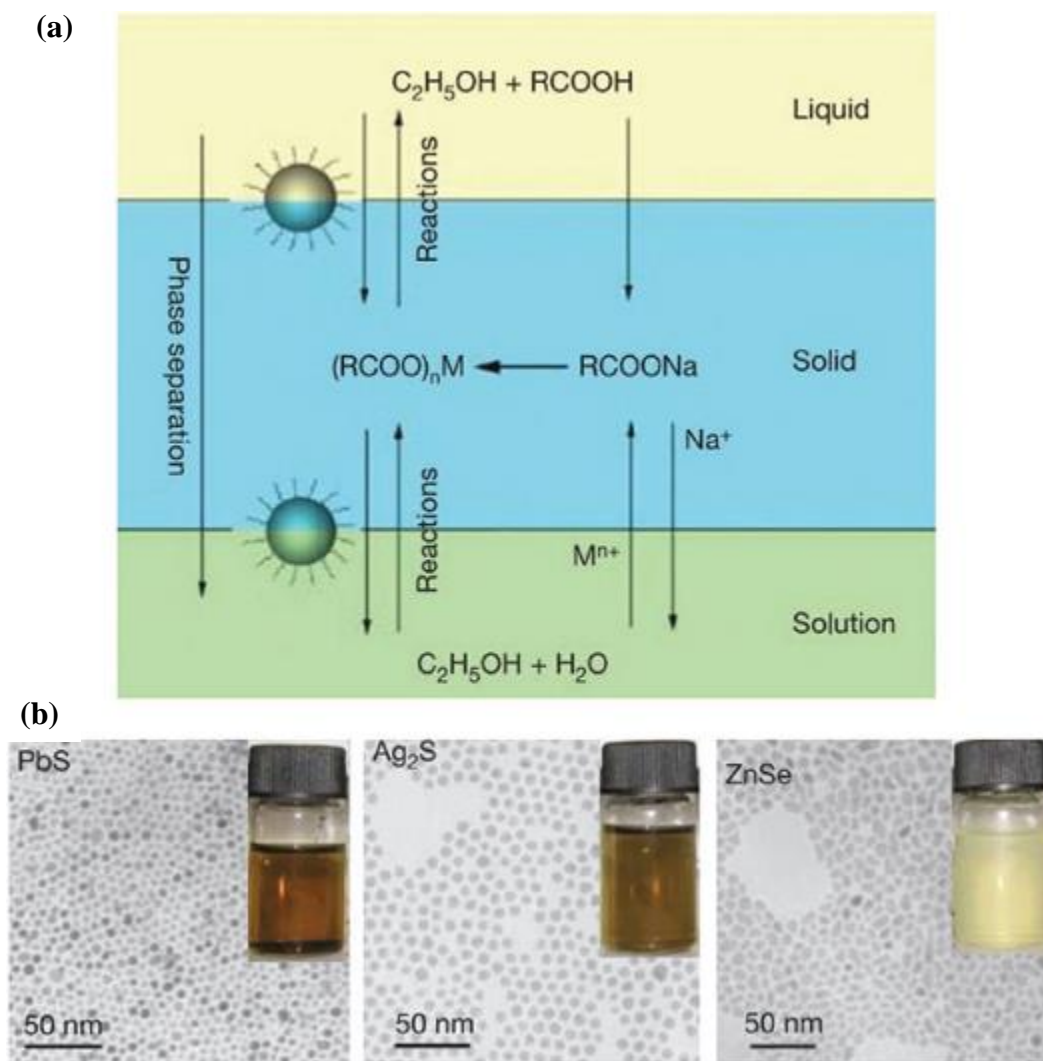


Figure 2.22. (a) Scheme of LSS phase transfer synthetic strategy. (b) TEM images of as-synthesized MC nanocrystals: PbS, Ag₂S, and ZnSe. Insets show cyclohexane solutions of corresponding MC nanocrystals.²⁵³

2.2.5 Liquid Exfoliation Method.

As aforementioned, many metal chalcogenides, such as TiS₂, Bi₂Te₃, GeS, SnS₂, etc., possess a layered structure. Typically, originating from the competition between the cationic d levels and anionic sp levels, most transition metal atoms (M) will react with chalcogen atoms (X) to form an X–M–X configuration with stoichiometry MX₂. Although the bonding within the hexagonal M layer and two X layers is covalent, adjacent sheets stack via weak van der

Waals interactions. This special layered structure makes these materials easy to form nanosheets by peeling or exfoliation by insertion of other compounds. Thus inspired by the first reports of the liquid phase exfoliation of sheets of clay materials in the early 1960s,²⁵⁴ the liquid exfoliation of bulk layered metal chalcogenides has become an important method to obtain large quantities of mono- or few-layer nanosheets.^{112, 255-258} This intercalation materials can be varied from organic molecules, halides to lithium ions.²⁵⁹ The whole intercalation process can be completed simply by soaking into the solutions contained intercalation substance under moderate temperature,²⁶⁰ or by electrochemical process,²⁶¹ or by solvothermal method.²⁶² The resulting intercalated compounds can be exfoliated to mono- and few-layer 2D nanosheets by simple ultra-sonication.^{260, 263, 264} Large quantity of 2D nanosheets could be fabricated using this simple and low cost method. However, this method only works within the layered structure MCs, morphology of the nanostructures are limited to 2D nanosheets, the control over the thickness of the product is also difficult.

The exfoliation of nanosheets is related with the tension of layered structures, which are controlled by several factors, such as the kind and amount of intercalation substance, the surface energy of the layered materials and the selection of solvent, in which selection of solvent is the easiest control way to achieve. Coleman et al.²⁶⁵ investigated the surface tension after dispersion and ultra-sonication of each inorganic starting material in about 30 common solvents by optical absorption spectroscopy. Finally they demonstrated that the best solvents have a surface tension close to 40 mJ/m².²⁶⁵ Thereby they proposed that successful solvents are those that minimize the energy of exfoliation. For example, N-methylpyrrolidone (NMP) and isopropanol (IPA) are very promising solvents for exfoliating various layered compounds.²⁶⁵

As an example, Zeng et al.²⁶¹ used a controlled electrochemical insertion of Li⁺ ions into powders of various transition metal dichalcogenides including MoS₂, WS₂, TiS₂ and TaS₂.

Then corresponding single layered nanosheets are obtained by the followed ultrasonic procesing, as shown in Figure 2.23. By a two-step expansion and intercalation method, Zheng et al.²⁶⁴ produced high-quality single-layer molybdenum disulphide sheets with unprecedentedly large flake size (up to 400 nm²). The process includes a pre-insertion of N₂H₄ into MoS₂ single crystal with heating; followed by second insertion of sodium naphthalenide simply by stirring in tetrahydrofuran (THF); finally the intercalated sample is put into water and dispersed by low energy ultrasonic.²⁶⁴ The two step insertion leads to easy separation of single layer MoS₂ and the low energy ultrasonic does not break the separated layers. Not only transition MCs, layered Bi₂Te₃ and Bi₂Se₃ could also be exfoliated by insertion of Li⁺ ions or the so called “chemical-exfoliation hydrothermal method”.^{262, 266}

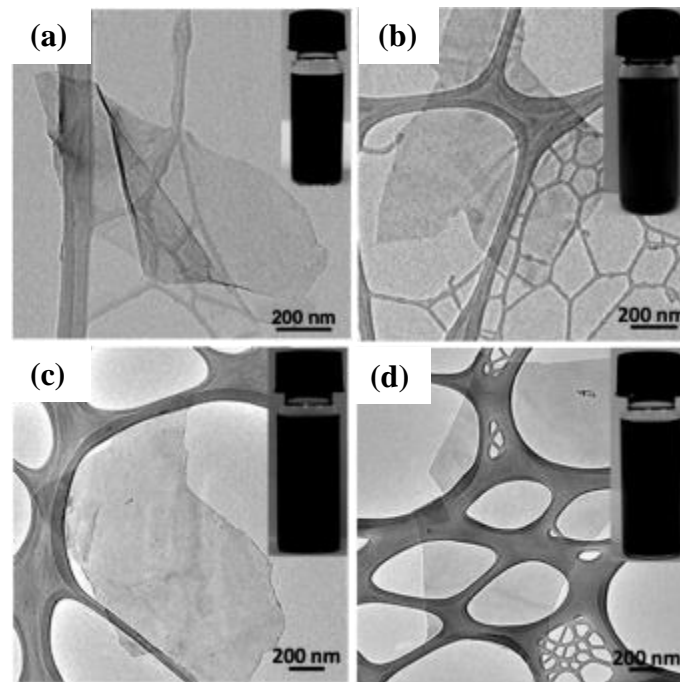


Figure 2.23. Nanosheets fabricated from electrochemical insertion of Li⁺ ions. (a) MoS₂; (b) WS₂; (c) TiS₂; (d) TaS₂.²⁶¹

2.2.6 Ion-exchange and Kirkendall-effect-induced Method.

Ion-exchange reactions, including cation exchange and anion exchange reaction, are a series

method that can convert one material to another in liquid solution. In common sense, the ion exchange reaction is based on the big difference of solubility product (K_{sp}) between original nanocrystals and the final product. Because the free Gibbs energy for insoluble materials (ΔG) can be expressed by Equation (2.5), in which R is gas constant, T is temperature of the reaction system, K_{sp} is the solubility product of the insoluble MCs (M_aX_b , M is metal element, X=S, Se, Te), J_{sp} can be calculated from Equation (2.6). $C(M^{b+})$ and $C(X^{a-})$ are the concentration of cation and anion in the system, respectively. Thus the transfer reaction from the higher K_{sp} material to lower one may happen spontaneously. However, according to Maskaeva's report,²⁶⁷ the judgement of whether the ion exchange reaction can happen or not is not a simple thing, because this procedure is very complex and related with many factors, such as the activation energy barriers of phase change and surface energy change, real concentration of ions in the solution, the effect of solvents, etc.. However, although the more correct criteria should be the solubility difference of reactants and product, we can still roughly make a judgement using solubility product.²⁶⁷ Moon et al.²⁶⁸ have summarized several tendencies for the solubility product of MCs. Normally the solubility products of MCs have a lower value as the ionic radius of chalcogen increases, i.e., $K_{sp}(\text{sulfides}) > K_{sp}(\text{selenides}) > K_{sp}(\text{tellurides})$.²⁶⁸ While for the same chalcogen, the sequence of solubility product is shown by Figure 2.24.²⁶⁸ The kinetic process of ion exchange reaction is related both with the outwards-diffusion of ions to the surface of reactants and the inwards-diffusion of ions from the solution into the reactants; simultaneously, the rearrangement of crystal structures may happen if the crystal structures of product and reactants are different.

$$\Delta G = RT \times \ln \frac{J_{SP}}{K_{SP}} \quad (2.5)$$

$$J_{SP} = C^a(M^{b+}) \times C^b(X^{a-}) \quad (2.6)$$

The cation exchange reaction, which is referred to alter the composition of the existing ionic nanocrystals by replacing the cations within the crystal lattice with a different metal ion, is particularly effective for the transformation of MC nanocrystals.²⁶⁸⁻²⁷⁰ Moreover, for cation exchange, morphology of the product is usually controlled by the properties of original reactant nanocrystals and the crystal structures of product. If the size of original nanocrystals is approximately or below a critical value (reaction zone width), the morphology of product would be controlled by the structure of product; while if the size of original nanocrystals is far bigger than this critical value, the product can keep original morphology of reactants.²⁶⁹ In addition, in the later case, the morphology of the product is also related with the volume change ($\Delta V = V_{\text{Product}} - V_{\text{Original}}$) between unit cell of original nanocrystals and products, according to the literature, if $\Delta V \leq 0$ (meaning volume shrinkage), the product would keep original morphology; while if ΔV is far bigger than 0 (big volume expansion), the product may be broken into fragments.²⁶⁸

			13	14	15	16
			Al	Si	P	S
28	29	30	31	32	33	34
Ni	Cu	Zn	Ga	Ge	As	Se
46	47	48	49	50	51	52
Pd	Ag	Cd	In	Sn	Sb	Te
78	79	80	81	82	83	84
Pt	Au	Hg	Tl	Pb	Bi	Po

$K_{\text{sp, chalcogenide}}$

 $<$

 $<$

Figure 2.24. The relative order in the solubility product of various metal chalcogenides.²⁶⁸

As aforementioned, the real ion exchange reaction is controlled both by the thermodynamic driving force and the kinetics of a transformation (activation barrier). It is also possible that the transform reaction from lower K_{sp} reactants to higher K_{sp} product via reaction conditions control. Such as the milestone reported by Alivisatos et al.²⁶⁹ that cation exchange reactions can occur completely and reversibly between CdSe and Ag₂Se under ambient conditions (Figure 2.25).

Similar with cation exchange reaction, the anion exchange reaction is also based on the difference of solubility of reactants and products.²⁶⁸ And many metal chalcogenides materials can be effectively prepared by anion exchange reaction.²⁷¹⁻²⁷³ However, the situation for anion exchange is much complex compared with cation exchange as usually anions in MCs are much larger than cations and usually forms the frame of crystal structures.²⁶⁸ Thus the exchange process, which is usually based on diffusion of ions, is much slower and need more energy than cation exchange. This means the anion exchange reaction usually happens under more harsh conditions, and morphology of product is also different with the reactants during anion exchange reaction.^{268, 273}

The ion exchange reactions can also be used to prepare nanocrystal heterostructures through the partial transformation of ionic nanocrystals. Typical examples include the CdS–Cu₂S binary nanorods reported by Alivisatos et al.²⁷⁴, the CdS–PtS, CdSe–PtSe, CdTe–PtTe, CdS–PdS, and CdSe–PdSe nanocrystals reported by Son et al.²⁷⁵, the ZnO–ZnS nanocables reported by Xue et al.,²⁷⁶ and the CuS–CuSe hollow structures reported by et al.²⁷¹

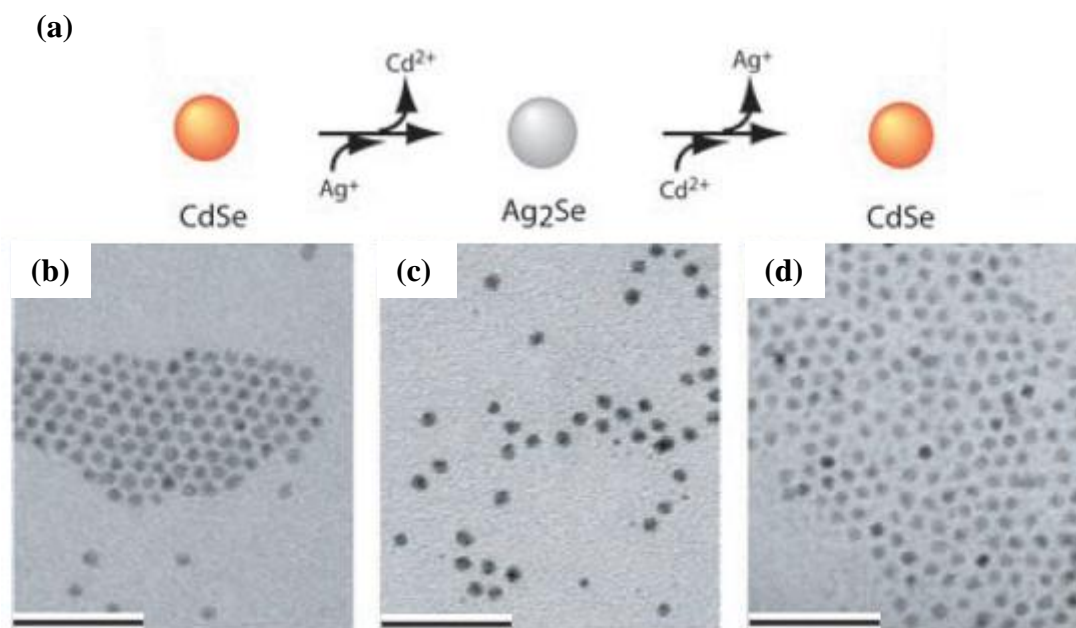


Figure 2.25. (a) Scheme of the forward cation exchange reaction and reverse cation exchange reaction between CdSe and Ag₂Se. (b) Initial CdSe, (c) Ag₂Se transformed from the forward cation exchange reaction, and (d) recovered CdSe nanocrystals from the reverse cation exchange reaction. Scale bars all present 40 nm.²⁶⁹

It is also notable that the ion exchange reaction may lead to the formation of hollowed structures, such as hollowed nanoparticles, nanotubes, nanocages, etc., as shown in Figure 2.26(a-d). This is related with the Kirkendall effect, which is a classical phenomenon in metallurgy. As explained by Figure 2.26(e), due to the non-equilibrium mutual diffusion ($J_{out} > J_{in}$, i.e., outwards diffusion is faster than the inwards diffusion) process happens near the interface of a diffusion couple, the net mass flow finally leads to formation of voids near the original interface and within the fast-diffusion side. Because the ion exchange reaction referred to a diffusion process of ions, thus it is possible to induce the Kirkendall effect, i.e., formation of hollowed structures.

Besides novel ion exchange reaction, alloying from a nanostructured chalcogen (such as Te nanowires) or metal source (such as Co nanoparticles) is also able to induce the Kirkendall

effect [Figure 2.26(e)]. A pioneering work from Yin et al.²⁷⁷ described the hollow Co_3S_4 , Co_9S_8 , or CoSe nanocrystals fabricated by reacting Co nanoparticles with Sulphur or selenium in solution through a Kirkendall mechanism. The average diameter of the inner hollowed part is less than the original Co particles, indicating the mutual diffusion of both outwards and inwards. They also found the quality of hollowed structure can be adjusted by temperature control because the diffusion process is dependent on temperature.²⁷⁸ With a low reaction temperature, a slow diffusion leads to multi-irregular voids, obvious fracture and open structures are also observed; on the contrary, if the reaction temperature is high, a single void formed, and a porosity/defect structure is detected in the shells.²⁷⁸ Thereby we can conclude that reaction temperature plays important role the quality of final product in the Kirkendall-effect-induced method. Besides, Co-X system, this Kirkendall-effect-induced method is widely used for preparing targeted hollowed nanostructures or heterostructures of various MC nanomaterials, such as RuSe_2 nanotubes,²⁷⁹ Bi_2Te_3 nanotubes,²⁸⁰ hollowed CdS nanoparticles,²⁸¹ and so on.

However, if nanostructured chalcogens are used as the reactants, the hollowed structure can't be formed because the net diffusion of atoms is inward ($J_{out} \leq J_{in}$) because the big size of anions (core part chalcogen). The high reactivity of Se and Te with various metals even at room temperature made them excellent templates for the synthesis of various metal chalcogenides, such as the situation of Ag_2Te nanowires shown in Figure 2.27(a), which are prepared from Te nanowires.²⁷⁰ It is also notable that the 100% volume expansion during the transformation into Ag_2Te nanowires caused considerable mechanical stress accumulated along the length direction and chopped the long Te nanowires (>10 nm) into short ones (1 nm long).²⁷⁰ However, many controversy reports can be found, as shown in Figure 2.27(b). Even using Te nanowires as precursor, obvious hollowed structure formed, which means a faster outwards-diffusion of Te.²⁸⁰ While in Figure 2.27(c), although no obvious hollowed structure

is observed in the final product, the hollowed Bi_2Te_3 nanotubes are detected at the initial stage of the reaction.²⁸² With progress of following Ostwald ripening, the nanotubes grew into nanowires again. In Figure 2.27(d), ultra-thin Bi_2Te_3 nanowires are obtained using ultra-thin Te nanowires as the templates.²⁸³ We can only infer that the detailed diffusion procedure can't be simply decided by ion radius, instead, many factors should be considered, such as the properties of solvents and surfactants, growth speed and time, defects in the products, and the properties of product, etc..^{270, 282-284}

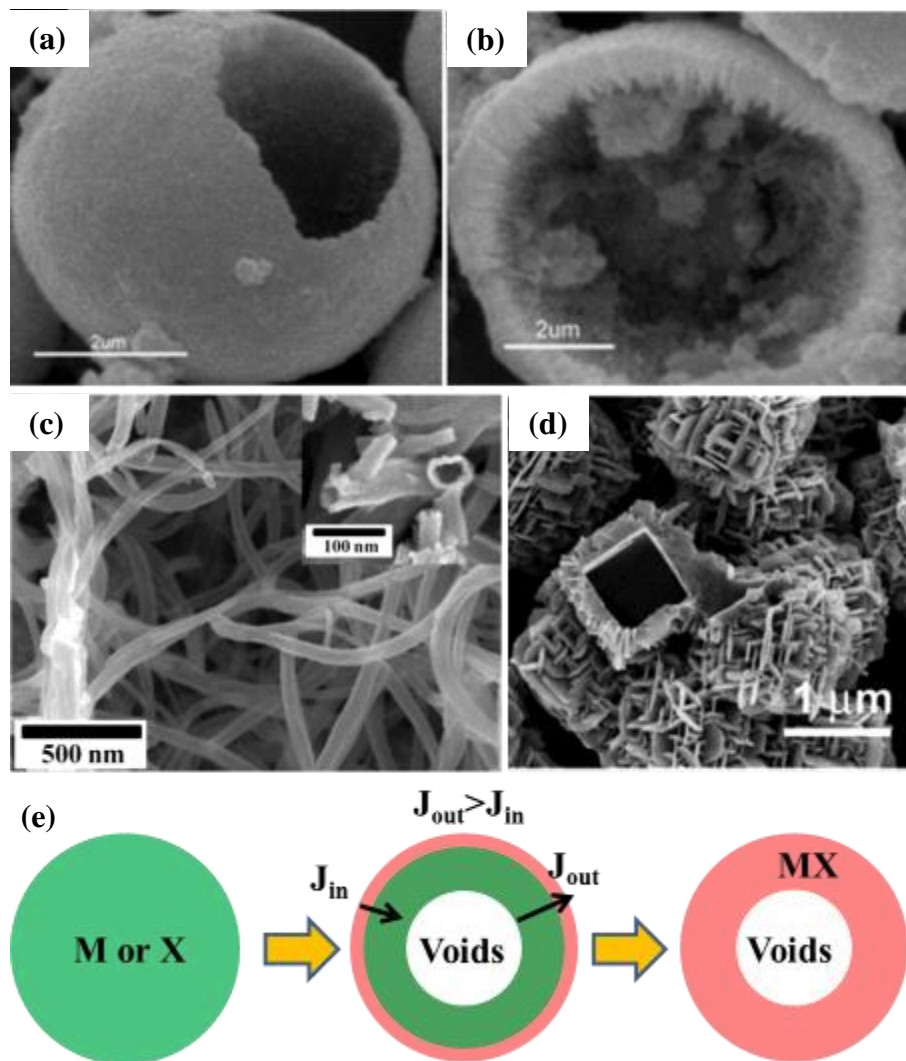


Figure 2.26. Some typical hollowed structures obtained from ion exchange reaction. (a-b) SEM image of hollowed PbS and CuS microspheres synthesized from ZnS microballs via cation exchange reaction.²⁸⁵ (c) SEM of CdSe nanotubes fabricated from anion exchange of

Cd(OH)₂ nanowires.²⁸⁶ (d) SEM image of the hollowed CuS nanocubes prepared from anion exchange of Cu₂O nanocubes.²⁸⁷ (e) Schematic of Kirkendall effect.

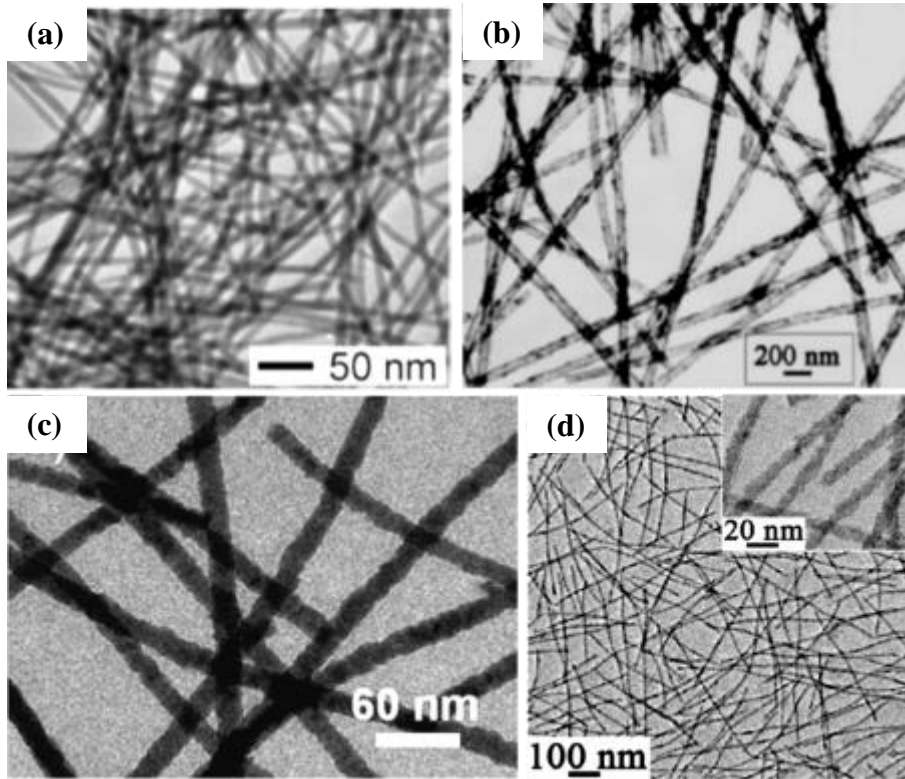


Figure 2.27. (a) TEM of Ag₂Te nanowires synthesized from Te nanowires.²⁷⁰ (b) TEM of Bi₂Te₃ nanotubes prepared from Te nanowires.²⁸⁰ (c) TEM of Bi₂Te₃ nanowires prepared from Te nanowires.²⁸² (d) TEM of the ultrathin Bi₂Te₃ nanowires fabricated from ultrathin Te nanowires.²⁸³

2.2.7 Electro-depositing Method.

This method is based on the cathodic reduction reaction under stable voltage and current in appropriate electrolytes. The substrate material, such as anodized aluminium oxide (AAO), indium-tin oxide (ITO) or other materials, is used as a cathode and is immersed into a solution containing a metal salt to be deposited. Then dissolved metallic ions are attracted to the cathode under electrical field and then being reduced to the metallic form. Usage of different cathode materials can lead to either nanoarrays/nanowires (such as using AAO) or

uniform film structures. Many different kinds of nanostructured MCs, such as CuTe nanobelts,²⁸⁸ Bi-Te nanowires and nanotubes;^{289, 290} or thin MCs films²⁹¹⁻²⁹³ could be obtained. Distinctive advantages of the electro-deposition method lie in that simple and accurate control over the quality of products, such as the thickness, morphology, and compositions of the deposited products, could be achieved via the current density, voltage, temperature, surfactants, concentration, selection of electrolyte and deposition substrate, etc.. For example, polycrystalline BiTe arrays of nanowires and nanotubes could be easily prepared by electro-deposition method using polycarbonate (PC) as cathode template in an electrolyte made from dissolving 0.01 M bismuth oxide and 0.01 M tellurium oxide in 2 M HNO₃.²⁸⁹ Under different potentials, p-type (Bi-rich) and n-type (Te-rich) BiTe can be obtained. Also the morphology changes between nanowires and nanotubes.²⁸⁹ While Li et al.²⁹³ fabricated the Bi₂Te₃ films from electrodeposition of a solution containing bismuth nitrate and tellurium dioxide in 1 M nitric acid onto gold-sputtered AAO substrates. They also found the ethylene glycol significantly affected the properties of final products.²⁹³

2.2.8 Electrospinning Method.

Electrospinning, which is based on electric force to draw charged threads of organic or inorganic solutions into the order of nanometers [Figure 2.28(a)], is mainly used to fabricate 1-dimensional structures. The diameters, compositions of the 1-dimensional structure could be easily controlled by the properties of solution, voltage between the spinning tip and target, injection speed, and diameters of spinning tips, etc.. The only prerequisite is that the precursors must be soluble or well dispersed in the initial solution. The process does not require the use of coagulation chemistry or high temperatures to produce solid threads from solution; thereby makes it easy to operate, simple, cheap, and scalable. 1-dimensional MC nanostructures, such as nanowires,²⁹⁴ nanotubes,^{295, 296} heterostructures,²⁹⁷ and double walled nanotubes could be steadily fabricated by this method, as shown by Figure 2.28(b-d).

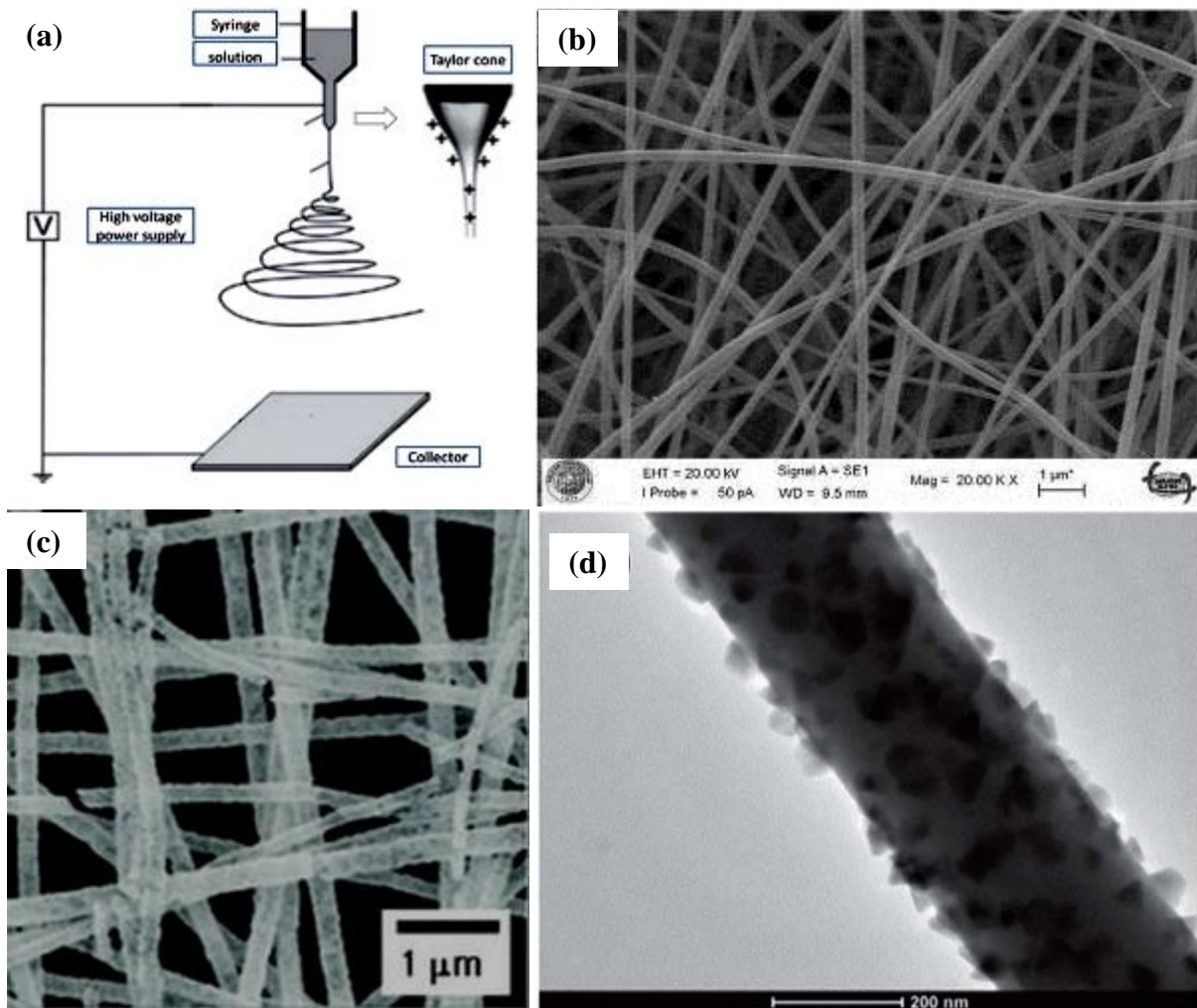


Figure 2.28. (a) Schematic of electrospinning method. (b) $\text{Cu}_2\text{FeSnS}_4$ nanowires,²⁹⁴ (c) Bi_2Te_3 nanotubes;²⁹⁵ and (d) CdS@ZnO core-shell nanowires²⁹⁷ prepared by electro-spinning method.

2.3 Application on Energy Storage and Conversion.

Despite that now most of our energy is still originated from burning of fossil fuels which are non-renewable in short period and may cause serious pollution to the environment; it has become a common sense that we human is facing with more and more serious energy crisis as well as environmental problems including global warming and pollutions. To save our future, now the developing and utilization of green renewable energy, such as solar energy, waste heat recovery, fuel cells, hydrogen and so on, has been one of the most hot topics all around

the world's scientists.

Especially, nanostructured MCs have many energy related applications ranging from energy storage to catalysts, from solar cells to thermoelectric, etc..^{9, 11, 177, 187} Thereby in the following parts, we focus on several most promising energy related applications of nanostructured MCs including thermoelectric technology, quantum dot solar cells, and the Lithium/Sodium ion batteries. Their basic working mechanisms, and basic concepts are explained; the wide application of different MCs nanostructures in these fields is also well deliberated.

2.3.1 Heat-electricity Conversion.

2.3.1.1 Working Mechanism of Thermoelectric Materials.

As might be expected, nowadays, more than half of our primary energy is utilized in the form of heat. Examples include the usage of fossil fuels to power engines; obtain electricity from steam power generators, etc. Nevertheless, the majority of the energy actually produced by Man is lost, mainly in the form of waste heat. Just to mention one example, in a vehicle, only ~10% of the energy produced from burning petrol in the internal combustion engine is converted to useful work, while the rest is wasted.²⁹⁸ For another example, in a steel works, according to the statistics, around 10^9 J heat would be wasted in the course of producing 1 ton of crude steel.²⁹⁹ Thus, the technologies for recovering this waste heat are a subject of great interest, because huge amounts of energy would be saved.

The phenomenon of thermoelectricity (TE), which has been known since the discoveries made by Seebeck, Peltier, and Thomson in the early 1800s, is such a technology that can convert heat into electricity directly via a solid-state conversion. As presented by Figure 2.29, its basic working mechanism is very simple: when a material is being heated, charge carriers

in the material would flow from the hot side to cold side. Thus, there is a voltage when a load is connected, so the material works as a thermoelectricity generator (TEG); on the other hand, if the material is placed in an electric field (connected to a power source), the temperature difference will be maintained, and the material will work as a thermoelectric refrigerator (TER).

This technology has distinct advantages, including: (1) thermoelectric conversion is reliable and operates in silence compared with other energy conversion technologies, as it works without mechanical movement; (2) thermoelectric devices are simple, compact and safe; (3) it is an environmentally friendly green technology because no heat, and no gaseous or chemical waste are produced during operation; (4) it can be widely used in places where other energy conversion technologies are unavailable, such as in the remote outer space.²⁹ However, the wide application of this technology is seriously hindered by its low energy conversion efficiency (η) between heat and electric. With a given temperature difference, η is mainly depends on a dimensionless value, called the “figure of merit” (ZT), which will be explained later.

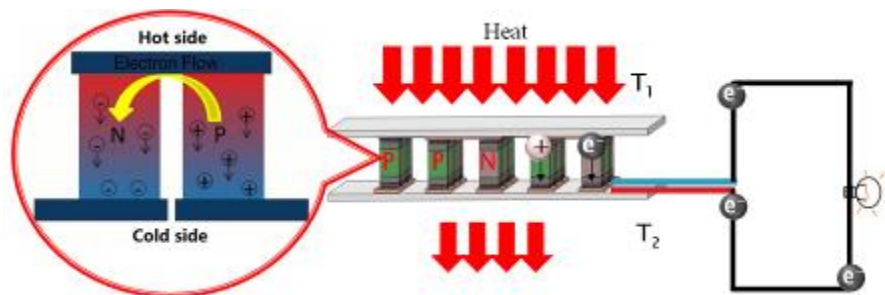


Figure 2.29. Working principle and structure of a thermoelectric generator (TEG) module.

2.3.1.2 Basic Concept and Parameters in Thermoelectric Technique.

Figure of merit (ZT): ZT is a dimensionless value used to characterize performance of thermoelectric property of a material. It could is given by Equation (2.7).

$$ZT = \frac{S^2 \sigma}{\kappa} T \quad (2.7)$$

In which S is the Seebeck coefficient, σ is the electrical conductivity, κ is the thermal conductivity, and $S^2 \sigma$ is called the power factor (P_F), T is the measuring temperature.

Electrical conductivity (σ): electrical conductivity is the reciprocal of electrical resistance, represents a material's ability to accommodate the transport of an electric charge. It could be calculated from the Equation (2.8), in which n is the charge carrier concentration, μ is the mobility of charge carriers, and e is the charge of one electron.

$$\sigma = ne\mu \quad (2.8)$$

The Seebeck coefficient (S , also known as thermal power): It is a measure of the magnitude of an induced thermoelectric voltage in response to a temperature difference across the material. It is more related with the carrier concentration (n), band structure and density of states of materials, as shown by Equation (2.9). m^* represents the effective mass of the charge carriers which usually decreases with increasing carrier mobility. k_B , h , and T are Boltzmann constant, Planck constant and measuring temperature, respectively.

$$S = \frac{8\pi^2 k_B^2}{3eh^2} m^* \times T \times \left(\frac{\pi}{3n}\right)^{2/3} \quad (2.9)$$

Thermal conductivity is the property of a material to conduct heat. It is related with vibration and transport of phonons in the material. It is composed by charge carrier thermal conductivity (k_e) and lattice thermal conductivity (k_l), as shown in Equation (2.10). In which k_e could be estimated by Wiedemann-Franz Law [Equation (2.11)].

$$k = k_e + k_l \quad (2.10)$$

$$k_e = ne\sigma \quad (2.11)$$

In semiconductors, usually > 90% of thermal conductivity comes from the lattice thermal conductivity (k_l), which is independent of the electrical conductivity (σ).

The heat to electrical conversion efficiency (η) is the ratio of the output electrical power and the total input of heat. η is strongly depends on the figure of merit (ZT) of the thermoelectric material, as described by Equation (2.12), where $\eta_c = 1 - T_2/T_1$, T_2 and T_1 are the temperatures of cold and hot sides of a thermoelectric generator, respectively.

$$\eta = \eta_c \times \frac{\sqrt{1+ZT} - 1}{\sqrt{1+ZT} + T_2/T_1} \quad (2.12)$$

2.3.1.3 Applications of Metal Chalcogenides in Thermoelectric Materials.

According to the above description, the three main factors that related with ZT (S , σ , κ), are strongly dependent on each other, and it is very challenging to improve them. The first generation of thermoelectric materials was developed over four decades ago, with ZT of ~0.8-1.0 and conversion efficiency (η) of 5-6% achieved on Bi_2Te_3 (from the 1950s to the 1990s). The second generation of bulk thermoelectric materials with ZT ranging from 1.3 to 1.7 with typical efficiency of 10% (1990s to 2010s).³⁰ Introducing of nanoscale inclusions or compositional inhomogeneity into existing materials boosts the ZT because abundant grain boundaries or defects of the nanostructures can significantly decrease the lattice thermal conductivity (κ_L) while preserving a relatively high power factor. Continued progress is now expected to raise the ZT by a factor of 2, with the predicted efficiency over 20%, a highly exciting prospect which will surely have a large impact in the energy production and conservation fields.³⁰

Compared with other kinds of thermoelectric materials, metal chalcogenide based

thermoelectric materials possess a higher power factor ($P_F = S^2\sigma$) due to the less covalent nature of their bonds due to low electronegativity. Their increased atomic weight compared to some other thermoelectric materials is of benefit for reducing thermal conductivity. In addition, the chalcogenide elements are easy-to-form compounds with different kinds of structures, which offer a good platform for investigating and improving thermoelectric performance. Moreover, the chalcogenides are easy to doped into n-type (by halides) or p-type (by pnictides) materials, which is important for assembling TEGs. It has been proved by many reports that metal chalcogenide based thermoelectric materials possess excellent performance. For example, hitherto, the highest ZT value ($ZT = 3.6$ at 580 K) was obtained in $\text{PbSe}_{0.98}\text{Te}_{0.02}/\text{PbTe}$ quantum-dot superlattices (QDSLs) grown by molecular beam epitaxy (MBE) method;³⁰⁰ while a ZT of 2.6 was obtained at 923 K for single crystal SnSe ;⁶⁷ Na doped full-scale structured PbTe exhibited a maximum ZT of 2.2 at 915 K.⁶⁸ Other binary MCs including Cu_2X , Ag_2X , In-X , layered transition MCs, etc. are also good thermoelectric materials with extremely high ZT than other thermoelectric materials.^{29, 30, 52, 167, 301, 302}

Another big point of superiority for metal chalcogenides based thermoelectric materials lies in for low cost on, both for material fabrication and for operation. Yadav et al.³⁰³ calculated the efficiency ratios of different kinds of materials using the ZT value divided by the fabrication cost. According to their results, metal chalcogenides (typically Bi_2Te_3 and PbTe , are slightly lower than for oxides and Zn_4Sb_3 due to relatively high price of Te element. ZnO , NaCoO_2 , and Zn_4Sb_3 are unstable; however.³⁰³ LeBlanc et al.³⁰⁴ evaluated the operating cost for TERs made from different thermoelectric materials under a constant temperature difference. They found that metal chalcogenide based materials possessed both the highest ZT values and the lowest operating cost.

2.3.2 Quantum dot Solar Cells.

2.3.2.1 Working Mechanism of QDSSC.

Solar energy, as a potential and marketable alternative energy for conventional fossil fuels, plays significant role in green renewable energy. According to the literature,³⁰⁵ every hour the solar energy our Earth received from sunlight reaches 4.3×10^{20} J; which is sufficient to support the energy consumption of human beings in a year (4.1×10^{20} J per year). Thus it is still very ideal even we can make use only several percent of this green energy. One of the most important utilization way of this green solar energy is by introduction of low-cost and high-efficiency solar cells, which includes variety forms including dye sensitized solar cells, bulk hetero junction solar cells, quantum sensitized solar cells, etc.. The development of solar cells could be generally divided into three stages. The first generation photovoltaic devices are based on single crystal hetero junction wafer, whose energy conversion efficiency can be as high as 27%.³⁰⁵ The thin inorganic film structure is the typical feature of the second generation solar cells. Compared with the first generation, they cost less, but a lower efficiency (<14%).³⁰⁵ There exists an upper limit for the conversion efficiency of the first generation solar cells called Shockley-Queisser thermal dynamics limit (33%).³⁰⁶ Thus in order to break this limit, the third generation solar cells are developed, it was predicted to possess medium cost but highest conversion efficiency. Some typical forms of the third generation solar cells including the dye-sensitized solar cells (DSSCs), quantum dot-sensitized solar cells (QDSSCs), colloidal quantum dot (CQD) solar cells, organic solar cells, etc..

The quantum dot sensitized solar cells (QDSSCs) is a developed based on the model of dye sensitized solar cells (DSSCs). Instead of using dye as sensitizer, the QDSSCs employ nano-sized semiconductors (usually called quantum dot), which possess lower fabricating cost,

good photostability, multi, tunable and broad photo-excitation and less hazardous during process than the organic dyes. However, QDSSCs possess much similar mechanism and structure with DSSCs, which are schematically shown by Figure 2.30. A typical QDSSC consists of three parts including a quantum dots (QD) sensitized photoanode (photoelectrode), a counter electrode (CE), and a salt electrolyte. The photoanode usually consists of quantum dots loaded on a mesoporous wide band gap semiconductor layer (such as TiO_2 , ZnO , and so on) that is attached to the conducting glass. When exposed to the light, the electrons in quantum dots are excited, the electron-hole pairs generated, and electrons are further transported to the wide band gap semiconductor layer and conducting glass via conduction band. The holes are left in the valence band and the QDs are in oxidized state, which is easy to be reduced by electrolytes. After the out circulation, the electrons flow to the counter electrodes. Then the electrons flow back to the photoanode via redox of electrolytes at the both the counter electrodes/electrolyte and photoanode/electrolyte interface. One notable thing is that the electrolyte of QDSSCs is usually sulfides ($\text{S}^{2-}/\text{S}_n^{2-}$ redox couple) instead of Iodides in DSSCs. The generated potential, which corresponds to the difference between the quasi-Fermi level of the electron in the photoanode and the redox potential of the sulfide electrolyte, is an evidence of the solar energy conversion to electric energy.

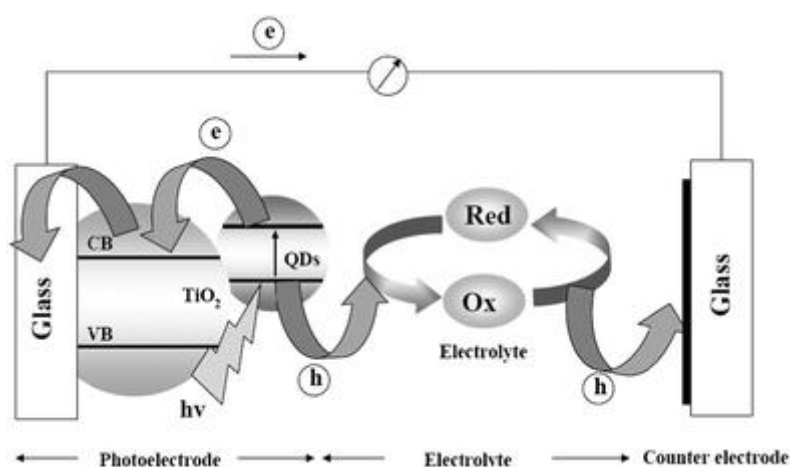


Figure 2.30. Working principle and structure of Quantum Dot Sensitized Solar Cells.³⁰⁷

2.3.2.2 Basic Concepts and Parameters in QDSSC.

Several basic concepts and parameters used for characterization performance of QDSSCs are listed as following:

Photocurrent density (I): When the QDSSCs are exposed to light, the quantum dots may absorb the energy of photons and electrons at low energy level are excited to form the photocurrent (I_c). Generally the photocurrent is related with the intrinsic properties of quantum dots, the intensity of lights and area of the solar cells. The photocurrent density (I) is the photocurrent formed by unit area of solar cells, and the unit is usually mA/cm^2 . I_{sc} represents the short circulate photocurrent density.

Photovoltage (V): Accompanied by the formation of photocurrent under light, a potential also formed, this is the photocurrent. V_{oc} is the open circulate current. The unit is mV.

Power output (P): The power output of the QDSSCs can be determined from the product of photocurrent and photovoltage, the unit is mW.

Fill factor (FF): At the maximum power output point (P_m), the photocurrent and photovoltage is the I_m and V_m , respectively. Then the Fill Factor (FF) can be expressed by Equation (2.13), e.g., the ratio of the actual maximum obtainable power to the product of the open circuit voltage and short circuit current. High fill factor means a low equivalent series resistance and a high equivalent shunt resistance, and less dissipated current in internal losses.

$$FF = \frac{I_m \times V_m}{I_{sc} \times V_{oc}} \quad (2.13)$$

Incident solar power density (P_s): The value of P_s is standardized at $1000 \text{ W}\cdot\text{m}^{-2}$ for photovoltaic cell tested at spectral intensity matching the sun's intensity on earth's surface at

an angle of 48.2° (equivalent to AM 1.5 spectrums).

Power conversion efficiency (η): The power conversion efficiency equals the ratio between the real maximum power output of the solar cells (P_m) and incident solar power density (P_s), as shown by Equation (2.14).

$$\eta = \frac{P_m}{P_s} = \frac{I_m \times V_m}{P_s} = I_{sc} \times V_{oc} \times FF / P_s \quad (2.14)$$

Incident photon to current efficiency (IPCE): IPCE is also called the external quantum efficiency. It is a measurement of the efficiency of light being transferred into charge carriers. Thus it equals to the ratio of charge carriers collected at the electrodes to the number of incident photons. IPCE at different wavelengths is determined from the short circuit photocurrents (I_{sc}) observed at different excitation wavelengths using the Equation (2.15).

$$IPCE = \frac{1240 \times J_{sc}}{\lambda \times I_{inc}} \times 100\% \quad (2.15)$$

where I_{inc} is the incident light power (i.e. the energy of the light incident on the electrode) and λ is wavelength. For an ideal solar cell, the J_{sc} value can be determined from the IPCE data with the standard AM 1.5 spectrums. However, in QDSSC, the case is not ideal. Thus the calculated J_{sc} might be an approximation for the measured J_{sc} under 1 sun (1000 W.m^{-2}).

2.3.2.3 Applications of Nanostructured Metal Chalcogenides in QDSSC.

Various MCs materials have been used as photoanode in QDSSCs because of their particular properties for photosensitization. These materials include ternary CdHgTe, CuInS₂, AgInSe₂, PbSeS and binary CdS, CdSe, PbS, ZnSe, CdTe, Ag₂S, SnS₂, SnSe₂ etc..^{305, 308} Among these materials, CdSe and CdS are frequently used because of their ease of fabrication and characterization.³⁰⁵

There are several ways to improve the performance of the solar cells using MCs quantum dots as the sensitizers (or photoanode). The most common ways is the increase of QD size or the surface area covered by the QDs on the photoelectrode, as well as nano-engineering on the TiO₂ layer.³⁰⁹ Another method was reported by Yu et al..³¹⁰ Instead of single CdS or CdSe, they used CdSe@CdS core/shell structures as the sensitizer, which may exhibit higher J_{SC}, V_{OC}, and η . Besides, the core/shell structure may effectively prevent charge recombination by reducing the surface states and accelerating charge separation.³¹⁰ Jung et al.³¹¹ produced a ZnS coated CdS QDs layer. The passivation layer reduced the recombination rate from TiO₂ to the electrolyte, resulting in higher η . Similar results has also been found in PbS QDSSCs with a CdS coating layer.³⁰⁹ Other materials with suitable excitation level may lead to formation of multi-layered, which can cause multi-excitation and improve QDSSC performance. Such as in the CdS/CuInS₂ system, a maximum η of 1.47% can be achieved while only 0.34% and 0.38% single QD.³¹² Other optimization on processing parameters such as annealing temperatures, could also affect QDSSC performance. As an example, Yu et al.³¹⁰ annealed TiO₂/CdSe/CdS/ZnS photoanode at around 300 °C and get a remarkable efficiency of 4.21%; while the one without annealing yielded only 3.20%. Mn doping is another effective way to further boost efficiency of CdS/CdSe co-sensitized QDSSCs, as reported by Santra and his coworkers, a conversion efficiency of 5.4% are obtained.³¹³ This is because the doping of Mn²⁺ into the CdSe QDs can raise its conduction band, accelerate the electron injection kinetics, reduce the charge recombination, as well as increase the electron lifetime. All of these effects lead to significantly improvement of the performances.^{313, 314}

As an important part of QDSSCs, the counter electrodes has a vital influence on the solar cell's overall performance.³¹⁵ Good counter electrode materials need to possess high conductivity, high catalyze activity towards redox of electrolytes, as well as high stability.

Because now generally the electrolytes for QDSSCs is sulfides,³¹⁶ the noble metal Pt counter electrodes, which works well in DSSCs, performs extremely bad in QDSSCs because that the Sulphur-containing compounds would adsorb strongly to the Pt surface and thus reduce its catalytic ability and conductivity. Instead, now Au, carbon materials, and metal chalcogenides are found to be efficient counter electrodes materials, among which nanostructured MCs possess both the highest catalyze activity and stability.³¹⁷⁻³²¹ A comprehensive review on the application of nanostructured MCs including sulfides of Cu, Fe, Co, Pb, Ni and selenides of Cu, Ni, Mn, Bi, Pb, W, Mo as counter electrodes materials of QDSSCs has been released by Meng et al..³¹⁷ Their results show that now the most promising counter electrodes for QDSSCs is sulfides or selenides of Cu with a maximum power conversion efficiency of above 6% employing CdS/CdSe as photoanode.^{252, 317}

2.3.3 Lithium/Sodium Ion Batteries.

2.3.3.1 Working Mechanism of LIBs/SIBs.

Energy storage is also another important issue should be considered during utilizing of all kinds of energy. As a kind of secondary energy storage device, Lithium ion batteries (LIBs) have been demonstrated to be one of the most successful examples in commercial applications since last century. Now it remains the major power sources for power tools, mobile phones, laptop computers, and telecommunication devices, etc. because it possesses many advantages compared with other battery systems (such as lead acid batteries, nickel cadmium batteries, etc.). First of all, LIBs own four times the energy and twice the power density of the nickel cadmium batteries. Meanwhile, LIBs show longer cycle life and no memory effect for recharging is observed. Finally, LIBs are environmentally friendly and has a low density ($\rho = 0.53 \text{ g.cm}^{-3}$).

The LIB works by means of lithium ions rocking between anode and cathode through

electrolyte, while energy is release or replenished inside the cell. Taking the conventional lithium-ion cell (graphite/LiCoO₂) as example (Figure 2.31), during the spontaneous discharge process, lithium ions move from the layered anode (graphite) to the cathode (LiCoO₂) via the electrolyte based on a redox reaction, while the electrons go through the external circuit in the same direction, converting the electrochemical energy into electrical energy. The potential of the cell is close to the redox potential between anode and cathode. During charge process, external electrical power source forces lithium ions move back from the cathode (LiCoO₂) to the anode (graphite, while the electrical energy is stored as electrochemical energy.

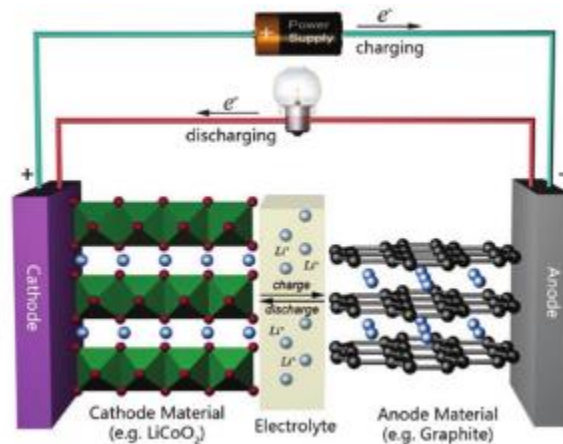


Figure 2.31. Schematic of working mechanism in a rechargeable LIB.³⁷

Compared with LIBs, Sodium ion batteries (SIBs) own a similar working mechanism. But sodium shows high abundance and low cost but larger ion size made the selection of electrode materials much difficult and their capacity is lower than LIBs.

2.3.3.2 Basic Concept and Parameters in Batteries.

Solid electrolyte interface (SEI): When the electrode is charged in a non-aqueous electrolyte for the first few cycles, along with the intercalation of Li/Na ions, the electrolyte may be decomposed and form a surface layer called solid electrolyte interface (SEI). The concept of

SEI is important for secondary batteries because it plays a critical role in their safety and cycle life.

Voltage (V): The open circuit voltage (V_{oc}) is the voltage measured across the terminals of a cell without external current flow. It is determined by the difference in electrochemical potential between the anode and the cathode; while the operating voltage of the cell should minus the potential consumed by internal resistance.

Capacity (Q): It refers to the total amount of charge for the redox reaction during the charge/discharge process of the cell, as demonstrated by Equation (2.16). Where $I(t)$ is the current; t is the time; t_1 and t_2 is the start and ending time of charge/discharge; n and z are the amount and valence of the ions, respectively; F is the Faraday constant.

$$Q = \int_{t_1}^{t_2} I(t)dt = nzF \quad (2.16)$$

Specific capacity (Q_s) is the capacity of cells in either per unit volume (volumetric specific capacity) or per unit weight (gravimetric specific capacity) of active materials in electrode.

The theoretical specific capacity (Q_{TSC}) of material is the capacity calculated from the following equation:

$$Q_{TSC} = \frac{1000 \times F \times m}{M \times 3600} \quad (2.17)$$

Where m is the number of electrons participating in the electrochemical reaction, F is the Faraday constant, and M is the molar mass of the active materials.

Coulombic efficiency (η_e) is the ratio of the charge capacity to the discharge capacity at the n^{th} cycle, which represents the cycling stability.

Capacity retention: The capacity retention is the ratio of charge or discharge capacity of a

later cycle to a previous one.

Rate capability (C-rate) is used to evaluate the transfer speed of lithium/sodium ions. C represents either the theoretical charge capacity of a cell or the nominal capacity of a cell. For example, 2C means a current allowing a full charge/discharge in 1/2 hours.

2.3.3.3 Applications of Nanostructured Metal Chalcogenides in LIBs/SIBs.

Benefiting from the unique physical and chemical properties including higher electrical conductivity, mechanical and thermal stability than those of their corresponding metal oxides, rich redox chemistry that contributes to their high specific capacity/capacitance, as well as the merits of nanostructures, nanostructured MCs, especially nanostructured metal sulfides and layered transition MCs have been stand out from other electrode materials for LIBs/SIBs in the past few decades.³²²⁻³²⁴

For example, Fe-S system (including FeS, FeS₂, Fe₃S₄) and Cu-S system [including CuS, Cu₂S, Cu_xS (1<x<2)] have long been investigated as interesting high-capacity anode materials of LIBs.^{323, 324} FeS₂ nanowires were fabricated by Li et al.³²⁵ in large scale from FeF₂ and exhibited a capacity of 668 mAh.g⁻¹ during the first discharge within the voltage range of 2.4-1.1 V vs. Li/Li⁺ at a speed of 89 mA.g⁻¹. Even after 50 cycles, the capacity retention still reached 52% with a capacity of 350 mAh.g⁻¹. Lai et al.²⁸⁹ prepared Cu₂S nanowire arrays on Cu foil and used it as electrodes directly. The charge–discharge tests show an initial capacity of 470 and 400 mAh.g⁻¹, respectively, with the potential range of 0.05 to 3.0 V vs. Li/Li⁺ and a high rate of 560 mA.g⁻¹. After 100 cycles, about 230 mAh.g⁻¹ is maintained. The high reversible capacity under high rate originated from two aspects: the low resistance caused by good contact between the nanowires and Cu substrate; and the 1-dimensional structure which is able to allow release of strain induced by electrodes reaction.

Some of the MCs are recognized as promising NIBs conversion anode candidates, such as Sb_2S_3 , SnS_2 , MoS_2 , WS_2 and so on.³²⁴ For instance, the composite of Sb_2S_3 and graphene showed an initial capacity of 594 mAh.g^{-1} at an extremely high rate of 1 A.g^{-1} ; moreover, after 400 cycles this value only faded to 500 mAh.g^{-1} .³²⁶

However, not only sulfides, selenides also presented excellent electrochemical performance. Yue et al.³²² fabricated and tested Cu_2Se nanostructures as a positive material for sodium ion batteries, which exhibited large reversible capacities (about 250 mAh.g^{-1}), good cyclic stabilities (within 100 cycles with a capacity of 113.6 mAh.g^{-1} under a rate of 25.3 mA.g^{-1}) and low polarization.

Chapter 3 Experiment

3.1 Chemicals and Materials.

The details about chemicals and materials used in this doctoral work are listed in Table 3.1.

Table 3.1 Chemicals and materials used in this thesis.

Materials/Chemicals	Formula	Purity (%)	Supplier
Acetone	CH_3COCH_3	>99	Ajax Finechem
Antimony (III) Chloride	SbCl_3	>99	Sigma Aldrich
Bismuth (III) Nitrate Pentahydrate	$\text{Bi}(\text{NO}_3)_3 \cdot 5\text{H}_2\text{O}$	>98	Sigma Aldrich
Carbon Black (Super P)	C	N.A.	Timcal Belgium
Carboxymethyl Cellulose Sodium (CMC)	$\text{C}_8\text{H}_{16}\text{NaO}_8$	N.A.	Sigma Aldrich
Copper (II) Acetate	$\text{Cu}(\text{CH}_3\text{COO})_2$	>99	Sigma Aldrich
Copper(II) Acetylacetonate	$\text{Cu}(\text{C}_5\text{H}_7\text{O}_2)_2$	>99	Sigma Aldrich
Copper (I) Bromide	CuBr	97	Sigma Aldrich
Copper (I) Chloride	CuCl	97	Sigma Aldrich

Copper (II) Chloride Dihydrate	$\text{CuCl}_2 \cdot 2\text{H}_2\text{O}$	>99	Sigma Aldrich
Copper (II) Chloride	CuCl_2	98	Sigma Aldrich
Copper Foil	Cu	N.A.	China
Copper (II) Fluoride	CuF_2	97	Sigma Aldrich
Copper (II) Nitrate Trihydrate	$\text{Cu}(\text{NO}_3)_2 \cdot 3\text{H}_2\text{O}$	99	Anala R
CR2032 type coin cells	N.A.	N.A.	China
Dichloromethane	CH_2Cl_2	>99	Sigma Aldrich
Diethyl Carbonate (DEC)	$\text{C}_5\text{H}_{10}\text{O}_3$	>99	Sigma Aldrich
Ethanol	$\text{C}_2\text{H}_5\text{OH}$	99	Ajax Finechem
Ethylene Carbonate (EC)	$\text{C}_3\text{H}_4\text{O}_3$	99	Sigma Aldrich
Fluoroethylene Carbonate (FEC)	$\text{C}_3\text{H}_3\text{FO}_3$	99	Sigma Aldrich
Fluorine doped Tin Oxide Glass (FTO)	N.A.	N.A.	Sigma Aldrich
Hexadecylamine	$\text{CH}_3(\text{CH}_2)_{15}\text{NH}_2$	98	Sigma Aldrich

Lead (II) Nitrate	$\text{Pb}(\text{NO}_3)_2$	>98	Sigma Aldrich
Lithium Hexafluorophosphate	LiPF_6	>99	Sigma Aldrich
Lithium Metal	Li	>99	Sigma Aldrich
Milli-Q water	H_2O	5 ppb (TOC)	Millipore USA
Octadecene	$\text{C}_{18}\text{H}_{36}$	90	Sigma Aldrich
Oleylamine	$\text{C}_{18}\text{H}_{35}\text{NH}_2$	70	Sigma Aldrich
Oleic Acid	$\text{C}_{18}\text{H}_{34}\text{O}_2$	97	Sigma Aldrich
Polypropylene separator	$(\text{C}_3\text{H}_6)_n$	Celgard2500	Hoechst Celanese
Polyvinylidene difluoride (PVDF)	$(\text{CH}_2\text{CF}_2)_n$	N.A.	Sigma Aldrich
Potassium Chloride	KCl	>99	Sigma Aldrich
Selenium Powder	Se	>99	Sigma Aldrich
Silver Nitrate	AgNO_3	>99	Sigma Aldrich
Sodium Borohydride	NaBH_4	>98	Sigma Aldrich
Sodium Sulfide Nonahydrate	$\text{Na}_2\text{S}\cdot 9\text{H}_2\text{O}$	>98	Sigma Aldrich

Sulphur	S	>99	Sigma Aldrich
Tellurium Powder	Te	>99	Sigma Aldrich
Tin (II) Chloride Dihydrate	SnCl ₂ .2H ₂ O	>99	Sigma Aldrich
Titanium Dioxide	TiO ₂	>99	Sigma Aldrich
Trioctylphosphine (TOP)	C ₂₄ H ₅₁ P	97	Sigma Aldrich
Trioctylphosphine Oxide (TOPO)	C ₂₄ H ₅₁ PO	99	Sigma Aldrich

3.2 Experimental Outline.

Figure 3.1 illustrates the whole experimental outline of this doctoral work, which is mainly made of two parts: the first part referred to fabrication and characterization of nanostructured/composite metal chalcogenides in three different ways; and the second part is that application of the as-fabricated metal chalcogenides as anode materials of coin-type Lithium Ion Batteries, counter electrodes of sandwich-structured quantum dot sensitized solar cells, or sintered pellets for thermoelectric generators.

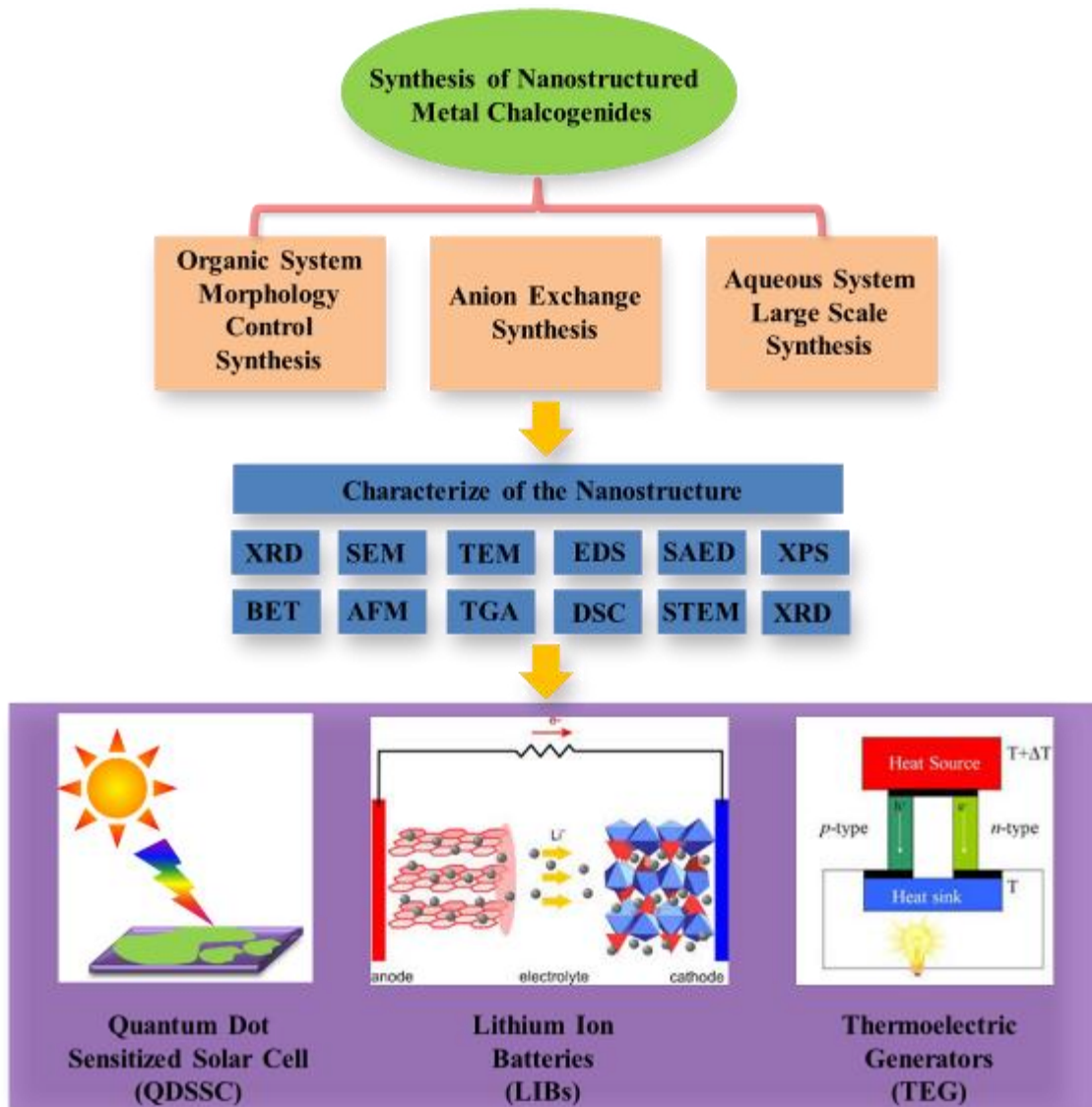


Figure 3.1. Outline of research procedures.

3.3 Synthesis Method.

Different kinds of nanostructured metal chalcogenides were prepared via three different methods, including classic hot injection method, reduction-precipitation method and anion exchange reaction. The details of these synthetic routes are well presented in this following section.

3.3.1 Reduction-Precipitate Reaction.

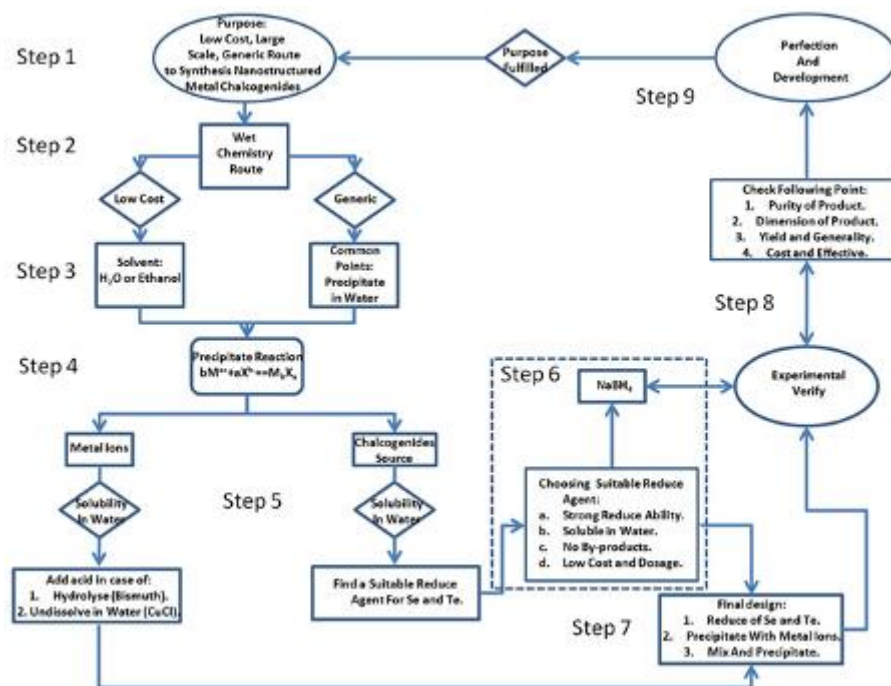


Figure 3.2. Design of the reduction-precipitation method.

As for most of wet chemical method, the cost, yield and good control are always hard to perfect. To get good control, surfactants, reaction temperature, as well as selection of solvents are necessary, which would definitely increase the cost and the yield is also limited. However, in this doctoral work, based on several simple and basic principles of chemistry, a two-step wet chemical method to fabricate different kinds of nanostructured MCs in large scale in fast speed with good control over the quality of product is designed, which is schematically in Figure 3.2.

In the first step, my goal was set to design a large scale, low cost, generic route to fabricate nanostructured MCs with good properties control. Thus basically wet chemical route was selected and water was suitable solvent to minimize the cost (Step 2). To tackle the requirement of "general", the common point that various kinds of MCs possess low solubility in water is found. Then in Step 3 and 4, I designed a precipitation reaction to get products.

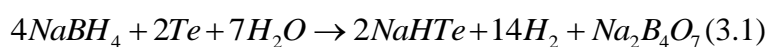
However, due to that the Se^{2-} and Te^{2-} ions are not stable in water and air; instead, Selenium or Tellurium powder, which are cheaper and more stable, are better starting precursors. Water soluble sulfide is still can be used as the Sulphur source because it's cheap and stable enough. Meanwhile, although most of metal precursor can be simply obtained from water soluble metal salts; some metal salts, such as BiCl_3 and SbCl_3 , is easy to be hydrolyzed in aqueous solution, thus it is necessary to use employ acid to adjust pH of the system. Besides, the acid is helpful to digest some insoluble metal salts, such as CuCl . Now the only one key problem becomes how to get Se^{2-} and Te^{2-} ions from Se and Te powder. A natural thinking is using of reduce agent, and thereby in Step 6 some basic requirements for the reduce agent are listed. Based on these conditions, several different chemicals including LiAlH_4 , NaBH_4 , N_2H_4 , etc. are chose as candidates. Combining the cost, safety, and the results from the followed verify experiments, NaBH_4 is found to be the best selection. After further perfection and development of this route, different kinds of surfactant-free metal chalcogenide nanostructures can be prepared by co-precipitation of cationic and anionic precursors in aqueous solution after a reduction procedure under room temperature.

This synthesis route is capable to prepare different kinds of surfactant-free nanostructured metal chalcogenides at room temperature in large scale with a high yield (>90%) within short reaction time (<5 hours). The total cost is very low as only water is used as solvent. The size and composition of metal chalcogenide nanostructures could be easily controlled by adjusting reaction parameters.

3.3.2 Anion Exchange Reaction.

As described in the literature review, ion exchange reaction now has been one important strategy to fabricate nanostructured MCs with good control over morphologies. Based on our reduction-precipitation synthesis route and solubility difference between metal chalcogenides, an aqueous, high-efficiency, scalable, and low-cost strategy to fabricate Cu_2Te

nanotubes and nanosheets at room temperature has been developed. Our results show that even in aqueous solution, Cu_2E ($\text{E} = \text{O}, \text{S}, \text{Se}$) nanoparticles can be transformed into Cu_2Te nanosheets and nanotubes via a simple anion exchange reaction under ambient conditions. For the first step, Te powder was completely reduced into Te^{2-} solution by excess amount of NaBH_4 [Equation (3.1)]; followed by adding the Cu_2Se nanoparticles, Cu_2Te nanosheets will form if the mixture was kept stationary and the nanosheets will be rolled into nanotubes with continuous stirring. The anion exchange reaction is expressed by Equation (3.2).



3.3.3 Hot-injection Method.

The hot injection method is one of the most popular experimental methods for synthesizing crystal and nanostructured metal chalcogenides with varies morphologies and compositions at moderate temperature. Usually this method referred to respectively dissolve metal precursor and chalcogen precursor in organic solvent at suitable temperature to form uniform solution and then one precursor was swiftly injected into another. The nucleation and growth of nanostructure could be well controlled via adjusting reaction parameters, such as solvents, ligands, temperature, concentrations of precursors, as well as reaction time. In our doctoral work, all the hot injection experiments are conducted in a Schlenk line [Figure 3.3(a-b)] in order to prevent the side effect of oxygen and water on the reaction. Detailed operation goes like this: before the reaction, solvents and precursors are first degassed and stirred at 100 °C for 1 hour to exclude all the oxygen and water; then inert gas (Argon or Nitrogen) is purged during the whole reaction and cooling procedure. Cu_xTe nanostructures are prepared by this method and Schlenk line and used to be tested as anode of lithium ion batteries on Landt Battery Test System, which is shown in Figure 3.3(c).

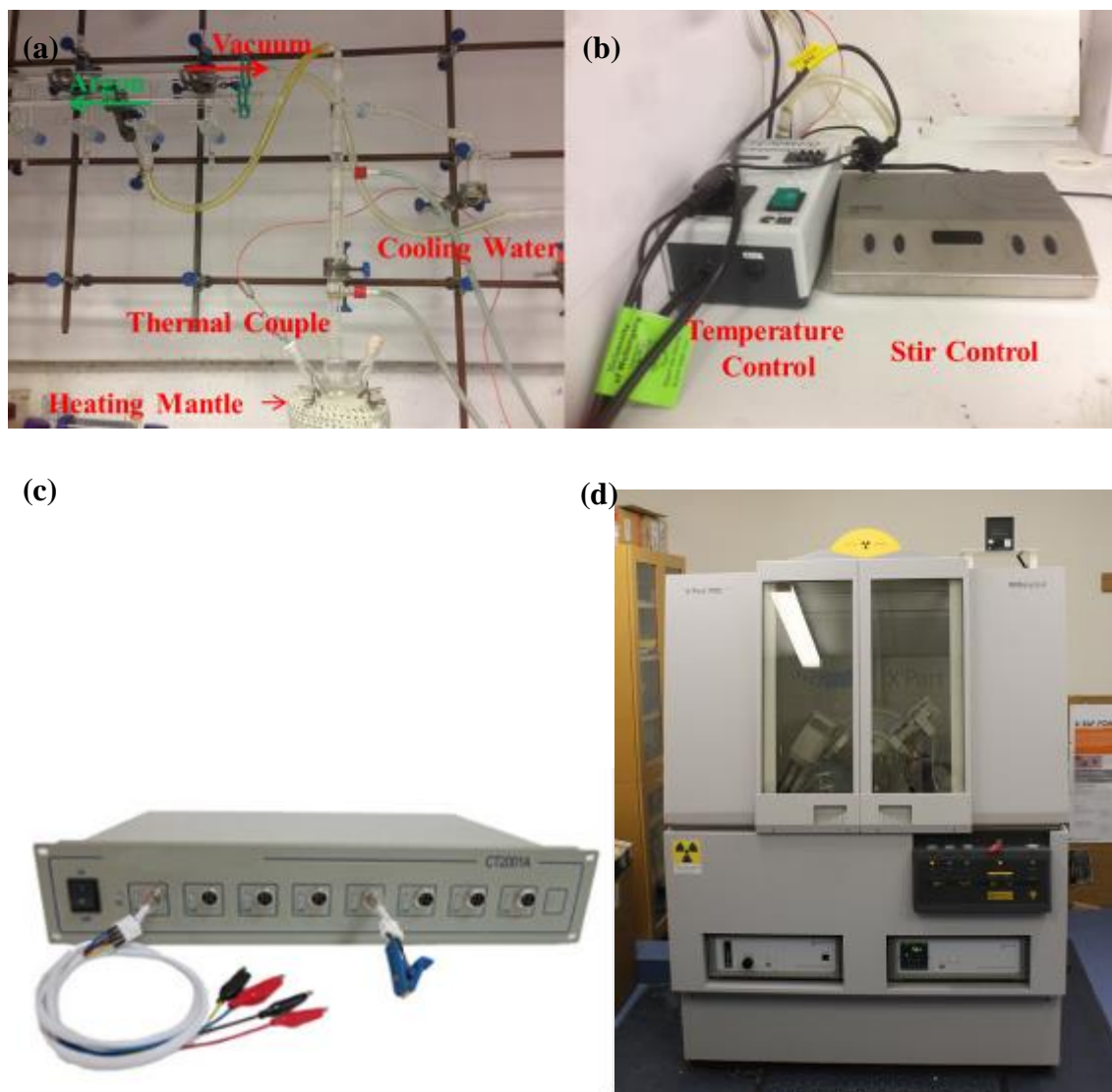


Figure 3.3. Standard Schlenk Line used for hot injection synthesis route. (a) Working part of Schlenk line; (b) temperature and stirring control part. (c) Landt Battery Testing System. (d) PANalytical diffractometer.

3.4 Composition and Morphology Characterization.

The structure, composition, morphology, and other basic physics properties (specific area, specific heat, charge carrier transport properties, etc.) characterization of the as-prepared nanostructured metal chalcogenides were achieved in ISEM, Electronic Microscopy Center (EMC) and the Australian Institute of Innovative Materials (AIIM) building. Other detailed experimental details about applications include QDSSCs, thermoelectric and batteries are

shown in corresponding chapters.

3.4.1 X-Ray Diffraction.

In this doctoral work, GBC-MMA X-ray diffractometer [Figure 3.4(a)] was commonly used to characterize the crystallographic materials with a Cu K_{α} radiation ($\lambda = 1.5418 \text{ \AA}$). The powder sample is placed at a small disc-shaped sample holder with a flattened surface. The whole measurement is conducted under room temperature in air.

3.4.2 Field Emission Scanning Electronic Microscopy.

The microstructure of the prepared nanostructured MCs are characterized by JOEL JSM-7500F field emission scanning electronic microscopy [FESEM, Figure 3.4(b)] in vacuum under room temperature. The samples are stuck onto sample holder by conductive carbon tape. Voltage and current of electron beam are 5 KV, 10 mA, respectively. At the same time, compositions of the samples are conducted by energy-dispersive X-ray spectroscopy (EDS, EDX, or XEDS) affixed within JOEL JSM-7500F. EDS is conducted under electron beam with voltage and current of 15 KV, 20 mA.

3.4.3 Transmission Electronic Microscopy.

Two types of TEM facilities are used in this doctoral work; JOEL JEM-2010 is used for general morphology and high resolution (fringe resolution) image. Scanning transmission electron microscopy-energy dispersive X-ray spectroscopy (STEM-EDS) spectra was collected using a JEOL ARM-200F equipped with an EDAX solid-state X-ray detector. The two facilities are respectively shown in Figure 3.4(c-d) and both operated under an accelerating voltage of 200 KV. Samples were prepared by drop-casting ethanol-dispersed nanostructures onto TEM copper grids. Lattice fringes were measured from the fast Fourier transforms (FFTs) of high resolution TEM (HRTEM) images using the Gatan software.

3.4.4 Brunauer Emmett Teller Surface Area Analysis.

In this study, Quantachrome Autosorb iQ machine (USA) [Figure 3.4(e)] is used to measurement the specific surface area of the as-prepared nanostructures. Nitrogen adsorption-desorption measurements were conducted at 77 K. Before measurements, the samples were degassed under vacuum at 120 °C for 6 h. The Brunauer-Emmett-Teller (BET) specific surface area was calculated from the adsorption data in the relative pressure (P/P₀) range from 0.05 to 0.35.

3.4.5 Thermal Analysis.

In this doctoral work, thermogravimetric analysis (TGA) was used to evaluate thermal stability of nanostructured MCs; while using DSC, specific heat (C_p) of the sample is measured, which is used to determine thermal conductivity. They both can be performed on TGA/DSC 1 machine [Figure 3.4(f)] from Mettler-Toledo Company. However, to get more accurate results about specific heat of materials, another specific DSC machine-"Netzsch 204F1" is also used. For TGA measurement, the sample was placed in an alumina crucible after being completely dried and weighted. While for DSC measurement, the standard reference method is used with single crystal of Al₂O₃ as the reference, e.g., the DSC curve of empty crucible, crucible with reference, and crucible with sample is respectively collected. Then the C_p value can be obtained by Equation (3.3), in which H_e, H_{e+s}, H_{e+r} represents the measured heat of empty crucible, empty crucible and sample, empty crucible and sample under same heating procedure, respectively; while C_R, m_R, m_S are the specific heat of reference materials, mass of reference materials and mass of samples, respectively. In both measurements, inert gas is needed to protect the sample from oxidation.

$$C_p = C_R \times \frac{H_{e+s} - H_e}{H_{e+r} - H_e} \times \frac{m_R}{m_S} \quad (3.3)$$

3.4.6 Physical Property Measurement System.

In this doctoral work, the electron transport properties, as well as low temperature thermoelectric performance were carried out using a 14 T physical properties measurement system [PPMS, Figure 3.4(g)], equipped with a vibrating sample magnetometer (VSM), over temperature range from 5 K to 300 K.

3.4.7 Atomic Force Microscopy (AFM).

In this doctoral work, the atomic force microscopy (AFM) measurement is conducted by Aylum AFM equipped with NCHR tapping mode [Figure 3.4(h)]. It is mainly employed to characterize thickness of Cu₂Te nanosheets prepared from anion exchange reaction. The samples were first dispersed into a solvent by ultrasonic and then dropped onto a horizontal positioned, cleaned silicon wafer. AFM tips were bought from the “Nanoworld” Company.

3.4.8 Inductively Coupled Plasma Atomic Emission Spectrometry (ICP-AES).

The inductively coupled plasma atomic emission spectrometry (ICP-AES) used in this doctoral work is shown in Figure 3.4(i), compositions of nanostructured Cu_xTe are analyzed by this technology. The sample (10-100 mg) was first digested by nitric acid to form a diluted solution; then its emission spectra was analyzed and compared with standard solution. Then the concentration of each element could be obtained.

3.4.9 X-ray Photoelectron Spectroscopy (XPS).

In this doctoral work, X-ray photoelectron spectroscopy (XPS) was employed to determine valence of elements and verify purity of the product. It was conducted using a SPECS PHOIBOS 100 Analyzer installed in a high-vacuum chamber with the base pressure below 10⁻⁸ mbar. X-ray excitation was provided by Al K_α radiation with the photon energy $h\nu = 1486.6$ eV at the high voltage of 12 kV and power of 120 W. The binding energy spectra were

recorded at the pass energy of 20 eV in the fixed analyzer transmission mode. All the spectra were calibrated with C 1s at 284.6 eV. Analysis of the XPS data was carried out using the commercial Casa XPS 2.3.15 software package. The XPS system is shown by Figure 3.4(j).

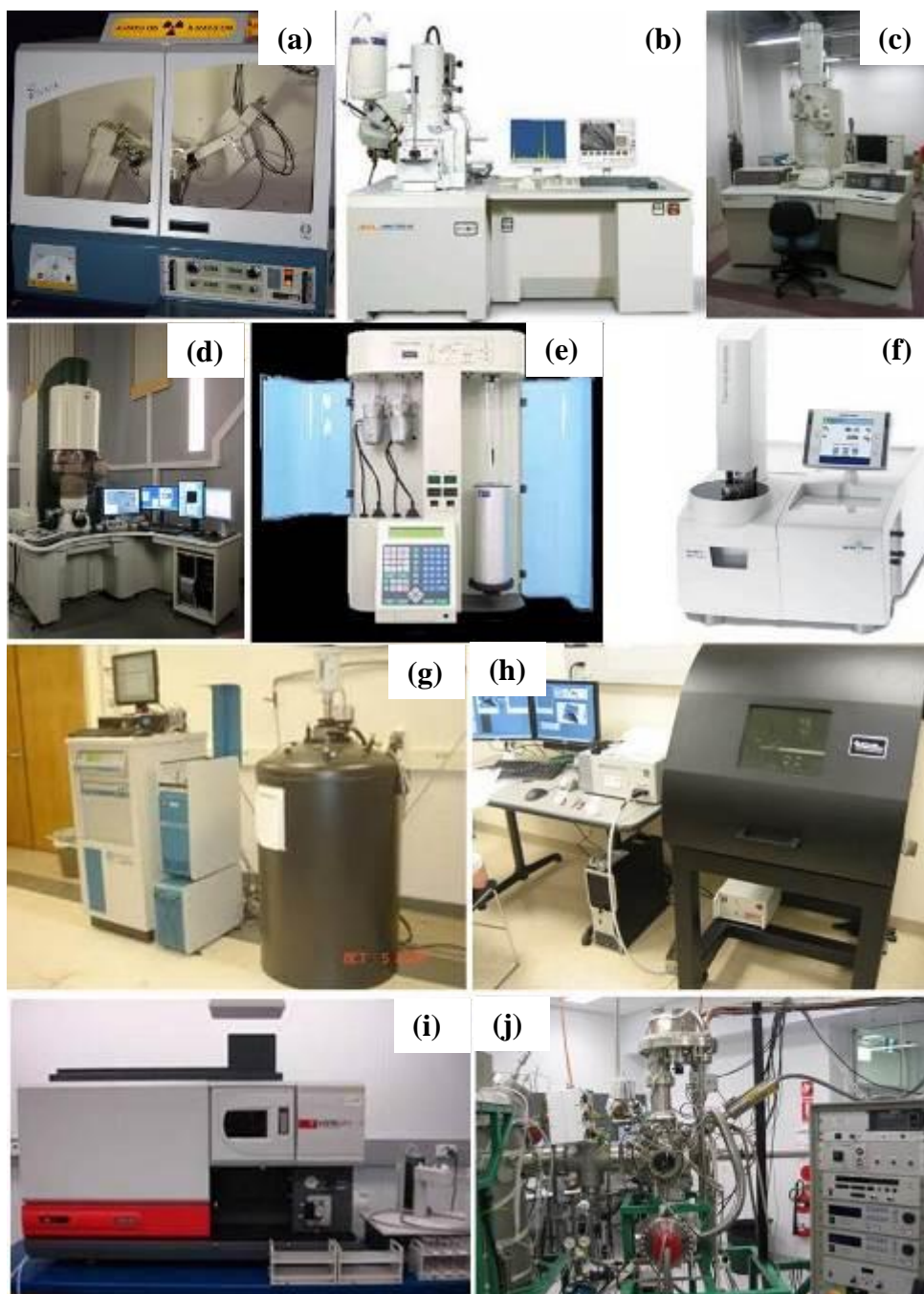


Figure 3.4. Pictures of (a) GBC-MMA X ray diffraction meter; (b) JSM-7500F field emission scanning electron microscopy; (c) JEM-2010 transmission scanning electron microscopy; (d) ARM-200F scanning tunnel electron microscopy; (e) Quantachrome Autosorb iQ

system; (f) Mettler-Toledo TGA/DSC 1 thermal analyze system; (g) physical property measurement system; (h) Ayslum atomic force microscopy; (i) VISTA MPX axial simultaneous ICP-AE spectrometer; (j) PHOIBOS 100 hemispherical XPS system.

Chapter 4. Robust Scalable Synthesis of Surfactant-free Binary Thermoelectric Metal Chalcogenide Nanostructures

4.1 Introduction.

Thermoelectric generators (TEG)/refrigerators (TER) can directly convert heat into electricity or vice versa. It is estimated that around 2/3 of energy produced is wasted as heat, and direct conversion of huge amount of waste heat into electricity by this green technology can significantly save energy and reduce carbon emissions because of its zero emissions and zero noise, excellent stability and reliability, and robust applicability.^{29, 327-329} To date, only niche applications have been achieved due to lacking high performance thermoelectric (TE) materials. The performance of such TE materials can be characterized by their “Figure of Merit” (or ZT) values.

Among the different types of TE candidates, metal chalcogenides, especially lead and bismuth based selenides and tellurides, have been extensively investigated and applied in TE devices due to their excellent and reliable performance in comparison with other candidates.^{68, 330-333} For example, Bi₂Te₃ based TE modules have been successfully commercialized with a ZT of around 1.¹⁸² More recently, the ZT values of conventional thermoelectric materials have been significantly improved to new records in the laboratory through nanotechnology, chemical doping, and engineering of electronic structure.^{68, 182, 333-336} For example, a ZT of 2.4 for Bi-Sb-Te superlattice was achieved at 300 K, and a ZT of 2.2 for Sr-, Na-doped bulk PbTe was realized at 915 K.^{68, 182} I-doped bulk Cu₂Se exhibited a ZT of 2.3 at 400 K,³³⁵ and its analogue Cu₂S had a ZT of 0.5 at 673 K.³³⁶ The high ZT and low cost of metal chalcogenides make them very promising in heat conversion.³⁰⁴

It has been demonstrated that the improvement of ZT in most metal chalcogenides in recent reports is attributable to the introduction of nano-precipitates (or nanograins), which can

effectively decrease their thermal conductivity. Although most metal chalcogenide nanostructures could be synthesized via ball milling in large scale,^{68, 178, 332, 337-339} this process is time-consuming, and the resultant nanostructures have a broad size distribution. Moreover, the product could be contaminated during the milling process.^{178, 339} Alternatively, nanostructured metal chalcogenides can be prepared by wet chemical methods.^{187, 194, 277, 340, 341} With novel hydrothermal and solvothermal approach, various metal chalcogenides with a good control of the size, shape distributions, and crystallinity, could be obtained; such as Sb_2X_3 nanobelts (X=S, Se, Te),¹⁹⁴ dendrite like Cu_{2-x}Se ³⁴² etc. With a so-called mixed solvothermal method, which is effective to form unique nanostructures within a mixed solvent under mild conditions, a variety of metal chalcogenides with different morphologies could be obtained. For example, unique ZnSe nanobelts could be obtained using $\text{NH}_3\cdot\text{H}_2\text{O}$, H_2O and diethylenetriamine (DETA) as a mixed solvent.³⁴³ However, the costs of these wet chemical methods are high, reaction conditions are harsh, and the yield is too low. Hence, the commercially used thermoelectric metal chalcogenides are usually prepared in bulk by high-temperature reactions with several heating and cooling steps. A robust, scalable, and greener method is highly desirable for preparing metal chalcogenide nanostructures.

In this work, an environmentally friendly, low cost, and scalable approach for the synthesis of a broad range of metal chalcogenide nanostructures (M_aX_b , M = Cu, Ag, Sn, Pb, Bi, Sb; X = S, Se, Te; a = 1 or 2; and b = 1 or 3) is developed. The reason we choose wet chemical method is due to its low cost and controllability of product properties.^{13, 80, 184, 187, 230, 243, 295, 343,}

³⁴⁴ The resultant nanopowders are consolidated into pellets through the spark plasma sintering (SPS) technique for investigation of their thermoelectric performance.

4.2 Experimental.

4.2.1 Chemicals.

All chemicals were acquired from Sigma-Aldrich and used as received without further purification. The main chemicals include Se powder (-100 mesh, $\geq 99.5\%$), Te powder (-200 mesh, $\geq 99.8\%$), NaBH_4 (caplets, $\geq 98\%$), $\text{Na}_2\text{S}\cdot 9\text{H}_2\text{O}$ ($\geq 98\%$), $\text{CuCl}_2\cdot 2\text{H}_2\text{O}$ ($\geq 99\%$), AgNO_3 ($\geq 99\%$), $\text{Bi}(\text{NO}_3)_3\cdot 5\text{H}_2\text{O}$ ($\geq 98\%$), $\text{Pb}(\text{NO}_3)_2$ ($\geq 98\%$), $\text{SnCl}_2\cdot 2\text{H}_2\text{O}$ ($\geq 99.99\%$), and SbCl_3 ($\geq 99\%$).

4.2.2 Synthesis of Metal Chalcogenide Nanostructures.

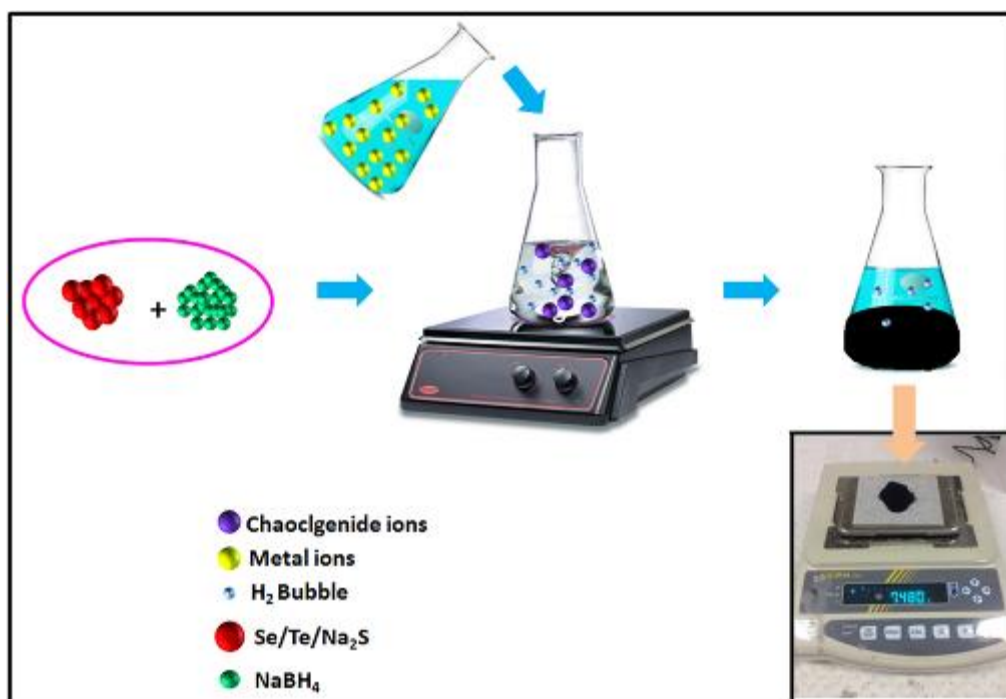


Figure 4.1. Schematic illustration of synthesis route; inset picture shows the weight of 40 mmol (theoretical yield) synthesized Cu_2Se powder.

Metal chalcogenide nanostructures were synthesized by an aqueous route under ambient condition via a reduction-precipitation process. The experimental design is based on the low water solubility of metal chalcogenides (Table 4.1) and the low cost of the wet-chemistry method. A typical synthesis is exemplified by cuprous selenide nanoparticles, as shown in

Figure 4.1, 3.16 g (40 mmol) Se powder was reduced by NaBH₄ in 400 ml H₂O under magnetic stirring with the protection of inert gas to form a colorless solution. 13.6 g (80 mmol) CuCl₂·2H₂O was completely dissolved in distilled water and added into the selenium precursor solution to immediately generate a black precipitate. The product was purified with distilled water and dried at 80 °C in a vacuum oven. The whole synthesis procedure was completed within 1 hour, and the yield was calculated to be 90 % (Figure 4.1, inset picture).

The syntheses of cuprous telluride and sulfide nanoparticles are similar to those of their selenide analogues, except that Te powder and Na₂S·9H₂O were used to replace Se powder. The reaction parameters for syntheses of other metal chalcogenide nanostructures are summarized in Table 4.2. It should be noted that inorganic acid (e.g. HNO₃) was added into the bismuth precursor to prevent its hydrolysis during the synthesis of bismuth chalcogenide nanostructures.

Table 4.1. Water solubility (K_{sp}) of different metal chalcogenides.

Material	Cu ₂ S	Cu ₂ Se	Cu ₂ Te	PbS	PbSe	PbTe	Bi ₂ S ₃	Bi ₂ Se ₃	Bi ₂ Te ₃	CuCl
-lg(K_{sp})	48.0	61.0	No report	28.1	36.2	38.9	97.0	130.0	No report	5.9

Material	SnS	SnSe	SnTe	Ag ₂ S	Ag ₂ Se	Ag ₂ Te	Sb ₂ S ₃	Sb ₂ Se ₃	Sb ₂ Te ₃
-lg(K_{sp})	27.5	34.5	36.4	49.7	58.9	63.5	90.0	113.0	No report

Table 4.2. Reaction parameters applied in the preparation of metal chalcogenide nanostructures.^a

Material	M ^b	HNO ₃	X ^c	M:X ^d	NaBH ₄ ^e	Atmosphere	Time ^f
Cu ₂ S			0.1M Na ₂ S solution		1:1	Air	0.5 h
Cu ₂ Se	400 ml 0.1 M CuCl ₂ solution	No	Selenium powder	2:1	3:1	Ar	0.5 h
Cu ₂ Te			Tellurium powder		3:1	Ar	5 h
PbS			0.1M Na ₂ S solution		No	Air	0.5 h
PbSe	400 ml 0.1 M Pb(NO ₃) ₂ solution	No	Selenium powder	1:1	2:1	Ar	0.5 h
PbTe			Tellurium powder		2:1	Ar	5 h
Bi ₂ S ₃			0.1M Na ₂ S solution		No	Air	0.5 h
Bi ₂ Se ₃	400 ml 0.1 M Bi(NO ₃) ₃ solution	40 ml 15 M	Selenium powder	2:3	2:1	Ar	0.5 h
Bi ₂ Te ₃			Tellurium powder		2:1	Ar	5 h

- All the experiments were conducted at room temperature;
- M represents the metal source;
- X represents the chalcogen source;

- d. Molar ratio;
- e. The amount of NaBH_4 is described by the molar ratio between NaBH_4 and the chalcogen source;
- f. Overall reaction time, mainly the time for dissolving the materials and reduction of the chalcogen.

4.2.3 Characterization.

X-Ray diffraction (XRD) measurements were carried out at room temperature with an X-ray diffractometer (GBC-MMA) using Cu-K_α radiation ($\lambda = 0.153 \text{ nm}$). Scanning electron microscopy (SEM) was conducted on a JEOL JSM-7500FA microscope. Transmission electron microscopy (TEM) images were obtained on a JEOL JEM-2010 microscope with an accelerating voltage of 200 kV. X-ray photoelectron spectroscopy (XPS) was conducted using a SPECS PHOIBOS 100 Analyzer installed in a high-vacuum chamber with the base pressure below 10^{-8} mbar, with X-rays provided by Al K_α radiation with the photon energy $h\nu = 1486.6 \text{ eV}$ at the high voltage of 12 kV and power of 120 W. The binding energy spectra were collected with the pass energy of 20 eV in the fixed analyzer transmission mode. Analysis of the XPS data was carried out using the commercial Casa XPS 2.3.15 software package. All spectra were calibrated with $\text{C } 1s = 284.6 \text{ eV}$.

4.2.4 Thermoelectric Performance Tests.

The as-synthesized nanostructures were loaded into a graphite die with a diameter of 20 mm and sintered into a disk using the spark plasma sintering (SP 10-4). The machine is shown by Figure 4.2(a). A rectangular block ($4 \times 1 \times 10 \text{ mm}^3$) was cut and assembled for testing the thermoelectric properties. Both the Seebeck coefficient and the electrical conductivity were measured simultaneously using an Ozawa RZ2001i (Japan) instrument [Figure 4.2(b)] in helium atmosphere. A Linseis LFA1000 (Germany) system [Figure 4.2(c)] was used to determine the thermal diffusivity of the samples, which were cut and polished into $\Phi 10 \times 1 \text{ mm}^2$ disks. Thermal conductivity (κ) was calculated using the equation $\kappa = D \times C_p \times \rho$, where D is the thermal diffusivity, C_p is the heat capacity, and ρ is the sample density measured by

the Archimedes method. The temperature dependence of heat capacity was determined on Netzsch 204F differential scanning calorimetric instrument [Figure 4.2(d)] using sapphire as reference material with a heating rate of 10 K/min and a N₂ flow of 50 ml/min.

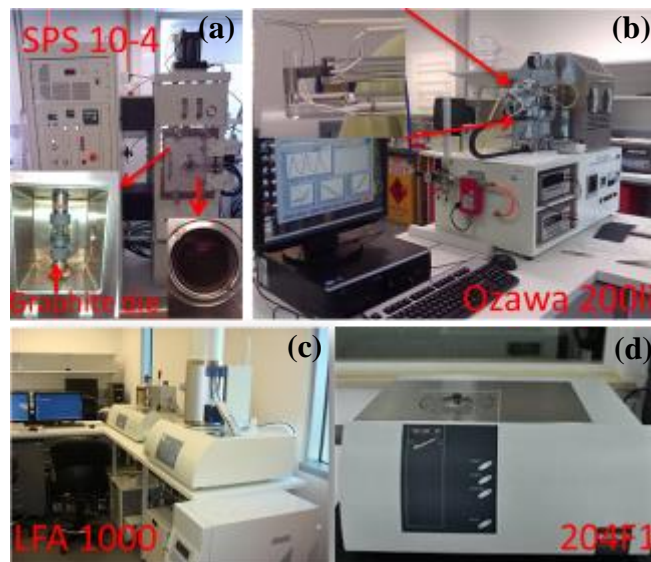


Figure 4.2. Pictures of the (a) SP 10-4, spark plasma sintering machine, inset at left down corner is the chamber and graphite die; (b) Ozawa RZ200li instrument, inset at left up corner shows the connection of samples onto electrodes; (c) Linseis LFA 1000 system; (d) Netzsch 204 F1 DSC machine.

4.3 Results and Discussion.

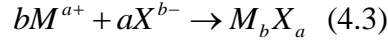
4.3.1 Fabricating of the Nanostructured MCs.

Surfactant-free metal chalcogenide nanostructures were prepared by co-precipitation of cationic and anionic precursors in aqueous solution. Selenium and tellurium powders were respectively selected as precursors of metal selenides and tellurides because they can be reduced by water-soluble NaBH₄, as their reduction potentials ($\varphi_{\text{Se}/\text{Se}^{2-}} = -0.924$ V; and $\varphi_{\text{Te}/\text{Te}^{2-}} = -1.143$ V) are lower than that of H⁺/H₂ (1.24 V). Their reduction could be simplified, as expressed by Equations (4.1) and (4.2).





Metal chalcogenides precipitate upon the addition of the metallic ions into the anionic solution because of their extremely low solubility, as indicated by the small K_{sp} in Table 4.1. The formation of metal chalcogenides can be generally expressed by Equation (4.3), in which M represents the metallic ions and X represents the anionic ions, respectively.



For metallic ions with variable valences, however, the formation mechanism is much more complex, because it involves reduction of the metallic ions. It is crucial to precisely control the ratio between the metallic precursor (such as Cu^{2+}) and the reducing agent during the preparation of these metal chalcogenide nanostructures, which is demonstrated by Cu_2Se nanoparticles prepared from $CuCl_2 \cdot 2H_2O$.³⁴⁵⁻³⁴⁸ In this process, the reduction of Cu^{2+} by $NaBH_4$ includes several reactions [Equations (4.4)-(4.14)], which are strongly dependent on their ratios and the pH of solution. According to the literature,³⁴⁵⁻³⁴⁸ $NaBH_4$ itself can be hydrolyzed to release H_2 and form a weak basic solution via Equations (4.4) and (4.5). The formed H_2 reacts with the hydroxyl ions (OH^-) to produce solvated electrons (e^-) [Equation (4.6)], which preferably reduce Cu^{2+} ions into Cu^+ by Equation (4.7), because the redox potential φ_{Cu^{2+}/Cu^+} (+ 0.153 V) is less than half of $\varphi_{Cu^{2+}/Cu}$ (+ 0.34 V).³⁴⁹ Under the acidic conditions (low pH value), reactions in Equations (4.8)-(4.11) are suppressed and the formed Cu^+ ions react with Se^{2-} ions to form Cu_2Se precipitates.³⁴⁵ In the basic solution (i.e. OH^- or $NaBH_4$ is excess), Cu_2O is formed through Equations (4.8)-(4.9). Also, the cation exchange Equation (4.12) was suppressed. Further increasing the amount of $NaBH_4$ leads to the increase in pH value and the formation of Cu [Equation (4.13)].³⁴⁶

Although the critical $NaBH_4$ amount for avoiding the formation of Cu_2O is impossible to theoretically predict as $NaBO_2$ is a weak electrolyte, in our case, the experimental ideal amount of $NaBH_4$ is 3 times that of the $CuCl_2$ or Se [i.e. the molar ratio of $NaBH_4$: $CuCl_2$

(Se) is 3:1 in Table 4.2], in which two thirds is consumed through the reduction of Se powder [Equation (4.1)] and one third is used for reduction of Cu^{2+} into Cu^+ .

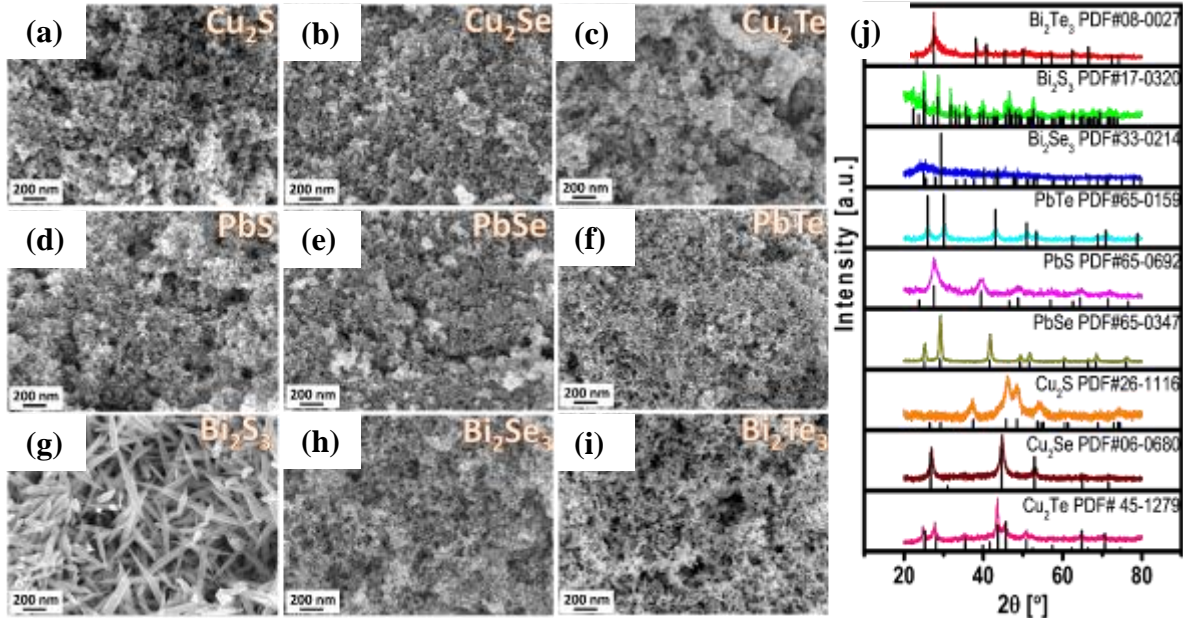
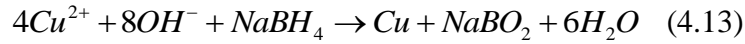
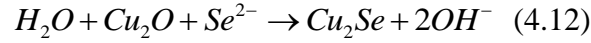
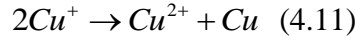
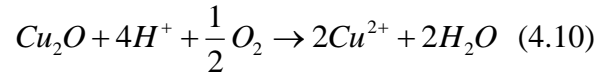
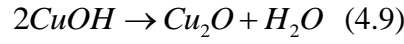
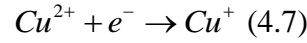
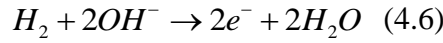
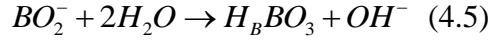
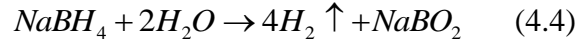


Figure 4.3. (a-i) SEM images and (j) XRD patterns of the as-prepared metal chalcogenide

nanostructures, with the black vertical lines marking the lines of the standard.

Use of this simple method can produce grams of cuprous selenide nanoparticles in a one-pot reaction with a yield over 90% (Figure 4.1, inset picture). The other metal chalcogenides, such as lead and bismuth chalcogenide nanostructures, can be prepared in a similar reduction-precipitation way. To confirm the formation of metal chalcogenide nanostructures, the resultant products were characterized by SEM and XRD, respectively. As shown in Figure 4.3, all the products are pure phase metal chalcogenide nanostructures with different morphologies. However, unlike other spherical metal chalcogenide nanoparticles, Bi_2S_3 has a shuttle-like morphology [Figure 4.3(g)]. In contrast to other well-crystallized metal chalcogenides, Bi_2Se_3 nanoparticles show amorphous features [Figure 4.3(j)]. The atomic ratio of Bi to Se is approximately 2:3, as determined by energy dispersive spectroscopy (EDS) in Table 4.3. Annealing the amorphous Bi_2Se_3 nanoparticles at 400 °C for 10 min drastically improved their crystallinity, and their XRD peaks [Figure 4.4(a)] fit well with those of the Bi_2Se_3 standard (JCPDS 33-0214). In the case of Bi_2Te_3 nanoparticles, although their XRD pattern is very close to the standard peaks of Bi_2Te_3 (JCPDS 08-0027), which was shown in Figure 4.4(b); the results of EDS and HRTEM of Bi_2Te_3 sample support the formation of Bi_2Te_3 . Figure 4.5(a) and Table 4.4 show the EDS spectrum and atomic ratio in this sample. Bi, Te, C, and O elements are detected in the sample, in which C and O arise from the conductive carbon tape. The atom ratio of Te to Bi is determined to be 1.8:1, indicating a slight Te excess which may come from the oxidation during preparation and purification. The HRTEM of Bi_2Te_3 sample with the lattice space of 0.323 nm is shown in Figure 4.5(b), which coincides with the (015) plane of Bi_2Te_3 (JCPDS 08-0027). The Fast Fourier Transfer (FFT) image [left top in Figure 4.5(b)] also confirms the crystal structure of Bi_2Te_3 .

Table 4.3. Elemental analysis (EDS) results for Bi_2Se_3 nanoparticles.

Element	series	[wt.%]	[norm. wt.%]	[norm. at.%]	[wt.%]
Bismuth	M-	50.503	61.45797	25.35357	50.503

	series	13			13
Selenium	L-series	26.529	32.28456	35.24961	26.529
		86			86
Oxygen	K-series	2.5340	3.083712	16.61639	2.5340
		43			43
Carbon	K-series	2.6080	3.173763	22.78043	2.6080
		42			42
	Sum:	82.175	100	100	
		08			

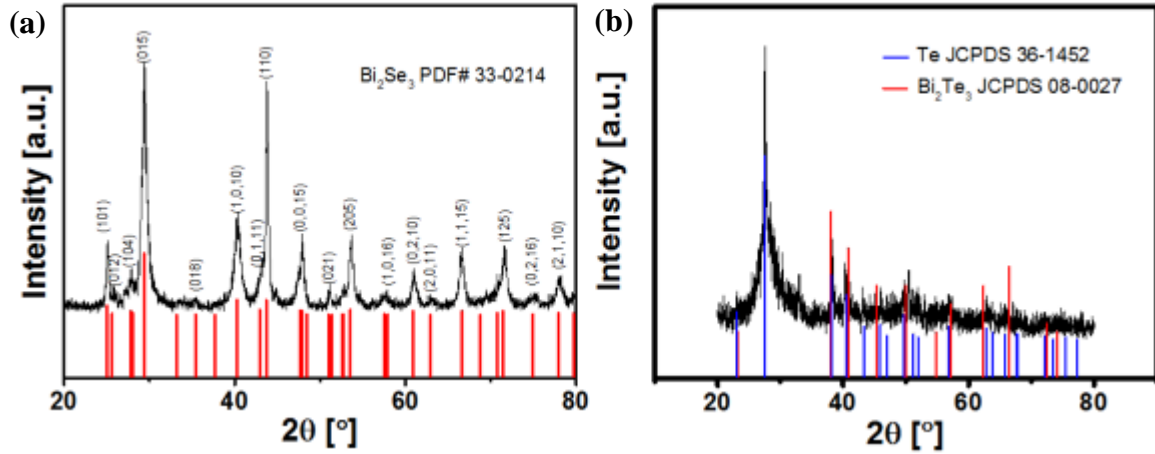


Figure 4.4. (a) XRD of the annealed Bi₂Se₃; (b) XRD of Bi₂Te₃ sample, the standard peaks of Te and Bi₂Te₃ are compared.

Table 4.4. EDS result of Bi₂Te₃ sample.

Element	series	[wt.%]	[norm. wt.%]	[norm. at.%]	[wt.%]	Error in wt.% (3 Sigma)
Oxygen	K-series	4.364902	5.096292	30.88003	4.364902	2.676619
Tellurium	L-series	42.21045	49.28331	37.44349	42.21045	3.987109
Bismuth	M-series	37.88959	44.23843	20.52208	37.88959	4.159201
Carbon	K-series	1.183637	1.38197	11.15441	1.183637	1.045344
	Sum:	85.64858	100	100		

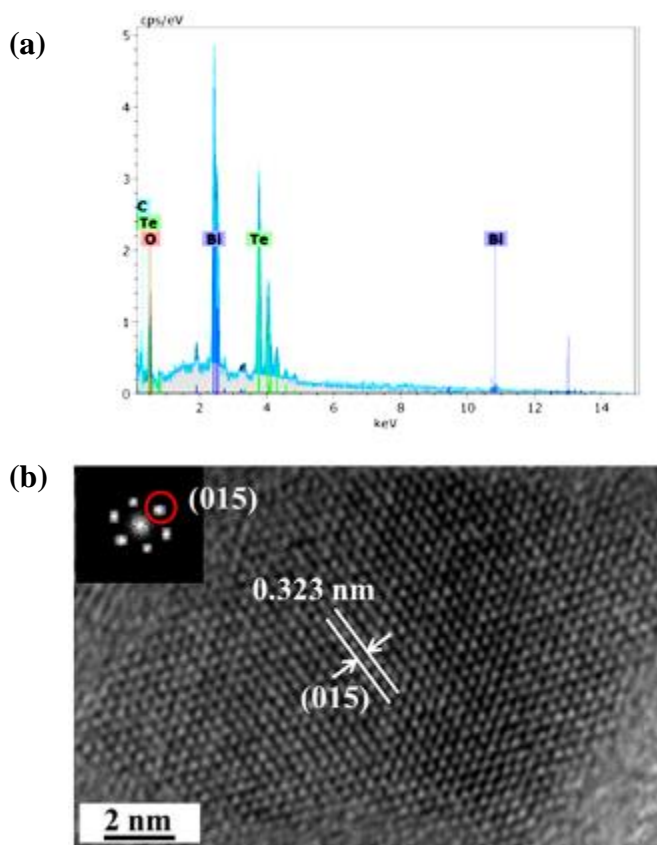


Figure 4.5. (a) EDS spectra and (b) HRTEM of Bi_2Te_3 sample.

To further confirm the purity of the metal chalcogenide nanostructures, all samples were checked using X-ray photoelectron spectroscopy (XPS) (Figure 4.6). The absence of other elements apart from C, O, M, and X demonstrates their high purity [Figure 4.6(a)]. The XPS spectra of the individual elements are displayed in Figure 4.6(b-d), and their binding energies are summarized and compared with previously reported values in Table 4.5. The good agreement with the literature values supports the high purity of our metal chalcogenide nanostructures, as shown in Table 4.5.

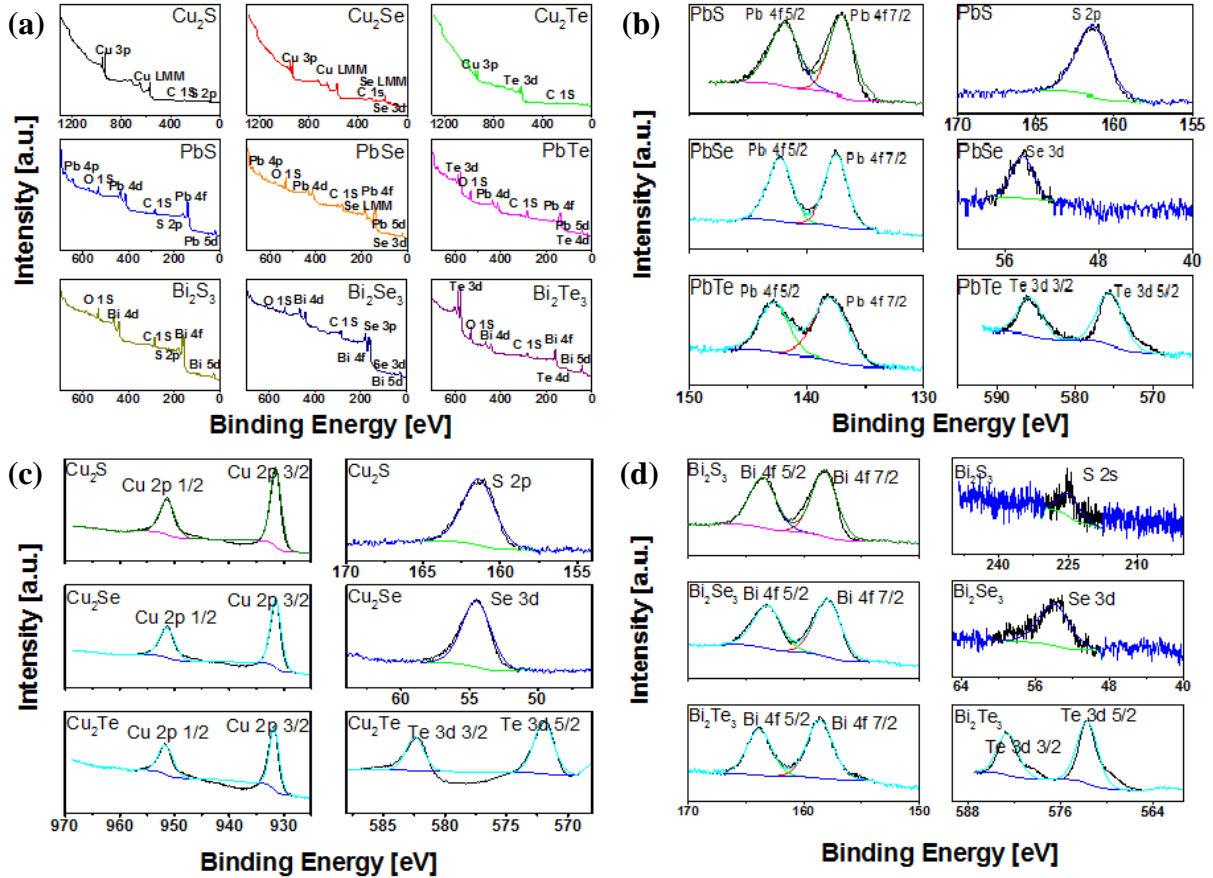


Figure 4.6. (a) XPS survey spectra for different metal chalcogenides; (b) peaks of Cu and the chalcogens in copper chalcogenides; (c) peaks of Pb and the chalcogens in lead chalcogenides; (d) peaks of Bi and the chalcogens in bismuth chalcogenides.

Table 4.5. XPS spectra of individual elements in different metal chalcogenides.

Material	Spectra	Metal peak		Chalcogenide		Literature value		Ref.
		Element	Peak (eV)	Element	Peak (eV)	Metal (eV)	Chalcogenide (eV)	
Cu ₂ S	Figure 4.6 (b)		931.5	S 2p	161.3	931.0	161.0	350
Cu ₂ Se		Cu 2p 3/2	931.6	Se 3d	54.2	931.0	54.0	252
Cu ₂ Te			931.8	Te 3d 5/2	571.8	932.0	571.8	351
PbS	Figure 4.6 (c)	Pb 4f 7/2	137.9	S 2p	160.4	137.7	161.0	352

PbSe		137.5	Se 3d	54.0	137.6	53.3	353
PbTe		137.0	Te 3d 5/2	572.3	137.3	572.0	354
Bi ₂ S ₃		158.0	S 2s	225.0	158.0	225.0	355
Bi ₂ Se ₃	Figure 4.6 (d)	157.9	Se 3d	53.6	157.5	53.0	356
Bi ₂ Te ₃	Bi 4f 7/2	158.6	Te 3d 5/2	575.4	158.7	575.7	357

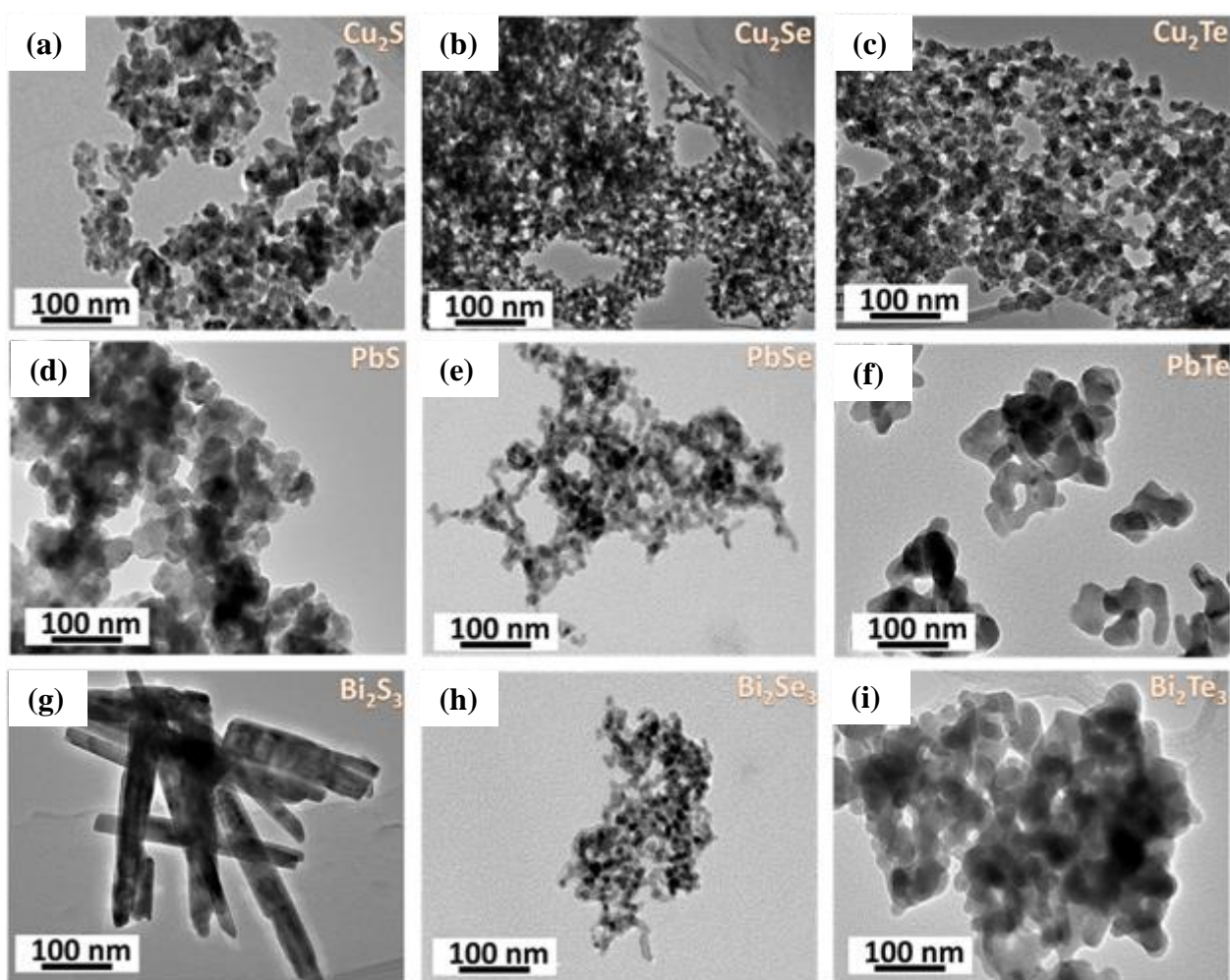


Figure 4.7. (a-i) TEM images of Cu-, Pb-, and Bi-based chalcogenide nanostructures.

The size and morphology of the metal chalcogenide nanostructures are characterized by TEM in Figure 4.7. The particle size distribution of each sample, counted from 200 particles, is

presented in Figure 4.8, from which it is easy to know that except for the Bi_2S_3 nanorods, other metal chalcogenides exhibit spherical morphology and have an average particle size of 10-20 nm with a narrow distribution. The formation of such small uniform nanoparticles in the absence of surfactants is attributed to the homogeneous precipitation in the aqueous solution and the extremely low solubility of the products.

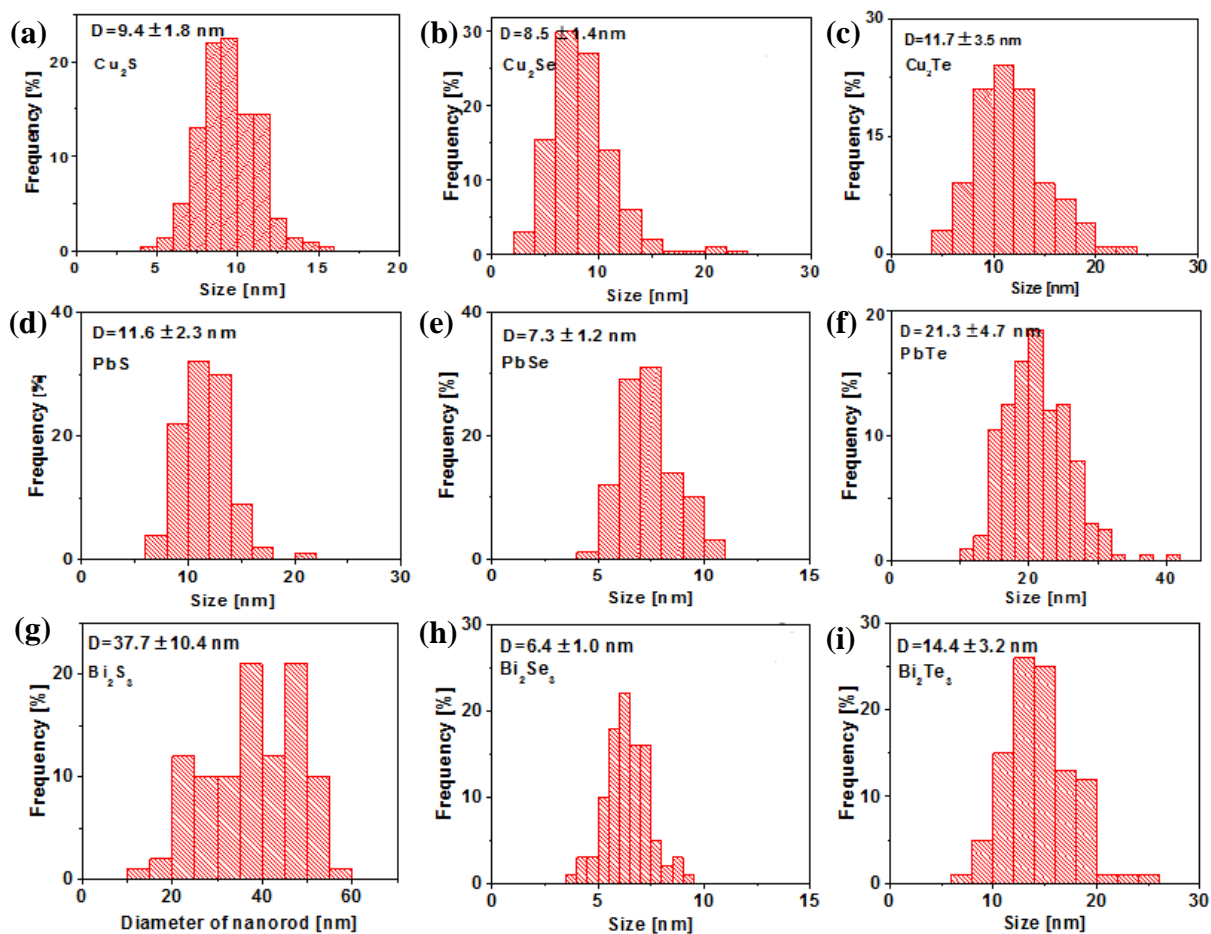


Figure 4.8. (a-i) Particle size distributions for different metal chalcogenides, counted from 200 particles in TEM images, with the values in (g) referring to the diameters of the nanorods.

Figure 4.7 and 4.8 clearly shows that metal selenides have the smallest size in comparison with metal sulfides and metal tellurides. The Gibbs free energy (ΔG) can be expressed by Equation (4.14), in which R is a constant, T is the temperature, and K_{sp} is the solubility

shown in Table 4.1. J_{sp} can be expressed by Equation (4.15), where $C(M^{b+})$ and $C(X^{a-})$ represent the concentrations of M^{b+} and X^{a-} , respectively.

$$\Delta G = RT \times \ln \frac{J_{SP}}{K_{SP}} \quad (4.14)$$

$$J_{SP} = C^a(M^{b+}) \times C^b(X^{a-}) \quad (4.15)$$

To better understand the formation of metal chalcogenide nanostructures, their formation energies were calculated according to the concentrations of M^{b+} and X^{a-} listed in Table 4.2 and Equations (4.14)-(4.15). The results are plotted in Figure 4.9(a). Although the K_{sp} values of some tellurides (e.g. Cu_2Te , Bi_2Te_3 , and Sb_2Te_3) are missing, it can be deduced that the formation energy of the metal chalcogenides increases as the chalcogen source changes from sulfides through selenides to tellurides; for example, the formation energy of lead chalcogenides is in an order of $\Delta G (PbS) = 146.3 \text{ kJ/mol} < \Delta G (PbSe) = 191.7 \text{ kJ/mol} < \Delta G (PbTe) = 206.9 \text{ kJ/mol}$. For metal selenides, the formation energy of Bi_2Se_3 (700.8 kJ/mol) is obviously higher than those of other metal chalcogenides, and then followed by Sb_2Se_3 (605.5 kJ/mol) and Cu_2Se (325.2 kJ/mol). From the thermodynamic perspective, larger ΔG usually indicates faster nucleation and growth, which leads to a smaller particle size. As displayed in Figure 4.7 and 4.8, the average particle size of PbSe ($7.3 \pm 1.2 \text{ nm}$) is smaller than that of PbS ($11.6 \pm 2.3 \text{ nm}$); the particle size of Cu_2Se ($8.5 \pm 1.4 \text{ nm}$) is smaller than that of Cu_2S ($9.4 \pm 1.8 \text{ nm}$); and the particle size of Bi_2Se_3 ($6.4 \pm 1.0 \text{ nm}$) is the smallest among all the selenides.

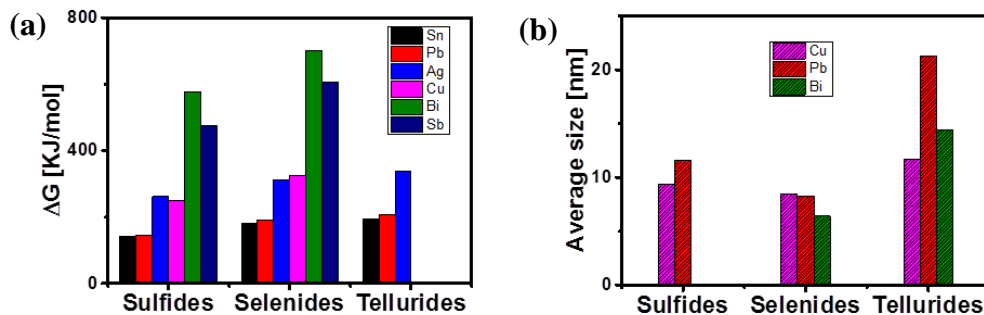


Figure 4.9. (a) Calculated formation energies of different kinds of metal chalcogenides; (b) average particle sizes of the Cu-, Pb- and Bi-chalcogenides, with the shuttle-like Bi₂S₃ nanorods excluded.

The particle sizes of metal tellurides are larger than those of their corresponding selenides [Figure 4.9(b)], however. For example, the particle size of Cu₂Te (11.7 ± 3.5 nm) is larger than that of Cu₂Se (8.5 ± 1.4 nm), the size of PbTe (21.3 ± 4.7 nm) is larger than that of PbSe (8.3 ± 1.2 nm), and the size of Bi₂Te₃ (14.4 ± 3.2 nm) is also larger than that of Bi₂Se₃ (6.4 ± 1.0 nm). This is in contrast to the sequence of their formation energies, e.g. ΔG (PbTe) > ΔG (PbSe), and the deviation demonstrates that the formation of nanostructured metal chalcogenides is not only dominated by their formation energy (or extremely low K_{sp}), but also could be related to other reaction parameters such as the release of H₂ bubbles (Figure 4.1), which could play the role of surfactant during formation of nanostructures.³⁵⁸⁻³⁶¹ During the preparation of metal tellurides, the reduction of Te powder usually lasted longer (around 5 hours in Table 4.2) than the reduction of selenium powder (30 min). The slow release of H₂ bubbles leads to less bubbles during precipitation and cannot effectively prevent the growth of nanoparticles, resulting in bigger particles than in their selenide analogues.

A simple set-up shown in Figure 4.10(a) was used to monitor the release of H₂ and the change of solution temperature against reaction time during the reduction of Se/Te powder (1 mmol) with NaBH₄ (3 mmol) in 10 ml H₂O. For the reduction of Se powder with NaBH₄ [Figure 4.10(b)], the release of H₂ is up to 260 ml within the initial 30 min, accompanied with the increase of temperature from 22 °C to 26 °C. There is almost no release of H₂ after 30 min, and the volume of H₂ slightly decreased to 255 ml due to the decrease of temperature to 23 °C. Figure 4.10(c) shows a similar trend in the release of H₂ during the reduction of Te powder. The release of H₂ also quickly increased to 245 ml in the initial 30 min, and didn't

change with reaction time till 270 min. The fast release of H₂ at the beginning of the reduction of Te powder mainly arises from the hydrolysis of NaBH₄. The solution temperature of Te system slightly increased from 18 °C to 19 °C and then kept constant during reduction. For both Se and Te system, despite the release of H₂ in both cases is close to the theoretical value [264.4 ml at 273 K under 1 atm for 3 mmol NaBH₄ according to Equation (4.1)-(4.4)] within the initial 30 min, the reduction of Te powder usually needs longer time. Thus the number of H₂ bubbles formed when metal ions are added in Te²⁻ solution is much less than that selenides formed, and finally this leads to the bigger tellurides nanoparticles.

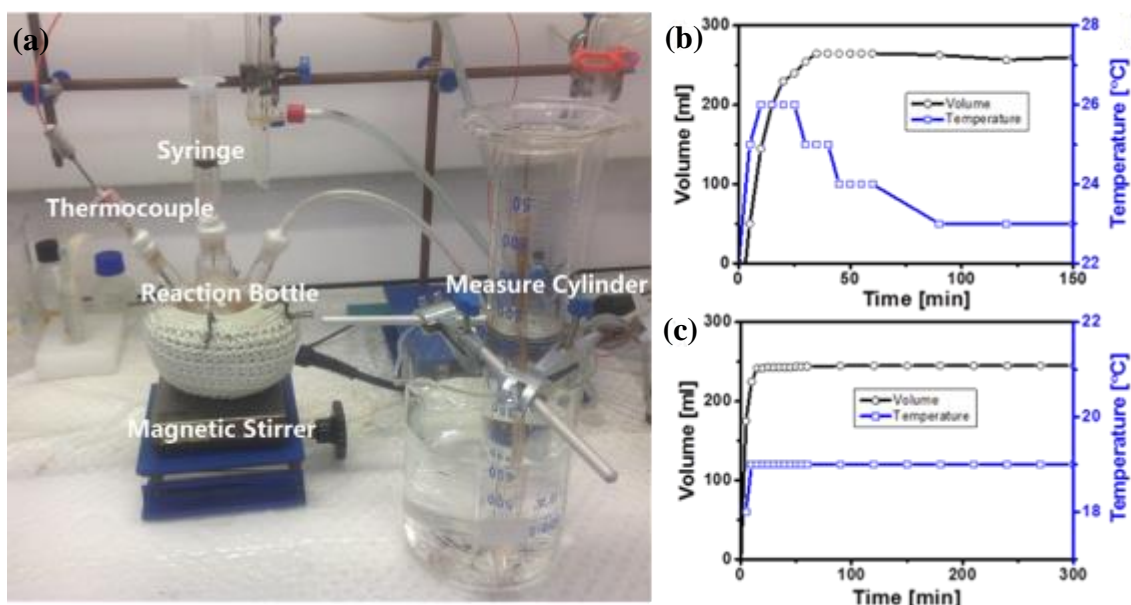


Figure 4.10. (a) Set up for measuring released H₂; and time-dependence of the release of H₂ and the change of temperature during reduction of (b) Se and (c) Te with NaBH₄.

As mentioned previously, Bi₂Se₃ nanoparticles are amorphous, unlike other metal chalcogenide nanostructures. According to the literature,³⁶²⁻³⁶⁵ this is related with the extremely high driving force [Figure 4.9(a), $\Delta G(\text{Bi}_2\text{Se}_3) = 700.8 \text{ kJ/mol}$], that can lead to fast nucleation and growth of the Bi₂Se₃ nanoparticles. In addition, as shown in Table 4.2,

inorganic acid (HNO_3) was added to the Bi-precursor to prevent its hydrolysis, and the addition of the Bi-precursor to the Se-precursor solution produced large amount of heat due to the reaction between H^+ and OH^- . As shown in Figure 4.11(a-b), the temperature of the solution was around $17.5\text{ }^\circ\text{C}$ before the addition of Bi^{3+} solution, and it rose to $21.9\text{ }^\circ\text{C}$ after the addition of Bi^{3+} solution into the selenium precursor. The release of heat could influence the crystallinity of the ultra-small nanoparticles because the melting point of nanoparticles is strongly dependent on particle size.^[53] Hence the small Bi_2Se_3 nanoparticles could form amorphous structure.

In the case of Bi_2S_3 nanorods, NaBH_4 was not used, but the same amount of HNO_3 (4 ml, 15 M) was added during the preparation (Table 4.2), which led to an increase in K_{sp} and a stronger acidic environment than in the cases of Bi_2Se_3 and Bi_2Te_3 . This slowed the nucleation and growth of the Bi_2S_3 according to Equation (4.14). Moreover, the reaction between H^+ and OH^- in the case of Bi_2S_3 is much milder than in the case of Bi_2Se_3 without using of NaBH_4 . As shown in Figure 4.11(c-d), the temperature difference before and after the formation of Bi_2S_3 nanorods is $2.0\text{ }^\circ\text{C}$ (i.e., from $20\text{ }^\circ\text{C}$ to $22\text{ }^\circ\text{C}$), smaller than the temperature difference ($4.4\text{ }^\circ\text{C}$) in the case of Bi_2Se_3 nanoparticles (i.e., from $17.5\text{ }^\circ\text{C}$ to $21.9\text{ }^\circ\text{C}$). All these factors make Bi_2S_3 nanoparticles to be highly crystalline.

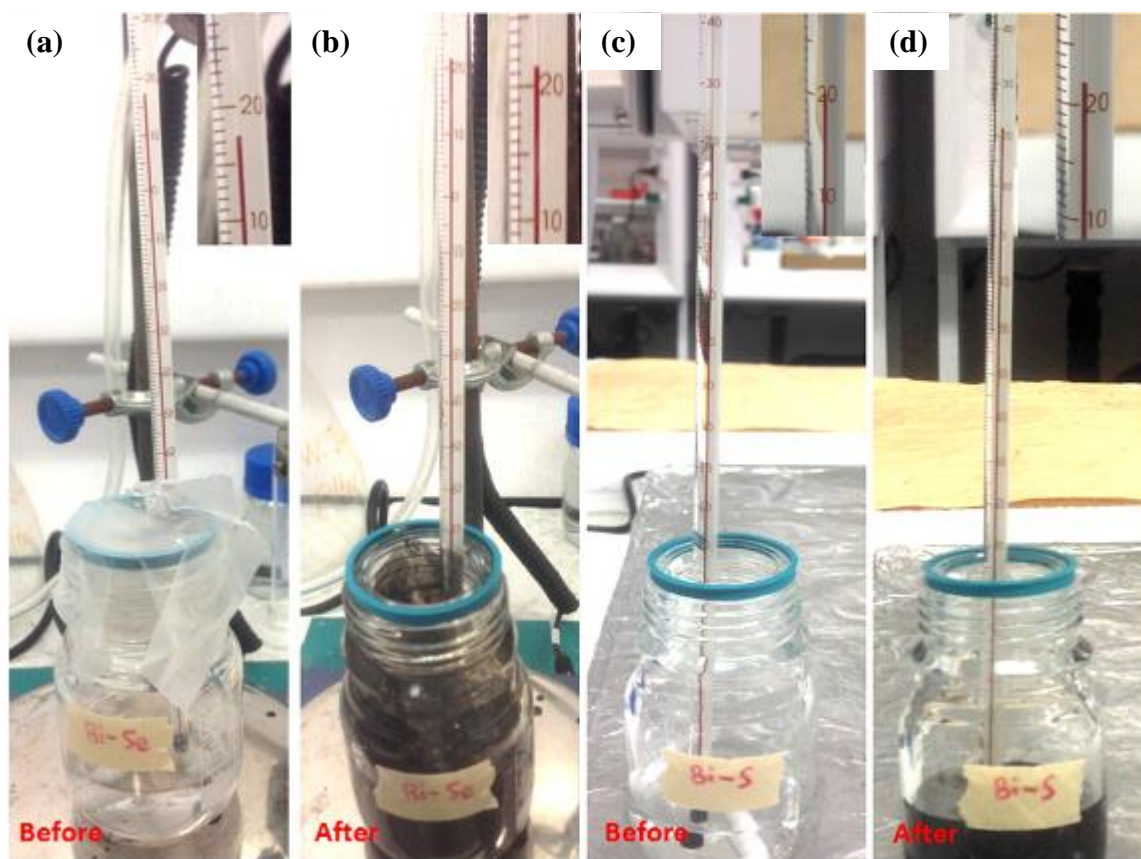


Figure 4.11. The changes in temperature in the (a-b) Bi-Se and (c-d) Bi-S systems before and after precipitation.

The formation of the shuttle-like nanorods is due to the different growth rates of Bi_2S_3 facets and the balance between etching and growth in an acidic environment.^{366, 367} Figure 4.12(a) clearly shows the incomplete growth at both ends of a typical nanorod. The importance of acidic conditions for the growth of rod-like Bi_2S_3 nanocrystals is further demonstrated by a control experiment, in which the amount of HNO_3 was decreased to the critical value (molar ratio of H^+ to Bi^{3+} of around 9:1) that can only prevent the hydrolysis of $\text{Bi}(\text{NO}_3)_3$. Amorphous nanoparticles were obtained after addition of Na_2S solution [Figure 4.12(b)].

To demonstrate the applicability of this robust approach, tin and silver chalcogenide nanostructures were also prepared in a similar way. The XRD patterns of the resultant nanostructures are shown in Figure 4.12(c-d). Similar to Bi_2S_3 with a small K_{sp} (Table 4.1), the resultant Sb_2S_3 nanoparticles obtained under the same conditions are amorphous [Figure

4.12(b)] due to the fast precipitation driven by the large ΔG (605.5 kJ/mol) arising from its low solubility.

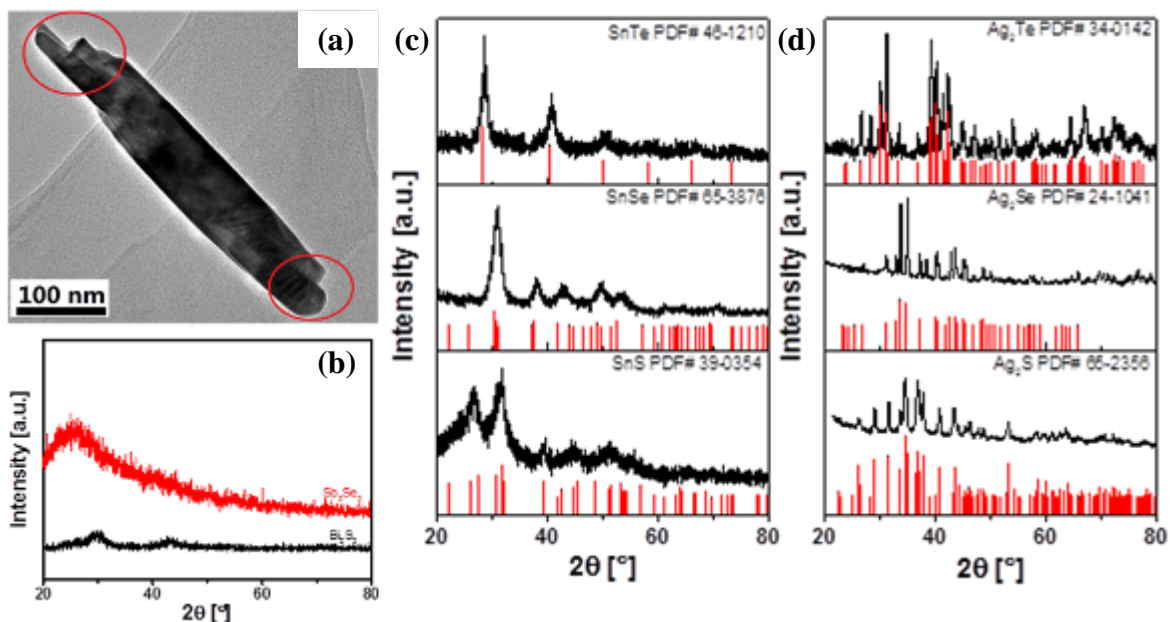


Figure 4.12. (a) TEM of Bi_2S_3 nanorod, the end of which are marked by red circle; (b) XRD of the Bi_2S_3 nanoparticles obtained by decreasing the amount of HCl and of the amorphous Sb_2Se_3 nanoparticles; XRD patterns of (c) tin and (d) silver chalcogenide nanostructures prepared by our method. The red vertical lines mark the line positions of the standard.

4.3.2 Size and Composition Control.

The compositions and particle sizes of metal chalcogenide nanostructures can be tuned by controlling the reaction parameters, which is demonstrated by the case of Cu_2Se nanoparticles. Detailed parameters for control of Cu_2Se nanoparticles are listed in Table 4.6. As discussed previously, NaBH_4 plays a crucial role in controlling the composition of metal chalcogenides (especially for Cu_2X), and the ideal molar ratio of NaBH_4 to Se for formation of Cu_2Se nanoparticles is 3:1. When the mole ratio of NaBH_4 : Se is decreased to 2:1, there is no reduction of Cu^{2+} , and the product is CuSe rather than Cu_2Se (Figure 4.13). When excessive

NaBH_4 was used (e.g. NaBH_4 : Se \geq 4:1), although all the Cu^{2+} ions can be reduced to Cu^+ , the formation of Cu_2O is unavoidable because of Equations (4.6)-(4.10) and suppression of the Equations (4.11) and (4.13), so the product is a mixture of Cu_2O and Cu_2Se . Further increasing the molar ratio of NaBH_4 to Se from 4:1 via 6:1 to 8:1 resulted in stronger and stronger Cu_2O peaks in the XRD patterns of the products [Figure 4.13(a)].

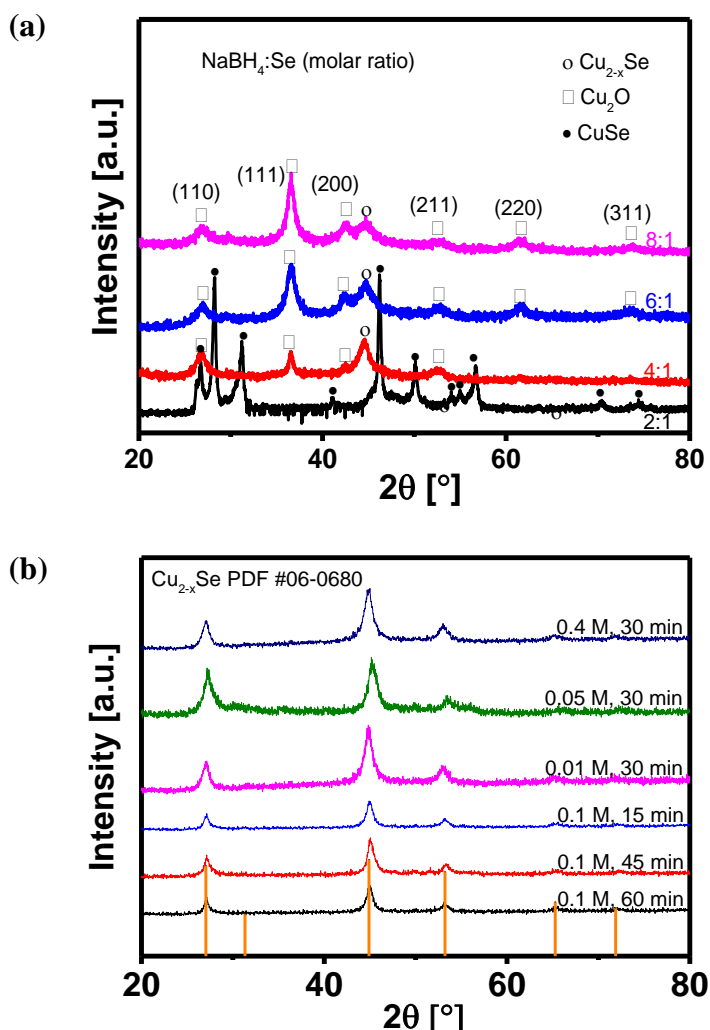


Figure 4.13. (a). XRD patterns of copper selenides synthesized with a ratio of NaBH_4 to Se increasing from 2:1 to 8:1; (b) XRD patterns of Cu_2Se nanoparticles prepared from different concentrations of Se precursors and with different reduction times.

The concentrations of precursor solutions have an important influence on the particle size. Figure 4.14 shows TEM images of the Cu_2Se nanoparticles synthesized with varying

concentrations of NaHSe solution. The average particle size increases from 6.6 ± 1.2 nm to 12.8 ± 3.1 nm as the concentration of NaHSe increases from 0.01 M to 0.4 M. The precursor concentration did not influence the composition of the final products, as their XRD patterns shown in Figure 4.13(b) are indexed to pure Cu_2Se .

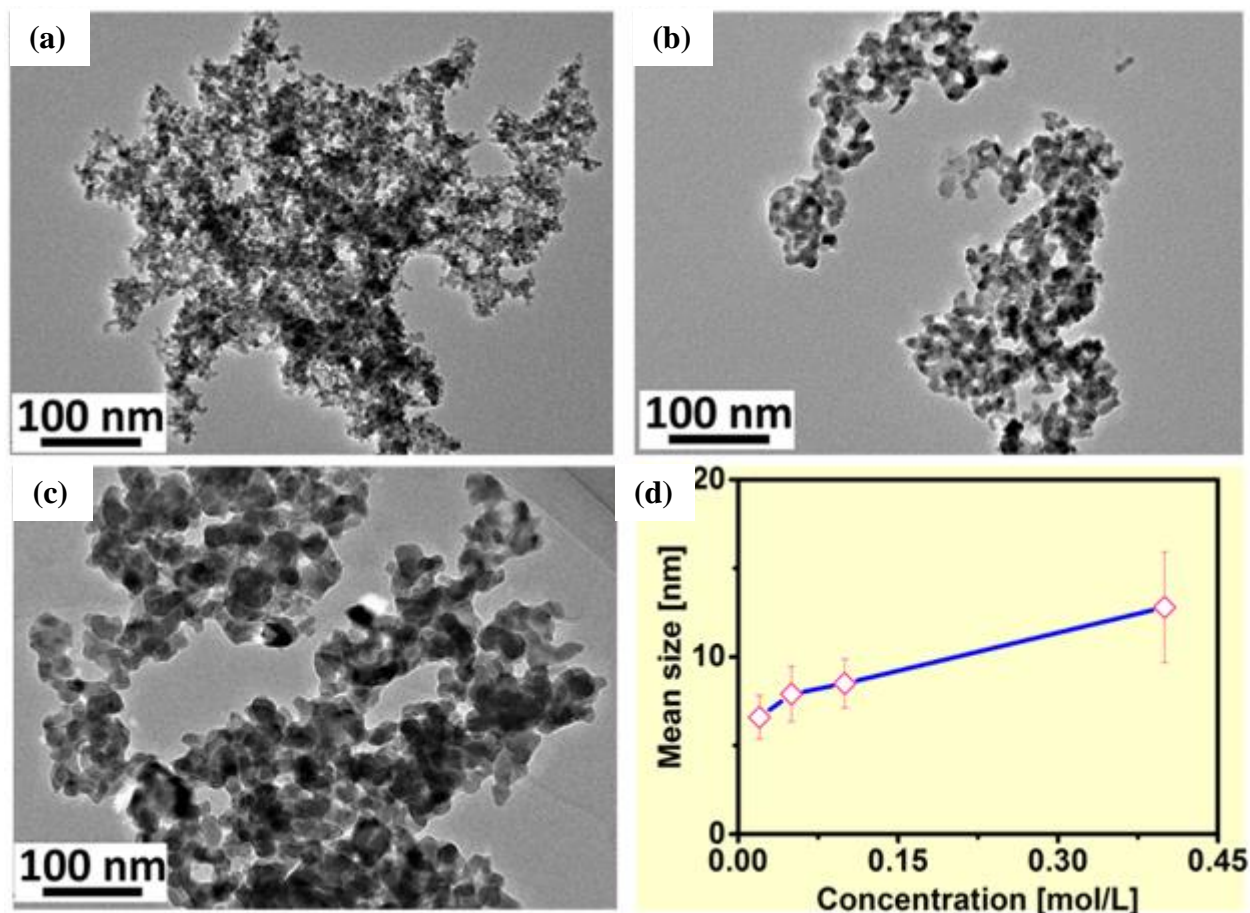


Figure 4.14. TEM images of Cu_2Se nanoparticles prepared from (a) 0.01 M; (b) 0.05 M; (c) 0.4 M NaHSe; (d) dependence of particle size on concentration of NaHSe.

As described previously, the release of H_2 bubbles during the reduction of Se powder could influence the subsequent precipitation of Cu_2Se , as they can prevent the aggregation of nanoparticles.^{358-360, 368} Prolonging the reduction time of the Se powder may reduce their influence [Figure 4.10(b)]. We therefore investigated the effect of reduction time on the particle size of the Cu_2Se precipitates. As demonstrated by Figure 4.15(a-c), with increasing

reduction time, the mean size of the Cu_2Se nanoparticles gradually increases from 6.8 ± 1.5 nm to 11.0 ± 1.7 nm [Figure 4.15(d)] without any change in their composition.

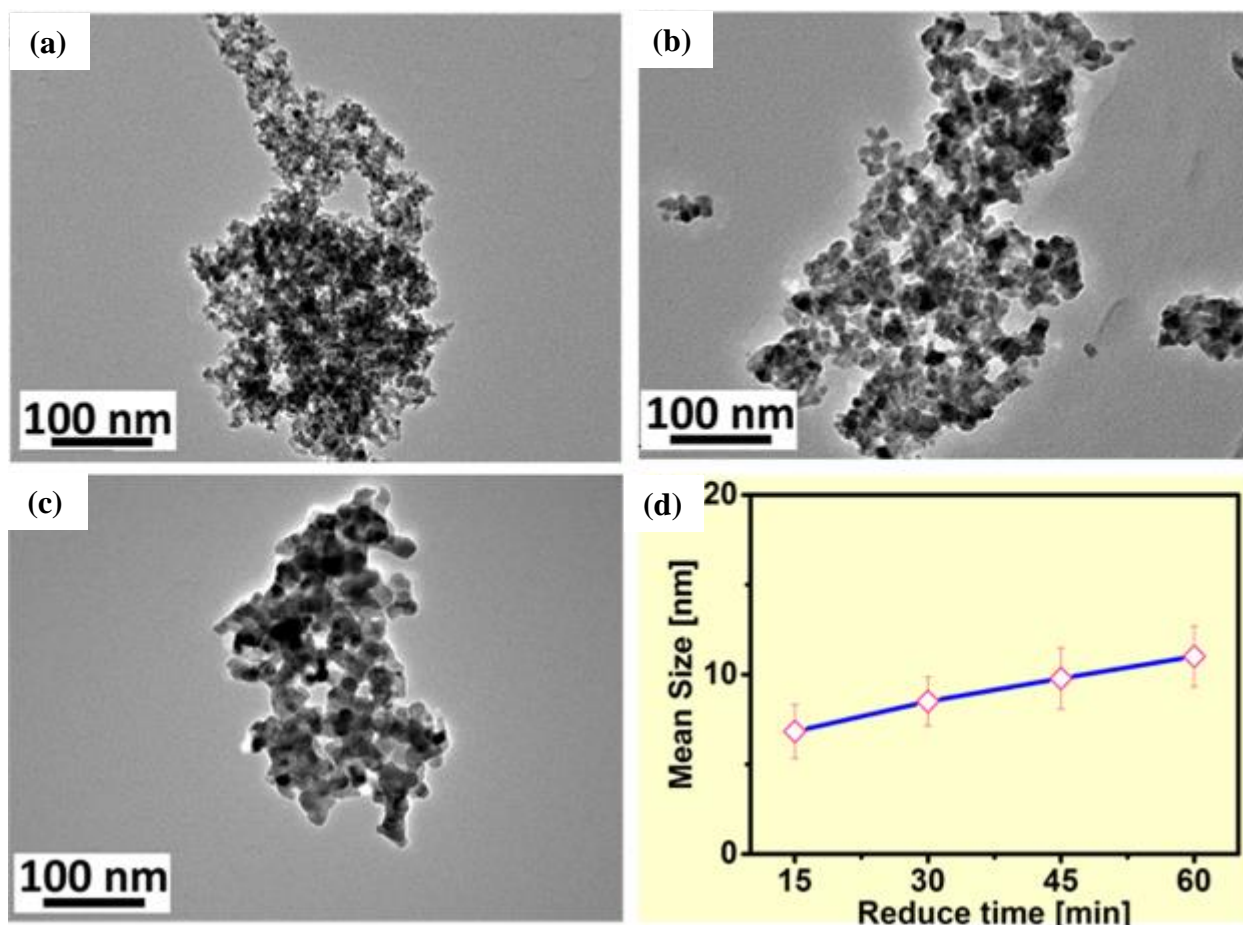


Figure 4.15. TEM images of Cu_2Se nanoparticles prepared by using different reduction times: (a) 15 min; (b) 45 min, and (c) 60 min. (d) dependence of particle size on reduction time.

In summary, our method is capable of producing various surfactant-free nanostructured metal chalcogenides at room temperature on a large scale with a high yield ($> 90\%$). Especially, for the first time, pure amorphous Bi_2Se_3 nanoparticle is successfully synthesized at room temperature.³⁶⁹⁻³⁷¹ The size and composition of the metal chalcogenide nanostructures could be easily controlled by adjusting the reaction parameters.

4.3.3 Thermoelectric Performance of Binary Selenides.

Four nanostructured metal selenides (i.e., Cu_2Se , Bi_2Se_3 , SnSe , and Ag_2Se) were chosen to investigate their thermoelectric properties, because these metal selenides are not only less toxic and relatively cheaper than their tellurides, but also exhibit better performance than the sulfides. Figure 4.16 shows the TEM image, size distribution, and XPS spectra of SnSe nanoparticles used for thermoelectric investigation. The average particle size is 9.3 ± 1.7 nm [Inset of Figure 4.16(a)]. The binding energies of Sn 3d and Se 3d coincide well with those of reported SnSe [Figure 4.16(b)].³⁷² Characterizations of Ag_2Se nanoparticles are presented in Figure 4.16 (c) and (d), which shows that the morphology of Ag_2Se is bigger and non-uniform in comparison with those of the other metal chalcogenide nanostructures; the binding energies of Ag 3d and Se 3d are consistent with those of reported Ag_2Se .³⁷³

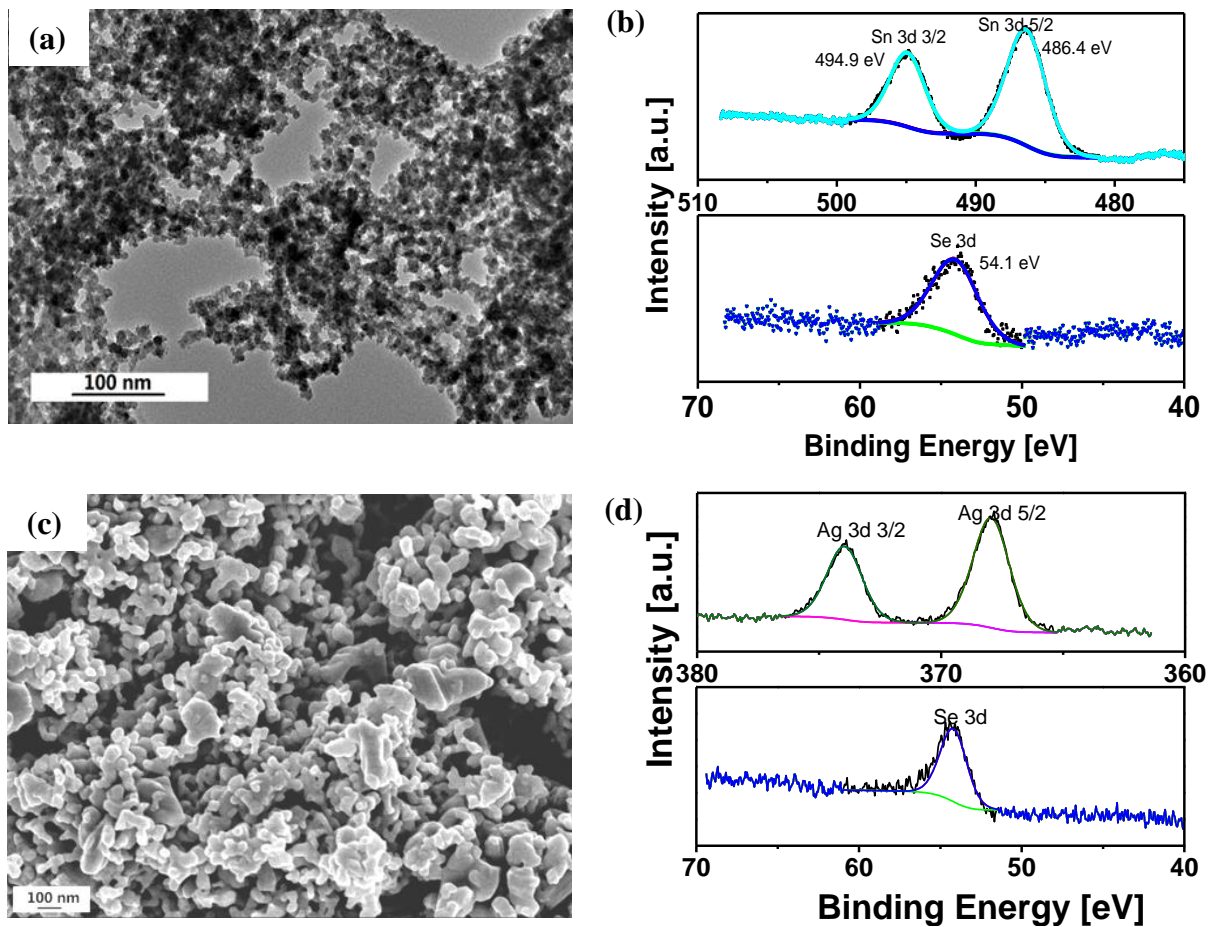


Figure 4.16. (a) TEM of the SnSe nanoparticles, inset is the size distribution; (b) XPS results of Sn 3d and Se 3d core level; (c) SEM image of prepared Ag₂Se nanoparticles; (d) XPS result.

The dried nanopowders were consolidated into pellets by the SPS technique, and the sintering parameters and relative density are listed in Table 4.6. The densities of SnSe and Bi₂Se₃ pellets are relatively low as we did not attempt to optimize the sintering conditions. Besides, as shown by TGA result (Figure 4.17), obvious weight loss could be detected in SnSe and Bi₂Se₃ above 320°C. The low pressure in the chamber of SPS machine led to the volatilization of sample during SPS process. The relation between porosity of pellet and thermoelectric performance has been extensively studied.³⁷⁴⁻³⁷⁶ Generally, there is a trading off between the adverse effect of pores on reducing carriers mobility and good effect on increasing phonon scattering, the size and concentration of pores should be carefully controlled.

Table 4.6. SPS parameters used for sintering Cu₂Se, Bi₂Se₃, SnSe, and Ag₂Se nanopowders, and the density of the resultant pellets.

Materials	Temperature (°C)	Dwell time (min)	Pressure (MPa)	Atmosphere	Theoretical density (g/cm ³)	Real density (g/cm ³)	Relative density (%)
Cu ₂ Se	430	10	65	vacuum	6.84	6.68	98
Bi ₂ Se ₃	370	20	50	vacuum	6.82	6.01	89
SnSe	350	5	40	vacuum	6.18	5.27	85
Ag ₂ Se	400	10	60	vacuum	8.17	8.20	99

The morphologies and XRD patterns of the sintered pellets are presented in Figure 4.18. It shows that after the SPS sintering, Cu₂Se nanoparticles grow into big particles with an average size of 100 nm [Figure 4.18(a)], uniform nanoplate-like structures appear in the sintered Bi₂Se₃ pellet [Figure 4.18(b)], and a mixture of plates and nanoparticles are observed

in the SnSe pellet [Figure 4.18(c)]. The sintered Ag₂Se pellet has higher density than the other 3 selenides, in addition to the presence of minor nanoscale pores [Figure 4.18(d)]. Compared with the original powder, there is no change in their crystal structures [Figure 4.18(e)]. Thermogravimetric analysis (TGA) was conducted on the 4 pellets to determine their thermal stability [Figure 4.17(a-d)]. The results confirm that the Cu₂Se pellet is stable below 450 °C, and the overall weight loss is smaller than 0.1 %. The Bi₂Se₃ and SnSe pellets respectively show an abrupt weight loss at around 322 and 335 °C, and the Ag₂Se pellet shows no weight loss below 350 °C. Their temperature-dependent heat capacities (C_p) are plotted in Figure 4.17(e-h). Obvious phase transitions at around 66 °C and 103 °C for the Cu₂Se and Ag₂Se pellets [Figure 4.17(e) and (h)] are observed, respectively, which are consistent with reports in the literature.^{167, 302} The C_p curves of the Bi₂Se₃ and SnSe samples show a dropping trend beyond 300 °C, which may be caused by the volatilization of the sample arising from instability above this temperature.

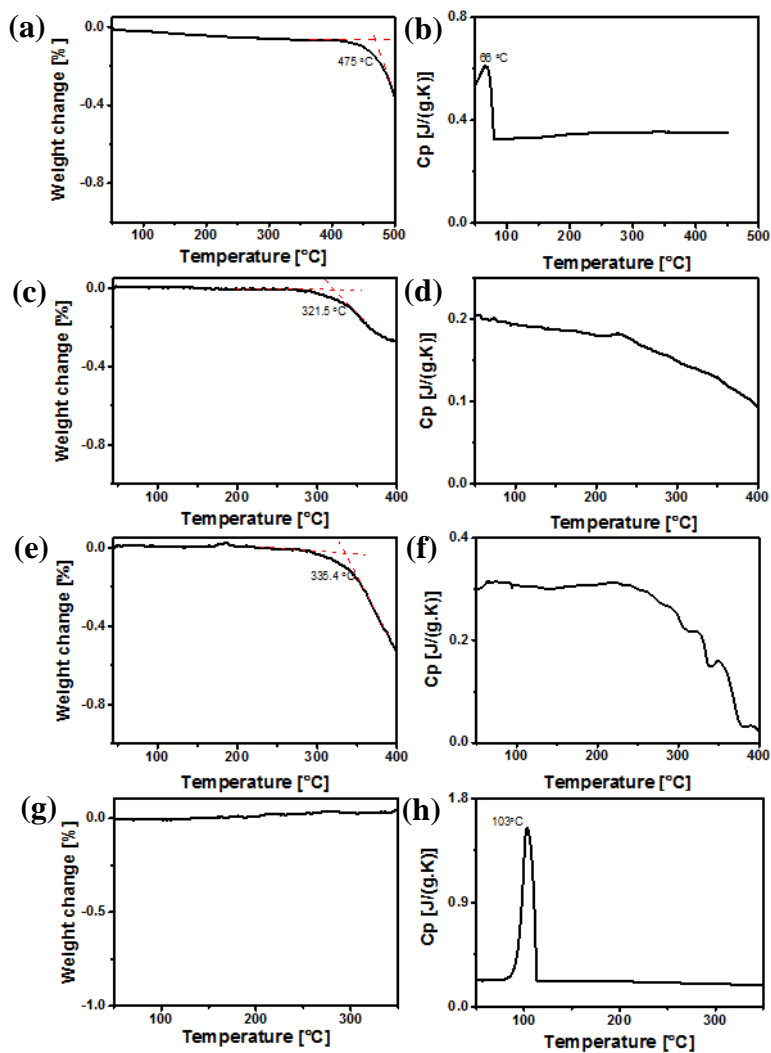


Figure 4.17. TGA and Cp curves for (a, e) Cu_2Se ; (b, f) Bi_2Se_3 ; (c, g) SnSe and (d, h) Ag_2Se pellets.

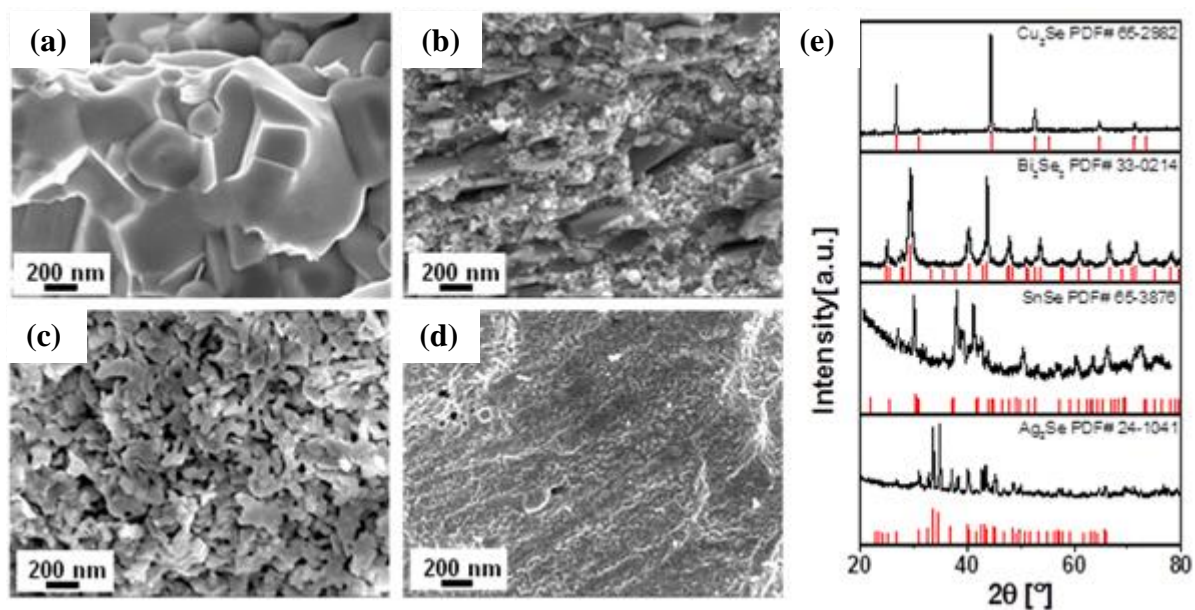


Figure 4.18. Morphology of cross-sections of (a) Cu₂Se pellet; (b) Bi₂Se₃ pellet; (c) SnSe pellet; and (d) Ag₂Se pellet. (e) XRD patterns of the sintered pellets, with the red vertical lines showing the line positions of the standard.

Figure 4.19(a-c) demonstrates the thermoelectric performance of the Cu₂Se pellet sintered from nanoparticles. A high electrical conductivity (σ), ranging from 1000 to 7000 S/cm, and a positive Seebeck coefficient [Figure 4.19(a)] were observed. The σ decreases with increasing temperature, and the S varies in the opposite way. Due to the phase transition, its thermal conductivity (κ) first decreases from 1.3 W/(m.K) at 50 °C to 0.3 W/(m.K) at 100 °C, followed by increasing to 0.9 W/(m.K) at 150 °C and slightly decreasing to 0.87 W/(m.K) at 450 °C. The ZT of our Cu₂Se pellet gradually increases with increasing temperature and reaches 0.45 at 450 °C, which is slightly lower than that of the corresponding bulk sample, as shown in Figure 4.19(c).¹⁶⁷ The difference may be caused by the presence of excess amount grain boundaries, which can decrease the thermal conductivity at the cost of electrical conductivity.³⁷⁷⁻³⁷⁹ The thermoelectric properties of the Bi₂Se₃ pellet are presented in Figure 4.19(d-f). Compared with Cu₂Se, the electrical conductivity (σ) of Bi₂Se₃ is lower, and it first decreases from 187 S/cm at 65 °C to 160 S/cm at 140 °C, and then increases to 205 S/cm at 230 °C. With increasing temperature, the Seebeck coefficient (S) increases from -75 μ V/K at 65 °C to -102 μ V/K at 230 °C. The thermal conductivity (κ) gradually decreases from 0.48 W/(m.K) at 68 °C to 0.38 W/(m.K) at 300 °C [Figure 4.19(e)]. As shown in [Figure 4.19(f)], the ZT value of our Bi₂Se₃ pellet is apparently higher than the literature value³⁸⁰ and reaches 0.27 at 230 °C. The higher ZT is mainly due to the ultra-low thermal conductivity caused by the presence of nanograins.

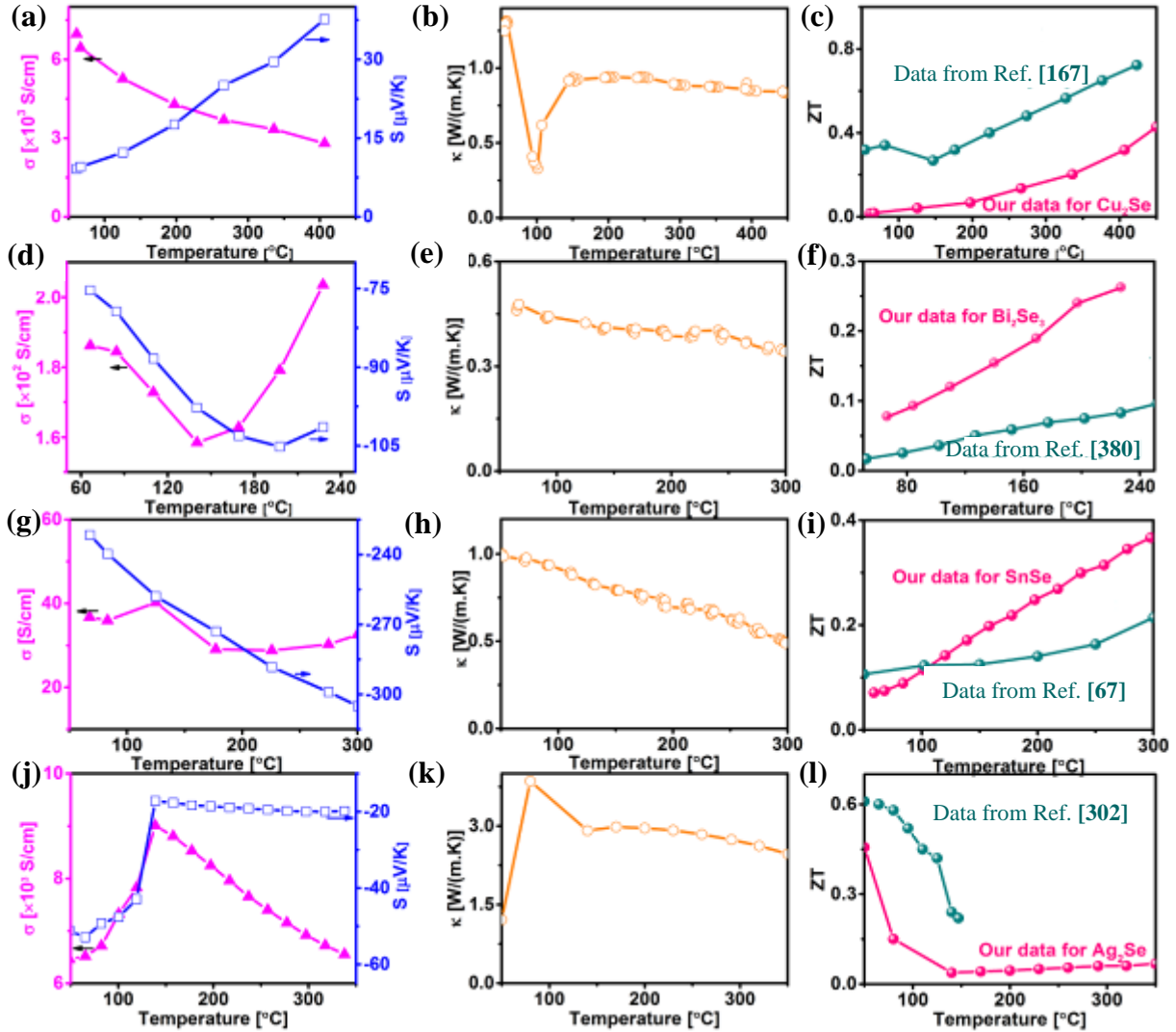


Figure 4.19. Temperature dependence of the thermoelectric properties, the electrical conductivity (left column), the thermal conductivity (middle column), and the ZT (right column), of (a-c) Cu_2Se pellet, (d-f) Bi_2Se_3 pellet, (g-i) SnSe pellet, and (j-l) Ag_2Se pellet in comparison with previous reports.

The SnSe pellet has lower electrical conductivity (σ) than the Bi_2Se_3 but a relatively higher Seebeck coefficient, as displayed in Figure 4.19(g). It should be noted that the σ of SnSe is not sensitive to temperature, i.e., σ fluctuates between 38 S/cm and 29 S/cm when the temperature is increased from 60 °C to 300 °C. The thermal conductivity of SnSe is notably decreased from 1 W/(m.K) at 50 °C to 0.5 W/(m.K) at 300 °C [Figure 4.19(h)]. Figure 4.19(i)

compares the temperature dependence of ZT for our sample with that of single-crystal SnSe.⁶⁷ The maximum ZT of our sample is 0.38 at 300 °C, higher than that of single crystal SnSe ($ZT = 0.21$) at the same temperature.

Figure 4.19(j-l) shows the thermoelectric properties of the Ag₂Se pellet. An obvious transition point arising from the phase transition is observed in the electrical conductivity and the Seebeck coefficient, i.e. the σ first increases from 2000 S/cm at 50 °C to 9000 S/cm at 140 °C, and then decreases to 2000 S/cm at 350 °C, while the Seebeck coefficient decreases from -55 $\mu\text{V/K}$ at 50 °C to -22 $\mu\text{V/K}$ at 140 °C and then remains constant to 350 °C [Figure 4.19(j)]. Similarly, the thermal conductivity first increases gradually from 1.2 W/(m.K) at 50 °C to 3.0 W/(m.K) at 140 °C, and then gradually decreases to 2.4 W/(m.K) at 350 °C [Figure 4.19(k)]. Similar to a previous report,³⁰² the ZT of our Ag₂Se drastically decreases from 0.45 at 50 °C to 0.05 at 140 °C and then remains constant to 350 °C [Figure 4.19(l)].

4.4 Conclusion.

A robust and scalable aqueous method to the synthesis of different nanostructured thermoelectric metal chalcogenides is developed. The solubility of metal chalcogenides and the amount of reducing agent play crucial roles in the formation of such nanostructures. The particle size and composition of metal chalcogenides could be easily tuned by the amount of reducing agent, the concentration of precursors, and the reduction time. The resultant nanostructured metal chalcogenides are tested as potential thermoelectric materials. Pronounced enhancement in the figure of merit values (ZT s) of some metal chalcogenide nanostructures was observed due to the presence of nanograins or nanopores, which can effectively decrease the thermal conductivity. This method is an environmental-friendly process for the preparation of low-cost metal chalcogenide nanomaterials for thermoelectric applications.

Chapter 5. Ambient Scalable Synthesis of Promising Surfactant-free Thermoelectric CuAgSe Nanoparticles with Reversible Metallic-n-p Conductivity Transition

5.1 Introduction.

Direct conversion of heat into electricity on the basis of the Seebeck effect (i.e. thermoelectric technology, TE) shows great potential in harvesting waste heat, because it is environmentally friendly, stable, reliable, and applicable in remote areas.^{29, 328, 381} This technology could lead to significant savings on energy consumption and reduce carbon emissions. It remains a challenge, however, for wide practical applications because of its low conversion efficiency arising from the lack of environmentally friendly, high performance, and low cost thermoelectric materials. The thermoelectric performance of materials is characterized by the “figure of merit” (ZT).

Great efforts have been devoted to optimization of these 3 factors for achieving a high ZT . It is very challenging, however, to simultaneously optimize them; an alternative way is the introduction of nanostructures or the use of phonon-glass electron-crystal (PGEC) or phonon-liquid electron-crystal (PLEC) materials to reduce the thermal conductivity (while the power factor is not seriously degraded) to achieve a high ZT .^{167, 382} For example, the ZT value of p -type PbTe can be improved to over 2 by the introduction of nanoprecipitates through chemical doping.⁶⁸ Non-stoichiometric superionic copper selenide (Cu_{2-x}Se) exhibits a ZT of 1.6 at 1000 K due to its unique PLEC property, arising from highly disordered cuprous cations around the chalcogen sublattice, which behave like a liquid at high temperature and minimize the thermal conductivity.¹⁶⁷

The high ZT of non-stoichiometric Cu_{2-x}Se has motivated substantial efforts in searching for high performance thermoelectric materials with a similar superionic structure. As an important ternary selenide, CuAgSe is such a candidate with the superionic property due to

the mobility of both Cu^+ and Ag^+ ions at high temperature. Extremely high electron mobility at low temperature and a ZT of 0.15 at room temperature and a ZT of 0.95 at 623 K have been reported in bulk CuAgSe.^{383, 384}

It should be noted that most research has been focused on bulk CuAgSe prepared by the solid state reaction at high temperature (> 1000 K),^{383, 384} and there is no report on the thermoelectric properties of CuAgSe sintered from its nanostructures due to the difficulties in efficient preparation of CuAgSe nanomaterials on a large scale. Small-scale CuAgSe nanotubes and dendrites can be prepared from Se and Ag_2Se nanotemplates, respectively.³⁸⁵

³⁸⁶ Herein, we synthesize surfactant-free CuAgSe nanoparticles from $\text{Cu}(\text{NO}_3)_2$, AgNO_3 , and Se precursors via a robust ambient approach based on the method developed in Chapter 4 (Figure 5.1). The whole synthesis process is very simple and effective (within 30 min) with a high yield. More importantly, the whole reaction is in an aqueous system without heating or any expensive/toxic solvents, and no dangerous waste was formed. This simple and scalable method was capable of producing large amounts of surfactant-free CuAgSe nanoparticles for investigation of the thermoelectric properties of their sintered pellets between 3 K and 623 K. The results show their excellent electric conductivity at low temperature (below 50 K) and semiconducting characteristics at high temperature, which can be reversibly switched from metallic conductor, n -type semiconductor to p -type semiconductor by varying the temperature. The ZT values of CuAgSe made from nanoparticles are 0.42 at 323 K and 0.9 at 623 K, respectively.

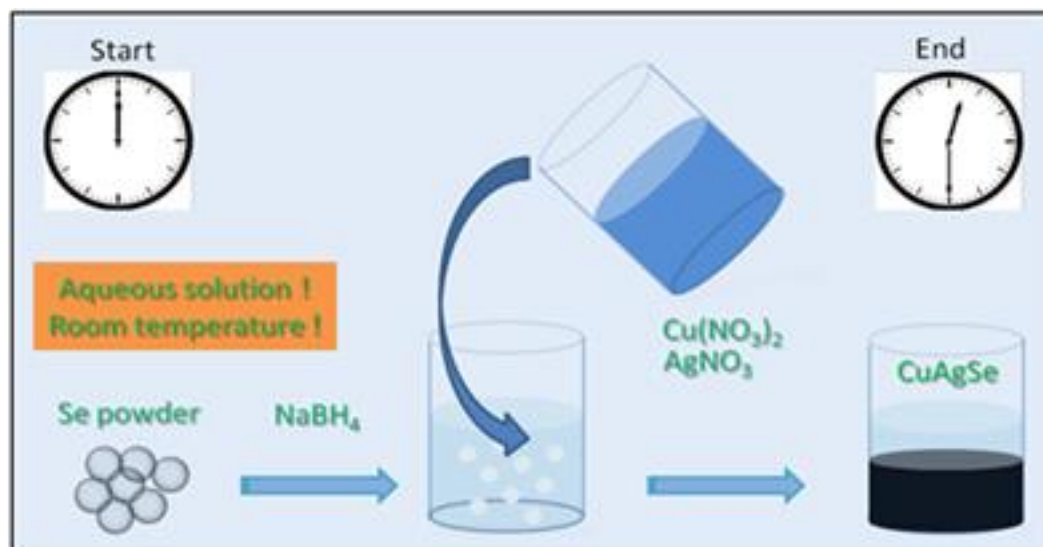


Figure 5.1. Schematic of the synthesis procedure of CuAgSe nanoparticles.

5.2 Experimental Section.

5.2.1 Synthesis of CuAgSe Nanoparticles.

All chemicals were bought from Sigma-Aldrich Pty. Ltd. and used as received without any further purification. In a typical synthesis, 3.16 g (40 mmol) Se powder (100 mesh, $\geq 99.5\%$) and 4.54 g (120 mmol) NaBH₄ (caplets, $\geq 98\%$) were dispersed in 400 mL distilled water, and the mixture was stirred for 25 min under the protection of Ar at room temperature to form a colorless selenium precursor solution. 9.7 g (40 mmol) Cu(NO₃)₂·3H₂O (97%) and 6.8 g (40 mmol) AgNO₃ (97%) were completely dissolved in 400 mL distilled water, and then quickly added into the Se-precursor solution to generate black precipitates. The black product was washed with distilled water several times, and then dried to a constant weight at 80 °C in a vacuum to give a yield over 90 %.

5.2.2 Characterization.

X-ray diffraction (XRD) studies were carried out at room temperature with an X-ray diffractometer (GBC-MMA) using Cu-K_{α1} radiation ($\lambda = 0.154$ nm). The sample was

characterized by X-ray powder diffraction (XRD) measurements in the temperature range between 20 and 300K using a PANalytical diffractometer [Figure 3.3(d)] with Cu-K α radiation ($\lambda = 0.154$ nm). Scanning electron microscopy (SEM) was conducted on a JEOL JSM-7500FA microscope. Transmission electron microscopy (TEM) was performed using a JEOL JEM-2011 microscope with an accelerating voltage of 200 kV. X-ray photoelectron spectroscopy (XPS) was conducted using a SPECS PHOIBOS 100 Analyzer installed in a high-vacuum chamber with the base pressure below 10^{-8} mbar. X-ray excitation was provided by Al K α radiation with the photon energy $h\nu = 1486.6$ eV at the high voltage of 12 kV and power of 120 W. The binding energy spectra were recorded at the pass energy of 20 eV in the fixed analyzer transmission mode. All the spectra were calibrated with C 1s at 284.6 eV. Analysis of the XPS data was carried out using the commercial Casa XPS 2.3.15 software package.

5.2.3 Thermoelectric Properties Test.

The as-synthesized CuAgSe nanoparticles (3 g) were loaded into a graphite die with a diameter of 20 mm and sintered into a pellet at 430 °C under 65 MPa pressure for 10 min by the spark plasma sintering (SPS) technique. The pellet was cut into rectangular pieces with dimensions of $4 \times 13 \times 1.2$ mm³ for thermoelectric characterization.

Low-temperature thermoelectric performance (i.e. from 3 K to 350 K) was tested on a physical properties measurement system (PPMS). The Seebeck coefficient, electrical conductivity, and thermal conductivity, as well as the ZT values, were obtained simultaneously. The high-temperature Seebeck coefficient and electrical conductivity were measured from 323 K to 623 K under helium atmosphere using an Ozawa RZ2001i (Japan) instrument. A Linseis LFA1000 (Germany) was used to determine the thermal diffusivity of samples, which were cut and polished into $\varnothing 10 \times 1$ mm² disks. The thermal conductivity (κ)

was calculated using the equation $\kappa = D \times C_p \times \rho$, where D is the thermal diffusivity, C_p is the heat capacity, and ρ is the mass density of the specimen, determined by the Archimedes method. The temperature dependence of the heat capacity (C_p) was determined using the differential scanning calorimeter (DSC) method on a DSCQ100 instrument with a heating rate of 10 K/min and a N_2 flow of 50 mL/min.

5.2.4 Theoretical Calculations.

The band structure calculations of tetragonal and cubic α -phase CuAgSe were performed using the generalized gradient approximation³⁸⁷ treated by the Perdew-Burke-Ernzerh (PBE) of exchange-correlation potential, as implemented in the DMol3 module in Materials Studio.^{388, 389} An all electrons double numerical atomic orbital augmented by d-polarization functions (DNP) was used as basis set, which has been successfully used to determine the electronic structures of nanomaterials.³⁹⁰ The calculation models were built according to the experimental lattice parameters.^{391, 392} The electronic Brillouin zone was sampled by using a Monkhorst–Pack grid of sample spacing 0.002\AA^{-1} .

5.3 Results and Discussion.

5.3.1 Preparation of CuAgSe Nanoparticles.

It is well known that CuAgSe has tetragonal, orthorhombic, and cubic structures (Figure 5.2), in which the tetragonal structure has lattice parameters $a = 4.1\text{ \AA}$, $b = 4.05\text{ \AA}$, and $c = 6.31\text{ \AA}$, and the orthorhombic one is an essentially a pseudo-tetragonal structure with a large supercell ($a = 4.1\text{ \AA}$, $b = 20.35\text{ \AA}$, and $c = 6.31\text{ \AA}$). There is no big difference between these two structures, except that the orthorhombic structure features a sequence which repeats itself periodically every five tetragonal cells in the b direction. They both possess a similar layered structure consisting of alternating stacking of the Ag and CuSe layers, in which Ag atoms

almost lie in the same plane and are bonded closely to Se atoms, allowing high mobility of Ag atoms and the formation of Ag-Ag metallic bonds.³⁹¹ Se atoms form a squashed tetrahedron, in which each corner is shared with adjacent tetrahedron, and Cu atoms are offset from the center within the tetrahedron. Each tetragonal cell contains two CuAgSe molecules, and the orthorhombic one has ten molecules. Both the tetragonal and the orthorhombic structures are stable at low temperature and can be reversibly transformed into the cubic structure at high temperature.

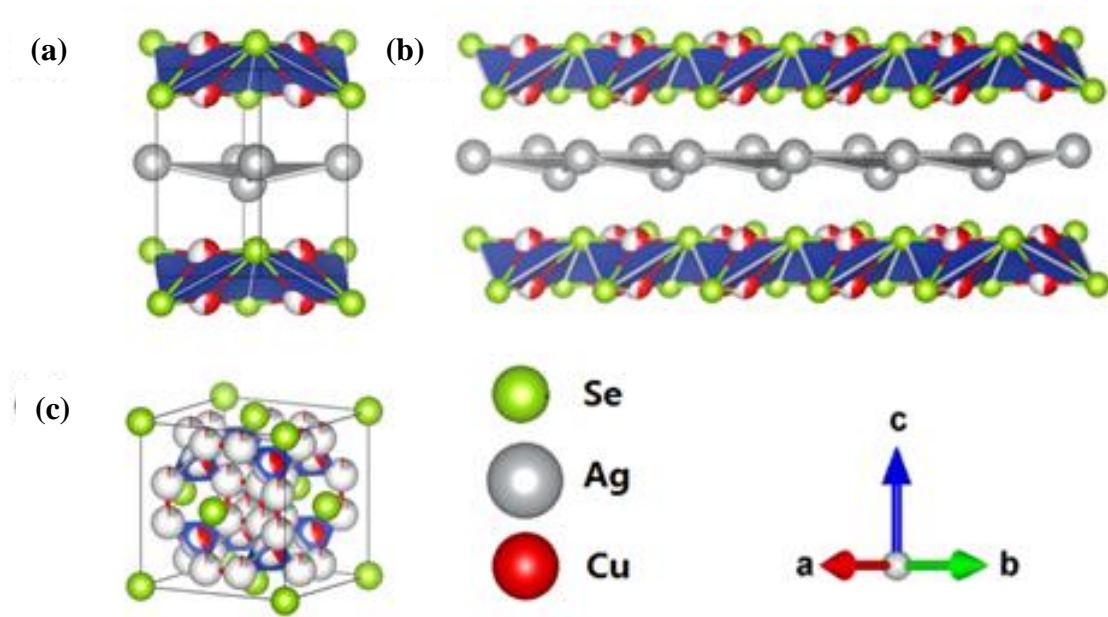


Figure 5.2. Schematic crystal structures of CuAgSe: (a) low temperature tetragonal CuAgSe; (b) low temperature orthorhombic CuAgSe; (c) high temperature cubic CuAgSe. The mixed gray and red mean randomly occupied by Ag or Cu atoms.

The crystal structure of the as-synthesized CuAgSe nanoparticles was determined by X-ray diffraction, and their XRD pattern is compared with those of standard orthorhombic CuAgSe (JCPDS 10-0451, black vertical lines) and tetragonal CuAgSe (JCPDS 25-1180, red vertical lines) in Figure 5.3(a). Most peaks and their intensity ratios are well matched with those of the orthorhombic structure, except for the peaks at $2\theta = 43.16^\circ$ (0,0,3), 44.02° (2,0,0), and 44.5° (0,2,0), which are marked with black dots in Figure 5.3(a) and can be solely attributed

to the tetragonal structure. The mixture of tetragonal and orthorhombic structures is attributed to the minor difference between them, and this could be caused by the nanoscale effects and the distortion of the crystal during the formation of nanoparticles.

The SEM and TEM images in Figure 5.3(b-c) show irregular CuAgSe nanoparticles with an average diameter of 20 nm. The high resolution TEM (HRTEM) image in Figure 5.3(d) clearly shows an inter planar spacing of 0.155 nm, which is consistent with the (1,10,2) plane. The fast Fourier transform (FFT) image in the inset of Figure 5.3(d) shows the diffraction spots from the (0,10,0) and (1,6,0) crystal planes.

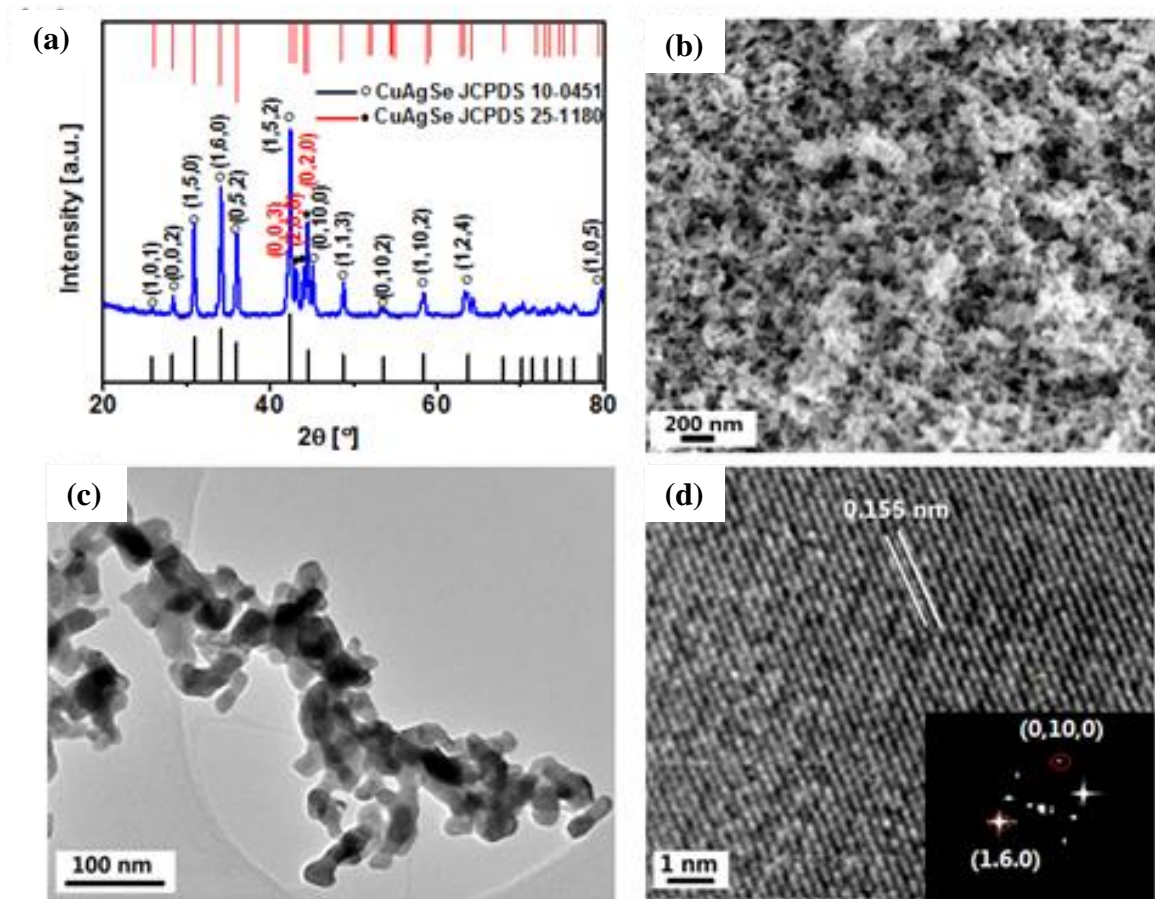


Figure 5.3. (a) X-Ray diffraction pattern, (b) SEM image of the prepared nanoparticles; (c) TEM and (d) HRTEM images of as-synthesized CuAgSe nanoparticles, inset picture is Fast Fourier Transform (FFT) pattern from HRTEM image.

The resultant CuAgSe nanoparticles were further characterized by XPS, and Figure 5.4 shows the binding energies of elements in the sample after calibration with the binding energy of C 1s at 284.6 eV. The absence of other elements apart from C, O, Cu, Ag, and Se indicates the high purity of the nanoparticles. The two distinct peaks at 931.9 eV and 952.0 eV in the Cu 2p spectrum are assigned to Cu 2p_{3/2} and Cu 2p_{1/2} of Cu⁺, respectively. The absence of a satellite peak at ~942.47 eV further supports the identification of the copper element as Cu⁺, rather than Cu²⁺. The peaks located at 368.0 and 374.0 eV represent the 3d_{5/2} and 3d_{3/2} orbital of Ag⁺, respectively. The Se 3d_{5/2} peak from Se²⁻ is located at 54.8 eV.³⁸⁵ The binding energies of Cu⁺, Ag⁺, and Se²⁻ ions are consistent with previous reports, demonstrating the formation of pure CuAgSe nanoparticles.³⁸⁵

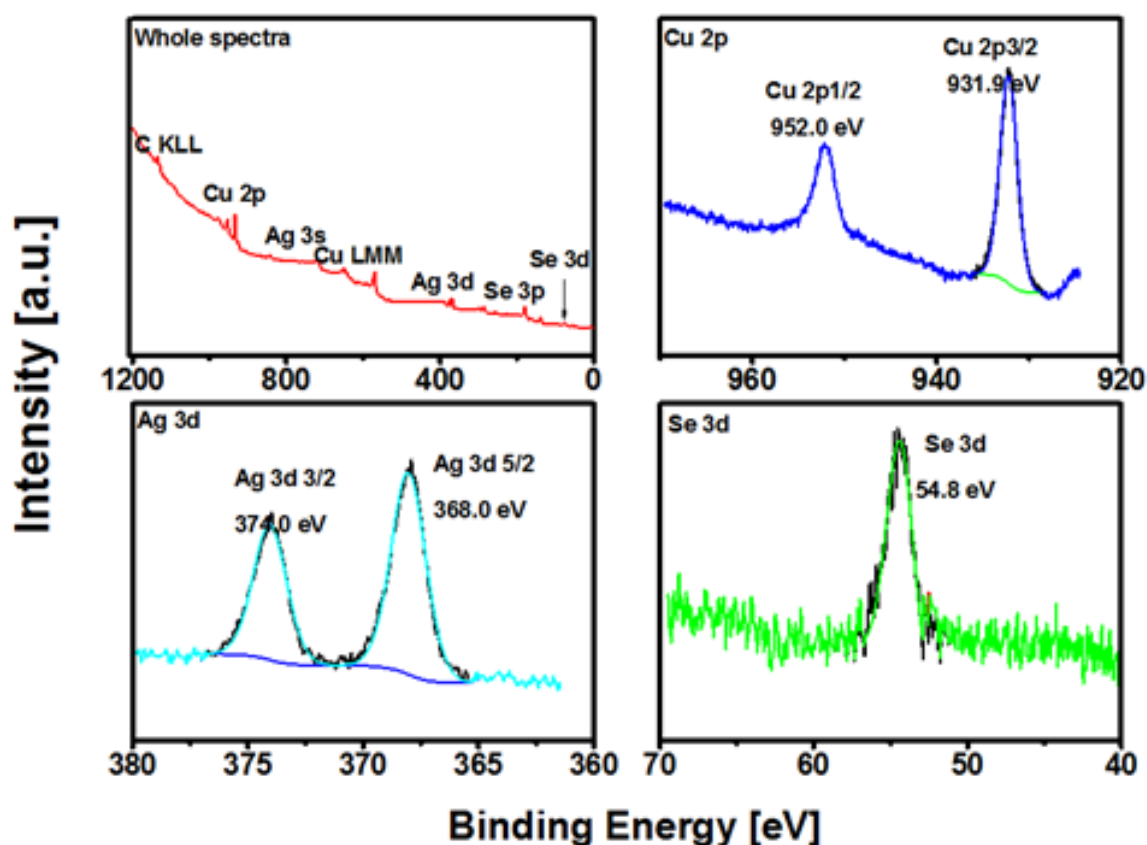
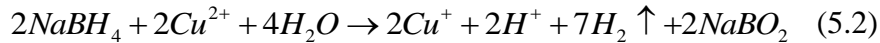


Figure 5.4. XPS results of the prepared CuAgSe nanoparticles.

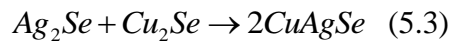
The above results demonstrate that pure CuAgSe nanoparticles can be simply synthesized from Cu(NO₃)₂, AgNO₃, and Se precursors in aqueous solution. The formation mechanism is not as simple as Figure 5.1 shown, however, and includes the following key steps. Firstly, selenium powder is reduced by NaBH₄ to form the colorless Se-precursor solution, as shown in Equation (5.1).



After addition of a mixture of Cu(NO₃)₂ and AgNO₃ into the Se-precursor solution, the excess NaBH₄ reduces Cu²⁺ into Cu⁺ through Equation (5.2) because the standard reduction potential of Cu²⁺/Cu⁺ (0.153 V) is smaller than that of Ag⁺/Ag (0.8 V).



Then, AgNO₃ reacts with NaHSe to form Ag₂Se precipitate first, due to the lower solubility of Ag₂Se compared to Cu₂Se [*K*_{sp}(Ag₂Se) = 2 × 10^{-63.7}; *K*_{sp}(Cu₂Se) = 1.58 × 10^{-60.8}], followed by the reaction of fresh Ag₂Se with Cu₂Se to form alloyed CuAgSe nanoparticles through Equation (5.3).^{385, 386}



To prove the above mechanism, a control experiment was conducted by using less reducing agent (i.e. Se/NaBH₄ molar ratio of 1:2) and using CuCl to replace Cu(NO₃)₂. After the Se powder was completely reduced by NaBH₄ to form a clear solution, the AgNO₃ solution was added into the Se-precursor solution to form a black suspension. A portion of the suspension was separated from solution and purified for analysis. CuCl powder was dissolved in HCl solution and added into black suspension under stirring. The mixture was stirred for 30 min at room temperature, and then the precipitate was collected. The XRD patterns and morphology of the black precipitates collected before and after addition of CuCl solution are shown in Figure 5.5(a-c). The results demonstrate that the precipitate collected before the addition of CuCl is pure Ag₂Se (JCPDS 24-1041), and the one collected after addition of CuCl is

CuAgSe mixed with a small amount of Ag_2Se . These results demonstrate that residual Se^{2-} ions react with Cu^+ to form Cu_2Se , which further reacts with Ag_2Se to form CuAgSe. This mechanism is further supported by the reaction between the as-prepared Cu_2Se nanoparticles and the Ag_2Se nanoparticles.

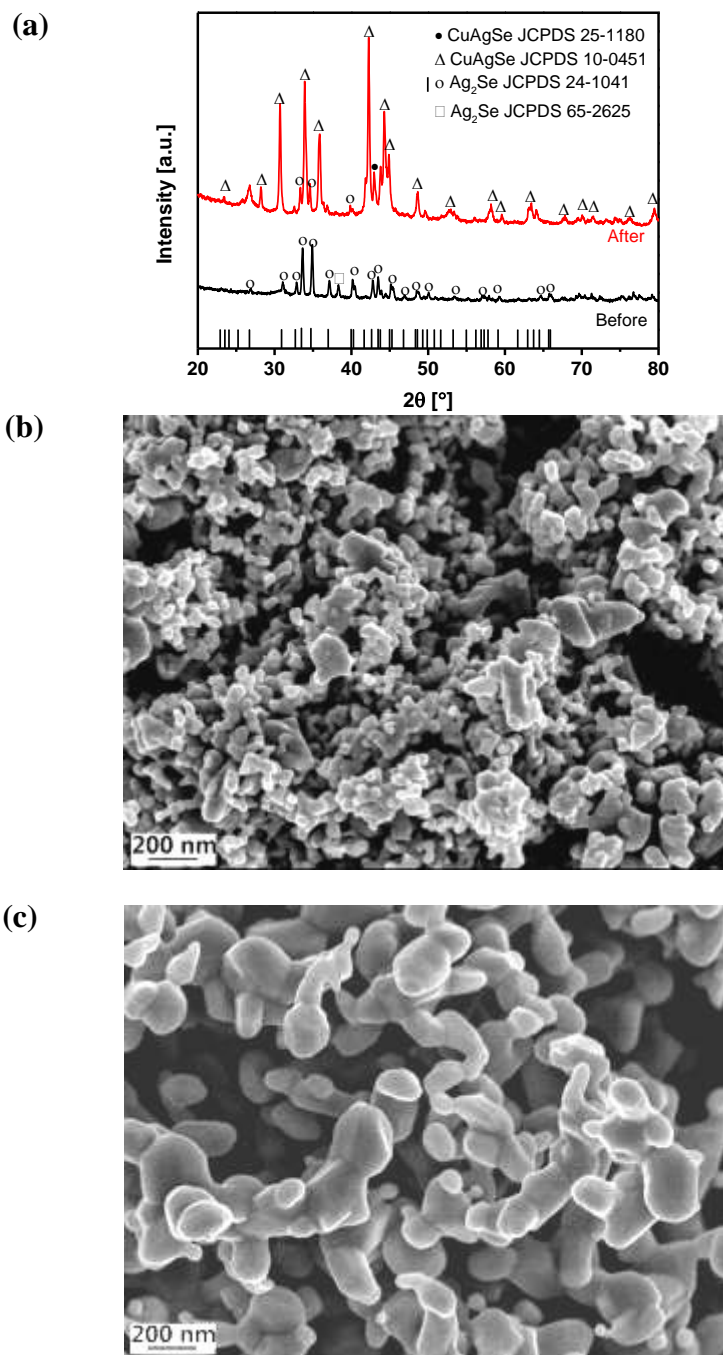


Figure 5.5. (a) XRD patterns and (b) SEM images of the precipitate before and (c) after the addition of CuCl solution.

And as displayed in Figure 5.6(a), the typical diffraction peak (1,6,0) from orthorhombic CuAgSe was observed in the mixture after it was stirred for 10 min at room temperature. The intensity of this peak was increased in the mixture after 30 h aging time under stirring [Figure 5.6(a)], indicating the increased amount of CuAgSe nanoparticles in the mixture, although the Cu₂Se and Ag₂Se nanoparticles were not completely transformed into CuAgSe. And the morphology changes are also detected, as shown by Figure 5.6(b-c).

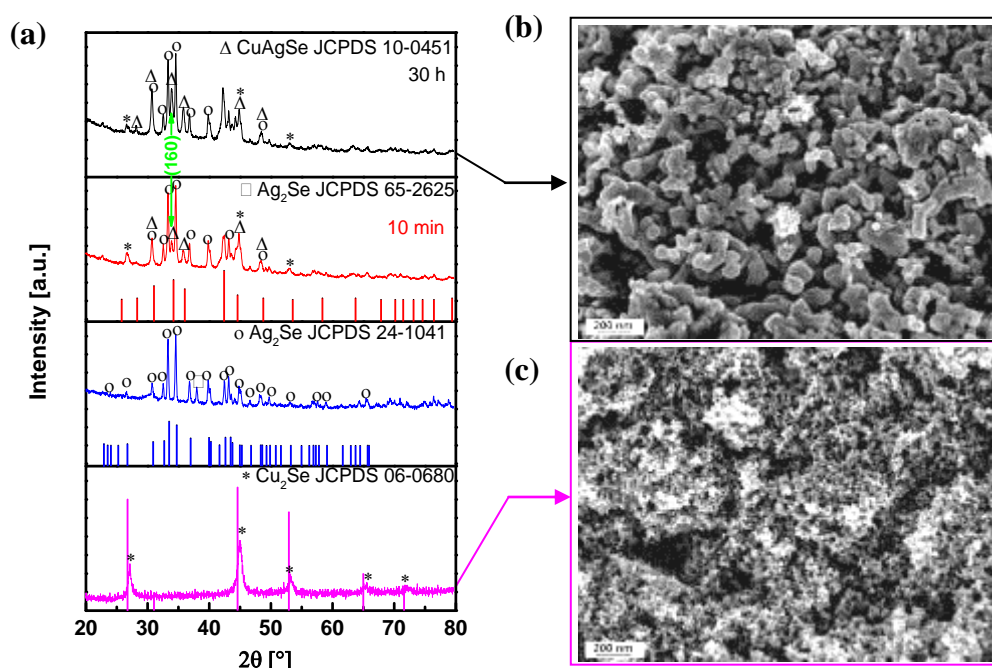


Figure 5.6. XRD patterns and SEM images of the precipitate obtained by mixing Cu₂Se and Ag₂Se in the aqueous system for different times, in comparison with that of nanoparticle precursors: (a) XRD patterns, (b) SEM image of the precipitate after stirring for 30 hours, and (c) SEM image of the Cu₂Se nanoparticle precursor.

According to the reaction mechanism, the compositions of the final products strongly depend on the precursor ratio of Cu²⁺:Ag⁺:Se²⁻ (*R*, molar ratio) and the amount of NaBH₄. As shown in Figure 5.7(a), CuAgSe nanoparticles can only be obtained with a ratio of 1:1:1. When a ratio of 1:2:2 was used, the product is a mixture of CuAgSe, Ag₂Se (JCPDS 24-1041), and Ag (JCPDS 65-2871) nanoparticles, as indicated by the XRD pattern. In the case of 2:2:1 ratio,

the product is a mixture of Ag₂Se and Ag nanoparticles. The appearance of Ag in both cases could be due to the reduction of Ag⁺ by slightly excess NaBH₄. When a 2:1:2 ratio was adopted, the product contained CuAgSe and a small amount of Cu₂Se (JCPDS 65-2982).

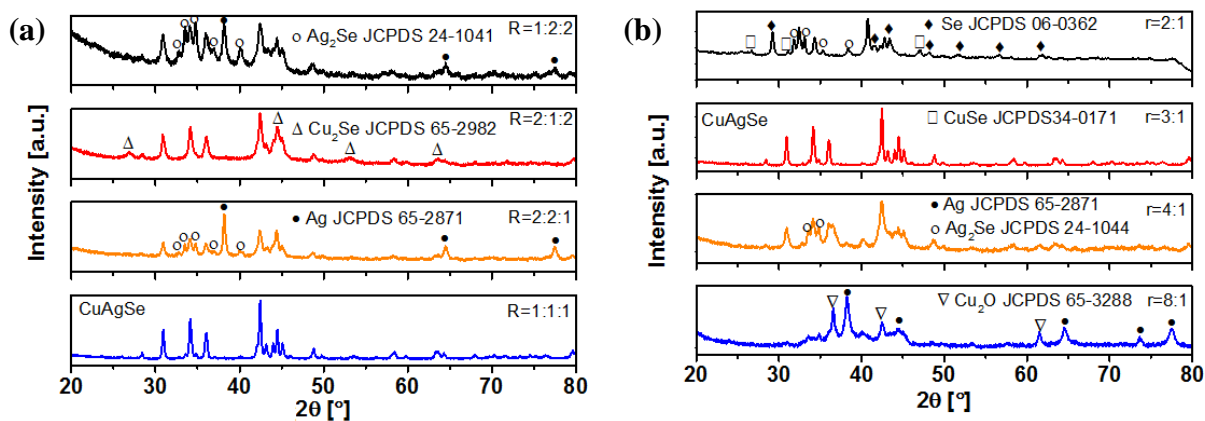


Figure 5.7. (a) X-ray diffraction patterns of samples synthesized with different Cu²⁺:Ag⁺:Se²⁻ ratios (*R*) and (b) different NaBH₄/Se ratios (*r*).

The role of NaBH₄ is to reduce both the Se powder and the Cu(NO₃)₂, and it is crucial to control the amount of NaBH₄. The ideal amount of NaBH₄ should be 3 times that of Cu(NO₃)₂ (or AgNO₃ or Se), i.e. their ratio *r* should be 3:1. When an inadequate amount of NaBH₄ was used (i.e. *r* = 2:1), the product is a mixture of Ag₂Se, CuSe, and Se, as shown in Figure 5.7(b), because NaBH₄ is not enough for reduction of the Se powder and Cu(NO₃)₂. When excessive NaBH₄ (e.g. *r* = 4:1 or 8:1) was used, Ag and Cu₂O were observed in the products [Figure 5.7(b)]. The formation of Cu₂O could be due to the increased solution pH caused by the hydrolysis of NaBH₄ and sodium borate.

5.3.2 Low Temperature TE for CuAgSe Nanobulk.

This simple green method is capable of producing CuAgSe nanoparticles on the gram scale in a one-pot reaction. The resultant surfactant-free nanoparticles can be directly used without surface modification for fabrication of pellets for thermoelectric study. Figure 5.8(a) presents

an SEM image of the cross-section of a pellet [the inset in Figure 5.8(a)], which was made from as-synthesized CuAgSe nanoparticles that were consolidated at 430 °C for 10 min under 65 MPa using the SPS technique. The relative density is about 90%, and the SEM image shows nanoscale pores- and particles in the pellet, although most nanoparticles were coarsened and aggregated to form larger grains. Compared with non-sintered powder, there is no distinct difference in its room-temperature crystal structure [Figure 5.8(b)], except that the diffraction intensity of the crystal planes [e.g. (0,0,3) peak] of the tetragonal phase is improved.

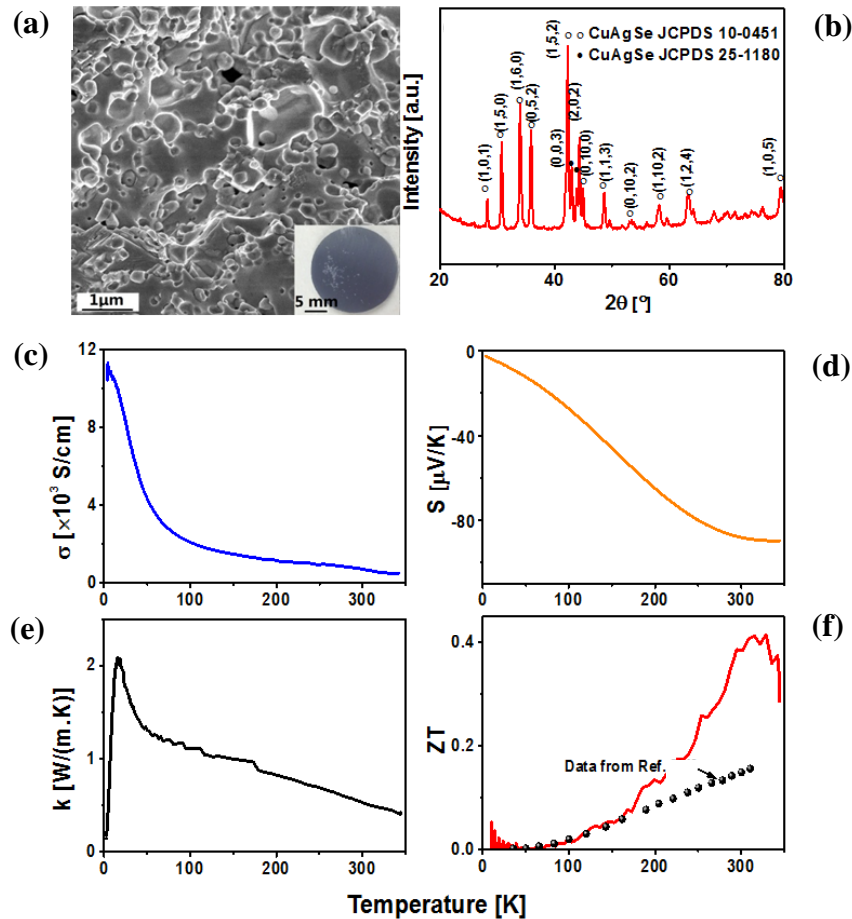


Figure 5.8. (a) SEM image of the consolidated pellet from the prepared CuAgSe nanoparticles, inset is the coin-like pellet; (b) XRD pattern of the pellet; (c-f) TE performance of the sintered CuAgSe nanoparticles from 3 K to room temperature. The black dot in (f) presents the data from the literature³⁸⁴.

The pellet was cut into pieces for thermoelectric investigation, and Figure 5.8(c)-(f) presents the results obtained on a PPMS instrument from low temperature to room temperature. The temperature dependence of the electrical conductivity in Figure 5.8(c) clearly demonstrates the metallic behavior of the pellet below 60 K, as indicated by the gradual increase of the electrical conductivity from 800 S/cm at room temperature to 3500 S/cm at 60 K, followed by a rapid increase to 11330 S/cm at 3 K. The tendency of the Seebeck coefficient is opposite to that of the electrical conductivity, and it decreases from -90 $\mu\text{V/K}$ to nearly 0 with temperature decreasing from room temperature to 3 K [Figure 5.8(d)].

The variation of the thermal conductivity with temperature is shown in Figure 5.8(e). It rises with temperature decreasing to reach the maximum value of 2.1 W/(m·K) at 22 K, and then decreases to 0.2 W/(m·K) at 3 K. The lattice thermal conductivity κ_l estimated from the equation $\kappa_l = \kappa - \kappa_e$ is shown by the dashed- dotted line in Figure 5.8(e), in which $\kappa_e = LT\sigma$ ($L = 2.1 \times 10^{-8}$ (W· Ω)/K²; T represents temperature; σ is the electrical conductivity). It clearly demonstrates that the thermal conductivity below 20 K is mainly contributed by the lattice thermal conductivity, as the movement of electrons is nearly “frozen”. The ultra-low lattice thermal conductivity [0.1 W/(m·K)] at room temperature can be attributed to the large lattice anharmonicity caused by the structure, which is reminiscent of amorphous solids.³⁹³ In addition, the nanoscale particles, pores, and grain boundaries that are present in the pellet also make contributions to the low thermal conductivity, because they can effectively scatter different wavelengths of phonons. The ZT value of the pellet is displayed in Figure 5.8(f), and it gradually increases with increasing temperature to achieve a value of 0.42 at 323 K, and then decreases with temperature. Compared with bulk CuAgSe³⁹³ [black dotted line in Figure 5.8(f)], the pellet made from nanoparticles exhibits a higher ZT due to its low thermal conductivity arising from nanoscale effects. This result supports that the use of nanoscale building blocks can effectively improve the performance of thermoelectric materials.

To investigate the abrupt metallic-*n* transition at around 60 K, temperature-dependent XRD of pellet was performed in the range of 20 K to 300 K (Figure 5.9). With the temperature decreasing from 300 K to 60 K, the strongest peak (152)_{orth} shifted to right. Meanwhile, the two peaks of (003)_{tetra} and (200)_{tetra} gradually merged into one around 70-60 K. The XRD patterns of the sample did not change below 60 K. The dependence of lattice parameters on temperature was calculated and shown in Table 5.1. Apparently, both the *c* value and the volume of unit cell reduced with decrease of temperature.

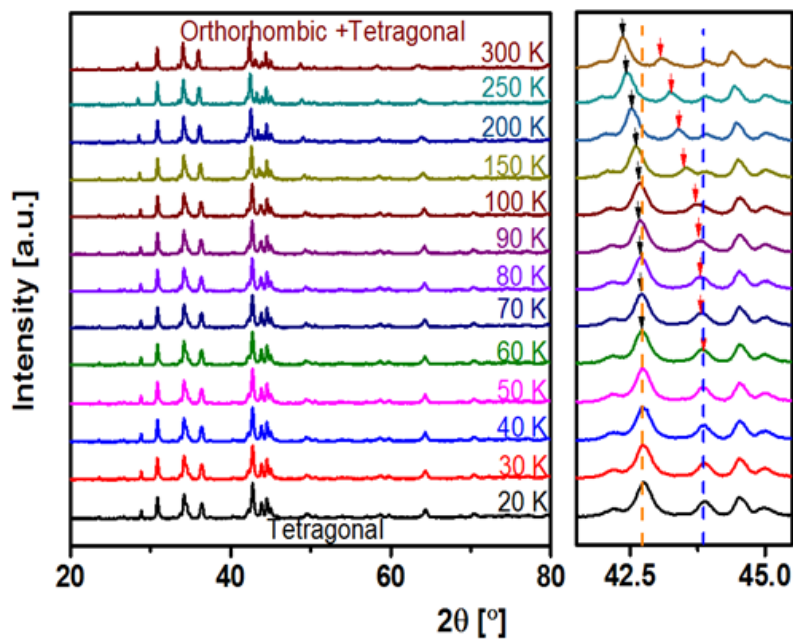


Figure 5.9. Temperature dependent XRD result for the sintered CuAgSe pellet from 20 K to 300 K.

Table 5.1. Calculated lattice parameters at different temperature for the orthorhombic CuAgSe.

Temperature (K)	$2\theta^a$ (degree)	d-space (nm)	Unit cell parameter (Å)			Volume per unit cell (Å ³)
			a	b	c	
300	42.366	0.2130	4.0963	20.5309	6.2886	528.8699
250	42.445	0.2127	4.0960	20.5013	6.2678	526.3255
200	42.524	0.2123	4.0946	20.4781	6.2477	523.8653
150	42.602	0.2120	4.0939	20.4598	6.2275	521.6197
100	42.681	0.2116	4.0956	20.4327	6.2096	519.6387
90	42.682	0.2116	4.0960	20.4283	6.2067	519.3375
80	42.707	0.2115	4.0961	20.4245	6.2031	518.9600
70	42.710	0.2114	4.0964	20.4224	6.2000	518.6782

60	42.734	0.2113	4.0972	20.4169	6.1969	518.3888
50	42.750	0.2112	4.0970	20.4160	6.1941	518.1002
40	42.750	0.2112	4.0979	20.4110	6.1918	517.8953
30	42.750	0.2112	4.0975	20.4168	6.1891	517.7662
20	42.750	0.2112	4.0986	20.4100	6.1874	517.5762

a. The peak refers to the strongest peak of Orthorhombic phase, e.g. peak (152).

The shrinkage of unit volume with temperature dropping is understandable. As illustrated previously, the tetragonal and orthorhombic CuAgSe are almost the same except that the later one has a sequence which repeats itself periodically every five tetragonal cells in the *b* direction. The relative positions of atoms could be rearranged with temperature, leading to the structure transition from orthorhombic to tetragonal phase. This phase transition makes the structure more symmetric with the unit cell changing from bigger orthorhombic to smaller tetragonal, which benefits to the reduction of scatterings of phonons and electrons. When the temperature is too low (i.e. < 60 K), CuAgSe could exhibit superconducting characteristics due to the presence of Ag-Ag metallic bond, leading to fast increase of the electrical conductivity below 60 K [Figure 5.8(c)]. The gradually reduced phonon scattering led to a high mobility, while reduced phonon scattering led to the increase on thermal conductivity with temperature decreasing to 22 K [Figure 5.8(e)].

The low temperature transport properties of CuAgSe were characterized by Hall Effect measurements. The detailed calculations are presented as below and the results are presented in Table 5.2 and Figure 5.10.

Hall resistivity (ρ_H) can be calculated according to Equation (5.4)-(5.5):

$$R = \frac{\rho_H \times W}{L \times T} \quad (5.4)$$

$$\rho_H = \frac{R \times L \times T}{W} \quad (5.5)$$

In which, ρ_H is the measured Hall resistivity [$\Omega \cdot m$]; R is the Hall resistance (Ω); L, W, T are

the dimensions of the sample (cm), respectively. Then Hall coefficient (R_H) is calculated by Equation (5.6)-(5.7), in which V_H is the voltage between V_+ and V_- [Figure 5.10(a)], or the Hall voltage; B is the magnetic field (Oe).

$$V_H = R \times I_S = R_H \times \frac{I_S \times B}{T} \quad (5.6)$$

$$R_H = \frac{R \times T}{B} \times 10^8 \left[\frac{cm^3}{C} \right] \quad (5.7)$$

Having obtained Hall coefficient, the charge carrier density is calculated by Equation (5.8). n is the charge carrier density (cm^{-3}); $e = 1.6 \times 10^{-19}$ C.

$$n = - \frac{1}{R_H \times e} [cm^{-3}] \quad (5.8)$$

And combining the Equation (5.9)-(5.10), the carrier mobility could be obtained. σ and μ are the conductivity and carrier mobility along the L (length) direction, respectively.

$$\sigma = ne\mu \quad (5.9)$$

$$\mu = R_H \times \sigma [cm^{-2} / (V.S)] \quad (5.10)$$

Detailed device assembly, the measured relationship between the Hall resistivity and the magnetic field, the calculated carrier density (n), and the carrier mobility (μ) are presented in Figure 5.10(a-d).

Table 5.2. Calculated n and μ at different temperatures.

Temperature (K)	Carrier	Hall Coefficient (cm^3/C)	Carrier density ($\times 10^{18} cm^{-3}$)	Carrier mobility ($cm^2/(V \cdot s)$)	Conductivity ($\times 10^3 S/cm$)
300	Electron	1.89±0.10	3.307	1965.6	1.04
200		1.55±0.11	4.032	1798.0	1.16
100		0.91±0.07	6.868	1883.7	2.07
10		0.71±0.06	8.803	7518.9	10.59

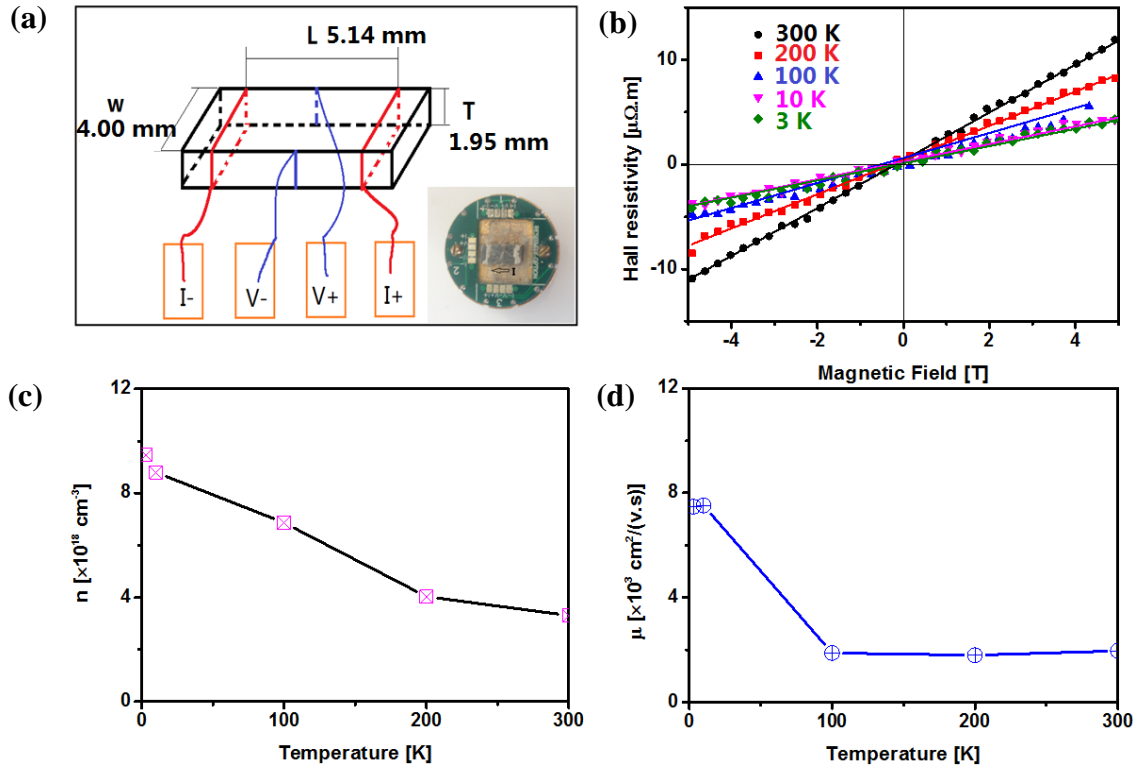


Figure 5.10. (a) Sample connections and dimensions for the measurement, inset is the assembled device for testing; (b) Hall resistivity as a function of magnetic field; (c) calculated n and (d) calculated μ as functions of temperature.

The Hall measurement results show that electrons are the main charge carriers in CuAgSe below 300 K. The carrier density (n) is approximately 10^{18} and decreases with rising temperature, while the carrier mobility first decreases from 7478 to 1798 $\text{cm}^2/(\text{V}\cdot\text{s})$ with increasing temperature from 3 K to 200 K, then slightly increases to 1966 $\text{cm}^2/(\text{V}\cdot\text{s})$ at 300 K. Both the carrier density and the carrier mobility are consistent with previous reports.^{393, 394}

5.3.3 High Temperature TE of CuAgSe Nanobulk.

The thermoelectric properties of sintered CuAgSe nanoparticles above room temperature were further investigated, and Figure 5.11 displays the results measured from room temperature to 623 K. The differences between the results around room temperature shown in

Figures 5.8 and Figure 5.11 originated from the error of different instruments. The temperature dependences of the electrical conductivity, Seebeck coefficient, thermal conductivity, and specific heat show an interesting transition at around 467 K, which is proved by the reversible first order phase transition displayed in the heating-cooling DSC curve in Figure 5.12(a). This means the occurrence of a phase transition during the heating process (i.e. changing from orthorhombic CuAgSe into cubic CuAgSe), which has been demonstrated in previous reports. As presented in Figure 5.2(c), the high-temperature cubic phase is composed of a face-centered-cubic Se lattice with Ag/Cu cations that are

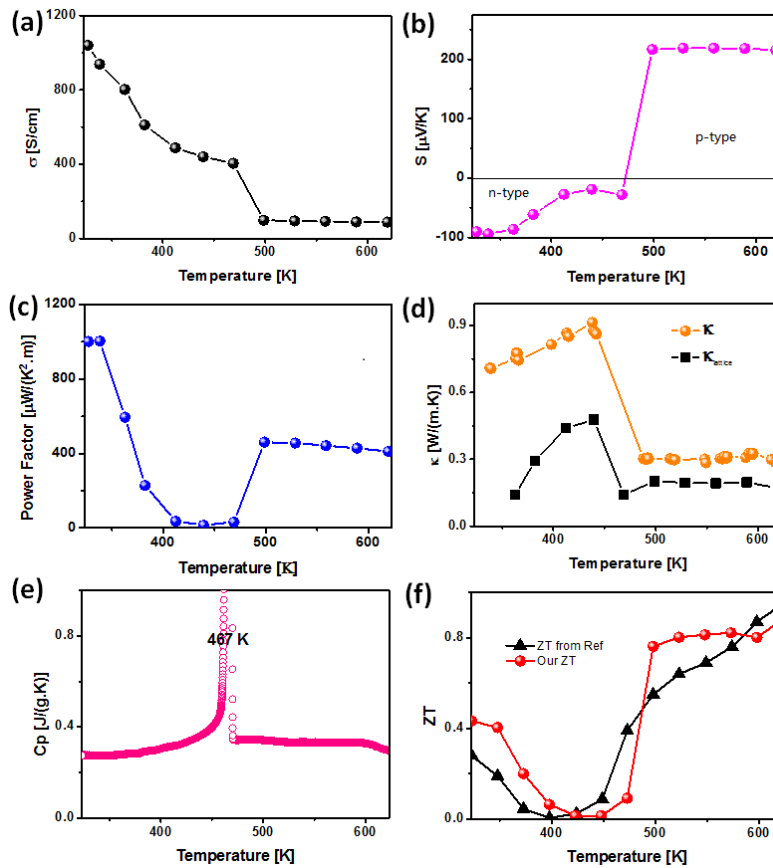


Figure 5.11. TE performance of sintered CuAgSe nanoparticles from 323 K to 623 K: (a) electrical conductivity; (b) Seebeck coefficient; (c) power factor; (d) thermal conductivity; (e) specific heat capacity; (f) ZT value, the black triangle represents the data from reference ³⁸³.

randomly distributed among the tetrahedral sites. This unique structure ensures the high mobility of the Ag/Cu cations and leads to super-ionic conductivity. The electrical conductivity of CuAgSe [Figure 5.11(a)] decreases from 1040 S/cm to 400 S/cm with increasing temperature from 323 K to 467 K. After the phase transition, the scattering of charge carriers is dramatically increased by the highly disordered Ag⁺ and Cu⁺ ions, resulting in a further decrease in the electrical conductivity to 100 S/cm, which remains unchanged up to 623 K. The independence of the electrical conductivity from temperature is attributed to their superionic characteristic arising from fast movement of the Ag⁺ and Cu⁺ ions at high temperature, which becomes predominant after the phase transition. The negative value of the Seebeck coefficient [Figure 5.11(b)] demonstrates that orthorhombic CuAgSe is an intrinsic *n*-type semiconductor before the phase transition. The Seebeck coefficient decreases from -90 μV/K to around -20 μV/K with increasing temperature from room temperature to the phase transition temperature. A sudden *n-p* transition occurs with the phase transition; and the cubic CuAgSe exhibits a nearly constant positive Seebeck coefficient of 226 μV/K [Figure 5.11(b)]. The transition of Seebeck coefficient (or type of charge carrier) is essentially due to the change of band structure, which is associated with the change of crystal structure arising from the variation of temperature. Increase of temperature leads to the transition from mixed orthorhombic and tetragonal phases into cubic structure, which has been reported in the bulk CuAgSe.³⁸³

The overall and lattice thermal conductivities ($\kappa_1 = \kappa - L\sigma T$, $L = 2.1 \times 10^{-8}$ (W·Ω)/K²) of CuAgSe in the range of 323 K to 623 K are presented in Figure 5.11(d). The overall thermal conductivity increases from 0.75 W/(m·K) at 370 K to around 0.92 W/(m·K) at 445 K, accompanied by increasing lattice thermal conductivity (κ_1) from 0.1 W/(m·K) at 370 K to 0.5 W/(m·K) at 445 K. After the phase transition, the overall thermal conductivity is reduced to around 0.3 W/(m·K), owing to the high mobility of Cu⁺ and Ag⁺ cations. The lattice thermal

conductivity increases to 0.2 W/(m·K), as the contribution of charge carriers is inhibited by the low electrical conductivity.

The temperature-dependent ZT of our CuAgSe nanoparticles is compared with that of bulk CuAgSe³⁸³ in Figure 5.11(f). A similar temperature dependence is observed in both nanostructured and bulk CuAgSe,³⁸³ although our room-temperature ZT is higher than reports in the literature (i.e. 0.42 vs. 0.15 at 323 K from PPMS; 0.42 vs. 0.28 at 323 K from high-temperature instruments). In the range of 500-575 K, our ZT values (~0.8) are also higher than the literature values.³⁸³ Our ZT values above 575 K are comparable to the bulk value (0.9 vs. 0.95 at 623 K) due to the extremely low electrical conductivity.

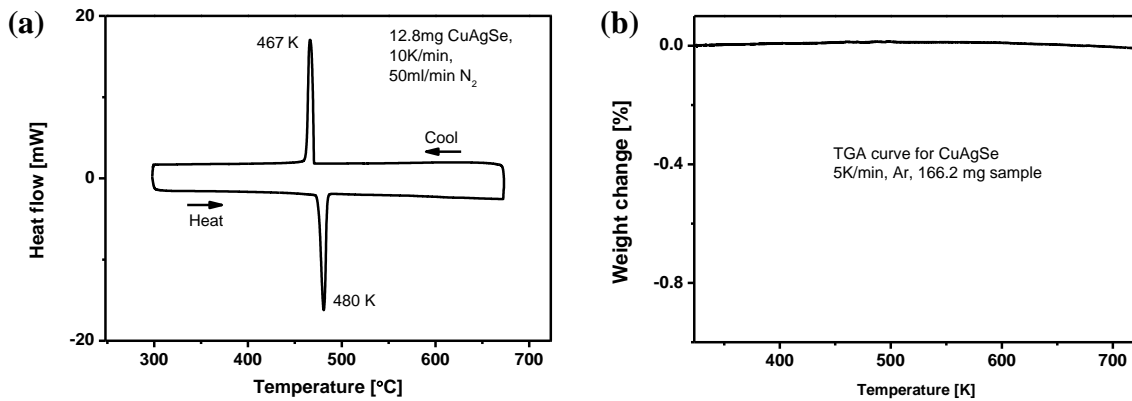


Figure 5.12. (a) DSC and (b) TGA curve of CuAgSe pellet.

5.3.4 Calculation on Band Structure of Low and High temperature phase of CuAgSe nanobulk.

To further understand the *n-p* transition of electrical conductivity, the electronic structures of tetragonal and cubic CuAgSe were calculated. Figure 5.13(a) illustrates the calculated band structure of tetragonal CuAgSe at the PBE level. Figure 5.13(b) is the magnified band structure at Γ point near the Fermi level. They both clearly show that one of conduction bands is crossing the Fermi level along the Z- Γ and Γ -X lines, while one valence band is just located below the Fermi level.³⁸⁴ Thus the tetragonal CuAgSe should possess two kinds of

charge carriers. The main charge carriers are electrons, however, and the conductivity is *n*-type. In addition, the conduction bands are relative sparse than valence bands, and more electrons are located near Fermi level as shown by Figure 5.13(a) and its total Density of States (DOS) [Figure 5.13(e)]. Figure 5.13(b) also demonstrates that both the conduction bands and valence bands are highly asymmetric at the Γ point, which means the tetragonal structure is highly anhomonic or disordered, leading to low thermal conductivity. Figure 5.13(c) is the calculated band structure of cubic CuAgSe and Figure 5.13(d) is the magnified band structure at Γ point where no band gap was observed.

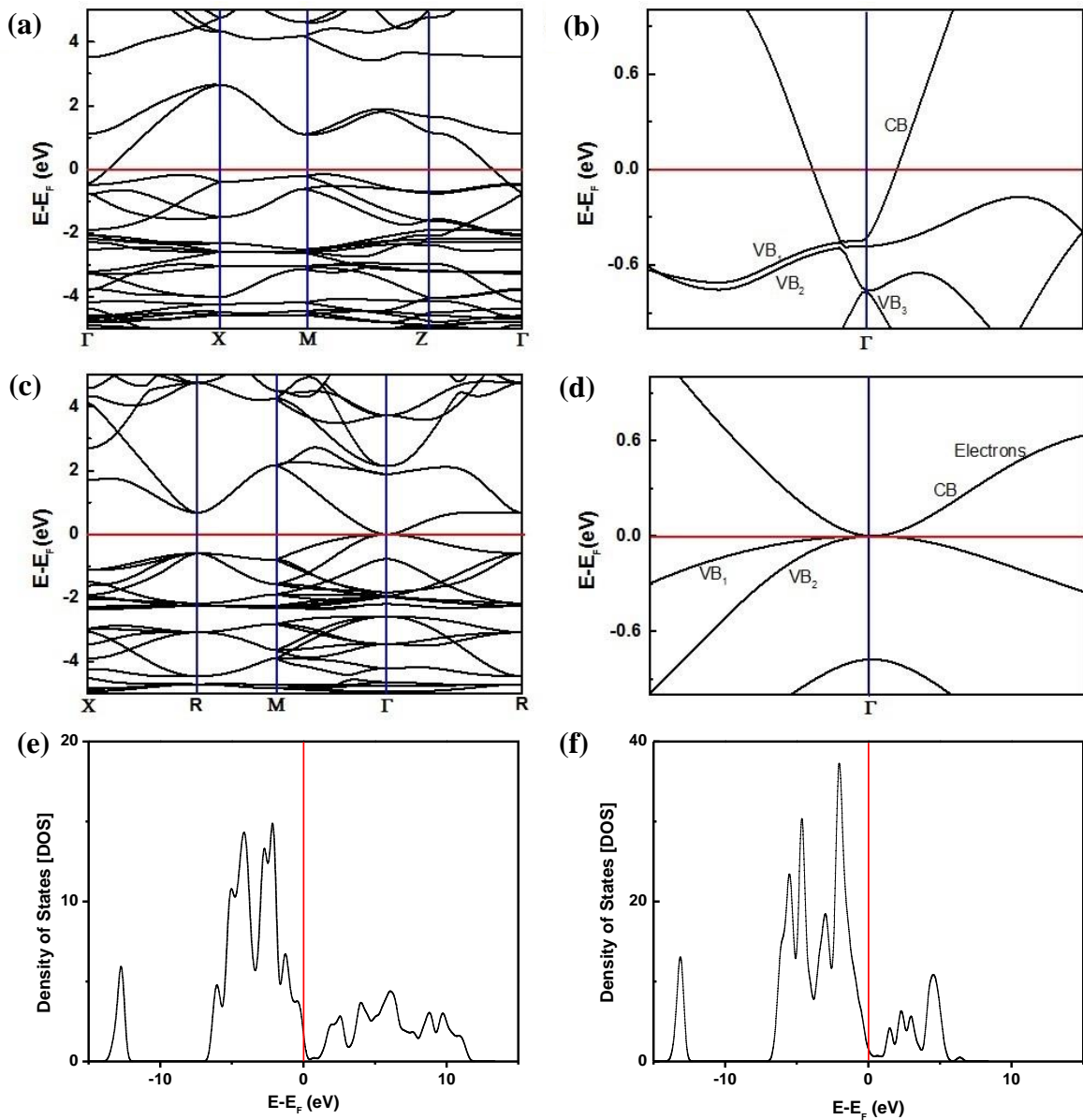


Figure 5.13. Calculated band structure for (a) tetragonal CuAgSe; (b) α -phase cubic CuAgSe; and (c-d) magnified part of Γ point. Total density of states for (e) low temperature β -tetragonal phase and (f) high temperature α -cubic phase CuAgSe.

The Seebeck coefficient could be expressed by the following equation:

$$S = A \times T \times \frac{m^*}{n^{2/3}} \quad (5.11)$$

In which A is a constant, T is temperature, n is the charge carrier density, m^* is the effective mass of charge carriers and equal to the reciprocal of the curvature of band edge when the band gap is 0 eV at Γ point. As displayed in Figure 5.13(d), the curvature of conduction band edge (CB) is bigger than any of the valence band edge (VB_1 and VB_2), the effective mass of holes ($m_h^* = m_{VB1}^* + m_{VB2}^*$) is heavier than the absolute value of electrons ($|m_e^*|$). The whole effective mass is positive, e.g. $m^* = m_e^* + m_h^* > 0$, which results in a positive S [Figure 5.11(b)]. In addition, the high-temperature phase CuAgSe possesses a cubic-face-centered Se frame, but both the conduction band and valence band at Γ point show high asymmetry [Figure 5.13(d)]. This implies the cations sublattice (Cu^+ and Ag^+) is highly disordered, which can enhance the phonon scatterings and reduce the thermal conductivity. Although the DOS of cubic structure shows the same concentration near Fermi level [Figure 5.13(e)] as tetragonal phase, the electrical conductivity is still low due to the disordered cations.

5.3.5 Cycle Stability on TE Performance of CuAgSe Nanobulk.

From the perspective of practical application, an important parameter is the cycling stability of thermoelectric materials during long-term operation. Therefore, we tested the stability of the consolidated CuAgSe pellet in a sealed chamber (Ozawa 200li) filled with a low pressure helium, and measured its electrical conductivity and Seebeck coefficient through 5 cycles of heating and cooling from room temperature to 623 K. There are no big differences in the

morphology, composition, and appearance of the pellet before and after 5 cycles. The morphology, composition, electrical conductivity, and Seebeck coefficient are plotted in Figure 5.14(a-d). Good reproducibility is observed in these data obtained from different cycles. The heating-cooling cycles demonstrate the good stability of the pellet, which is also supported by the zero loss in weight during the thermogravimetric analysis (TGA). Figure 5.12(b) shows the TGA curve from room temperature to 723 K. No oxidation or evaporation occurred during analysis. In addition, XPS was also employed to characterize the sample after 5 cycles [Figure 5.14(e)]. No other elements were detected, and the valence states of Cu, Se and Ag did not change. The same results were obtained before and after 5 cycles of tests, which demonstrate that our CuAgSe pellet consolidated from nanoparticles is stable under cycling.

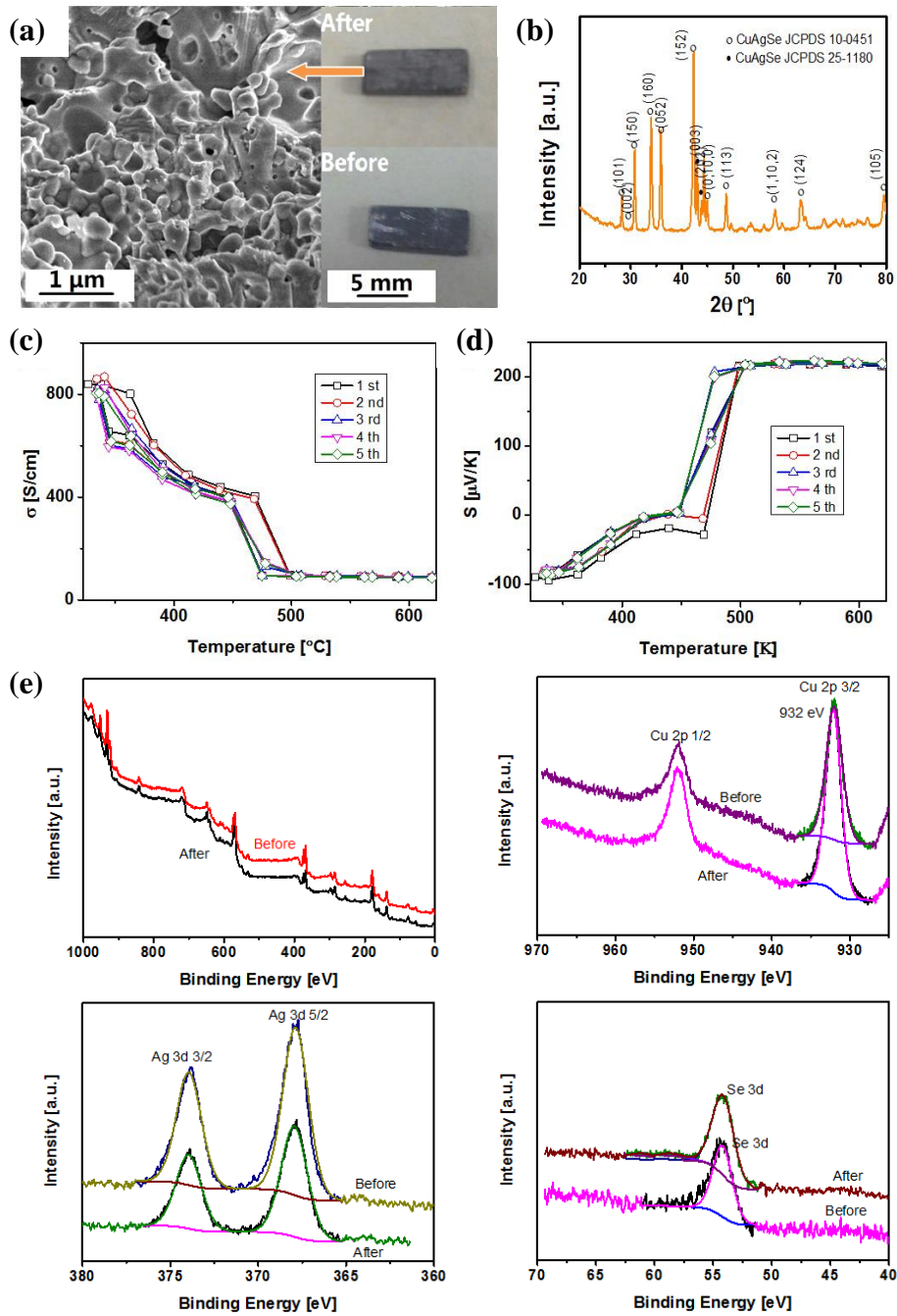


Figure 5.14. TE properties of sintered CuAgSe nanoparticles tested over 5 cycles (heating and cooling): (a) micromorphology after 5 cycles; right side is the macro-morphology before and after 5 cycles; (b) XRD pattern after 5 cycles; (c) electrical conductivity; (d) Seebeck coefficient. (e) XPS spectra of CuAgSe pellet before and after 5 cycles.

5.4. Conclusion.

Large-scale surfactant-free CuAgSe nanoparticles were successfully synthesized via a robust environmentally friendly aqueous method. The resultant CuAgSe nanoparticles were sintered into pellets by an advanced SPS technique for thermoelectric investigation in the range of 3 K to 623 K. The results show an interesting temperature-dependent transport property accompanied by a phase transition, i.e. sintered CuAgSe nanoparticles exhibit metallic characteristics below 60 K, *n*-type semiconductor behavior in the range of 60 K to 480 K, and *p*-type semiconducting behavior above 480 K. The pellet displays a *ZT* of 0.42 at 323 K and 0.9 at 623 K, and exhibits excellent cycling stability. The temperature-dependent *n-p* transition and the excellent stability of CuAgSe enable it to simultaneously serve as a promising *n*-type and promising *p*-type (at different temperatures) thermoelectric candidate for conversion of heat into electricity.

Chapter 6. Ambient Aqueous Growth of Cu₂Te Nanostructures with Excellent Electrocatalytic Activity towards Sulfide Redox Shuttles

6.1 Introduction.

As an important type of copper chalcogenides, copper telluride nanostructures, with a direct band gap between 1.1 and 1.5 eV, are conventionally used as back conductive contact materials for high-efficiency CdTe based solar cells.³⁹⁵⁻³⁹⁹ Similar to other copper chalcogenides, the copper deficiency in Cu_{2-x}Te leads to a unique localized surface plasma resonance (LSPR) in the near infrared (NIR) area, which makes it very attractive for surface-enhanced Raman scattering (SERS) and photo acoustic imaging.^{169, 222, 400-403} In addition, copper tellurides also are promising for potential applications in lithium ion batteries, photo-thermal therapy, detection of toxic CO, and thermoelectric applications,^{222, 351, 402, 404, 405} although these applications are strongly obstructed by the difficulty in controlled synthesis of their nanostructures with defined morphology, crystal structure, and composition.

In virtue of the complexity of tellurides and the inert property of Te element, the synthesis of nanostructured copper tellurides is more difficult than commonly reported prototypical semiconductors and usually needs harsh reaction conditions, such as high temperature, high pressure, or the usage of toxic organics.^{169, 222, 400-403} For example, cube-, plate-, and rod-like copper telluride nanomaterials were prepared under the assistance of expensive LiN(Si(CH₃)₃)₂ by the hot injection method.⁴⁰² Copper telluride nanocubes, nanosheets and hollow nanoparticles were synthesized by Han et al.³⁵¹ in organic solvent at temperature above 200 °C. These methods appeared to be either time or energy consuming, not to mention their low yield.

Herein, the highlight of this article lies in two aspects. First, we report a robust and scalable synthesis of surfactant free Cu₂Te nanosheets and Cu₂Te nanotubes from Cu₂E (E = O, S, Se)

nanoparticles via a simple anion exchange route at room temperature in aqueous solution. In principle, the anion exchange is similar to cation exchange based on the solubility difference of products. However, anion exchange is much more complex, because anion diffusion usually requires longer reaction times and higher temperatures than cation exchange due to the larger size of anions. In addition, changes in the morphology often accompany anion exchange reactions as anions usually form the framework of a structure.^{270, 273, 406-410} All these features make anion exchange more challenging than cation exchange to control both composition and morphology.^{269, 409, 410} However, detailed investigations on the mechanisms behind morphology change during the anion exchange reaction are rare, and such changes have been simply ascribed to the Kirkendall effect.^{268, 273, 406, 407, 409} In this article, we propose a novel exchange-peeling mechanism for anion exchange reaction instead of simple Kirkendall effect, and the effect of different reaction parameters on morphologies of final product were thoroughly investigated.

Second, the morphology-dependence catalytic reactivity of Cu_2Te nanostructures has been observed for the first time. A potential application of Cu_2Te nanostructures is its excellent electro-catalytic property towards sulfide redox couples for use as counter electrodes (CEs) of quantum dot sensitized solar cells (QDSSCs). As an important member of QDSSCs, CdS and CdSe co-sensitized solar cells have attracted considerable attention, not only because the semiconductor quantum dot (QD) possess extraordinary light harvesting ability due to their tunable band gaps, but also because the inorganic nature of QD absorbers endow the device with good stability.^{318, 411-416} The CE of solar cells is an important part of the external circuit, and plays a pivotal role in catalyzing the redox reaction in the electrolyte, which is usually polysulfide electrolyte for CdS and CdSe co-sensitized solar cells.⁴¹⁷⁻⁴²¹ Most noble metals, such as Pt, show poor performance in polysulfide electrolyte because their surfaces are passivated by actively adsorbing Sulphur atoms to result in lower conductivity, and

considerable over-potential is generated to slow electrolyte reduction.^{420, 421} Other alternatives include carbon materials and metal chalcogenides. Nevertheless, carbon materials, such as carbon black, graphene and carbon nanotubes have disadvantages; carbon black lacks thickness for effective charge conduction although it possess large surface area, while graphene has poor catalytic activity even though it has high charge conduction.⁴¹⁸ Metal chalcogenides, such as metal sulfides and selenides (e.g. Cu_2S and Cu_2Se), are found to show high power conversion efficiency (PCE).^{418, 419, 421} For example, by employing Cu_2S as CE and ZnS/SiO_2 coated CdSeTe as photo-anode, the maximum power conversion efficiency (PCE) of Cd chalcogenide QDSSCs was boosted to 8.21 %.⁴²¹ In this paper, the performance of a new family of materials-nanostructured Cu_2Te with different morphologies as counter electrodes in CdS/CdSe co-sensitized solar cells has been investigated. Cu_2Te based nanostructures show high electrocatalytic activity in addition to low fabrication cost.

6.2 Experiment Section.

6.2.1 Synthesis of Cu_2Te nanotubes and nanosheets.

As illustrated in Figure 6.1, a typical synthesis of Cu_2Te nanotubes is as follows: 127 mg of tellurium powder (1 mmol, 100 mesh, $\geq 99.5\%$) and 3 g of NaBH_4 (caplets, $\geq 98\%$) were added into 100 mL of Milli-Q water, with continuous stirring under the protection of inert gas. Several minutes later, a light purple (or colorless) Te precursor solution formed. The Cu_2Se nanoparticle precursor was prepared according to the method described in Chapter 4. First, 1 mmol of selenium powder (100 mesh, $\geq 99.5\%$) was reduced with 3 mmol of NaBH_4 in distilled water for 30 min, then precipitated with a 10 mL, 0.2 M $\text{CuCl}_2 \cdot 2\text{H}_2\text{O}$ ($\geq 99\%$) solution. The as-obtained Cu_2Se nanoparticles were purified, dried, and ultrasonically dispersed into 40 mL H_2O . Then, the dispersed turbid suspension was mixed with the Te precursor at room temperature, followed by continuous stirring for 30 min under protection of

inert gas, and Cu_2Te nanotube structures were obtained. To form the Cu_2Te nanosheets, after the solution was mixed with the turbid suspension, the stirring was immediately stopped, and the suspension was simply held for 30 min.

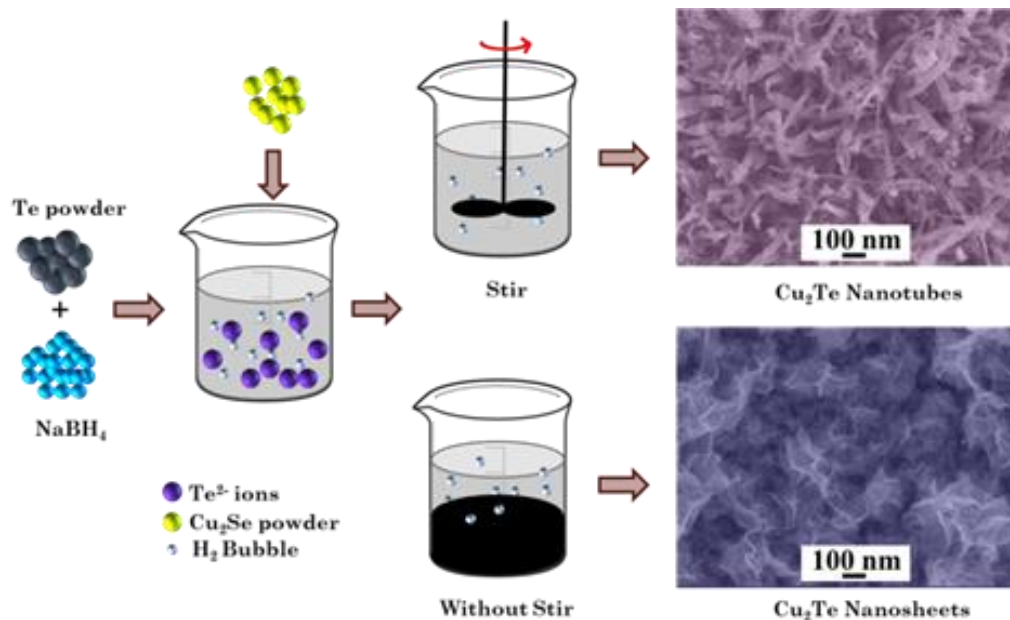


Figure 6.1. Schematic illustration of the synthesis of Cu_2Te nanosheets and nanotubes from Cu_2Se nanoparticles.

Cu_2Te nanotubes and nanosheets can be also synthesized by the above procedure from Cu_2O nanoparticles and Cu_2S nanoparticles. The synthesis of Cu_2O and Cu_2S nanoparticles is similar to Cu_2Se , according to the method developed in Chapter 4. Cu_2S was obtained by first mixing 1 mmol of $\text{Na}_2\text{S}\cdot 9\text{H}_2\text{O}$ ($\geq 99.5\%$) with 1 mmol of NaBH_4 in distilled water for 30 min, then precipitating it with 10 mL, 0.2 M $\text{CuCl}_2\cdot 2\text{H}_2\text{O}$ ($\geq 99\%$) solution. Cu_2O was simply prepared by adding a 10 mL, freshly prepared 0.1 M solution of NaBH_4 to 10 mL, 0.2 M $\text{CuCl}_2\cdot 2\text{H}_2\text{O}$ solution.

6.2.2 Characterization.

X-ray diffraction (XRD) studies were carried out at room temperature with an X-ray diffractometer (GBC-MMA) using $\text{Cu-K}\alpha$ radiation ($\lambda = 0.154$ nm). Scanning electron

microscopy (SEM) was conducted on a JEOL JSM-7500FA microscope. Transmission electron microscopy (TEM) was performed using a JEOL JEM-2010 microscope with an accelerating voltage of 200 kV. Scanning transmission electron microscopy-energy dispersive X-ray spectroscopy (STEM-EDS) spectra was collected using a JEOL ARM-200F operating at 200 kV with an EDAX solid-state X-ray detector. Samples were prepared by drop-casting ethanol-dispersed nanostructures onto TEM copper grids. Lattice fringes were measured from the fast Fourier transforms (FFT) of high resolution TEM (HRTEM) images using the Gatan software. Atomic force microscope (AFM) images were collected using an Asylum AFM equipped with NCHR tapping mode. AFM tips were bought from the “Nanoworld” Company. Nitrogen adsorption-desorption measurements were conducted at 77 K with a Quantachrome Autosorb iQ machine (USA). Before measurements, the samples were degassed under vacuum at 120 °C for 6 h. The Brunauer-Emmett-Teller (BET) specific surface area was calculated from the adsorption data in the relative pressure (P/P_0) range from 0.05 to 0.35. X-ray photoelectron spectroscopy (XPS) was conducted using a SPECS PHOIBOS 100 Analyzer installed in a high-vacuum chamber with the base pressure below 10^{-8} mbar. X-ray excitation was provided by Al K_α radiation with the photon energy $h\nu = 1486.6$ eV at the high voltage of 12 kV and power of 120 W. All the spectra were calibrated with respect to C 1s at 284.6 eV.

6.2.3 Fabrication and Testing of CdS/CdSe Co-sensitized Solar Cell.

Preparation of photoelectrodes: CdS/CdSe quantum dots (QDs) co-sensitized TiO_2 working electrodes were prepared by a previously developed technique.^{415, 422} The Cu_2Te counter electrodes (CEs) were fabricated by depositing various pastes on fluorine-doped tin oxide (FTO) substrates using the doctor blade technique.^{415, 422} Then, the newly formed films were annealed at 350 °C for 30 min in Argon atmosphere. For comparison, Au electrodes were

prepared by sputtering a thickness of ~ 50 nm film on the substrate (obtained from the sputtering calibration curve).

The QDSSC devices were fabricated by assembling the counter electrode, either gold or Cu_2Te in nanosheet (NS), nanotube (NT), or nanoparticle (NP) form (Cu_2Te -NS, Cu_2Te -NT, Cu_2Te -NP, and Au), and a QD-sensitized TiO_2 film photo-electrode with a binder clip separated by a $60 \mu\text{m}$ thick spacer. A metal mask with a window area of 0.16 cm^2 was clipped onto the TiO_2 side to define the active area of the cell when testing. The polysulfide electrolyte was composed of 2 M Na_2S , 2 M S, and 0.2 M KCl in Milli-Q water. For QDSSCs assembled under each set of conditions, at least 6 cells were prepared and tested in parallel, and average value was used as the final data. For electrochemical impedance spectroscopy (EIS) and Tafel-polarization measurements, symmetric dummy cells were assembled from two identical CEs, using the same polysulfide electrolyte. The active area of the dummy cells was 0.64 cm^2 .^{415, 422}

The photocurrent density-voltage (J-V) tests on the DSSCs were performed under the same sun conditions using an air mass (AM) 1.5 solar simulator (Oriel), which was carefully calibrated with certified silicon solar cells. The light intensity of the solar simulator was adjusted to $100 \text{ mW}\cdot\text{cm}^{-2}$ by using an optical power meter (Newport, 1918-c) with a detector (818P-040-25). J-V curves were obtained by applying an external bias to the cell, and measurements were recorded by a Keithley model 2420 digital source meter. The EIS data were measured with dummy cells using a Solartron 1260 Frequency Response Analyzer in combination with a Solartron 1480 Potentiostat in the dark. The applied bias voltage and AC amplitude were set at 0 V and 10 mV, respectively. The frequency ranged from 10^6 to 0.1 Hz. The Tafel-polarization measurements were recorded with a scan rate of $20 \text{ mV}\cdot\text{s}^{-1}$ on an electrochemical workstation (CHI660d). All the machines used for solar cells testing are shown in Figure 6.2.



Figure 6.2. Pictures of (a) solar simulator (Oriel); (b) Keithley model 2420 digital source meter; (c) Solartron 1260 Frequency Response Analyzer (upper) in combination with a Solartron 1480 Potentiostat (lower); (d) CHI660d electrochemical workstation.

6.3 Results and Discussion.

6.3.1 Reaction Mechanism.

The Cu_2Se precursor and final precipitates prepared from the schedule shown in Figure 6.1 were collected and characterized, respectively. Their morphologies were elucidated in Figure 6.3(a-i); and the compositions were verified by the XRD patterns shown in Figure 6.4, which can be unambiguously indexed to Cu_2Se (JCPDS 06-0680) and Cu_2Te (JCPDS 10-0421), respectively. As shown in Figure 6.3(a-c), Cu_2Se precursor is made up of uniform nanoparticles ranging from 10-20 nm in size, whose lattice and FFT pattern can be well indexed to be face-centered cubic (fcc) Cu_2Se . After being added into the Na_2Te solution and kept stationary for 30 min, the Cu_2Se nanoparticles are transformed into flower like nanosheets [Figure 6.3(d-e)]. The HRTEM and FFT images show a clear lattice of (220)

planes of Cu_2Te [Figure 6.3(f)], while rolled tubular nanostructures are observed if the turbid mixture of Cu_2Se and Te precursor is well stirred, as shown in Figure 6.3(g-i). This result demonstrates that Cu_2Te nanosheets and nanotubes can be effectively synthesized via a simple and fast anion exchange from Cu_2Se nanoparticles in aqueous solution at room temperature without any surfactants. The whole reaction procedure can be expressed by Equations (6.1)-(6.2).

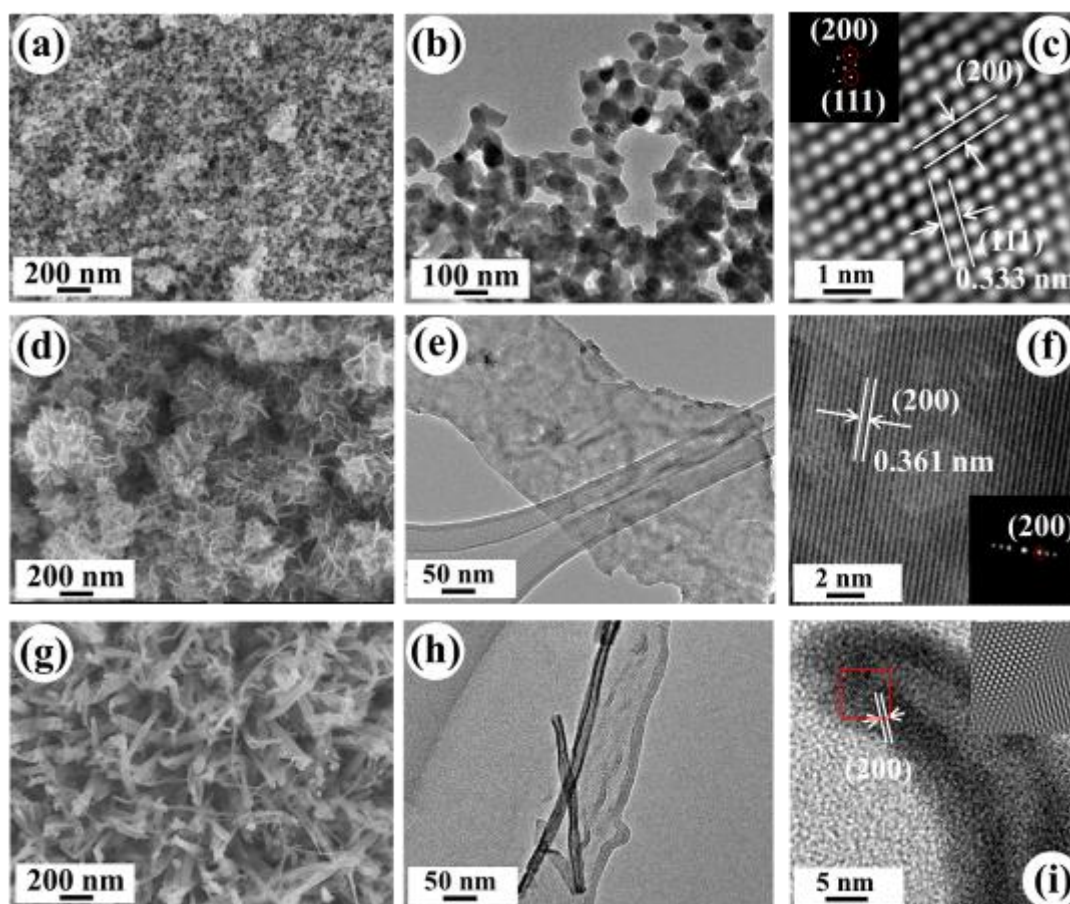
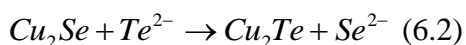


Figure 6.3. (a) SEM, (b) TEM, and (c) HRTEM images of Cu_2Se nanoparticle precursor; (d) SEM, (e) TEM, and (f) HRTEM images of the as-prepared Cu_2Te nanosheets; (g) SEM, (h) TEM, and (i) HRTEM images of Cu_2Te nanotubes. The insets to (c) and (f) are the

$$\Delta G = RT \times \ln \frac{J_{SP}}{K_{SP}} \quad (6.3)$$

$$J_{SP} = C^2(\text{Cu}^+) \times C(\text{Se}^{2-}) \quad (6.4)$$

The driving force of Equation (6.3) originates from the difference between the solubility (K_{sp}) of Cu_2Se and Cu_2Te in aqueous solution.^{269, 409, 410, 423} Although the solubility of Cu_2Te is unavailable, according to the literature,²⁶⁸ the solubility of metal chalcogenides always decrease with increasing ionic radius of the chalcogen element, i.e., $K_{sp}(\text{Cu}_2\text{O}) > K_{sp}(\text{Cu}_2\text{S}) > K_{sp}(\text{Cu}_2\text{Se}) > K_{sp}(\text{Cu}_2\text{Te})$ (Table 6.1); and we can infer that the driving force for the conversion from Cu_2E (E=O, S, Se) to Cu_2Te has the same tendency, e.g. $\text{Cu}_2\text{O} > \text{Cu}_2\text{S} > \text{Cu}_2\text{Se}$. The inference that transfer reactions from $\text{Cu}_2\text{O}/\text{Cu}_2\text{S}/\text{Cu}_2\text{Se}$ to Cu_2Te are all energy favorable has been confirmed by the results shown in Figure 6.5. In addition, because the structure of Cu_2Se (fcc) is totally different from the hexagonal structure of Cu_2Te , the derived energy differences, as well as the surface energy changes, play a pivotal role in the activation barrier of the transfer reaction (Table 6.1).

Table 6.1. Some physical-chemical parameters of cuprous chalcogenides.

Material	$-\lg(K_{sp})$	JCPDS card number	Crystal structure	Molecular number in each unit cell	Volume of unit cell (\AA^3)
Cu_2O	15	05-0667	Cubic Pn-3m (224)	2	77.85
Cu_2S	48	26-1116	Hexagonal P63/mmc(194)	2	91.47
Cu_2Se	61	06-0680	Cubic F-43m(216)	4	189.02
Cu_2Te	-	10-0421	Hexagonal P3m1(156)	24	1307.13

To investigate the transfer procedure from Cu_2Se nanoparticles to Cu_2Te nanosheets, a series of control experiments were conducted, and the detailed parameters are listed in Table 6.2. In

the first group of experiments (Group E1), the reaction was slowed down by an ice bath and diluting the Te precursor to 0.01 M. After the addition of Cu_2Se precursor for 2 min, 5 min,

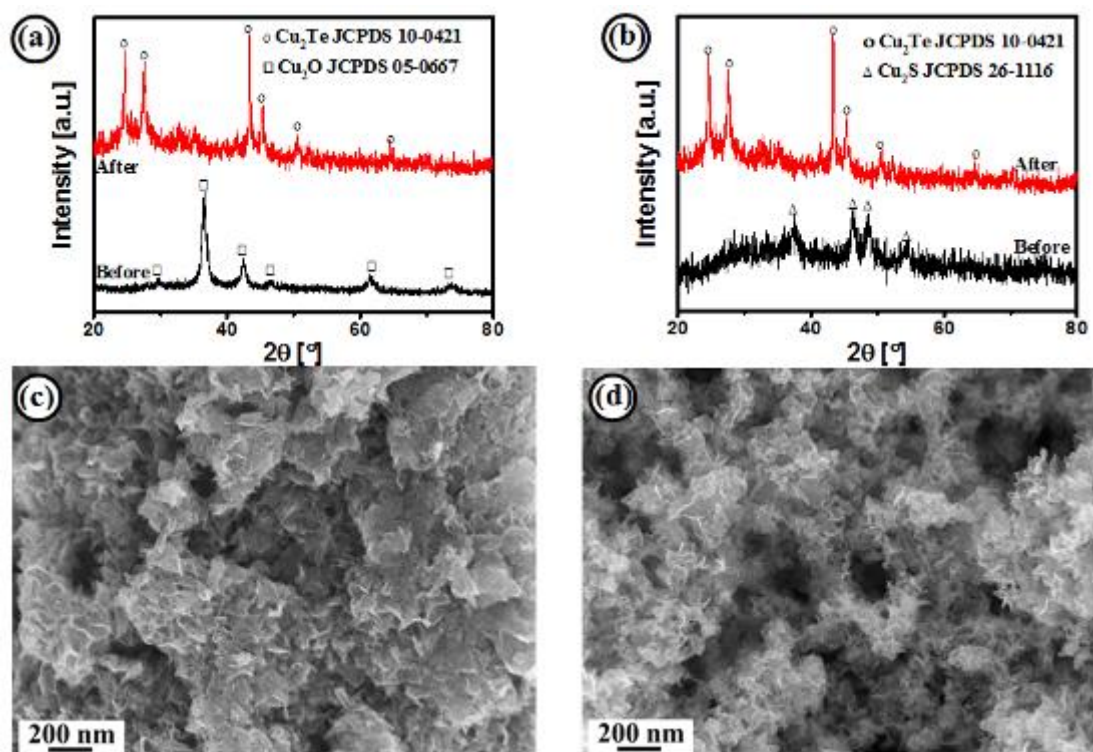


Figure 6.5. XRD patterns of Cu_2Te transferred from (a) Cu_2O and (b) Cu_2S in comparison with that of precursors. SEM images of the Cu_2Te nanosheets transferred from (c) Cu_2O and (d) Cu_2S .

Table 6.2. Reaction parameters for preparation of Cu_2Te nanostructures.

Group	Number	$\text{Cu}_2\text{Se}:\text{Te}$ (molar ratio)	Size of Cu_2Se (nm)	Concentration of Na_2Te (mol/L)	$\text{NaBH}_4:\text{Te}$ (Molar ratio)	Stirring speed (rpm)	Reaction time (min)
E1	E1-1	1:1	11.9	0.01	80:1	-	2
	E1-2	1:1	11.9	0.01	80:1	-	10
	E1-3	1:1	11.9	0.01	80:1	-	20
	E1-4	1:1	11.9	0.01	80:1	-	30
E2	E2-1	20:1	25.5	0.01	80:1	-	30
	E2-2	10:1	25.5	0.01	80:1	-	30
	E2-3	5:1	25.5	0.01	80:1	-	30
	E2-4	2:1	25.5	0.01	80:1	-	30
E3	E3-1	1:1	15.0	0.1	80:1	-	30
	E3-2	1:1	15.0	0.05	80:1	-	30

	E3-3	1:1	15.0	0.02	80:1	-	30
	E3-4	1:1	15.0	0.01	80:1	-	30
E4	E4-1	1:1	11.9	0.1	9:1	-	30
	E4-2	1:1	15.0	0.1	9:1	-	30
	E4-3	1:1	22.5	0.1	9:1	-	30
	E4-4	1:1	25.5	0.1	9:1	-	30
E5	E5-1	1:1	22.5	0.1	9:1	-	30
	E5-2	1:1	22.5	0.1	18:1	-	30
	E5-3	1:1	22.5	0.1	36:1	-	30
	E5-4	1:1	22.5	0.1	80:1	-	30
E6	E6-1	1:1	11.9	0.01	80:1	100	30
	E6-2	1:1	11.9	0.01	80:1	300	30
	E6-3	1:1	11.9	0.01	80:1	800	30
	E6-4	1:1	11.9	0.01	80:1	1000	30

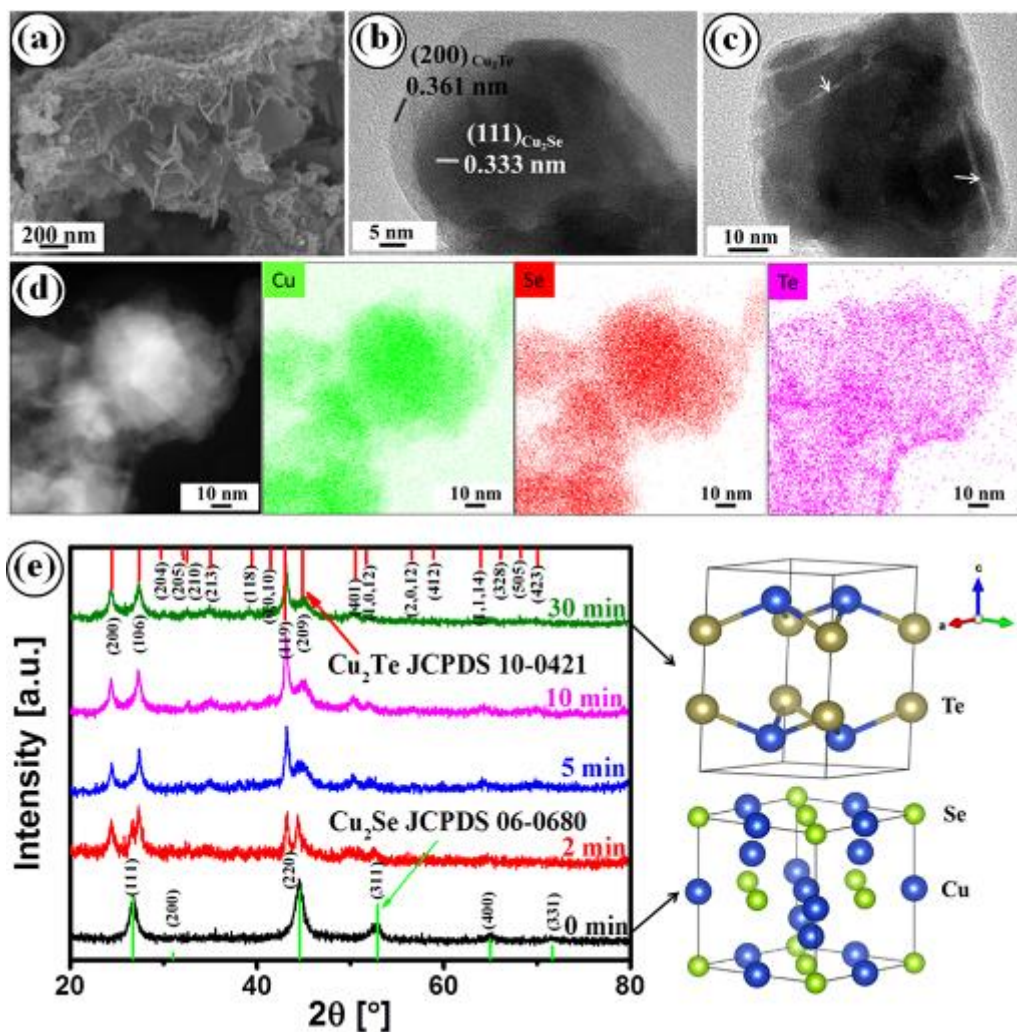


Figure 6.6. (a-c) SEM and TEM images of the precipitate after reaction of 2 min (d) EDS mapping of the precipitate after reaction of 2 min; (e) XRD patterns of the precipitates

obtained from different reaction times; right side shows crystal structures of hexagonal Cu_2Te (top) and fcc Cu_2Se (bottom), respectively.

10 min, and 30 min, respectively, some of the turbid suspension was taken out, and water was immediately removed by a suction filter to stop the reaction. The precipitate was then characterized after being washed several times with absolute ethanol. Figure 6.6(a) shows a typical SEM image of the sample taken out after 2 min: both nanoparticles and nanosheets can be identified. Figure 6.6(b-c) shows the typical TEM images of this sample. A core-shell structure is clearly observed in Figure 6.6(b), the planar spacing of the inner darker part (core) is 0.333 nm, which can be indexed to the (111) planes of fcc Cu_2Se . The outer layered fringe shows a planar spacing of 0.361 nm, which coincides with the (200) planes of hexagonal Cu_2Te . Thus, Cu_2Se nanoparticles are wrapped by thin Cu_2Te layers to form core-shell $\text{Cu}_2\text{Se}@ \text{Cu}_2\text{Te}$ structure after reaction of 2 min. The composition of a similar structure was further identified by EDS mapping conducted on a JOEL ARM-200F [Figure 6.6(d)], and the results show that the Se element is mainly distributed in the inner bright part, while the Te element covers the whole area, supporting that Cu_2Se was wrapped by Cu_2Te . In addition, obvious cracks (marked by white arrows) are observed in some particles as displayed in Figure 6.6(c). The X-ray diffraction patterns of the samples taken out after different reaction times are presented in Figure 6.6(e). In accordance with the SEM and TEM results, after 2 min reaction, the diffraction peaks of both hexagonal Cu_2Te (JCPDS 10-0421) and fcc Cu_2Se (JCPDS 06-0680) are detected; while after 5 min, the transfer reaction from Cu_2Se to Cu_2Te is almost completed, as indicated by vanishing of the Cu_2Se peaks (JCPDS 06-0680). The XPS results presented in Figure 6.7 are consistent with the XRD results. From comparison of the peaks of our samples with the literature,^{351, 424} it is easy to identify that before the reaction starts (0 min), the composition of the precursor is pure Cu_2Se .⁴²⁴ After 2 min reaction, the Se^{2-} peaks are still observed with appearance of Te peaks. The peaks at 571.9 eV and 582.5

eV can be assigned to the peaks of Te^{2-} ; while the other two peaks located at 575.4 eV and 585.8 eV are the peaks from oxidation of the sample.³⁵¹ After reacting for 30 min, the peak of Se totally disappears, and the composition of the final product becomes pure Cu_2Te . As mentioned previously, the crystal structure of product Cu_2Te (JCPDS 10-0421) is different to that of Cu_2Se precursor (JCPDS 06-0680). Cu_2Te shows an obvious layered structure in Figure 6.6(e), and the calculated volume expansion ($\Delta V/V_{\text{Cu}_2\text{Se}}$) for Cu_2Se converted into Cu_2Te is as high as 91.53 % (Table 6.1) for each Cu_2Se unit cell.

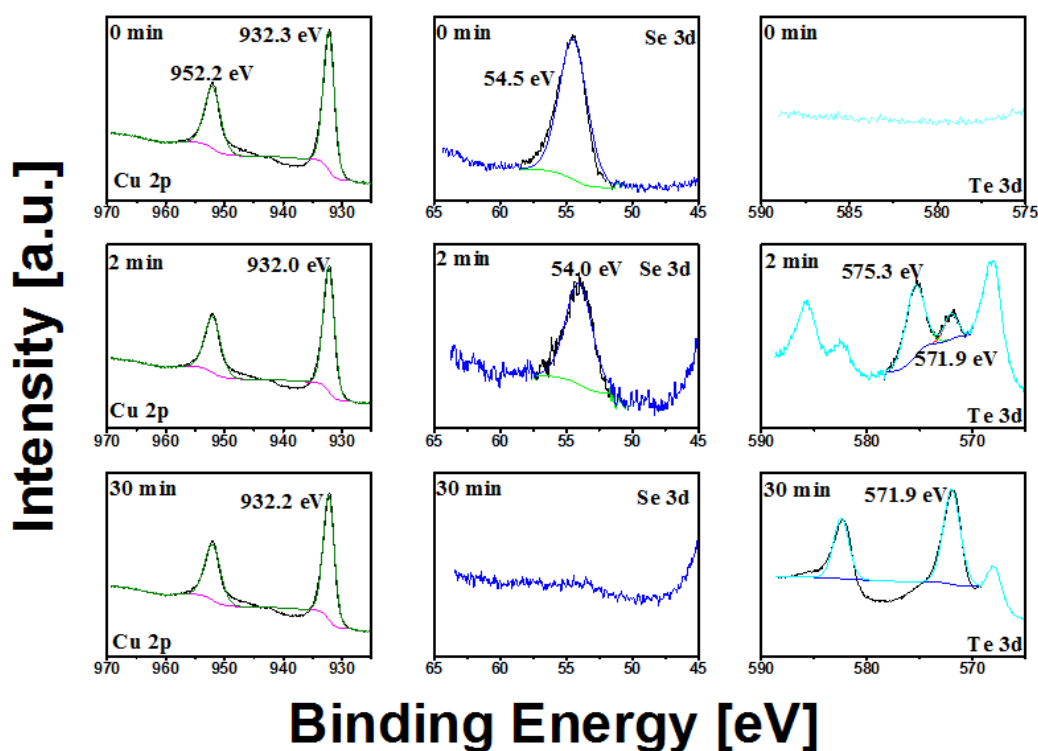


Figure 6.7. XPS spectra of Cu_2Se nanoparticle precursor and the precipitates taken out after reaction of 2 min and 30 min, respectively.

To further clarify the evolution mechanism, another group of control experiments was conducted (Group E2 in Table 6.2). The molar ratio between the Cu_2Se precursor and Te was varied from 20:1 to 2:1, and the thickness of the Cu_2Te layers wrapped around Cu_2Se nanoparticles was investigated by TEM. The results are presented in Figure 6.8(a-d). It is

obvious that there are both uniform and continuous wrapping layers outside the particles; and the lattice spacing of the inner and outer parts can be indexed to (111) of Cu_2Se and (200) of Cu_2Te , respectively.

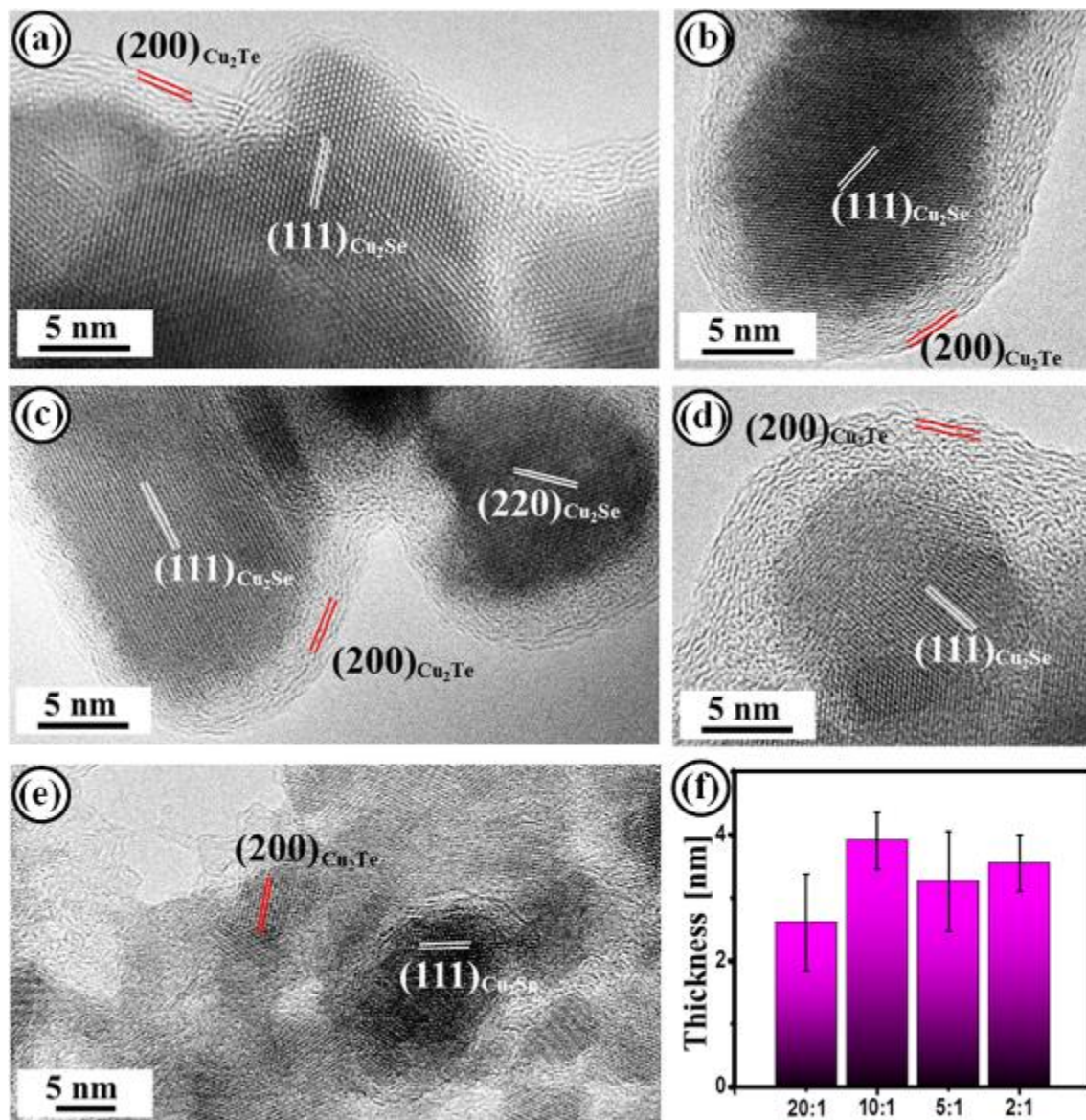


Figure 6.8. HRTEM images of the samples obtained from different mole ratios of $\text{Cu}_2\text{Se}:\text{Te}$ equal to (a) 20:1; (b) 10:1; (c) 5:1; and (d) 2:1. (e) Hybrid structure consisting of sheets and nanoparticles in the sample obtained from a ratio of 10:1. (f) Statistical thickness of Cu_2Te layers in (a-d).

Meanwhile, a hybrid structure consisting of nanosheets and nanoparticles can be easily detected in the sample obtained from a ratio of 10:1, as shown in Figure 6.8(e). The statistics on the thickness of outer layers are presented in Figure 6.8(f), which does not monotonically increase with decreasing Cu_2Se to Te ratio; instead, the thickness of Cu_2Te layer first increases from 2.61 ± 0.77 nm to 3.91 ± 0.45 nm, then decreases to 3.26 ± 0.79 nm, and finally increases again to 3.55 ± 0.44 nm. Combining the cracks shown in Figure 6.6(c) and the hybrid structure presented in Figure 6.8(e), we can deduce that a peeling of the Cu_2Te layers occurred when their thickness beyond 4 nm.

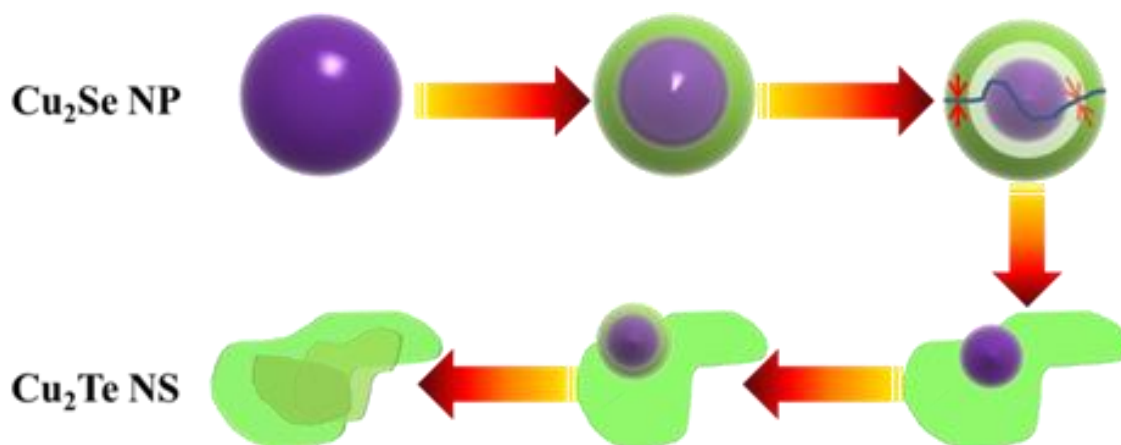


Figure 6.9. Schematic illustration of the transfer reaction from Cu_2Se nanoparticles to Cu_2Te nanosheets.

Based on the above results, the transfer procedure from Cu_2Se nanoparticles to Cu_2Te nanosheets can be schematically illustrated in Figure 6.9. When Cu_2Se nanoparticles are added into the Te^{2-} solution, the Cu^+ ions on particle surface react with Te^{2-} ions immediately to form a layer of hexagonal Cu_2Te , due to the lower solubility of Cu_2Te than Cu_2Se . With the formation of Cu_2Te layer, the Cu^+ ions diffusing outwards and the Te^{2-} ions diffusing inwards react at the interface between core and shell to form new Cu_2Te and increase the thickness of Cu_2Te layer. Benefiting from the large volume expansion [Table 6.1, $\Delta V/V_{\text{Cu}_2\text{Se}} = 91.53\%$] between fcc Cu_2Se and hexagonal Cu_2Te , tension and defects accumulate with the growth of the Cu_2Te layer, finally leading to peeling of Cu_2Te from Cu_2Se .²⁶⁸ As long as the

mass transport between Cu_2Se and Cu_2Te exists, the growth and peeling of Cu_2Te would continue until Cu_2Se is completely converted. The peeled Cu_2Te layers can grow into large nanosheets because of unique layered structure of Cu_2Te [Figure 6.6(e)]. As shown in Figure 6.3(g-i), the obtained Cu_2Te nanosheets could be further rolled into Cu_2Te nanotubes through the effects of continuous stirring and tension (including both surface tension of the nanosheets and tension in the crystals). The conversion process can be summarized into two steps. The first step is a diffusion process related Kirkendall effect to form Cu_2Te shell, which is similar to the transfer reactions between Cu_2E ($\text{E} = \text{O}, \text{S}, \text{Se}$) compounds;⁴²⁵⁻⁴²⁷ the second step is the peeling and continued growth of the Cu_2Te layer into nanosheets as proved by Figure 6.6(c) and Figure 6.8.

Similarly, Cu_2O and Cu_2S nanoparticles can be converted into Cu_2Te nanosheets. The volume changes between Cu_2O , Cu_2S , and Cu_2Te reach 479 % and 229 %, respectively (Table 6.1). Due to the pronounced differences in their K_{sp} (Table 6.1), the conversion of Cu_2O and Cu_2S nanoparticles into Cu_2Te nanosheets is easier than the conversion of Cu_2Se nanoparticles. On the contrary, compared with conversion of Cu_2E ($\text{E} = \text{O}, \text{S}, \text{Se}$) into Cu_2Te , the volume expansions between them (i.e. Cu_2O and Cu_2S , Cu_2O and Cu_2Se , and Cu_2S and Cu_2Se) are much less and reach 17.5 %, 42.8 %, and 6.6 %, respectively. Therefore, the anion exchange between Cu_2E ($\text{E} = \text{O}, \text{S}, \text{Se}$) nanoparticles can preserve the original morphology and can be simply explained by the Kirkendall effect.⁴²⁵⁻⁴²⁷

6.3.2 Morphology Control by Adjusting Reaction Parameters.

Another group of control experiments (Group E3 in Table 6.2,) were conducted to verify the effects of the Te^{2-} concentration on the thickness of the Cu_2Te nanosheets. As illustrated by the SEM images of samples shown in Figure 6.10(a-d), the concentration of Te^{2-} had a significant impact on the morphology of the final Cu_2Te . When the concentration of Te^{2-} de-

creased from 0.1 M to 0.05 M, 0.02 M, and 0.01 M, the thickness of the Cu_2Te nanosheets obviously decreased, and they became more and more flexible. The Cu_2Te nanosheets also became smaller and more inhomogeneous. This phenomenon could be well explained by the formation mechanism of the nanosheets (Figure 6.9). When the concentration of Te^{2-} is higher (e.g. 0.1 M), a thicker initial Cu_2Te layer formed in a very short time, which could yield a homogeneous large and thick nanosheets [Figure 6.10(a)]. On the contrary, if the concentration of Te^{2-} is lower, a thinner Cu_2Te layer is formed at the initial stage; while multi peeling from nanoparticles leads to smaller and inhomogeneous nanosheets [Figure 6.10(b-d)].

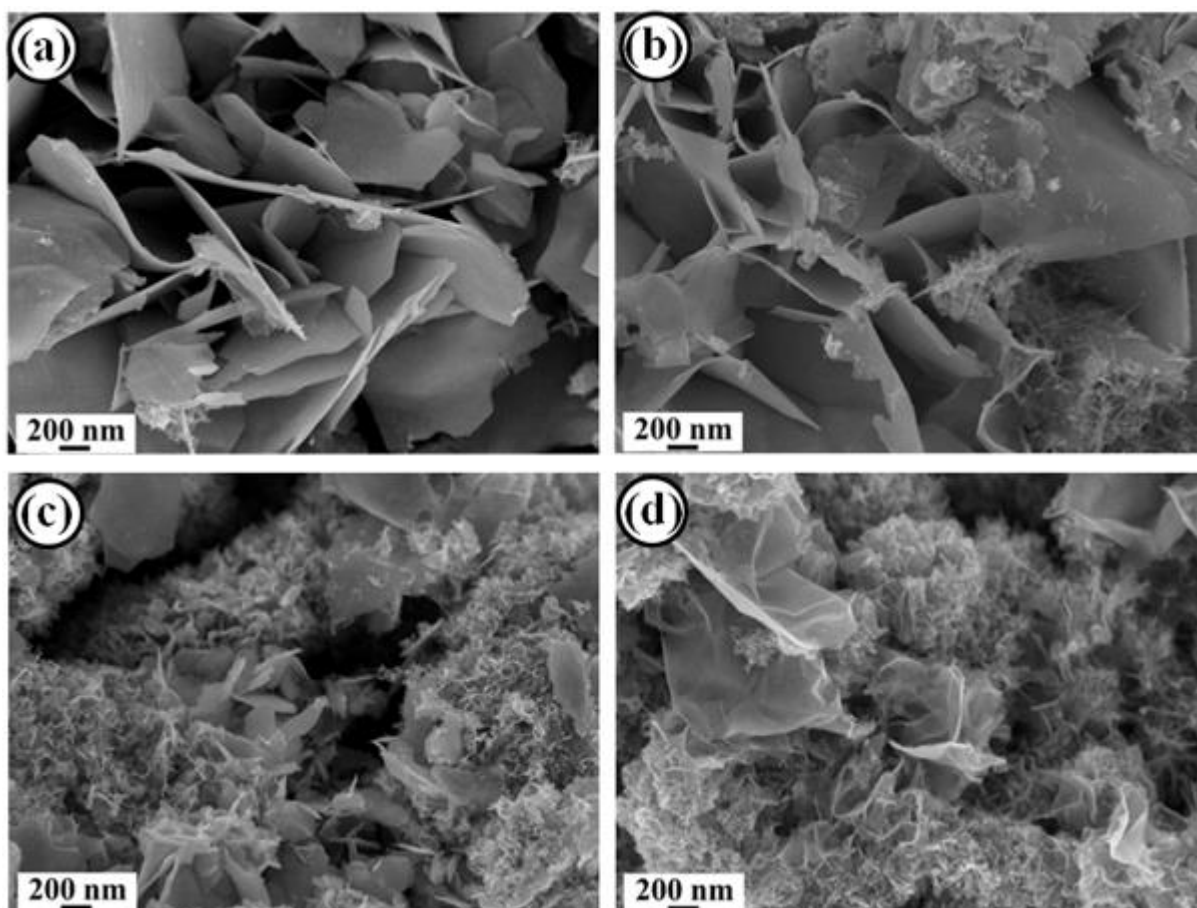


Figure 6.10. SEM images of Cu_2Te nanosheets prepared from different concentrations of Na_2Te : (a) 0.1 M; (b) 0.05 M; (c) 0.02 M; (d) 0.01 M.

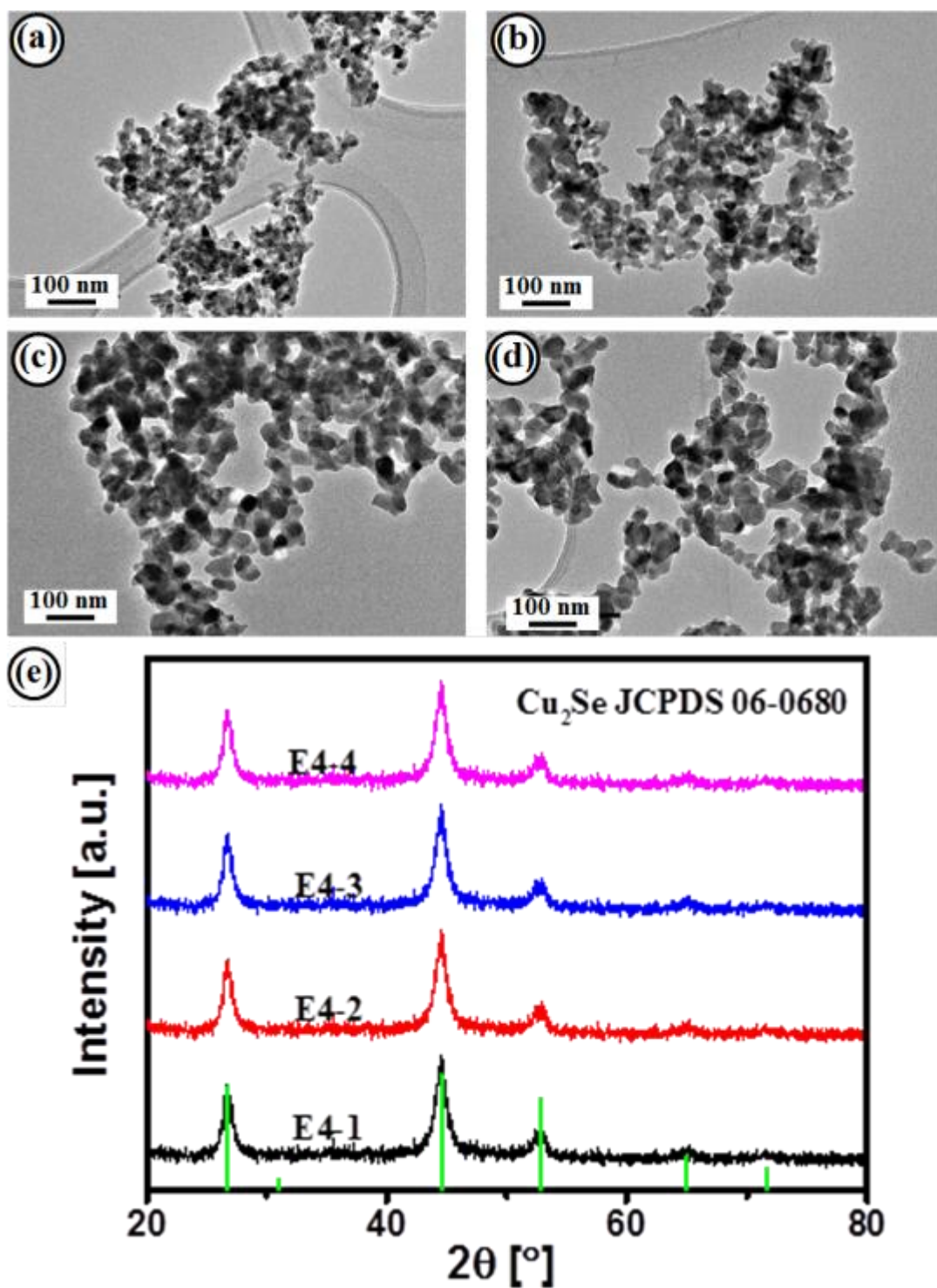


Figure 6.11. TEM images of different sized Cu_2Se nanoparticle precursors used in the experiments: (a) E4-1; (b) E4-2; (c) E4-3; (d) E4-4. (e) XRD results of E4-1 to E4-4.

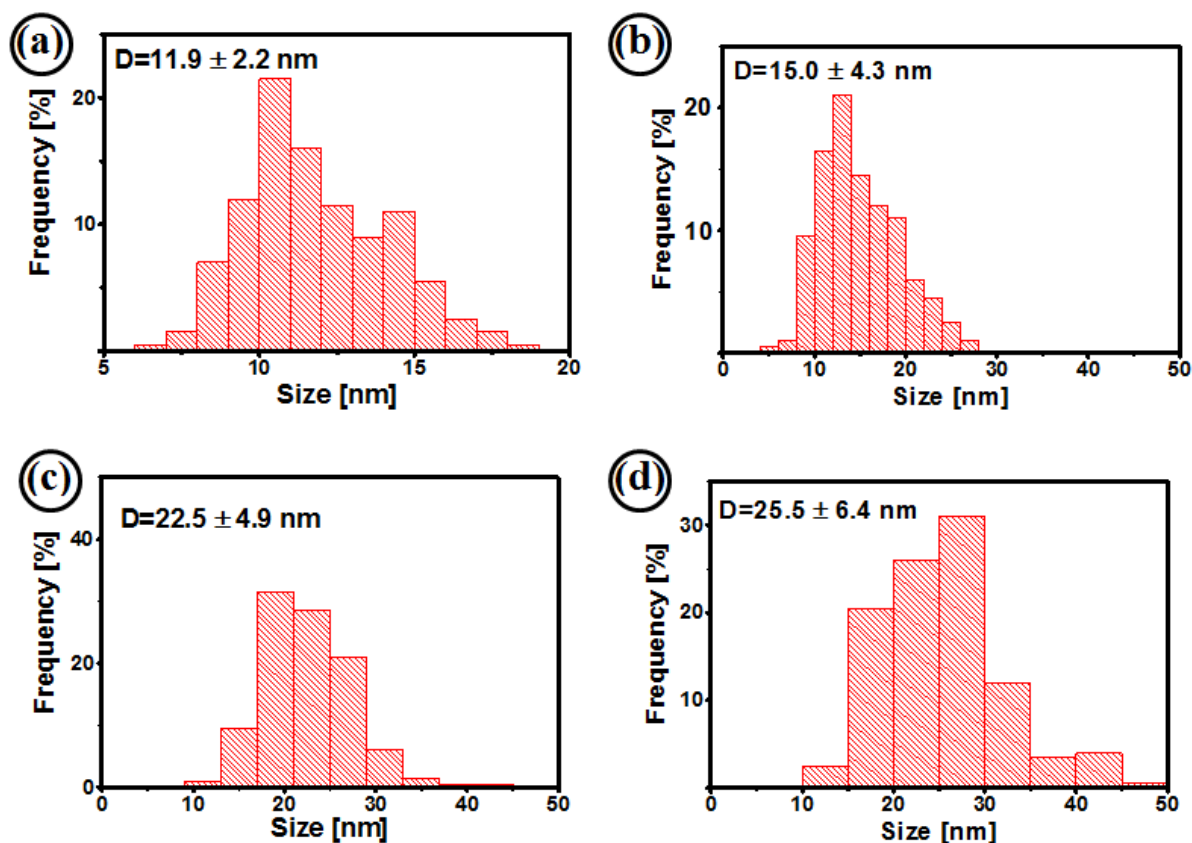


Figure 6.12. Size distributions of Cu_2Se nanoparticles used in the experiments: (a) E4-1; (b) E4-2; (c) E4-3; (d) E4-4.

As the transfer reaction [Equation (6.2)] is a solid-solution reaction, the size of Cu_2Se nanoparticle precursor also plays an important role in the morphologies of Cu_2Te nanosheets. To investigate this effect, we first synthesized four batches of Cu_2Se nanoparticles [Group E4 in Table 6.2,] with different sizes according to the literature.⁴²⁴ The TEM images, XRD patterns, and size distributions of the four Cu_2Se precursors are respectively presented from Figure 6.11 to Figure 6.12. The morphologies of thus-formed Cu_2Te nanosheets are presented in Figure 6.13, in which is hard to see any difference. To reveal the impact, the thickness of Cu_2Te nanosheets fabricated from different Cu_2Se precursors was determined by AFM [Figure 6.14(a-d)]. With increasing size of the Cu_2Se precursor, the average thickness measured from tens pieces of Cu_2Te nanosheets are 4.2 ± 0.7 nm, 3.7 ± 0.5 nm, 4.3 ± 0.9 nm, and 3.2 ± 0.4 nm for E4-1 to E4-4, respectively. The thickness of Cu_2Te nanosheets varied

slightly. The surface area of Cu_2Se nanoparticles and Cu_2Te nanosheets were analyzed by BET analysis, and the results are plotted in Figure 6.14(e). With increasing Cu_2Se nanoparticle size from 11.9 nm to 25.5 nm, its specific surface area decreased from $38.4 \text{ m}^2/\text{g}$ to $21.2 \text{ m}^2/\text{g}$. After being transformed into Cu_2Te nanosheets, the specific area increased to a different extent. For example, the maximum ratio appeared in Cu_2Se nanoparticles with a size of 25.5 nm (E4-4), and the specific surface area increased from $21.2 \text{ m}^2/\text{g}$ to $32.8 \text{ m}^2/\text{g}$, while in the case of 22.5 nm Cu_2Se (E4-3), the specific surface area increased slightly from $22.4 \text{ m}^2/\text{g}$ to $23.5 \text{ m}^2/\text{g}$.

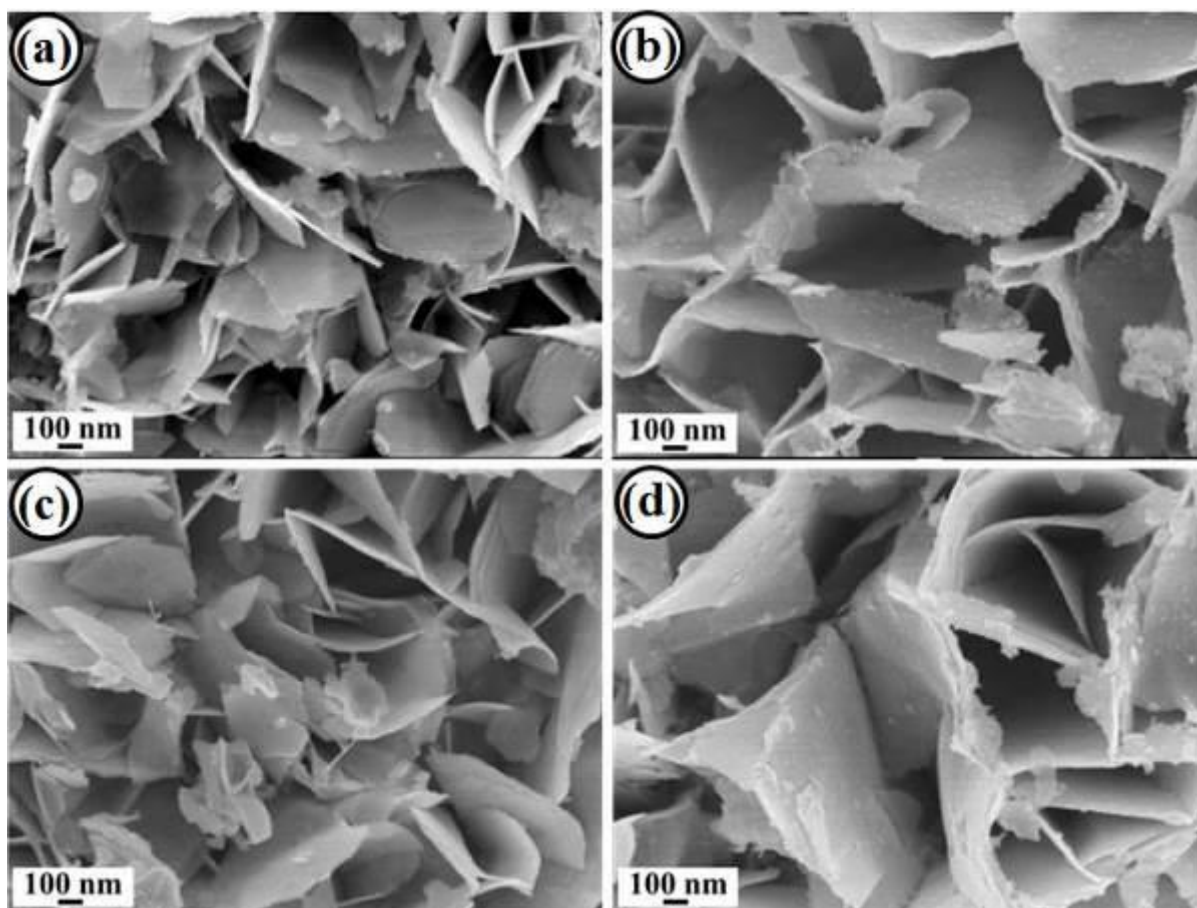


Figure 6.13. SEM images of Cu_2Te nanosheets fabricated from different sized Cu_2Se precursors. (a) E4-1; (b) E4-2; (c) E4-3; (d) E4-4.

Another factor influencing the morphology of the final product is the amount of NaBH_4 . When the mole ratio between NaBH_4 and Te is raised from 9:1 to 18:1, 36:1, and 80:1

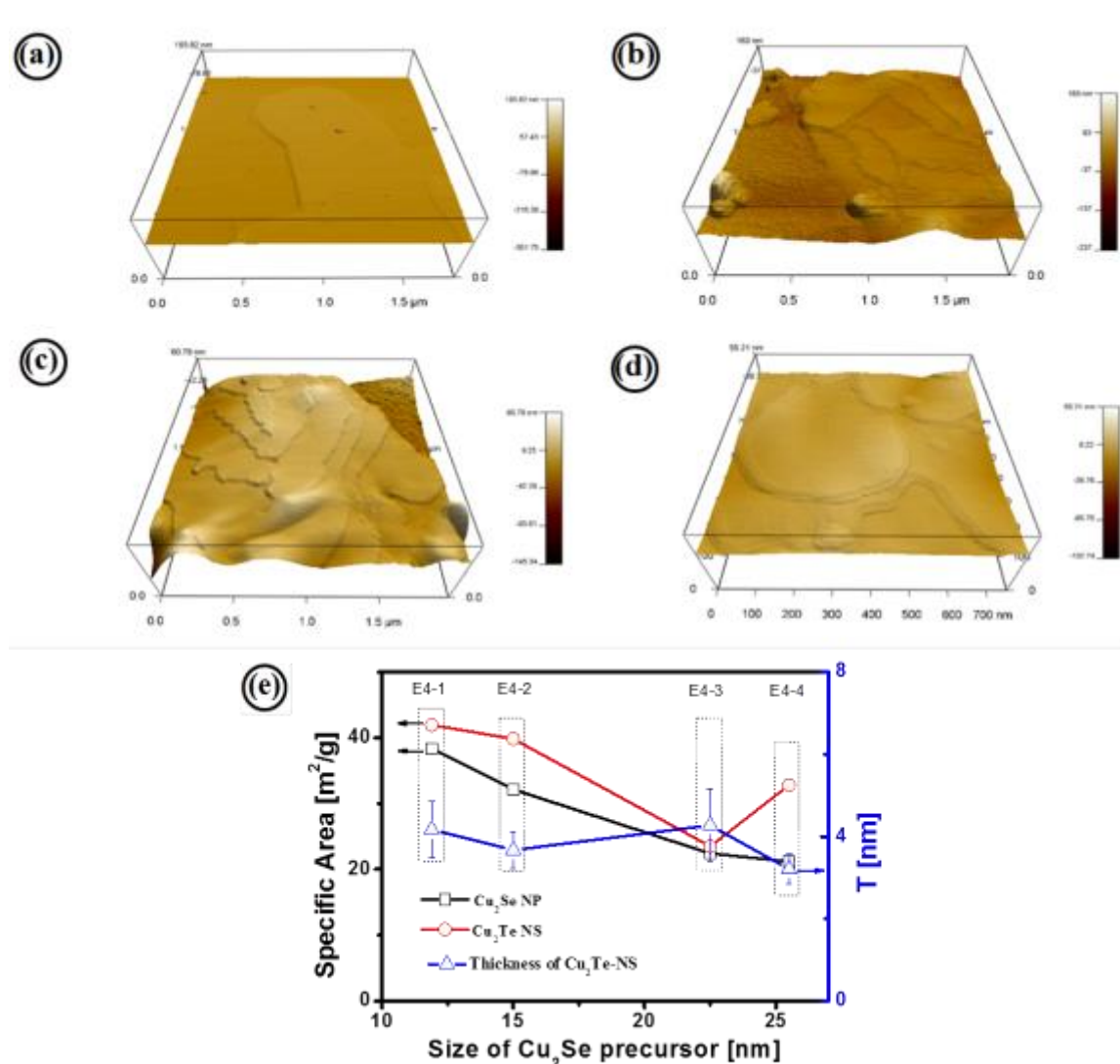


Figure 6.14. 3D AFM images of Cu_2Te nanosheets fabricated from different sized Cu_2Se precursors. (a) E4-1; (b) E4-2; (c) E4-3; (d) E4-4. (e) The effect of Cu_2Se nanoparticle size on the specific surface area and thickness of E4-1, E4-2, E4-3 and E4-4 Cu_2Te nanosheets.

[Group E5 in Table 6.2], we can conclude from Figure 6.15 that the thickness of the Cu_2Te nanosheets increases. This result is related to the property of Se^{2-} , which is very easy to hydrolyze in aqueous solution [Equation (6.5)],⁴²⁸⁻⁴³⁰ while the addition of NaBH_4 will lead to an increased pH value due to the formation of NaBO_2 [Equation (6.6)-(6.7)].⁴²⁴ Although Te^{2-} could also hydrolyze into HTe^- as shown in Equation (6.8), the hydrolysis is much

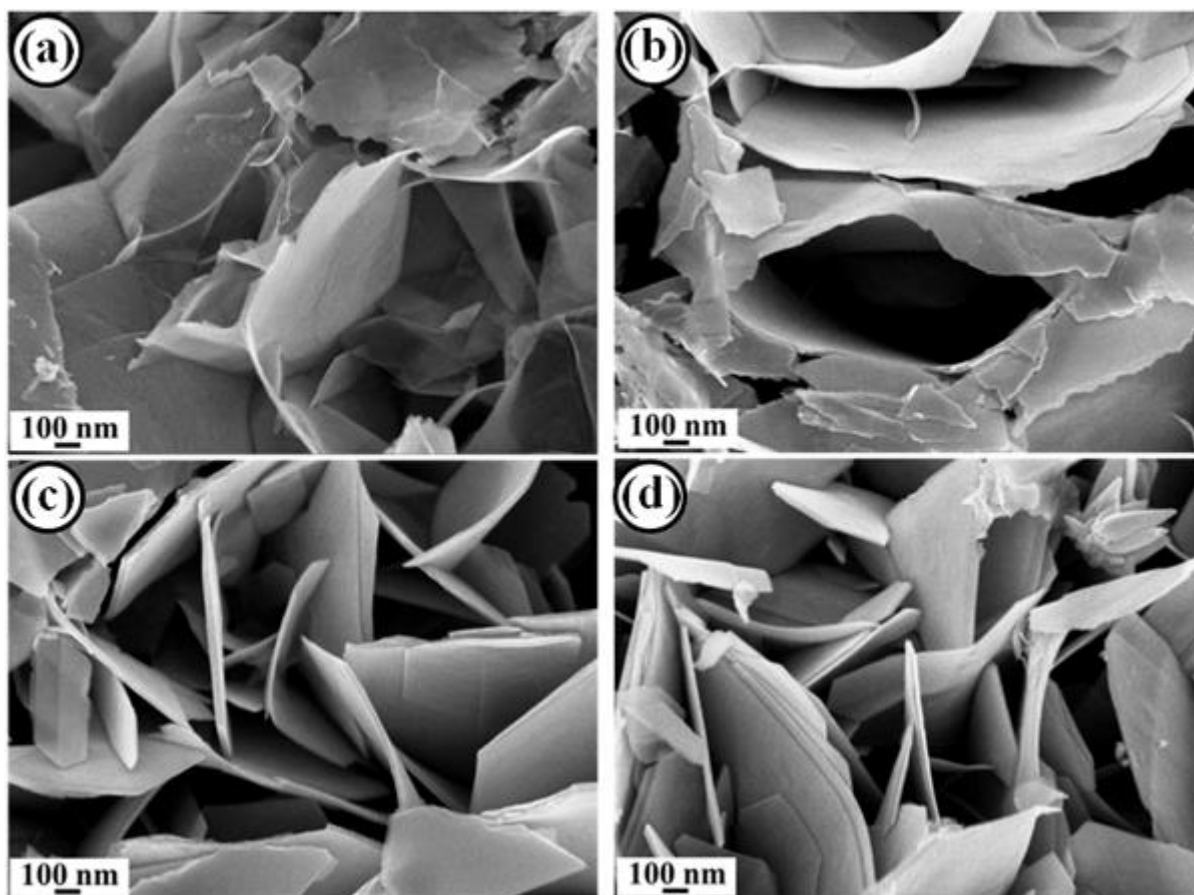
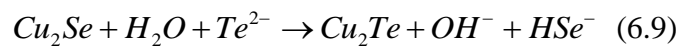
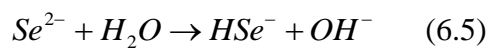


Figure 6.15. Cu_2Te nanosheets prepared with different mole ratios of $NaBH_4$ to Te . (a) 9:1; (b) 18:1; (c) 36:1; (d) 80:1.

weaker than Se^{2-} as $pK_b(HSe^-)=10.2 < pK_b(HTe^-)=11.4$. As a result, the increase of solution pH would suppress the conversion of Cu_2Se according to Equation (6.9), leading to slow growth and less defects of Cu_2Te nanosheets.



As seen from Figure 6.3(h), the Cu_2Te nanotubes are generated by rolling of the formed Cu_2Te nanosheets with assistance of stirring, the effect of stirring speed on the properties of nanotubes was investigated, and the detailed experimental conditions are presented in Table 6.2 (Group E6). As shown in Figure 6.16, the length of the rolled nanotubes gradually decreased with the stirring speed increasing from 100 rpm to 1000 rpm.

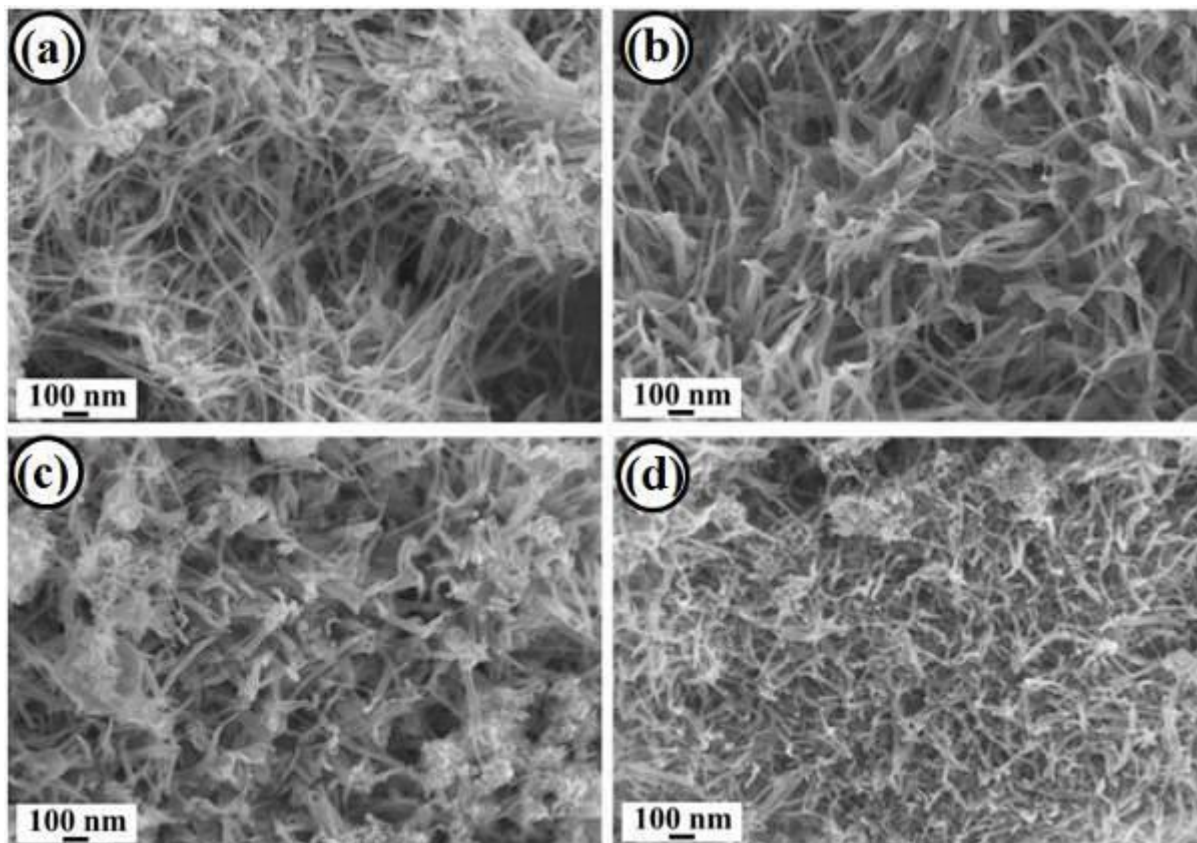


Figure 6.16. SEM images of Cu_2Te nanotubes synthesized with different stirring speeds: (a) 100 rpm; (b) 300 rpm; (c) 800 rpm; (d) 1000 rpm.

6.3.3 Performance of Different Cu_2Te nanostructures as Counter Electrodes of QDSSCs.

To test the potential application of obtained Cu_2Te nanosheets (Table 6.2, E1-4) and nanotubes (Table 6.2, E6-1) as counter electrodes [Figure 6.17(a)] in solar cells, CdS/CdSe

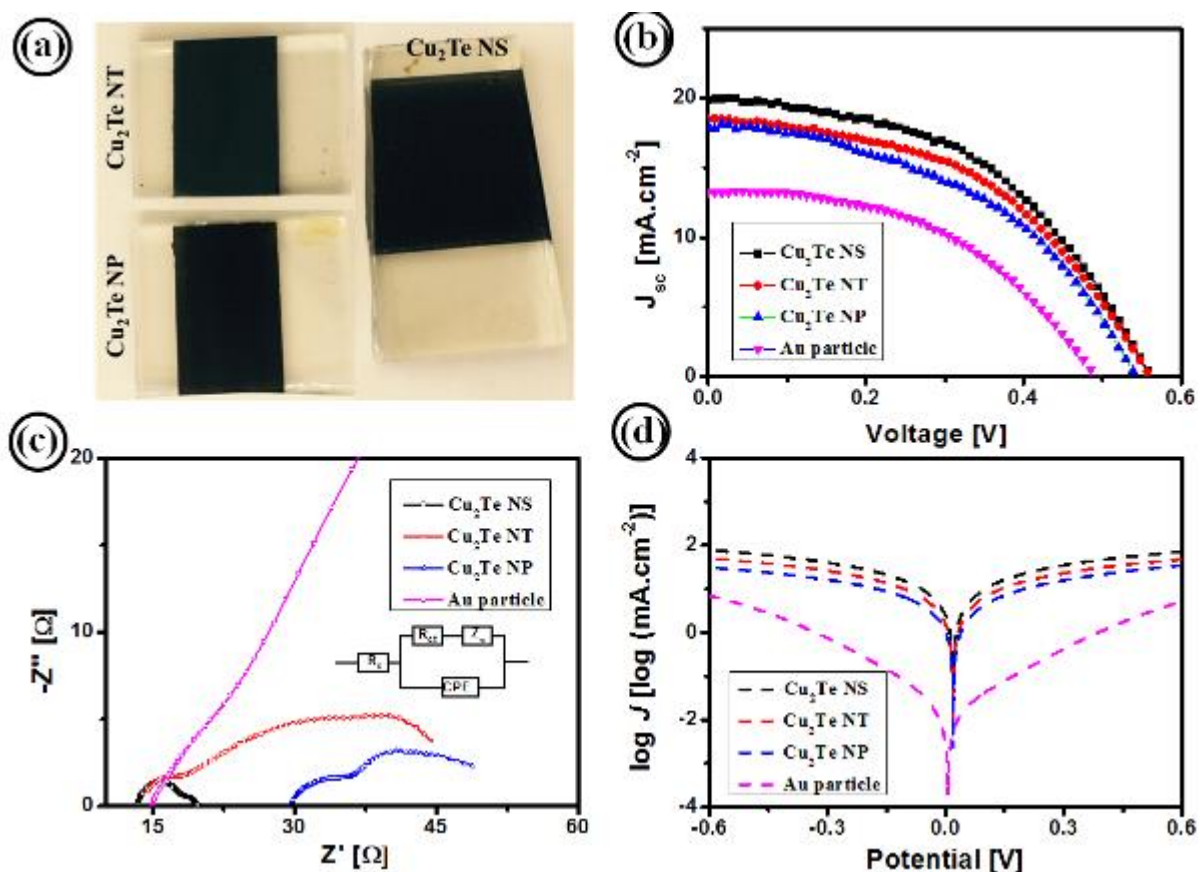


Figure 6.17. (a) Photograph of the assembled Cu_2Te CEs; (b) J-V curves for the different CEs; (c) electrochemical impedance spectra for the CEs, with the inset showing the equivalent circuit; (d) Tafel-polarization curves for the CEs.

Table 6.3. Photovoltaic performance^{a)} of QDSSCs with different CEs and EIS parameters^{b)} in cells assembled with the same CdS/CdSe QD working electrodes.

Sample	J_{sc} ($\text{mA}\cdot\text{cm}^{-2}$)	V_{oc} (Voltage)	Fill Factor	η (%)	R_s (Ω)	R_{ct} (Ω)	Z_w (Ω)
Cu_2Te NS	19.87	0.57	0.472	5.35	13.21	5.08	3.9
Cu_2Te NT	18.49	0.56	0.476	4.75	13.73	5.93	33.2
Cu_2Te NP	18.13	0.546	0.452	4.47	29.24	8.41	23.0
Au	13.20	0.492	0.486	3.16	14.97	46.25	73.4

^{a)} J_{sc} : Short-circuit current; V_{oc} : Open-circuit voltage; η : Energy conversion efficiency; ^{b)} R_s : Series resistance, R_{ct} : Charge transfer resistance at the CE/electrolyte interface; Z_w : Warburg impedance.

co-sensitized solar cells were assembled. Cu_2Te nanoparticle based counter electrodes were also prepared to investigate the effects of morphology on performance. The preparation and characterizations of Cu_2Te nanoparticles are detailed in Chapter 4 (Table 4.2 and Figure 4.7). As a reference, an Au film counter electrode was also fabricated. The photocurrent density-voltage (J–V) curves of the 4 CEs (Cu_2Te -NS CE, Cu_2Te -NT CE, Cu_2Te -NP CE, and Au CE) under standard simulated AM 1.5 illumination are shown in Figure 6.17(b). The corresponding photovoltaic performance parameters are summarized in Table 6.3. The Cu_2Te -NS CE shows the highest short-circuit current of $19.87 \text{ mA}\cdot\text{cm}^{-2}$, with open-circuit voltage (V_{oc}) of 0.57 V, and fill factor (FF) of 0.472, yielding the highest power conversion efficiency (PCE, η) of 5.35 %. The Cu_2Te -NT CE exhibits a conversion efficiency of 4.75 %, a lower J_{sc} ($18.49 \text{ mA}\cdot\text{cm}^{-2}$) and V_{oc} (0.56 V) compared with Cu_2Te -NS CE, despite its slightly higher FF of 0.476. The performance of Cu_2Te -NP CE is inferior to that of the Cu_2Te -NT sample due to its smaller J_{sc} ($18.13 \text{ mA}\cdot\text{cm}^{-2}$), V_{oc} (0.546 V), and fill factor (0.452). The Au CE presents the lowest J_{sc} ($13.20 \text{ mA}\cdot\text{cm}^{-2}$) and V_{oc} (0.486 V), but the highest fill factor (0.492) among the 4 CEs, respectively. The conversion efficiency of solar cells made with Au CE only reaches 3.16 %, which is obviously lower than that of solar cells with Cu_2Te CEs. It is safe for us to conclude that our low-cost Cu_2Te CEs yield better performance than noble Au CEs. It is also clear that the morphology of Cu_2Te influenced the performance of solar cells.

To further clarify the electrochemical characteristics of various Cu_2Te -based CEs in catalyzing the redox couple of the electrolyte (S^{2-}/S_n^{2-}), electrochemical impedance spectroscopy [EIS, Figure 6.17(c)] and Tafel-polarization measurements [Figure 6.17(d)] were carried out. The Nyquist plots for the dummy cells with different CEs plotted in Figure 6.17(c) with the equivalent circuit are used to interpret the spectra. The impedance spectra of the CEs can be modelled by several circuit elements, such as for series resistance (R_s), charge

transfer resistance (R_{ct}), and Warburg diffusion impedance (Z_W). The value of R_s can be evaluated from the high-frequency intercept on the real axis, which comprises the bulk resistance of the CE material, the resistance of the substrate, and the contact resistance. The R_{ct} can be obtained by fitting the arc in the middle-frequency region, which corresponds to the charge-transfer process at the CE/electrolyte interface. This value is a direct indicator of catalytic activity. The arc in the low-frequency range indicates Z_W , which arises from diffusion of the electrolyte.^{411, 415, 431} All these parameters were determined by fitting the impedance spectra using the Z-view software and are summarized in Table 6.3.

As enumerated in Table 6.3, the R_{ct} values of Cu_2Te -NS CE (5.08 Ω), Cu_2Te -NT CE (5.93 Ω), and Cu_2Te -NP CE (8.41 Ω) are far below that of the Au CE (46.25 Ω), which indicates their excellent catalytic activity towards the S^{2-}/S_n^{2-} redox couple. This is consistent with the increased J_{sc} and V_{oc} displayed in Table 6.3. The superior catalytic property of Cu_2Te -NS CE is mostly due to the higher surface area which enables much more active sites for the catalytic redox reaction. This is verified by the BET results shown in Figure 6.18(a) and Figure 6.18(b). The Cu_2Te -NS sample possesses the highest specific surface area (36.6 m^2/g), while the specific surface area of the Cu_2Te -NP sample is the lowest (22.5 m^2/g). In addition, the R_s of Cu_2Te -NS and Cu_2Te -NT CE, which reached 13.21 Ω and 13.73 Ω , respectively, is obviously lower than for Cu_2Te -NP CE (29.24 Ω) and close to Au CE.

The difference in the performance of nanostructured Cu_2Te CEs could be attributed to their different morphology. In the Cu_2Te nanoparticle (0-dimensional) film, charges were transported through a zigzag way and readily trapped by surface defects, leading to lower conductivity. The series resistance was significantly reduced in both Cu_2Te -NT and Cu_2Te -NS CEs, which is owing to the better charge pathway provided by 1-dimensional nanotubes and 2-dimensional nanosheets shown in Figure 6.18(b). The lower series resistance would lead to higher FF and V_{oc} . The diffusion resistances for the electrolyte have been evaluated

from the values of Z_W and are shown in Table 6.3. The Z_W of Cu_2Te -NS CE (3.9Ω) is significantly lower than for the other three CEs, indicating much easier and faster diffusion of the electrolyte. The Z_W value of Cu_2Te -NT CE reaches 33.2Ω , which is the highest among the three Cu_2Te CEs. This may be due to difficult diffusion of electrolyte into the nanotubes. The high value of Z_W decreased the overall energy conversion efficiency ($\eta = 4.75 \%$) of solar cells made with Cu_2Te -NT CE. Compared with the other two Cu_2Te CEs, Cu_2Te -NP CE shows the highest R_s and R_{ct} , and a moderate Z_W (23.0Ω). It thus possesses the lowest fill factor (0.452) and conversion efficiency of 4.47 %. The highest Z_W value (73.4Ω) is achieved with the Au CE.

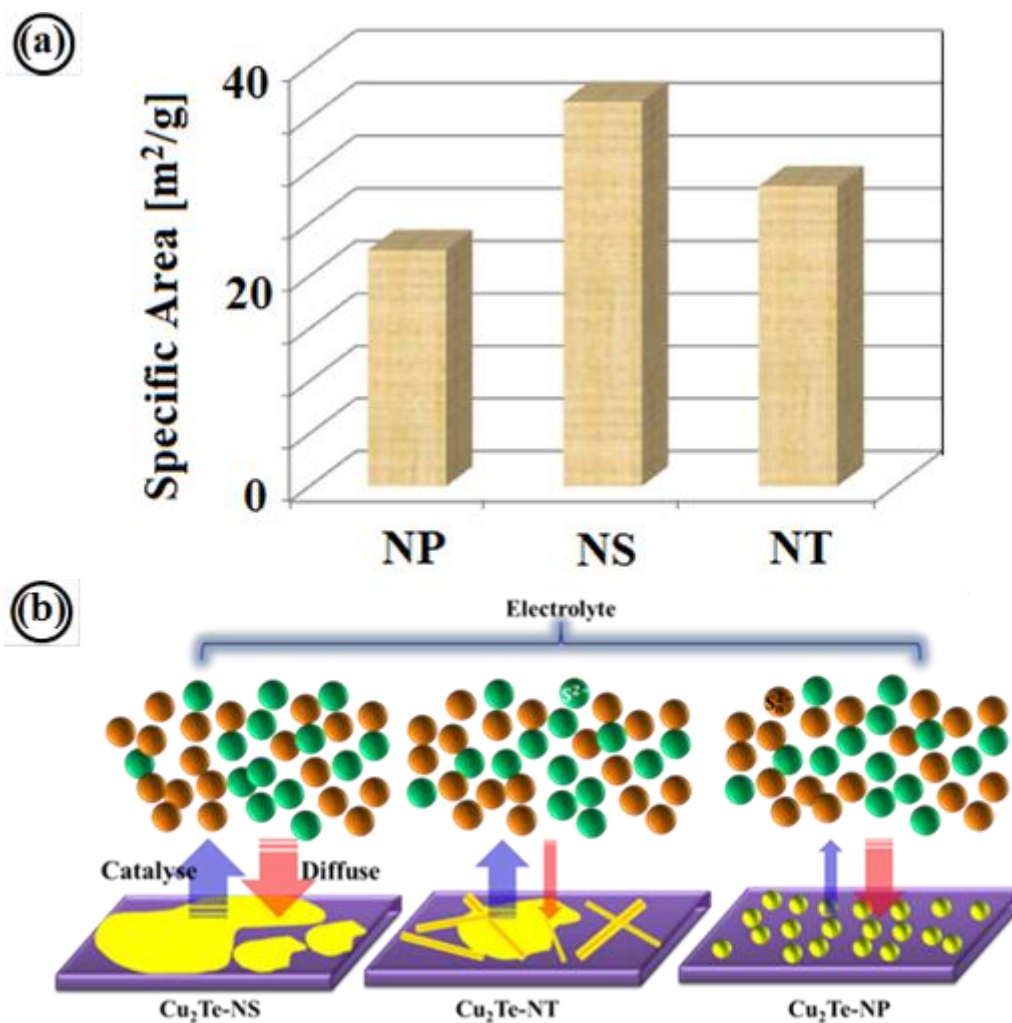


Figure 6.18. (a) BET results of Cu_2Te nanoparticles, nanosheets, and nanotubes; (b)

Schematic illustration of different Cu_2Te CEs

The Tafel-polarization curves of the cells used for EIS measurements are plotted in Figure 6.17(d). The curves represent the logarithm of the current density ($\log J$) as a function of the potential (V) for the S^{2-} / S_n^{2-} redox couple of the electrolyte. The slopes for the electrodes indicate the exchange current density (J_0), which is related to R_{ct} in terms of Equation (6.10). R , T , F , and n respectively represent the gas constant, temperature, Faraday constant, and number of electrons involved in the redox reaction of the electrolyte; while R_{ct} is the charge transfer resistance. As shown in Figure 6.17(d), the slopes of the Tafel curves for the four CEs are in the order of $\text{Cu}_2\text{Te-NS} > \text{Cu}_2\text{Te-NT} > \text{Cu}_2\text{Te-NP} > \text{Au}$, which coincides with the order of the R_{ct} values listed in Table 6.3.

$$J_0 = RT / (nFR_{ct}) \quad (6.10)$$

6.4. Conclusion.

A fast, aqueous, cost-effective, and green strategy to prepare Cu_2Te nanotubes and nanosheets from Cu_2E ($E = \text{O}, \text{S}, \text{Se}$) at room temperature is developed, which can be ascribed to an exchange-peeling mechanism and the unique crystal structure of Cu_2Te . The morphologies of the Cu_2Te nanosheets and nanotubes could be easily controlled by adjusting the precursor concentrations, particle size of the Cu_2Se precursor, and the amount of NaBH_4 , as well as the stirring speed. Thus-formed Cu_2Te nanostructures can be used as counter electrodes in CdS/CdSe co-sensitized solar cells and show excellent catalytic activity towards the electrolyte compared with expensive Au counter electrodes. The performance of Cu_2Te strongly depends on its morphology, in which Cu_2Te nanosheets showed the maximum conversion efficiency of 5.35 % and Cu_2Te nanoparticles showed a value of 4.47 %. Considering their low cost and high catalytic activity, these Cu_2Te nanostructures have great potential in energy conversion.

Chapter 7. Graphite-Nanoplate-Coated Bi_2S_3 Composite with High-Volume Energy Density and Excellent Cycle Life for Room-Temperature Sodium Ion Batteries

7.1 Introduction.

Global warming and dwindling nonrenewable energy resources have recently become increasingly hot topics. The best solution to solve these issues is the effective utilization of clean and renewable energy. Therefore, it is very vital to find a large scale and cost-effective energy storage system (EES). Among the various energy storage devices, such as Sulphur-metal batteries, lithium-ion batteries (LIBs), and sodium-ion batteries (SIBs), the SIBs are impressive because of their lower cost than LIBs due to abundance of sodium.⁴³²⁻⁴³⁴ Another effective EES is sodium–Sulphur batteries, which have been utilized for commercial applications for the past 50 years. Nevertheless, a high operating temperature of at least 300 °C is required to sustain sufficient sodium diffusion in the solid electrolyte.⁴³⁵⁻⁴³⁷

After sodium–Sulphur batteries were introduced, some serious safety problems were revealed, however, which result from the reactive and corrosive nature of the molten Na and S at such high temperatures. Moreover, from the energy-saving point of view, the high operating temperature makes the high-temperature sodium–Sulphur (HT Na–S) batteries unsuitable for EESs. Therefore, it appears very important to develop cathode materials for room-temperature sodium–Sulphur (RT Na–S) batteries.

As a metal sulfide, Bi_2S_3 , can be used either as cathode of RT Na-S batteries or anode of SIBs because the similar Na^+ storage mechanism. The combination of alloying elements to form compounds has been considered an efficient way to develop excellent electrode materials for LIBs and SIBs, because it makes full use of the advantages of each element. For example, $\text{Sn}_{4+x}\text{P}_3$ ($0 < x < 1$),^{438, 439} SnS_2 ,³²⁶ Sb_2S_3 ,⁴⁴⁰ and SnSb ⁴⁴¹ have shown better cycling performance or higher capacity than their counterparts containing single elements in SIBs. While for RT

Na-S batteries, a Na/ Ni_3S_2 cell exhibited good cycling performance over 15 cycles, with a high initial capacity of 420 mAh.g^{-1} .⁴⁴² The nickel in this compound, however, is electrochemically inactive. If an electroactive element was introduced to form a sulfide compound, however, not only the cycling stability but also the capacity would be enhanced. Recently, Su et al. reported that Bi is electroactive in SIBs through an intercalation/extraction mechanism; they showed that its discharge potential plateau was in the range of 0.4–0.6 V with a capacity of 563 mAh.g^{-1} in the second cycle.⁴⁴³ Bi is considered to be a stable element with a density of 9.78 g.cm^{-3} , which is higher than that of Sn (gray, 5.77 g.cm^{-3}) and Sb (6.70 g.cm^{-3}). This higher density means that the Bi delivers a relatively higher volumetric energy density.

Moreover, the price of the Bi precursor is low, comparable to those of Sn that are commonly used in electrode materials for LIBs and SIBs. The Bi_2S_3 compound prepared by the high-energy-consumption hydrothermal method delivered a capacity as high as 690 mAh.g^{-1} at the second cycle, which is higher than that of Bi (563 mAh.g^{-1}).⁴⁴⁴ Its cycling performance is bad, however, with capacity of 119.8 mAh.g^{-1} after six cycles, because of its low electronic conductivity.

In this work, we synthesized Bi_2S_3 by a facile and energy-efficient precipitation method at room temperature, which is described in Chapter 4. Compared with the hydrothermal method, this method features not only low energy consumption but also high yield. To improve the electronic conductivity of Bi_2S_3 , the as-prepared Bi_2S_3 was subsequently mixed with graphite to obtain carbon-covered Bi_2S_3 embedded in a graphite nanoplate composite ($\text{Bi}_2\text{S}_3@\text{C}$), which could be produced on a larger scale by ball milling and meets the requirements for commercial applications. The preparation process is shown in Figure 7.1. The as-obtained $\text{Bi}_2\text{S}_3@\text{C}$ composite was tested as anode for sodium ion batteries, and its sodium storage

mechanism was explored through scanning transmission electron microscopy (STEM) and ex situ X-ray diffraction (XRD).

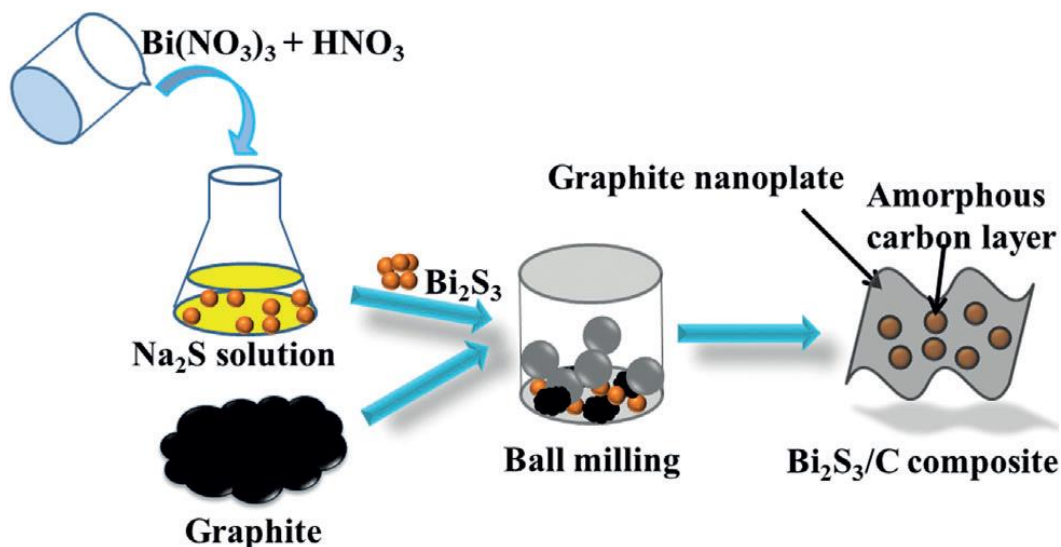


Figure 7.1. Preparation process for the $\text{Bi}_2\text{S}_3/\text{C}$ composite.

7.2 Experimental Section.

7.2.1 Synthesis of Bi_2S_3 Nanoparticles and $\text{Bi}_2\text{S}_3/\text{C}$ Composite.

$\text{Bi}(\text{NO}_3)_3$ (2 mmol) was dissolved in HNO_3 solution (1.5 M, 20 mL) under vigorous stirring to obtain a clear solution, denoted as solution A. $\text{Na}_2\text{S}\cdot 9\text{H}_2\text{O}$ (3 mmol) was added into deionized water (30 mL) to form a clear S precursor solution (solution B). Solution B was then added into solution A, and a brown-black Bi_2S_3 precipitate was formed.

Bi_2S_3 nanoparticles (700 mg) and graphite (300 mg) were put into a tungsten carbide ball-milling vial (the carbon percentage is 30 wt%). The weight ratio of milling balls to powder was 50:1. The vial was assembled in an argon-filled glove box and then mounted on the planetary ball mill [Figure 7.2(a)]. The rotation speed of the mill was set to 500 rpm for 10 h.



Figure 7.2. (a) PULVERISETTE-7 planetary ball milling machine and (b) HR800 Raman spectrometer.

7.2.2 Characterization of the $\text{Bi}_2\text{S}_3@\text{C}$ Composite.

The crystalline structure of the active powder was characterized by powder X-ray diffraction on a GBC MMA diffractometer with a Cu K_α source. The morphology of the sample was investigated by FESEM (JEOL JSM-7500FA) and TEM (JEOL JEM-2010, 200 keV). Raman spectra were collected by using a JOBIN Yvon Horiba Raman spectrometer model HR800 [Figure 7.2(b)], with a 10 mW helium/neon laser at 632.8 nm excitation in the range of 150–2000 cm^{-1} . XPS was conducted with a SPECS PHOIBOS 100 analyzer installed in a high vacuum chamber with a base pressure below 10^{-8} mbar. X-ray excitation was provided by Al K_α radiation with photon energy of 1486.6 eV at a high voltage of 12 kV and power of 120 W. The XPS binding-energy spectra were collected at pass energy of 20 eV in the fixed analyzer transmission mode. Analysis of the XPS data was carried out with the commercial CasaXPS 2.3.15 software package. All spectra were calibrated with $\text{C 1s}=284.6$ eV. The sodium storage mechanism of Bi_2S_3 was determined by STEM (JEOL ARM200F) and EDS.

7.2.3 Electrochemical Measurements.

The Bi_2S_3 @C composite electrodes were prepared by mixing 70% active materials, 5% carbon black, and 5% carbon nanotubes as the conductive additives, together with 20% carboxymethyl cellulose (CMC) binder, by weight to form an electrode slurry, which then was coated on copper foil, dried in a vacuum oven overnight at 80 °C, and then pressed at 10 MPa. The electrodes were punched into disks with a loading of 3 $\text{mg}\cdot\text{cm}^{-2}$. The sodium foil was cut by the doctor blade technique from sodium bulk stored in mineral oil, which was then employed as both the reference and counter electrode. The electrolyte was 1.0 $\text{mol}\cdot\text{L}^{-1}$ NaClO_4 in an ethylene carbonate–diethyl carbonate solution (1:1 v/v), with or without the addition of 5 vol% of fluoroethylene carbonate (FEC). The cells were assembled in an argon-filled glove box. The electrochemical performances were tested with a Landt Test system in the voltage range of 0–2.5 V (vs. Na^+/Na).

7.3 Results and Discussion.

7.3.1 Characterization of Bi_2S_3 and Bi_2S_3 @C Composite.

Bi_2S_3 was synthesized by a facile and energy-efficient method at room temperature. As shown in Figure 7.1, Na_2S aqueous solution was mixed with an HNO_3 solution of $\text{Bi}(\text{NO}_3)_3$, and a brown-black Bi_2S_3 precipitate was obtained. The details are given in the Experimental Section. The purity of the as-prepared Bi_2S_3 was confirmed by XRD and X-ray photoelectron spectroscopy (XPS). Figure 7.3(a) presents the XRD pattern of Bi_2S_3 , which was indexed to the orthorhombic phase (JPCDS 65-2431; $a=1.129$ nm, $b=1.115$ nm, $c=0.3978$ nm). XPS spectrum of pure Bi_2S_3 has been shown in Figure 4.6(d), Chapter 4. The as-prepared Bi_2S_3 was then ball milled with graphite to yield the Bi_2S_3 @C composite.

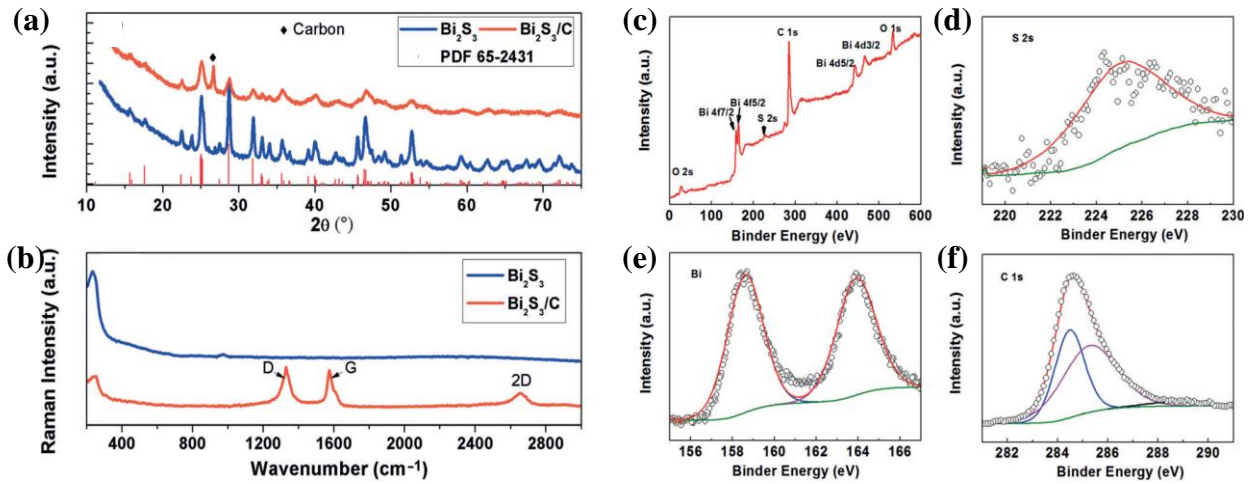


Figure 7.3. (a) XRD patterns and (b) Raman spectra of Bi_2S_3 and the $\text{Bi}_2\text{S}_3/\text{C}$ composite.

XPS spectra of the $\text{Bi}_2\text{S}_3/\text{C}$ composite: (c) survey spectrum; (d) S 2s; (e) Bi 4f ; (f) C 1s.

After ball milling, all of the peaks of Bi_2S_3 became broad and the intensities became weak, which suggests that the crystal size of Bi_2S_3 had become smaller. Moreover, the characteristic peak (2θ) of graphite appeared 26.58° , as shown in 7.3(a). The Raman spectrum of Bi_2S_3 is plotted in Figure 7.3(b) and is consistent with the reported one.⁴⁴⁵ Apart from the peaks of Bi_2S_3 , three peaks appeared at 1335 , 1570 , and 2660 cm^{-1} in the Raman spectrum of the $\text{Bi}_2\text{S}_3/\text{C}$ composite; these peaks correspond to the D-band, G-band, and 2D-band of carbon, respectively. Moreover, the ratio of the D-band to the G-band is 1.14, which suggests that the graphite in the composite became disordered to some extent. The state of the carbon was further confirmed by XPS analysis. Figure 7.3(c) shows the XPS survey spectrum of the $\text{Bi}_2\text{S}_3/\text{C}$ composite, which indicates that the composite consists of the elements Bi, S, C, and O (with the O signals coming from the adsorbed oxygen atoms on the surface of the sample). The C 1s spectrum and its fitting curves are presented in Figure 7.3(f). The peaks at the binding energies of 284.6 and 285.4 eV correspond to the C=C and C-OH groups, respectively. The C 1s spectrum of the $\text{Bi}_2\text{S}_3/\text{C}$ composite is similar to that of graphite nanoplates,⁴⁴⁶ which suggests that the carbon in the $\text{Bi}_2\text{S}_3/\text{C}$ composite exists in the form of graphite nanoplates.

The morphologies of the Bi₂S₃ and the Bi₂S₃@C composite were characterized by field-emission scanning electron microscopy (FE-SEM) and transmission electron microscopy (TEM). The as-prepared Bi₂S₃ presents a shuttle-like morphology, with shuttles that are 500 nm in length and approximately 50 nm in width [Figure 7.4(a–d)]. Figure 7.4(e–h) shows the morphology of the Bi₂S₃@C composite. After milling, the shuttle-like morphology of the Bi₂S₃ particles changes into small particles covered by a carbon layer [Figure 7.4(e)]. As shown in Figure 7.4(f), the elements C, S, and Bi can be observed all over the samples, which indicates uniform mixing of C and Bi₂S₃ in the composite. Figure 7.4(g) contains a TEM image of the Bi₂S₃@C composite. Clearly, the Bi₂S₃ particles were embedded in the graphite nanoplates. A high-resolution TEM image of the Bi₂S₃@C composite was obtained from the edge of one particle, as shown in Figure 7.4(h).

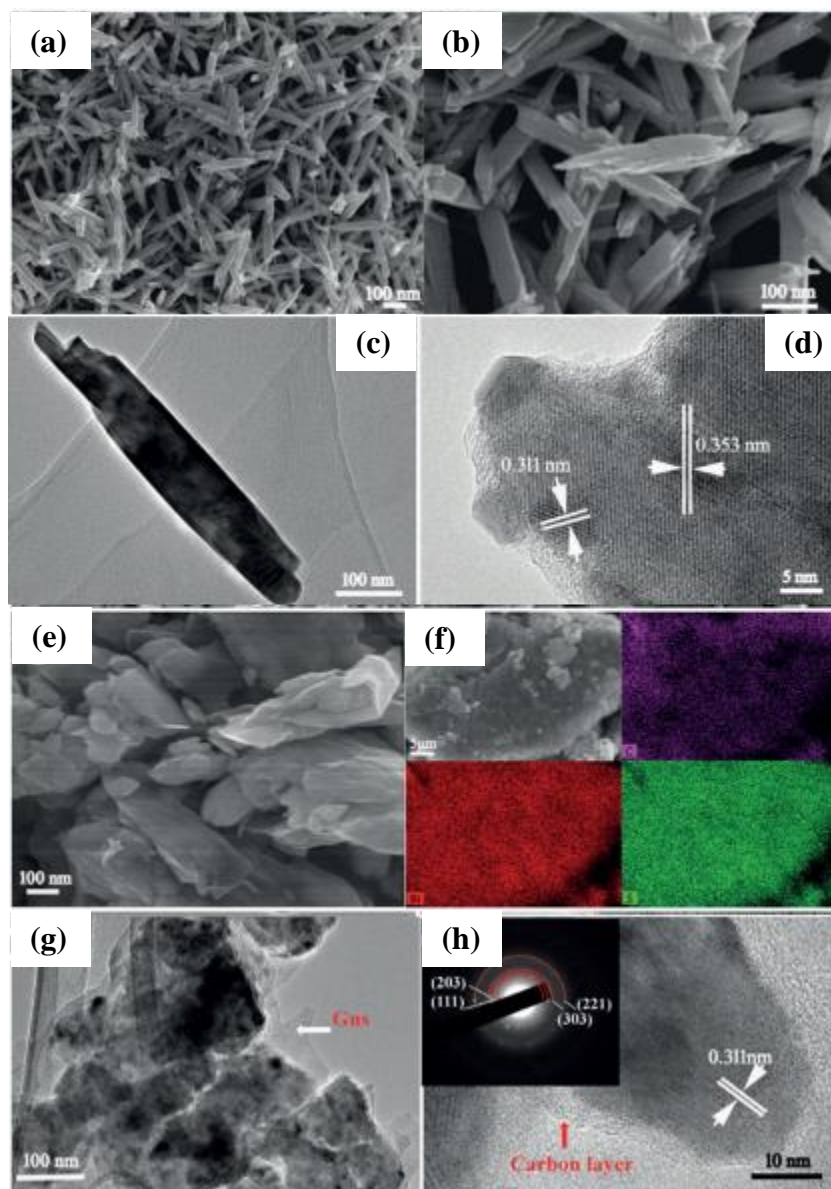


Figure 7.4. Morphologies of (a–d) the as-prepared Bi_2S_3 and (e–f) the $\text{Bi}_2\text{S}_3@\text{C}$ composite: (a), (b), and (e) SEM images; (f) EDS mapping; (c) and (g) low-magnification TEM images; (d) and (h) are high-magnification TEM images; inset of (h) is SAED pattern.

It presents a Bi_2S_3 particle covered by a 2–3 nm thick carbon layer. Moreover, the lattice fringes are clear, with d-spacing of 0.311 nm, which corresponds to the (203) plane of Bi_2S_3 . Thus, the morphology of the $\text{Bi}_2\text{S}_3@\text{C}$ composite can be described as Bi_2S_3 nanoparticles wrapped in a double carbon layer, in that the amorphous-carbon-covered Bi_2S_3 nanoparticles are embedded in graphite nanoplates. Furthermore, the selected area electron diffraction

(SAED) pattern [inset of Figure 7.4(h)] confirmed the coexistence of crystallized Bi_2S_3 and amorphous carbon.

7.3.2 Electrochemical Performance of $\text{Bi}_2\text{S}_3@C$ Composite.

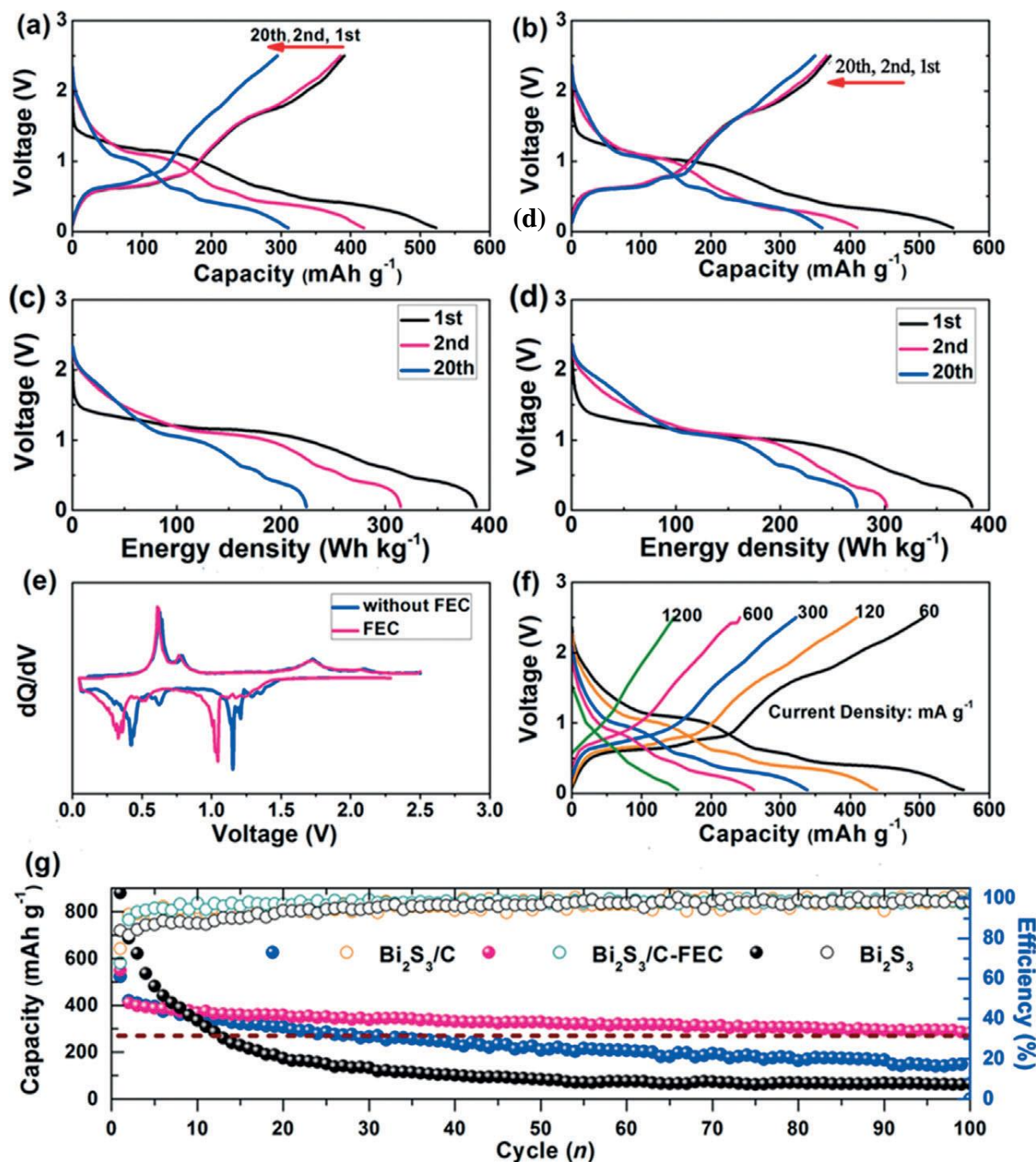


Figure 7.5. Electrochemical performance of the $\text{Bi}_2\text{S}_3@C$ composite electrode tested in the voltage range of 0–2.5 V. (a) Charge–discharge curves for selected cycles for the $\text{Bi}_2\text{S}_3@C$ composite charged at $60 \text{ mA}\cdot\text{g}^{-1}$ in $1\text{m NaClO}_4/(\text{EC}:\text{DEC})$ electrolyte a) with and (b) without

FEC additive; energy density of the electrode in the electrolyte (c) with and (d) without FEC additive; (e) dQ/dV curves of the $\text{Bi}_2\text{S}_3@C$ composite with and without FEC additive at the first cycle; (f) rate capability tested at different current densities; (g) cycling performance of the $\text{Bi}_2\text{S}_3@C$ composite.

The electrochemical performance of the $\text{Bi}_2\text{S}_3@C$ composite was tested in a sodium ion battery in an electrolyte composed of 1M NaClO_4 in ethylene carbonate (EC) and diethyl carbonate (DEC) in the voltage window of 0–2.5 V. All of the capacities and energy densities of the $\text{Bi}_2\text{S}_3@C$ composite were calculated on the basis of the composite weight. Figure 7.5(a) shows the charge–discharge curves of the $\text{Bi}_2\text{S}_3@C$ composite in the 1M $\text{NaClO}_4/(\text{EC}:\text{DEC})$ electrolyte at a current density of $60 \text{ mA}\cdot\text{g}^{-1}$ ($1 \text{ C}=600 \text{ mA}\cdot\text{g}^{-1}$). The $\text{Bi}_2\text{S}_3@C$ composite delivered a discharge capacity of $523 \text{ mAh}\cdot\text{g}^{-1}$ in the first cycle, with an initial coulombic efficiency of 74.8 %. This reversible capacity and initial coulombic efficiency of the $\text{Bi}_2\text{S}_3@C$ composite are larger than those of reported by Hwang et al.⁴⁴⁷ The discharge curve shows three distinct potential plateaus at 1.18, 0.61, and 0.42 V. Correspondingly, there are three potential plateaus at 0.64, 0.78, and 1.70 V in the charge curve. It is obvious that the potential hysteresis between the discharge and charge curves is low, which suggests low polarization of the $\text{Bi}_2\text{S}_3@C$ composite. Nevertheless, the capacity gradually dropped to $310 \text{ mAh}\cdot\text{g}^{-1}$ over 20 cycles. If fluoroethylene carbonate (FEC) additive was added into the electrolyte, the $\text{Bi}_2\text{S}_3@C$ composite delivered a slightly higher initial discharge capacity of $550 \text{ mAh}\cdot\text{g}^{-1}$, as shown in Figure 7.5(b). The extra capacity came from electrolyte decomposition to form the solid electrolyte interphase (SEI) film. FEC can promote intact SEI formation on the surface of electrodes.^{438, 439, 448} Consequently, the $\text{Bi}_2\text{S}_3@C$ composite with FEC additive in the electrolyte showed better stability than that of the electrode charged without the FEC additive, with a capacity retention of 87.8% (based on the second cycle) compared with 73.8% over 20 cycles.

The corresponding specific-energy-density profiles of $\text{Bi}_2\text{S}_3@\text{C}$ in the electrolyte with and without FEC additive are displayed in Figure 8.5(c-d). $\text{Bi}_2\text{S}_3@\text{C}$ has approximately 390 Wh.kg^{-1} specific energy in the initial discharge process [Figure 7.5(c)], and with the introduction of FEC additive into the electrolyte, the $\text{Bi}_2\text{S}_3@\text{C}$ composite delivers stable specific energy in the range of 275-300 Wh.kg^{-1} [Figure 7.5(d)] in subsequent cycles.

To clearly reveal the electrochemical differences between electrodes of the $\text{Bi}_2\text{S}_3@\text{C}$ composite with and without FEC additive, their dQ/dV curves at the first cycle are plotted in Figure 7.5(e). The dQ/dV curve is for a small change in charge for a small change in voltage (which still equals capacitance over that small range). This curve is generally used to measure the alignment of electrodes within full LIBs/SIBs without the use of the 3-electrode cell and allows to learn cell degradation mechanisms. It is clearly seen that the main differences in the dQ/dV curves appear in the discharging process. The cathodic peaks of the $\text{Bi}_2\text{S}_3@\text{C}$ electrode are shifted towards lower potential positions in the electrolyte with FEC additive, which suggests that the polarization has increased. It is possible that there was more SEI formation with the introduction of FEC, which would result in increased resistance of the electrode.

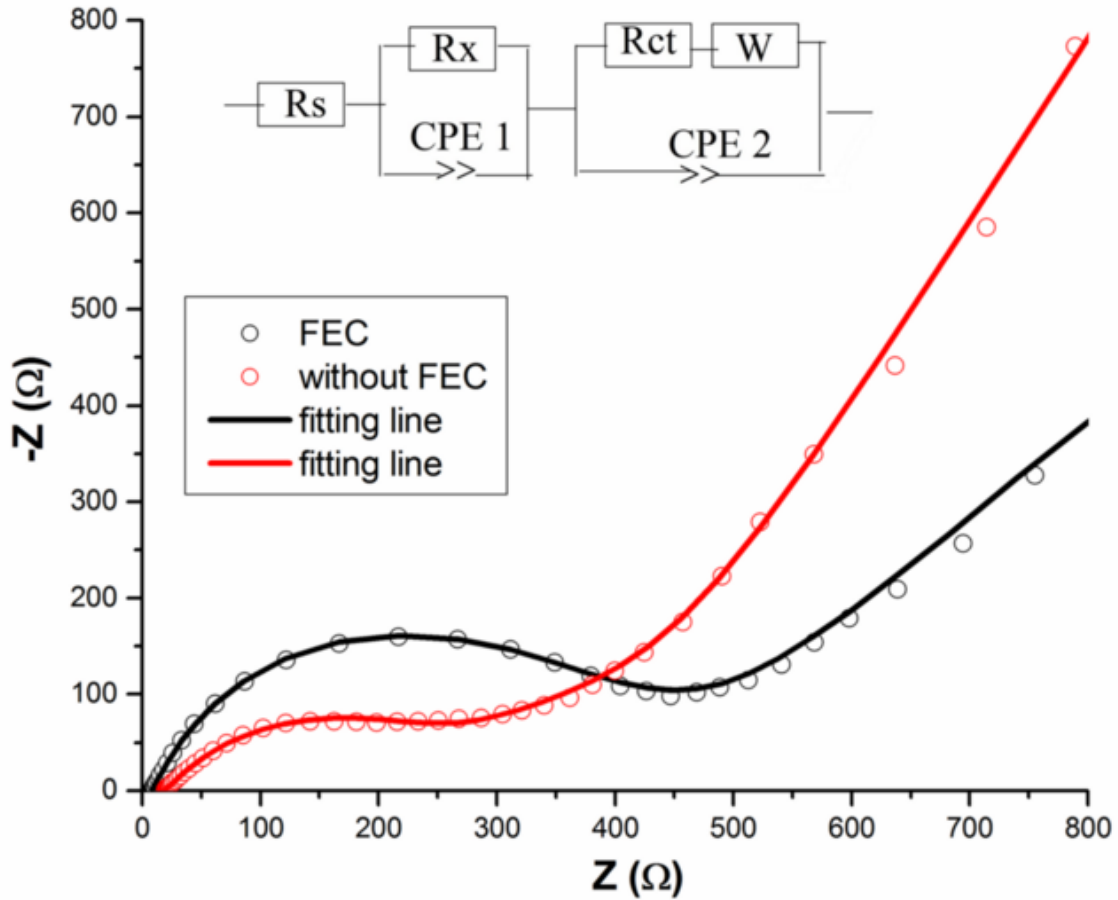


Figure 7.6. Electrochemical impedance spectroscopy (EIS) of the $\text{Bi}_2\text{S}_3@C$ electrodes after 5 cycles. Inset is the equivalent circuit.

To confirm this point, electrochemical impedance spectroscopy was conducted. Figure 7.6 contains Nyquist plots of the $\text{Bi}_2\text{S}_3@C$ composite electrodes charged to 0.65 V after 5 cycles (vs. Na^+/Na) in the electrolyte with and without FEC additive. Both impedance curves of the $\text{Bi}_2\text{S}_3@C$ composite feature two semicircles in the medium-frequency and low-frequency regions, which could be assigned to the resistance due to sodium-ion diffusion through the SEI film (R_x) and the charge transfer resistance (R_{ct}), respectively. Obviously, the R_{ct} value of the electrode in the electrolyte with FEC additive (252 Ω) is larger than that of the electrode in the electrolyte without FEC (40 Ω), as calculated by using the equivalent circuit shown in the inset of Figure 7.6. From Figure 7.5(e), it is clear that there are two strong cathodic peaks

in the dQ/dV curves of the $\text{Bi}_2\text{S}_3@C$ composite. The cathodic peaks at 1.34 and 1.16 V could be attributed to the reaction of Bi_2S_3 with Na to form Na_xS ($0 < x < 2$).⁴⁴⁹ For the lithium-ion battery, the peaks related to this reaction are at 1.79 and 1.70 V, which are values higher than those for SIBs. This is because the standard electrode potential difference between Li and Na is 0.33 V. The peaks at 0.3–1.0 V are assigned to the reactions with bismuth, based on previous reports that the bismuth does not go through the alloying mechanism with Na ions, which is different from the case with lithium.^{443, 444}

The rate capability of the $\text{Bi}_2\text{S}_3@C$ composite was tested at different current densities from 60 to 1200 mA.g^{-1} . Even at the high current density of 1200 mA.g^{-1} , the capacity of the $\text{Bi}_2\text{S}_3@C$ composite remained 153 mAh.g^{-1} [Figure 7.5(f)]. Figure 7.5(g) shows the cycling performance of the $\text{Bi}_2\text{S}_3/C$ composite. It is clear that the $\text{Bi}_2\text{S}_3@C$ composite exhibited excellent cycling stability compared with that of Bi_2S_3 . In particular, with FEC additive, the capacity of the $\text{Bi}_2\text{S}_3@C$ composite can still reach 282 mAh.g^{-1} over 100 cycles, with capacity retention of 69 %.

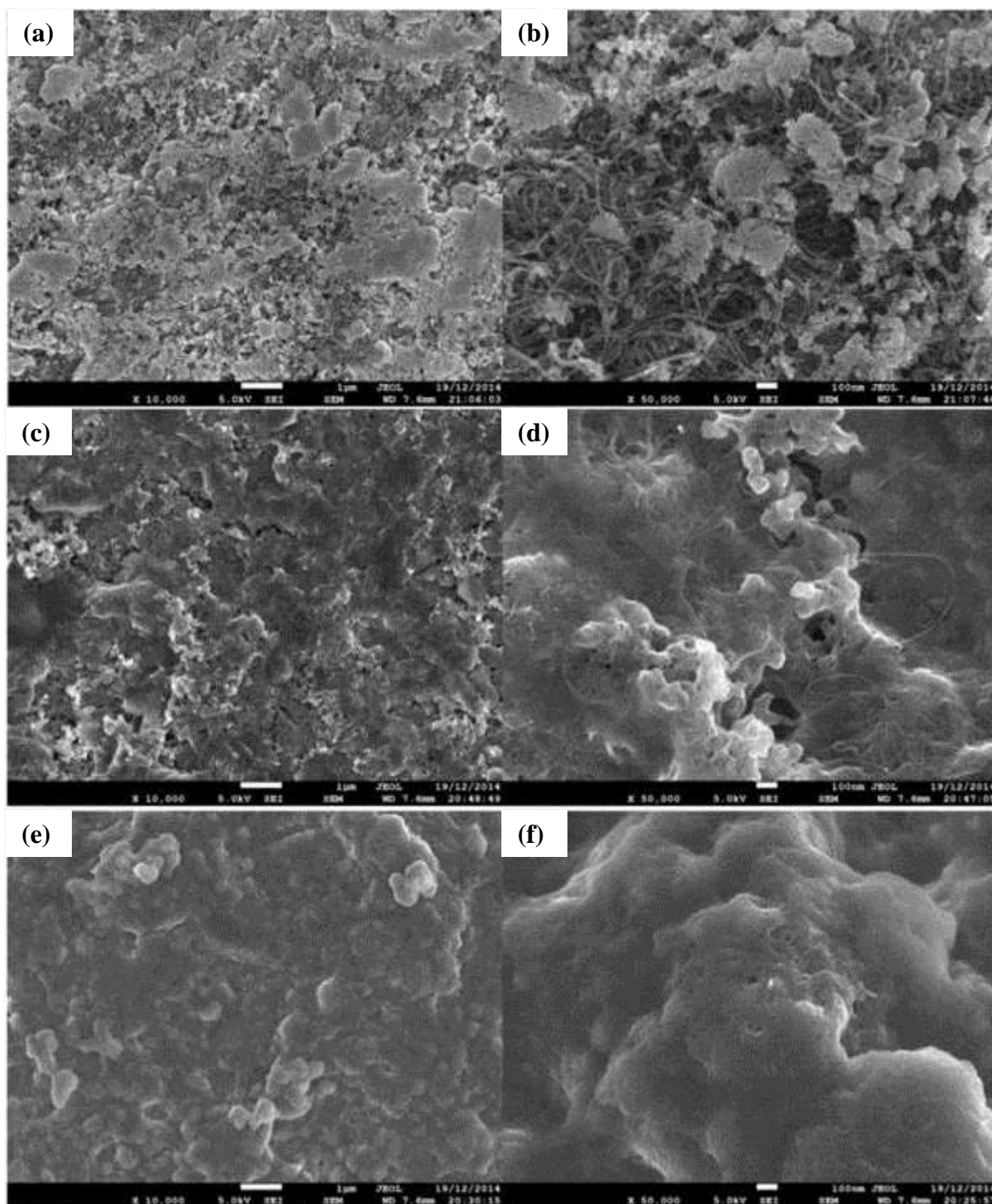


Figure 7.7. Low and high magnification SEM images of the Bi_2S_3 @C electrodes (a, b) before and (c-f) after cycling in the electrolyte (c, d) without FEC and (e, f) with FEC.

To investigate the reason for the better cycling performance of Bi_2S_3 @C in the electrolyte with FEC than that without FEC addition, the morphologies of the electrodes after cycling

were observed by SEM. Obvious SEI layer formed on the surface of the electrode after cycling, but it was not dense [Figure 7.7(a-d)]. With the introduction of FEC additive into the electrolyte, a compact SEI layer formed on the surface of the electrode [Figure 7.7(e-f)] and acted as a buffer to relieve the stress resulting from the volume change. Moreover, superior cycling stability is possible due to the unique structure of the $\text{Bi}_2\text{S}_3@\text{C}$ composite with its double carbon coating. The Bi_2S_3 particles were coated with amorphous carbon, which can improve the electronic conductivity and prevent the dissolution of polysulphides during cycling. The $\text{Bi}_2\text{S}_3@\text{C}$ particles were then wrapped in graphite nanoplates, which can not only buffer the stress from the volume expansion to avoid pulverization but can also serve as a protective layer to hinder the polysulfide dissolution in the liquid electrolyte. Therefore, the $\text{Bi}_2\text{S}_3@\text{C}$ composite can exhibit excellent cycling performance, compared with that of bare Bi_2S_3 . To be certain of the contribution of the carbon in the capacity of the $\text{Bi}_2\text{S}_3@\text{C}$ composite, we milled the graphite under the same experimental conditions. The cycling performance of the milled graphite is shown in Figure 7.8(a). The milled graphite delivered a first discharge capacity of 261 mAh.g^{-1} ; the huge irreversible capacity is due to the SEI formation on the surface of the milled graphite particles that results from the electrolyte decomposition. In the second cycle, the milled graphite delivered 156 mAh.g^{-1} capacity [Figure 7.8(a)]. The sodium storage mechanism of milled graphite is possibly similar to that of graphene; that is, the sodium adsorbed/desorbed on/from the graphite nanoplates and (or) active sites.⁴⁵⁰ Thus, the contribution of carbon in the $\text{Bi}_2\text{S}_3@\text{C}$ composite cannot be neglected.

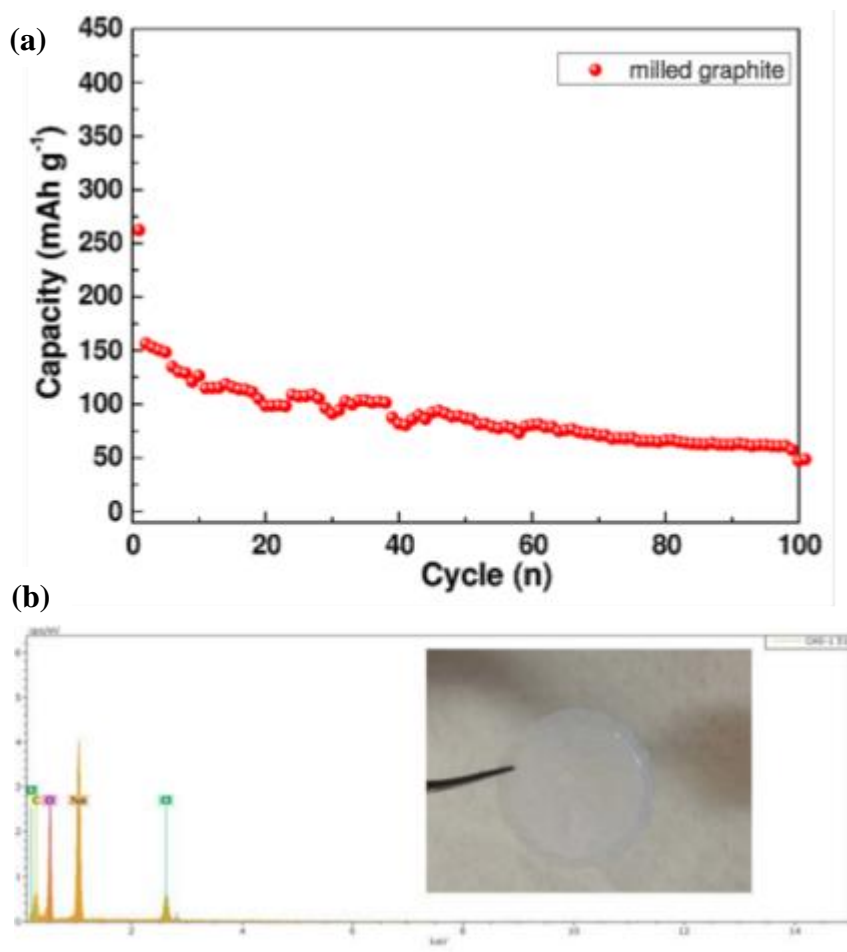


Figure 7.8. (a) The cycling performance of the milled graphite; (b) EDS spectrum of the separator in the cell cycled for 100 cycles (inset: photograph of the separator).

To confirm the role of the unique morphology of the $\text{Bi}_2\text{S}_3@\text{C}$ composite, characterization of the electrodes and the separator after cycling was conducted by TEM and SEM with energy dispersive spectroscopy (EDS) elemental analysis. The cycled cell was disassembled in an argon-filled glove box. Figure 7.9 shows the morphology of the $\text{Bi}_2\text{S}_3@\text{C}$ electrode after 100 cycles. Clearly, the structure of the nanoparticles embedded in the graphite nanoplates was still retained after sodiation/desodiation [Figure 7.9(a)]. After cycling, the particle size became smaller (<10 nm) due to the pulverization [Figure 7.9(b)]. The small particles were still wrapped by the graphite nanoplates, however, so the integrity of the composite was maintained, which facilitates the electronic integrity of the electrode. Moreover, the separator

was characterized by SEM and EDS, as shown in Figure 7.8 (b). The EDS elemental analysis shows that no Sulphur at all could be detected from the separator, which suggests that polysulfide dissolution in the electrolyte was avoided for the $\text{Bi}_2\text{S}_3@\text{C}$ electrode. Thus, the EDS results and TEM images of the electrodes after cycling further demonstrate that the unique double carbon coating of the $\text{Bi}_2\text{S}_3@\text{C}$ composite structure can not only suppress the dissolution of polysulfides but can also maintain the integrity of the electrode to achieve the significantly enhanced cycling stability of the $\text{Bi}_2\text{S}_3@\text{C}$ electrode.

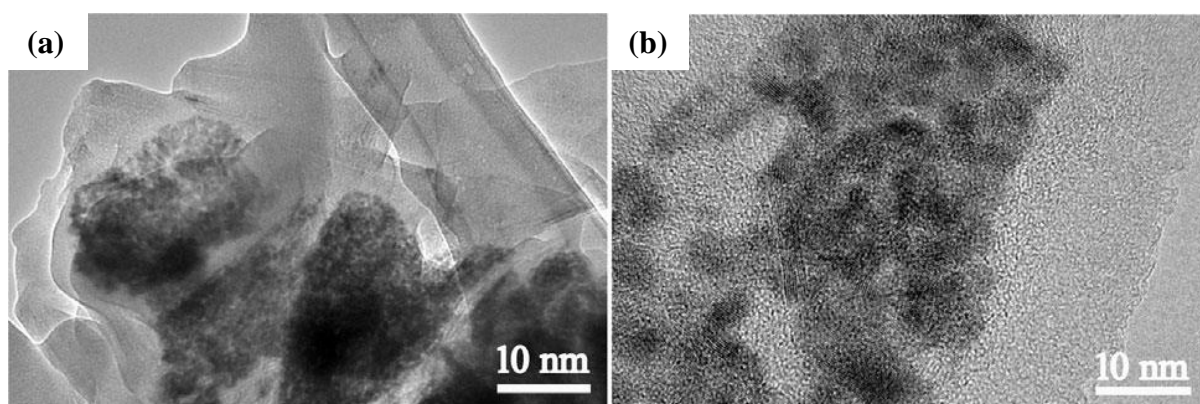
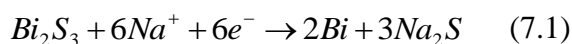


Figure 7.9. TEM of the $\text{Bi}_2\text{S}_3@\text{C}$ electrode after 100 cycles. (a) Low magnification; (b) high magnification.

7.3.3 Investigation of the Sodium Storage Mechanism of Bi_2S_3 .

In order to explore the sodium-ion storage mechanism of Bi_2S_3 , the structural evolution of Bi_2S_3 during the charge–discharge process was characterized by ex situ XRD and STEM. Figure 7.10 shows the ex situ XRD patterns of the $\text{Bi}_2\text{S}_3@\text{C}$ electrodes charged or discharged to various states. It can be clearly seen that there are four peaks at 27.16, 37.95, 39.62, and 48.70 ° that appear if the electrode is discharged to 1.0 V, which can be indexed to the (012), (104), (110), and (202) planes of the Bi phase (JPCDS 44-1246). Notably, in the subsequent charge–discharge process, these peaks can still be detected, which suggests that the Bi does not react with the Na ions to form an alloy during the charge–discharge process. This result is

consistent with the ex situ XRD of bismuth as an anode for sodium-ion batteries.⁴⁴³ When the electrode was fully discharged at 0 V, some peaks of Na_2S were detected, which demonstrates that the electrochemically active element of Bi_2S_3 is S, which reacts with sodium ions to form the Na_2S alloy [Equation (7.1)].



In the charging process, the peaks of Na_2S gradually become weak and then disappear in the fully charged state, whereas the peaks of Bi can be detected in the fully charged electrode.

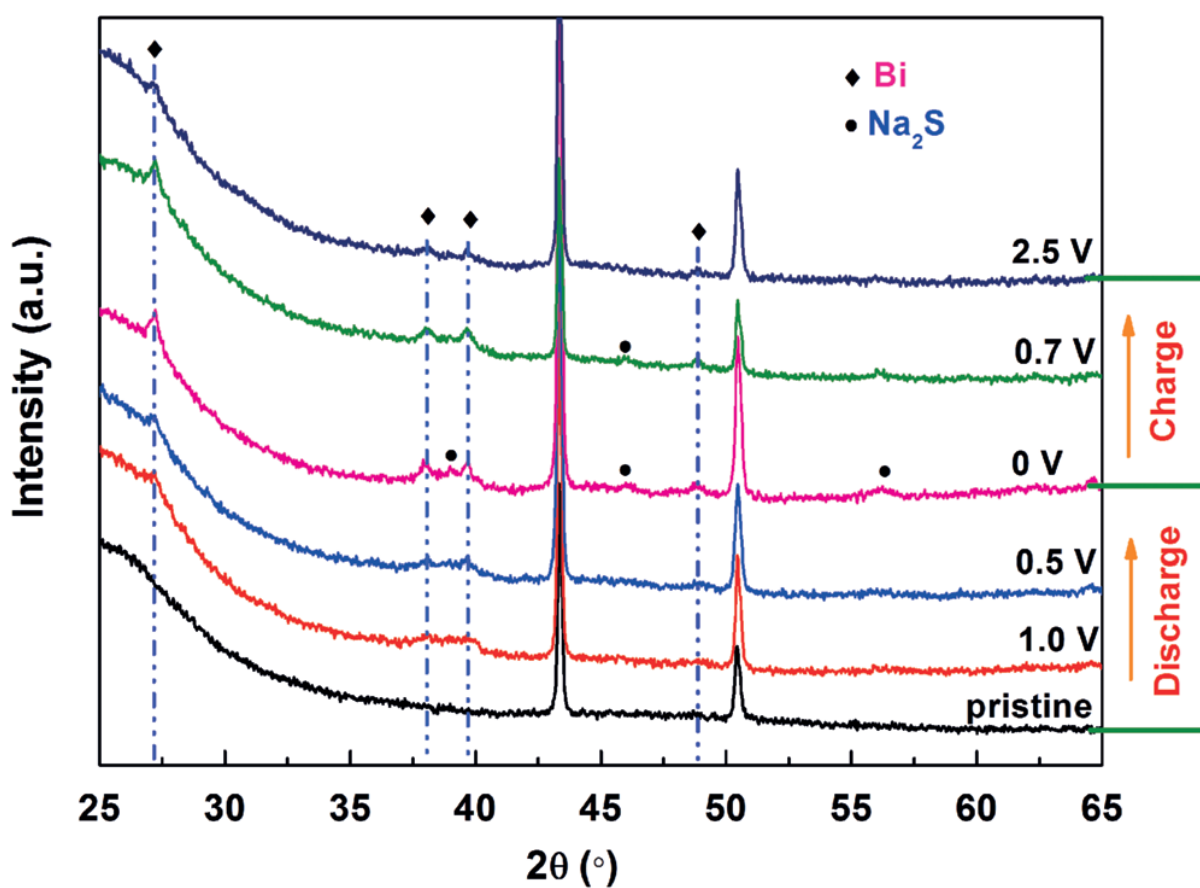
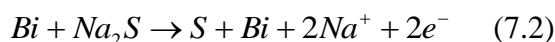


Figure 7.10. Ex-situ XRD patterns of the Bi_2S_3 electrodes charged or discharged to different states.

To further observe the changes in the structure, the fully discharged and charged Bi_2S_3 electrodes were also analysed with STEM. Figure 7.11 shows the EDS elemental mapping of

the electrode discharged to 0 V. Apart from Bi and S, the elements C, O, and Na were observed after the electrode was discharged [Figure 7.11(a)]. The element Cl, however, was not detected in the EDS spectrum, which suggests that the elements O and Na do not come from the remaining NaClO_4 electrolyte salt. The elements C and O are possibly from the SEI film resulting from decomposition of the carbonate electrolyte on the surface of the electrode, whereas the element Na possibly comes from the alloy compound resulting from the reaction between Bi_2S_3 and Na. In order to confirm this, SAED analysis was carried out. The SAED patterns show diffraction rings from two phases, which are indexed to the crystal planes of Bi ((012), (110), (202), (122), and (214)) and Na_2S [(202) and (311)]. They demonstrate that the electrode that was fully discharged to 0 V is composed of Na_2S and Bi [Figure 7.11(b)]. The element distribution of the electrode charged to 2.5 V is shown in Figure 7.11(c). Clearly, at the end of the cycle, the element S did not overlap very well with the element Bi, which suggests that the electrode composition cannot restore the original Bi_2S_3 phase after cycling. Moreover, Na, C, and O are also observed after cycling, and they overlap each other well. They are assigned to the composition of the SEI layer that forms during the discharging process. SAED patterns of the Bi_2S_3 electrode charged to 2.5 V were also collected [Figure 7.11(d)]. It is obvious that the SAED patterns present some diffraction spots indexed to S and Bi phases. Thus, the reaction for the charging process is described by Equation (7.2).



Accordingly, based on the ex situ XRD and STEM results, the sodium-ion storage mechanism of Bi_2S_3 can be determined. During the discharge process, the Bi_2S_3 decomposes into Bi and S, and then S is alloyed with Na to form Na_2S , whereas Bi does not go through the alloying reaction with Na but undergoes a sodium-ion insertion process.

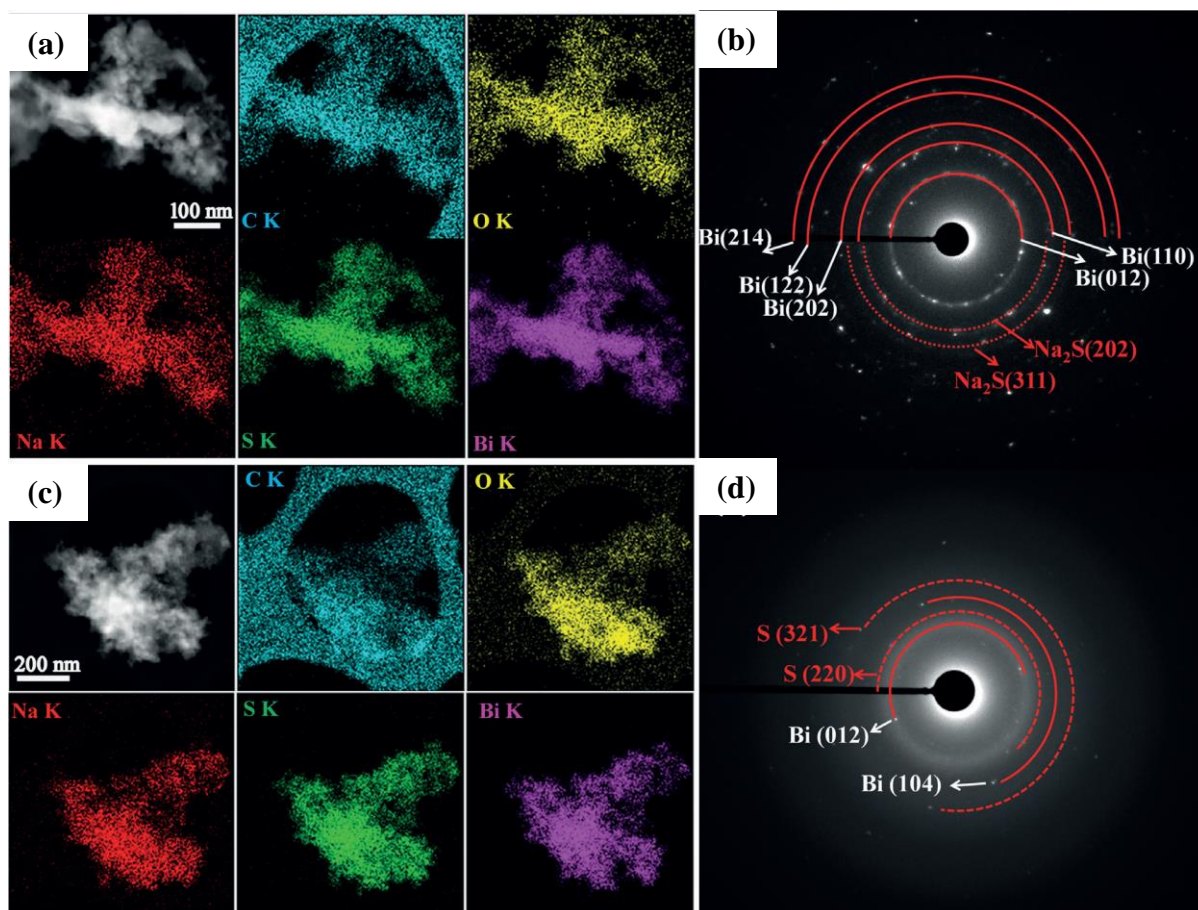


Figure 7.11. STEM characterization of the Bi_2S_3 electrodes (a-b) discharged to 0 V and (c-d) charged to 2.5 V. (a) and (c) are EDS mapping; (b) and (d) are SAED patterns.

7.4 Conclusions.

In summary, A Bi_2S_3 @C composite was fabricated by a facile, scalable, and energy-efficient precipitation method combined with ball milling. In the composite, the Bi_2S_3 active material particles are covered by an amorphous carbon layer and then wrapped with graphite nanoplates. The amorphous carbon layer plays a role in improving the electronic conductivity of Bi_2S_3 and prevents the dissolution of the active material. The graphite nanoplates serve as both conductive layers and a buffer to alleviate the stress from volume expansion to avoid pulverization. Thus, the Bi_2S_3 @C composite exhibits excellent cycling stability compared with Bi_2S_3 . Over 100 cycles, the Bi_2S_3 @C composite delivered $282 \text{ mAh}\cdot\text{g}^{-1}$, with 69%

retention of the capacity in the second cycle. Moreover, the Bi₂S₃@C composite possesses two active elements, Bi and S, and can deliver a reversible capacity as high as 550 mAh.g⁻¹ for sodium storage. The ex situ XRD and STEM results demonstrate that the sodium storage mechanism of Bi₂S₃ is the substitution and insertion reaction, in which Bi₂S₃ reacts with Na to form Bi and Na₂S, then Na is inserted into Bi layers to form 3 NaBi molecules. The low polarization, high density, and excellent cycling performance make Bi₂S₃@C a promising anode candidate for sodium ion batteries.

Chapter 8. Controlled Synthesis of Copper Telluride Nanostructures for Long-cycling Anode in Lithium Ion Batteries

8.1 Introduction

During the past several decades, copper chalcogenides (Cu_{2-x}E , $0 \leq x \leq 1$, $\text{E} = \text{O}, \text{S}, \text{Se}, \text{Te}$) have attracted considerable attention, because their wide range of compositions and phases allows tuning of their properties for diverse applications, ranging from energy storage and conversion to sensors, from bio-application to environmental science.^{177, 222, 322, 395-397, 400, 403,}

⁴¹³ One of the important applications is in energy storage as copper chalcogenides have shown great potential in lithium ion batteries (LIBs) and sodium ion batteries (SIBs). For example, copper sulfide powders and films have been well investigated as cathodes for LIBs;⁴⁵¹⁻⁴⁵³ and CuSe_2 , CuSe , and Cu_2Se nanostructured thin films have been also utilized as promising cathodes for LIBs with capacities of 201.7, 258.4, and 210.2 mAh/g, respectively.⁴⁵⁴ Recently they were proved to be good cathodes for SIBs with a capacity of 250 mAh/g.³ Compared with copper sulfides and copper selenides, there is no report on the battery applications of copper tellurides despite their similar molecular formulas. According to the literature report,^{322, 451-453} the reaction mechanisms of copper chalcogenide electrodes during charging and discharging is attributed to the “replacement reactions” between Li/Na ions and Cu ion. The heavy copper tellurides should have less volume expansion/constriction during charging and discharging processes, and should have high volumetric capacity due to its high density (7.27g/cm^3 for Cu_2Te) which is essential for fabricating smaller batteries. We therefore aim to prepare copper telluride nanostructures and test their performance as anodes in LIBs.

It should be noted that copper tellurides have much more complicated crystal structures and variable Cu/Te ratios, in comparison with other copper chalcogenides. They can exist as

orthorhombic CuTe, hexagonal Cu₂Te, Cu₃Te₄, Cu₇Te₅, non-stoichiometric Cu_{2-x}Te, and so on. Such diversity of copper tellurides is mainly because the partially filled d-shell in transition metals allows them to adopt multiple oxidation states,⁴⁰² so that it remains a challenge to synthesize copper telluride nanostructures with well-defined composition, crystal structure, and morphology. Their typical synthetic routes include hydrothermal and solvothermal approaches.^{222, 402, 455, 456} The hydrothermal routes usually employ a strong alkaline solution (such as NaOH) as reaction medium to prepare copper telluride nanostructures under high pressure and high temperature.^{455, 456} The solvothermal approaches involve decomposition of organometallic precursors or injection of precursors into organic solvents at relative high temperature.^{222, 402} Recently, Li et al.⁴⁰² used the hot injection method to synthesize cube-, plate-, and rod-like copper telluride nanomaterials under the assistance of moisture-sensitive LiN(Si(CH₃)₃)₂. They found that LiN(Si(CH₃)₃)₂ played a significant role in the formation of copper telluride nanostructures (i.e. serving as activator), and the absence of LiN(Si(CH₃)₃)₂ led to the formation of irregular big nanostructures. Here, we prepare copper telluride nanocubes, nanoparticles, and nanosheets within short reaction time (10 mins) without any activator. In addition, to the best of knowledge, 2-D copper telluride colloidal nanosheets were first reported. The effects of different preparation parameters, such as copper precursors, precursor ratios, and solvents, were investigated. The resultant copper telluride nanostructures have been tested as anodes for LIBs for the first time. The assembled cells show extremely high cycling stability, up to 5000 cycles.

8.2 Experiment.

8.2.1 Materials.

Copper (I) chloride (CuCl, 97%), copper (I) bromide (CuBr, 97%), copper (II) chloride (CuCl₂, 98%), copper (II) fluoride (CuF₂, 97%), copper (II) acetate (Cu(ac)₂, 99.999%),

copper(II) acetylacetonate ($\text{Cu}(\text{acac})_2$, 97%), oleylamine (technical grade, 70%), oleic acid (OA, 97%), tellurium powder (-200 mesh, 99.8%), trioctylphosphine oxide (TOPO, 99%), tri-n-octylphosphine (TOP, 97%), and hexadecylamine (HDA, 90%) were all purchased from Sigma-Aldrich and used as received without purification. All syntheses were carried out with a standard Schlenk line set-up. A glove-box ($\text{H}_2\text{O} < 0.1$ ppm, $\text{O}_2 < 0.1$ ppm) was used for storing and handling air and moisture-sensitive chemicals.

8.2.2 Synthesis.

Synthesis of TOPTe stock solution: 10 mmol Te powder (1.27 g) and 10 mL TOP were loaded into a 50 mL three-neck flask. The mixture was degassed for 30 min at 100 °C using the Schlenk line [Figure 3.2(a-b)], and then filled with Ar and heated to 200 °C for 4 hours to form a clear yellow solution. The concentration of the resultant TOPTe solution is 1.0 M.

Synthesis of copper telluride nanocubes and nanosheets: Copper telluride nanostructures were prepared by using the standard Schlenk line technique. In a typical synthesis, 0.2 mmol CuCl (0.02 g) was mixed with 10 mL TOP, and then degassed at 100 °C for 30 min. The mixture was heated to 250 °C to form a colorless solution under the protection of Ar. After the solid was completely dissolved and the temperature became stable, 40 μL of as-prepared TOPTe solution (1.0 M) was quickly injected into it. The resultant mixture was kept at 250 °C for another 10 min, and the solution changed from light yellow to brown. After that, the solution was cooled to room temperature, and the resultant nanostructures were precipitated by ethanol and separated by centrifugation. The product was purified by several cycles of re-dispersion and precipitation with dichloromethane and ethanol.

The other syntheses were performed in a similar way, except that different conditions were applied. The detailed preparation parameters are listed in Table 8.1.

Table 8.1. Reaction parameters for synthesising nanocubes and nanosheets^[a]

Group	Number	Copper precursor	Concentration (mol/L)	Temperature (°C)	Reaction time (min)	Cu:TOP Te	Solvent	Ligands ^[b]
Time dependence	E1-1	CuCl	0.02	250	10	5:1	TOP	-
	E1-2	CuCl	0.02	250	8	5:1	TOP	-
	E1-3	CuCl	0.02	250	6	5:1	TOP	-
	E1-4	CuCl	0.02	250	5	5:1	TOP	-
Different concentrations of copper precursor	E2-1	CuCl	0.01	250	10	5:1	TOP	-
	E2-2	CuCl	0.05	250	10	5:1	TOP	-
	E2-3	CuCl	0.2	250	10	5:1	TOP	-
Different reaction temperature	E3-1	CuCl	0.02	230	10	5:1	TOP	-
	E3-2	CuCl	0.02	270	10	5:1	TOP	-
Different ratio of Copper precursor and TOPTe	E4-1	CuCl	0.02	250	10	10:1	TOP	-
	E4-2	CuCl	0.02	250	10	2:1	TOP	-
	E4-3	CuCl	0.02	250	10	1:1	TOP	-
	E4-4	CuCl	0.02	250	10	1:2	TOP	-
Different solvents	E5-1	CuCl	0.02	250	10	5:1	Oleylamine	-
	E5-2	CuCl	0.02	250	10	5:1	Oleic Acid	-
	E5-3	CuCl	0.02	250	10	5:1	TOPO	-
Different ligands	E6-1	CuCl	0.02	250	10	5:1	TOP	Oleylamine
	E6-2	CuCl	0.02	250	10	5:1	TOP	Oleic Acid
	E6-3	CuCl	0.02	250	10	5:1	TOP	TOPO
Different copper precursor	E7-1	CuBr	0.02	250	10	5:1	TOP	-
	E7-2	CuCl ₂	0.02	250	10	5:1	TOP	-
	E7-3	CuF ₂	0.02	250	10	5:1	TOP	-
	E7-4	Cu(CH ₃ COO) ₂	0.02	250	10	5:1	TOP	-
	E7-5	Cu(acac) ₂	0.02	250	10	5:1	TOP	-
Different reaction temperature	E8-1	CuCl	0.02	230	10	5:1	Oleylamine	-
	E8-2	CuCl	0.02	270	10	5:1	Oleylamine	-
Different	E9-1	CuCl	0.05	250	10	5:1	Oleylamine	-

concentrations of copper precursor							mine	
	E9-2	CuCl	0.005	250	10	5:1	Oleyla mine	-
Different ratio of copper precursor and TOPTe	E10-1	CuCl	0.02	250	10	3:1	Oleyla mine	-
	E10-2	CuCl	0.02	250	10	2:1	Oleyla mine	-
	E10-3	CuCl	0.02	250	10	1:2	Oleyla mine	-

[a] All the different parameters are marked by red colour;

[b] The amount of ligands is 0.1 mmol in 10 mL TOP.

Synthesis of hollowed Cu_{2-x}Te nanoparticles: In order to investigate the effect of materials shapes on battery performance, hollowed Cu_{2-x}Te nanoparticles were synthesized. $\text{Cu}(\text{acac})_2$ (0.25 mmol), HDA (4.18 g), and TOP (2 ml) were loaded into a 100 ml three neck flask. After being degassed at 100 °C for 30 min, the mixture was heated to 250 °C under protection of Ar and a yellow copper precursor solution formed. The solution was kept at 250 °C for 10 min to let the temperature stable and the solution changed into brown, 125 μl , 1 M TOPTe solution was swiftly injected into the copper precursor. The temperature of the copper precursor decreased no more than 1 °C and was kept at 250 °C for another 10 min, the solution turned into black. The product was purified by repeatedly precipitating and re-dispersing in ethanol and dichloromethane, respectively.

8.2.3 Characterization.

The as-prepared copper telluride nanostructures were characterized with state-of-the-art facilities. The transmission electron microscope (TEM) images were recorded with a JOEL JEM-2010 microscope operating at 200 kV accelerating voltage. Scanning electron microscopy (SEM) was performed using a JOEL JSM-7500FA Field Emission microscope. Powder X-ray diffraction (XRD) patterns were obtained with Cu K_α ($\lambda = 0.154 \text{ nm}$) radiation

in the reflection geometry on a GBC-MMA instrument operating at 40 kV and 25 mA. X-ray photoelectron spectroscopy (XPS) was conducted using a SPECS PHOIBOS 100 Analyser installed in a high-vacuum chamber with the base pressure below 10^{-8} mbar, with X-ray excitation provided by Al K α radiation with photon energy of 1486.6 eV at the high voltage of 12 kV and power of 120 W. The XPS binding energy spectra were recorded at the pass energy of 20 eV in the fixed analyzer transmission mode. The XPS data were analyzed with the commercial Casa XPS 2.3.15 software package. All spectra were calibrated using the C1s peak at 284.6 eV. The exact sample compositions were determined by inductively coupled plasma atomic emission spectrometry (ICP-AES) after digestion with nitric acid.

8.2.4 Battery Performance Testing.

The electrode slurry for lithium ion batteries was prepared by mixing 70 wt% copper telluride nanomaterial (active material), 20 wt% carbon black, and 10 wt% carboxymethyl cellulose (CMC). The slurry was pasted on copper foil. After being dried in a vacuum oven overnight at 80 °C, the coated pieces of foil were pressed with a pressure of 30 MPa to enhance the contact between the mixture and the copper foil. Lithium foil was employed as both reference and counter electrode. The electrolyte was 1.0 mol/L LiPF₆ in an ethylene carbonate (EC) - diethyl carbonate (DEC) solution (1:1 v/v). The cells were assembled in an argon-filled glove box, and their electrochemical performance was tested with a Landt Battery Test System [Figure 3.2(c)] in the voltage range of 0 – 2 V (vs. Li⁺/Li).

8.3 Results and Discussion.

8.3.1 Synthesis of Copper Telluride Nanocubes.

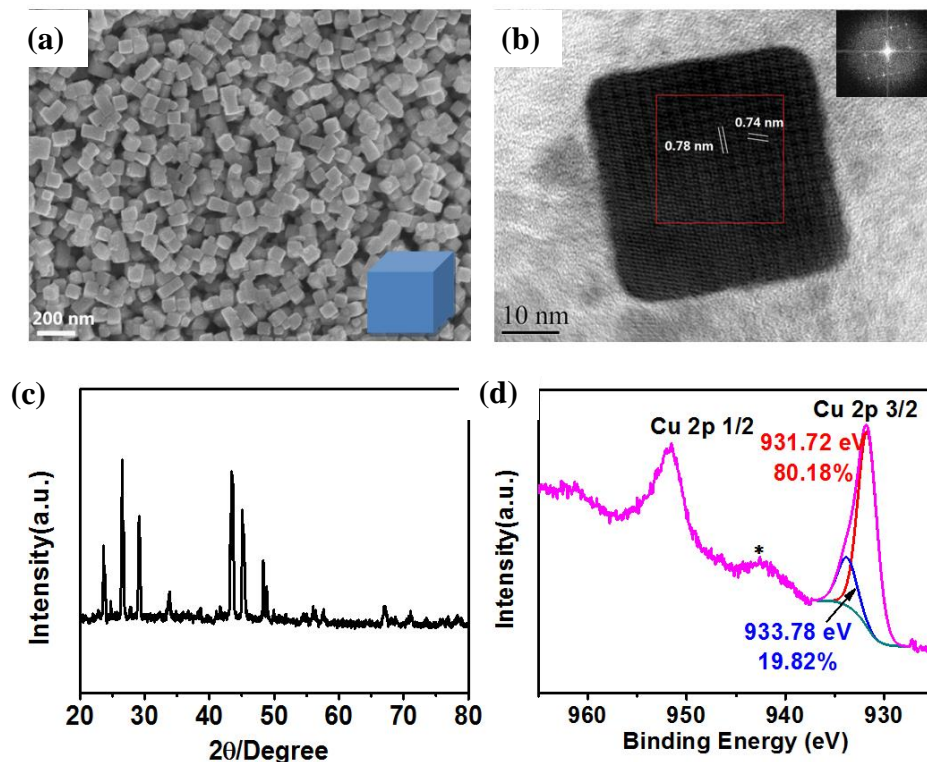


Figure 8.1. (a) SEM image of copper telluride nanocubes; insets are the size distribution of the nanocubes, and a nanocube model; (b) HRTEM image with the FFT pattern (inset) of a selected area (marked by red rectangle); (c) X-ray diffraction pattern of copper telluride nanocubes; (d) XPS spectrum of Cu 2p from copper telluride nanocubes, with the satellite peak marked by “*” indicating the presence of Cu^{2+} arising from oxidation.

The copper telluride nanostructures were prepared in organic solvents by using the standard Schlenk line set-up. Figure 8.1 shows the morphology, crystal structure, and composition of the sample obtained under the conditions for E1-1 in Table 8.1 (0.02 M CuCl, 250 °C, 10 min, CuCl/TOPTe = 5). As shown in Figure 8.1(a), the products are nanocubes with a size of (75.4 ± 6.7) nm. The high-resolution TEM image in Figure 8.1(b) clearly shows lattice fringes of 0.78 nm and 0.74 nm, which are very close to the interplanar spacing of the (012) and (003)

planes of hexagonal Cu_2Te (JCPDS 53-0524), respectively. The inset in Figure 8.1(b) is the fast Fourier transform (FFT) image of the selected area (marked by the red rectangle), clearly showing the single-crystal nature of the nanocubes. The X-ray diffraction pattern of the nanocubes [Figure 8.1(c)] is consistent with the previous report,⁴⁰³ and the sharp diffraction peaks indicate that these nanocubes are well crystallized. Fig 8.1(d) shows the binding energies of Cu 2p in these nanocubes. Two distinct peaks at 932 eV and 952.1 eV are assigned to Cu 2p_{3/2} and Cu 2p_{1/2}, respectively. The satellite peak marked by “*” (942.47 eV) proves the presence of Cu^{2+} species arising from slight oxidation of Cu^+ .^{222, 457, 458} The atomic ratio of Cu^{2+} to Cu^+ can be estimated from the intensity ratio of the two peaks at 933.78 eV and 931.72 eV, which are fitted from Cu 2p_{3/2}. Their intensity ratio is calculated to be approximately 1:4, and the average valence of copper ions in these nanocubes is around +1.2. The XPS spectrum of Te 3d for the nanocubes is shown in Figure 8.2(a). The peaks with binding energies of 571.84 eV and 582.14 eV are consistent with those of Te 3d_{5/2} and 3d_{3/2} from Te^{2-} , respectively.^{222, 457, 458} The shoulder peaks at 574.56 eV and 586.06 eV are characteristics of oxidized layers, which support the slight oxidization of the sample because of exposure to the atmosphere. Another peak at 567.60 eV is assigned to the Cu peak. From the XPS results, we can roughly deduce the ratio of Cu to Te to be 1.67, which matches well with that determined by ICP-AES measurement (1.67 in Table 8.2). This means that XPS can be used to estimate the Cu/Te ratio in the products. We identify the above nanocubes as $\text{Cu}_{1.67}\text{Te}$.

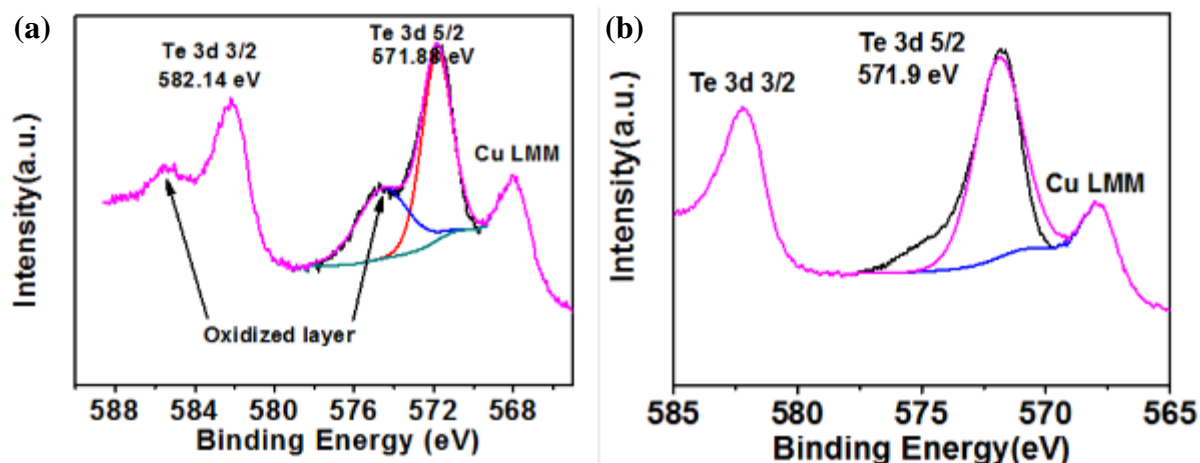


Figure 8.2. XPS spectra of Te 3d from (a) copper telluride nanocubes and (b) copper telluride nanosheets.

Table 8.2. Inductively coupled plasma atomic emission spectrometry (ICP-AES) measurements of Cu_xTe nanocubes.

Sample	Weight (mg)	Cu (mg/ml)	Te (mg/ml)	Cu/Te (atom ratio)
E1-1	0.38	22	26.5	1.67
E4-2	1.22	62	67.2	1.83
E4-3	1.35	60	72.9	1.63
E4-4	1.68	76	89.3	1.71
E7-1	1.31	56	66.2	1.70
E7-2	1.02	45	52.5	1.71
E7-4	1.96	76	88.2	1.73
E7-5	1.43	59	71.2	1.66

In order to investigate the effects of different reaction parameters on the morphologies and compositions of copper telluride nanostructures, several groups of experiments were carried out (Table 8.1). The size and shape evolution of the nanocubes were first investigated by taking out sample liquor at different reaction times (E1 group in Table 8.1). It should be noted that reaction time less than 5 min is not enough for the formation of copper telluride nanostructures, as the color of the mixture did not change, and no precipitate was obtained after addition of ethanol. Figure 8.3 shows the SEM images and particle size distributions of

the nanostructures collected at 5 min, 6 min, and 8 min, respectively. After reaction for 5 min, nanocubes were formed and their size is (54.2 ± 11.9) nm [Figure 8.3(a) and (d)]. Prolonging the reaction time to 6 min leads to nanocubes with a size of (69.6 ± 15.1) nm [Figure 8.3(b) and (e)]. Further increasing the reaction time to 8 min produces bigger nanocubes with a size of (74.4 ± 18.8) nm [Figure 8.3(c) and (f)], which is similar to the average size of the final nanocubes [i.e. collected at 10 min, as shown in Figure 8.1(a)]. These results indicate that the nucleation process is much slower than the growth process in our system.

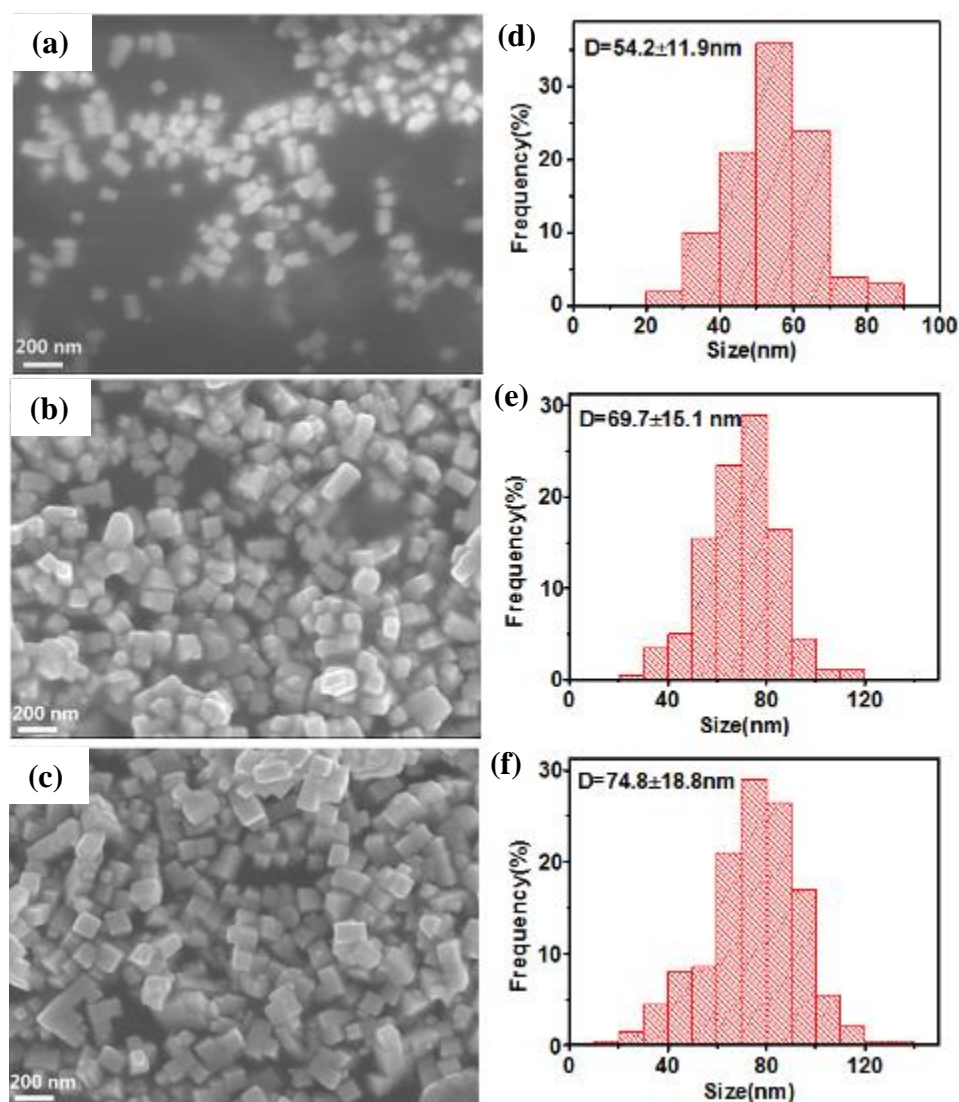


Figure 8.3. SEM images and size distributions of copper telluride nanocubes prepared from different reaction times: (a, d) 5min, (b, e) 6min, and (c, f) 8min.

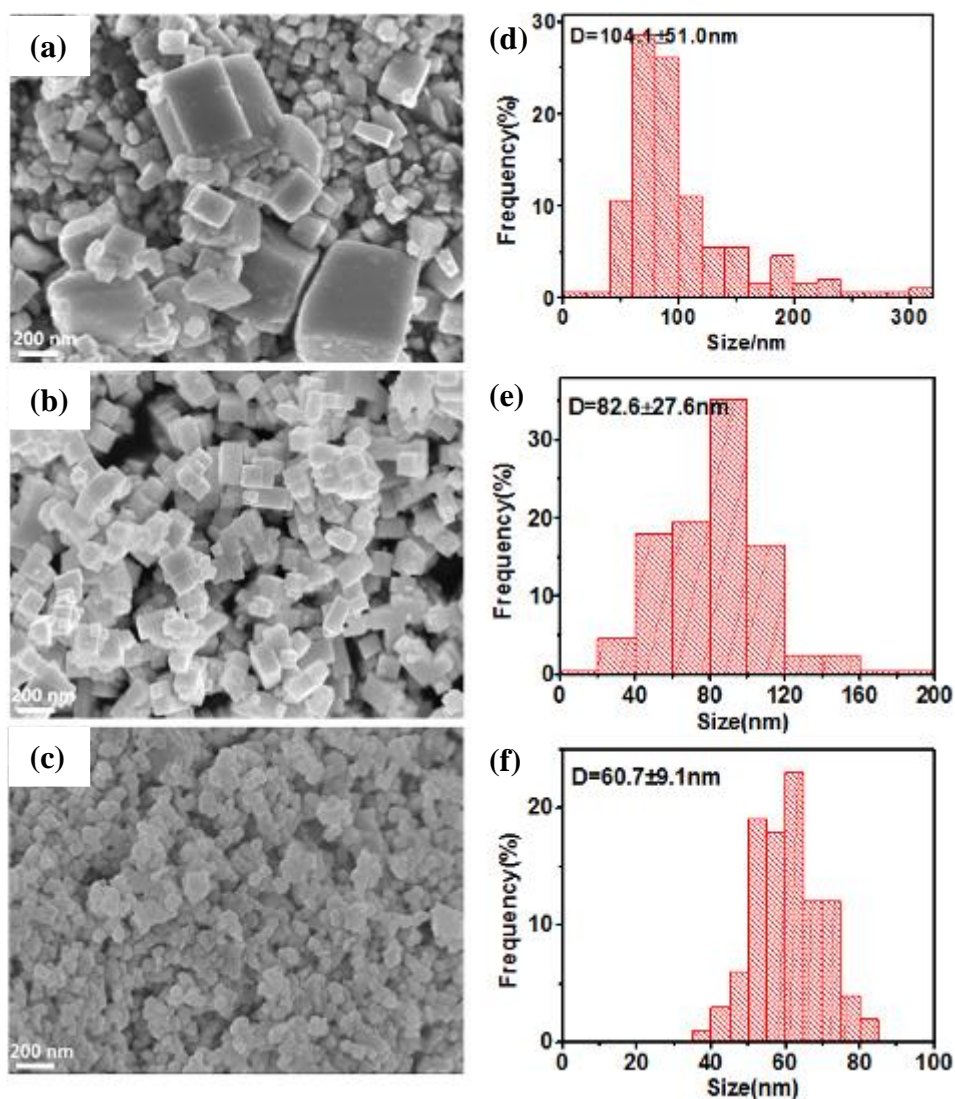


Figure 8.4. SEM images and size distribution of nanostructures prepared using different CuCl concentrations at 250 °C: (a, d) 0.2 M, (b, e) 0.05 M, and (c, f) 0.01M.

In order to tune the size of nanocubes, different CuCl concentrations were tested (E2 group in Table 8.1). Figure 8.4 shows the morphologies and size distributions of samples prepared at 250 °C with a concentration of 0.2 M, 0.05 M, and 0.01 M, respectively. Figure 8.4 clearly demonstrates that decreasing the CuCl concentration from 0.2 M to 0.05 M led to a smaller particle size and a narrower size distribution, i.e., the nanocube size decreases from (104.1 ± 51) nm [Figure 8.4(a, d)] to (82.6 ± 27.6) nm [Figure 8.4(b, e)]. Further decreasing the CuCl concentration from 0.05 M to 0.02 M resulted in even smaller nanocubes, as displayed in Figure 8.1(a), (75.4 ± 6.7) nm. However, when 0.01 M CuCl was used, irregular small

nanoparticles with a size around (66.7 ± 9.1) nm were obtained [Figure 8.4(c, f)]. This group of experiments demonstrates that the minimum CuCl concentration for the formation of nanocubes is 0.02 M.

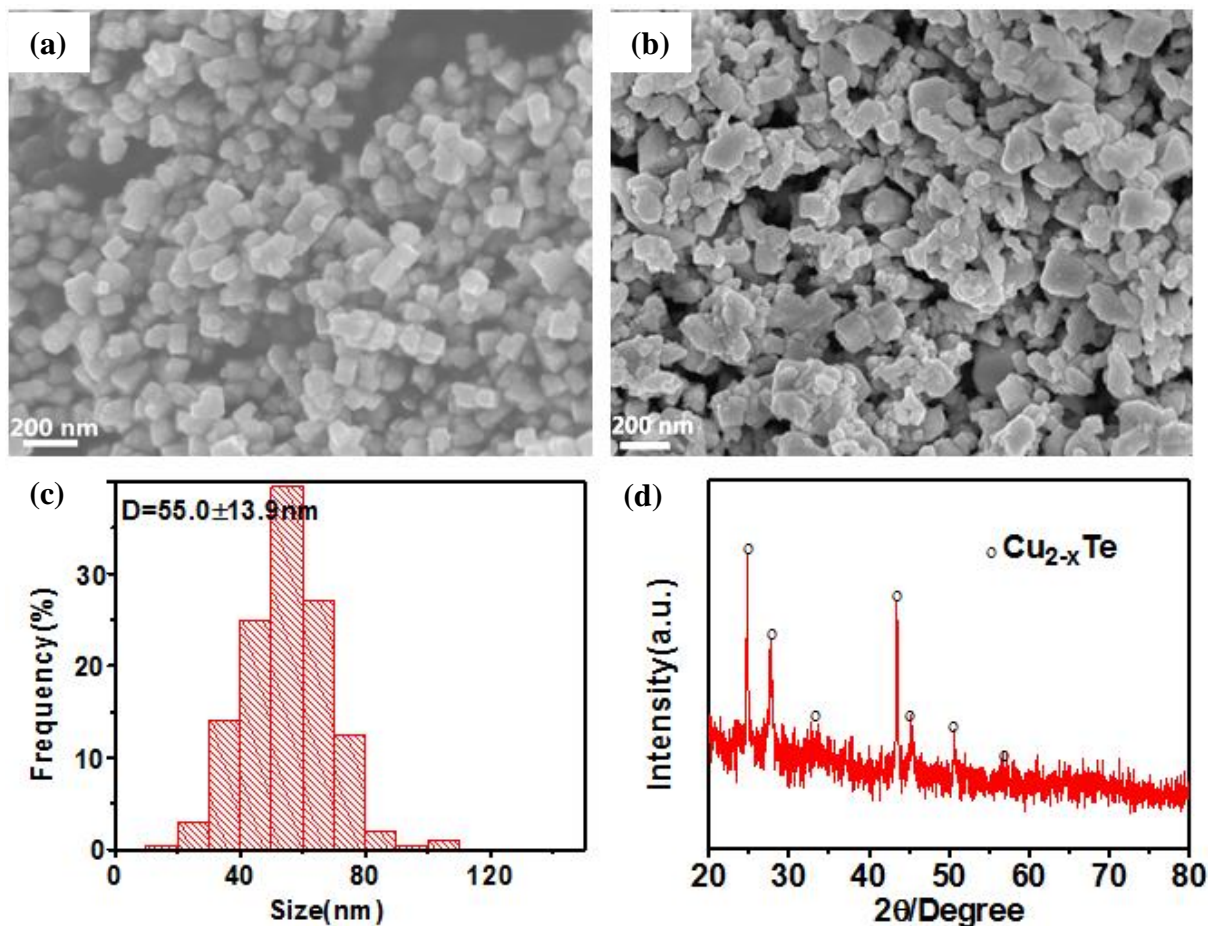


Figure 8.5. (a-b) SEM images of samples prepared at 230 °C and 270 °C using 0.02 M CuCl; (c) size distribution of sample prepared at 230 °C; (d) XRD pattern of sample prepared at 270 °C.

The influence of reaction temperature (E3 group in Table 8.1) on the formation of copper telluride nanocubes is presented in Figure 8.5. Compared with the nanocubes prepared at 250 °C, nanocubes synthesized at 230 °C [Figure 8.5(a)] have a smaller average size and a broader size distribution of (55.0 ± 13.9) nm [Figure 8.5(c)]. Increasing the reaction temperature from 250 °C to 270 °C leads to simultaneous changes in the morphology [Figure 8.5(b)] and composition. The crystal structure of this sample matches well with that of Cu_2 .

$_x\text{Te}$ (JCPDS 10-0421), as shown in Figure 8.5(d). The experimental results indicate that the lowest temperature for the formation of nanocubes within 10 min is 230 °C.

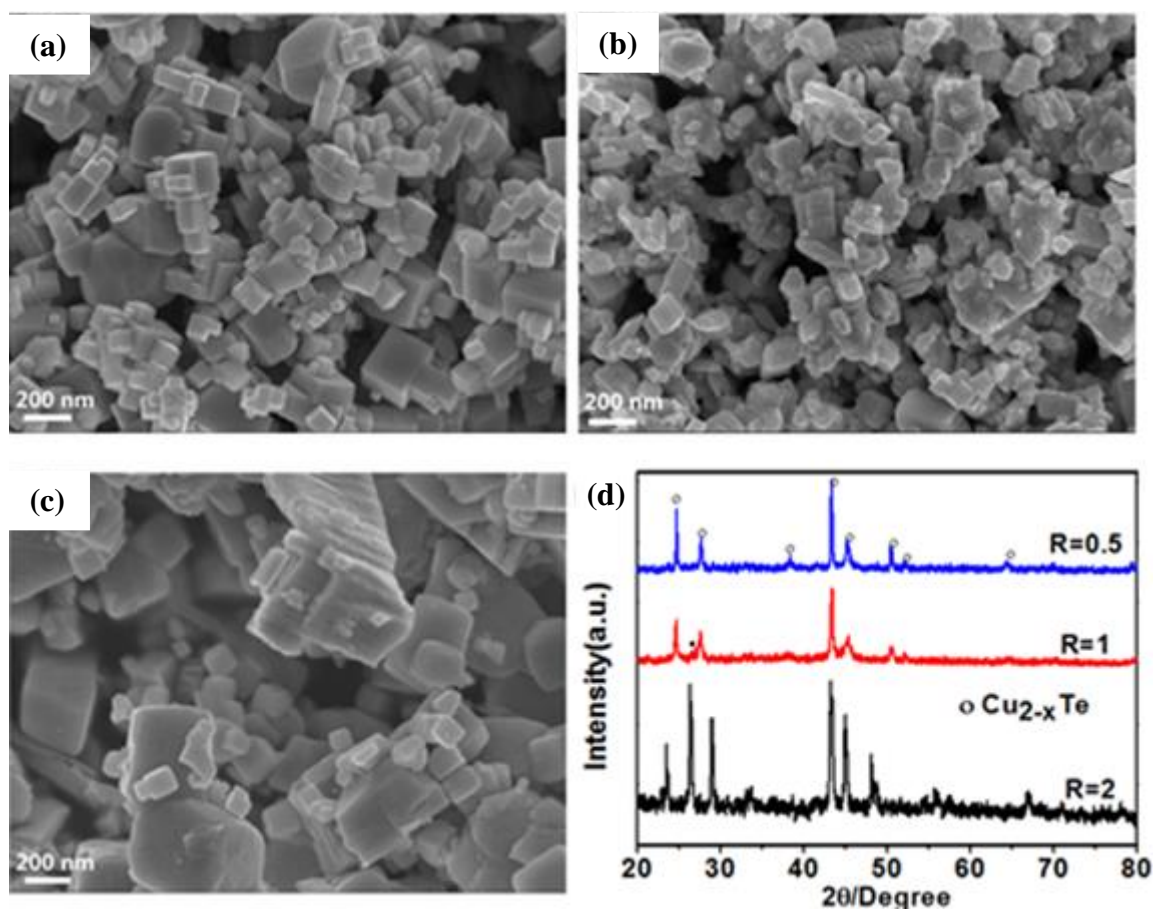


Figure 8.6. SEM images and XRD patterns of copper telluride nanostructures prepared from different Cu/Te ratios (R) by using 0.02 M CuCl reacted with 1 M TOPTe at 250 °C for 10 min: (a) R=2; (b) R=1; (c) R=0.5; (d) XRD patterns of the 3 samples.

Besides the above mentioned parameters, the CuCl/TOPTe ratio (R) also significantly influences the shape, composition, and crystal phase of the final products (E4 group in Table 8.1). The CuCl/TOPTe precursor ratio was varied from 10 to 0.5. As shown in Figure 8.6, the products changed from big irregular particles into rigid cubes as the ratio increased from 0.5 to 2. Higher R (i.e. more CuCl) leads to uniform nanocubes, which is demonstrated by the sample obtained from a ratio of 5, as shown in Figure 8.1(a). Their crystal structures and compositions also changed with increasing R [Figure 8.6(d)]. The Cu/Te ratios in the final products were identified by ICP measurements (Table 8.2, samples in E4 group), and they

slightly varied between 1.63 and 1.83, despite their different crystal structures. When R is higher than 5 (e.g. the sample prepared from a ratio of 10 in Figure 8.7), there is no difference in the sample morphology, particle size, or composition, in comparison with that prepared with a ratio of 5. The optimal Cu/Te precursor ratio for the formation of nanocubes is 5.

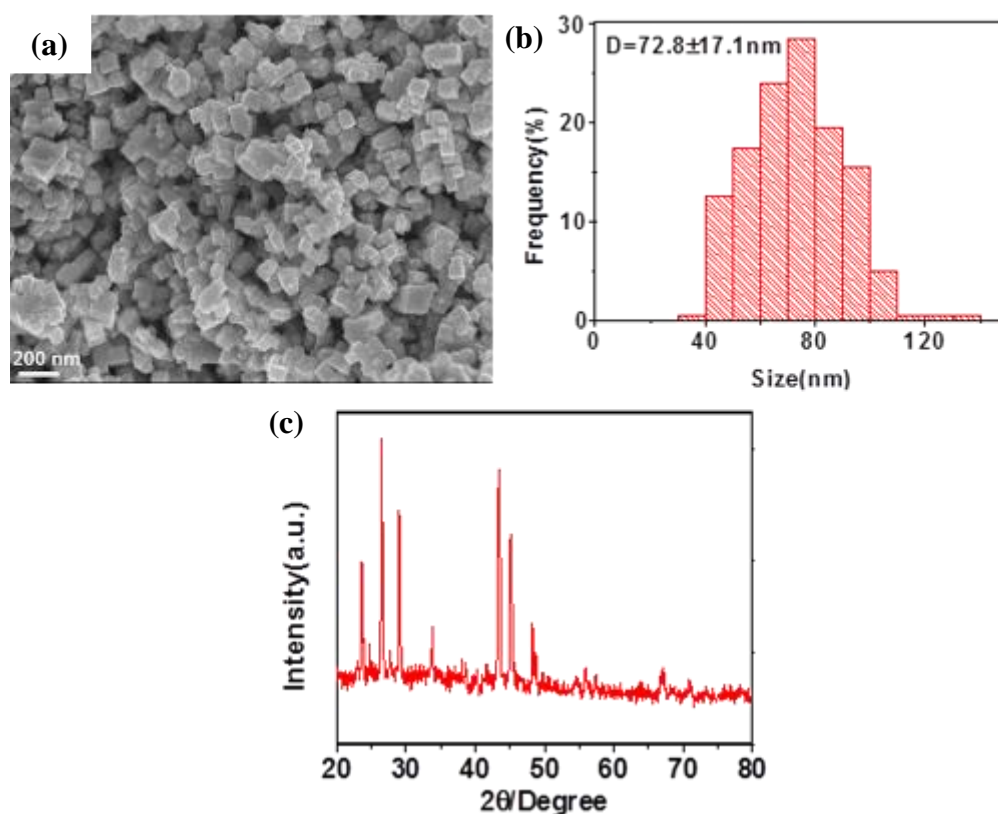


Figure 8.7. (a) SEM image, (b) size distribution and (c) X-ray diffraction pattern of copper telluride nanocubes synthesized with a ratio of 10 (CuCl/TOPTe).

The influence of TOP on the formation of copper telluride nanocubes was also investigated. A group of control experiments were carried out under the same conditions, except that the solvent was changed from TOP to oleylamine, oleic acid, and TOPO, respectively (E5 group in Table 8.1). The XRD patterns of the resultant products are displayed in Figure 8.8(a), showing that the product obtained in oleylamine is pure sheet-like Cu_{2-x}Te [Figure 8.8(b) and (d)], while the sample prepared in pure TOPO is a mixture of Te and CuTe, and the one prepared from oleic acid is also a mixture of $\text{Cu}_{1.85}\text{Te}$ and Cu_4Te_3 [Figure 8.8]. This result

demonstrates the importance of TOP in the formation of the pure cube structure. In order to further demonstrate its importance, traces of oleic acid, oleylamine, and TOPO (0.1 mmol in 10 ml TOP) were added into the TOP solution (E6 group in Table 8.1). Figure 8.9 presents the morphologies and crystal structures of the obtained products, which demonstrate that the size distribution of the nanocubes was seriously broadened in comparison with Figure 8.1(a) after the addition of small amounts of the ligands, especially when oleic acid was added [Figure 8.9(c)].

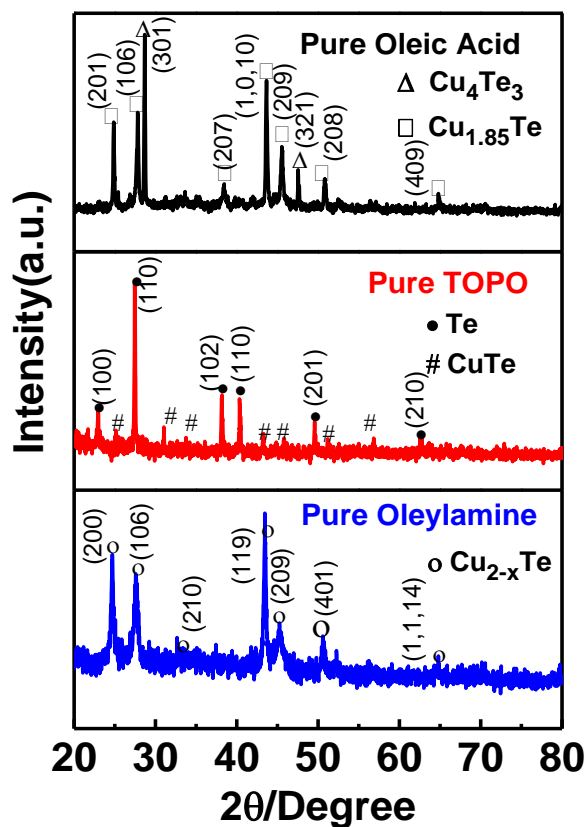


Figure 8.8. XRD patterns of samples prepared in oleic acid, TOPO and oleylamine.

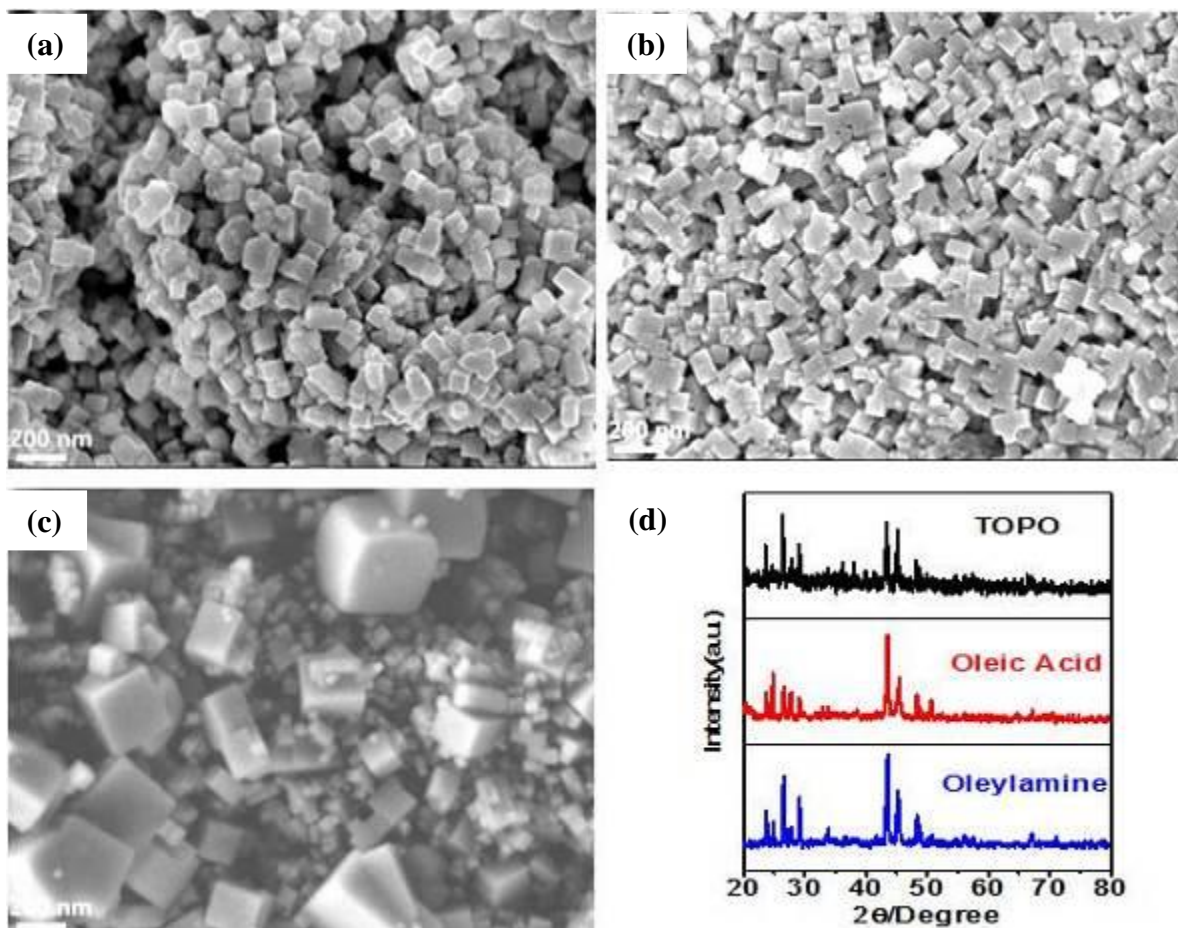


Figure 8.9. SEM images and XRD patterns of nanocubes prepared by adding small amount of ligands into TOP: (a) oleylamine; (b) TOPO; (c) oleic acid.

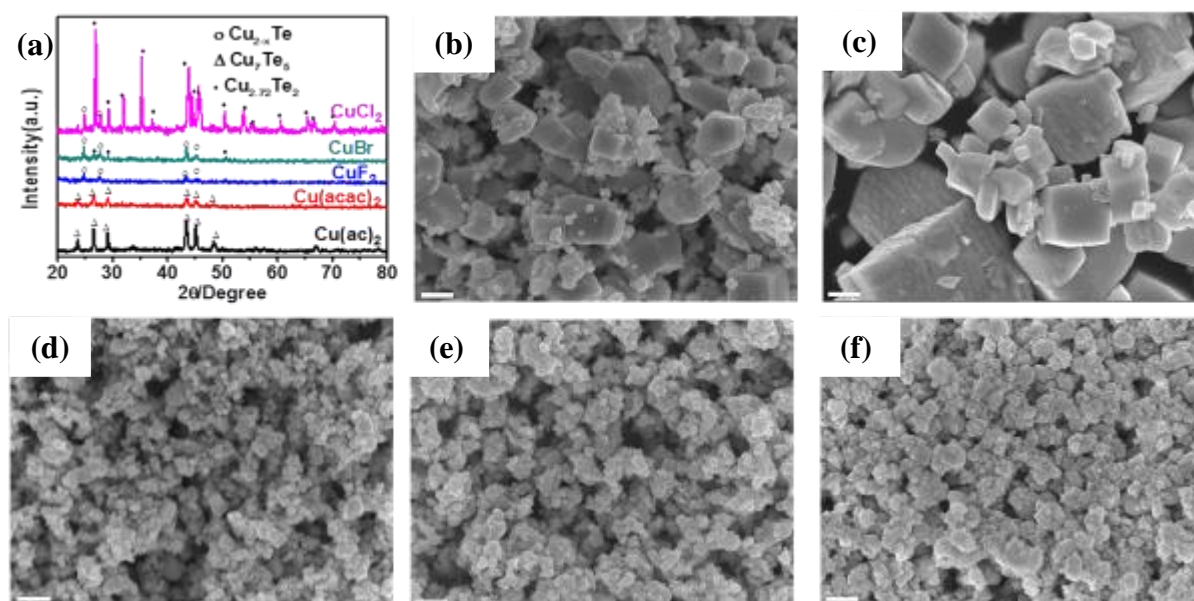
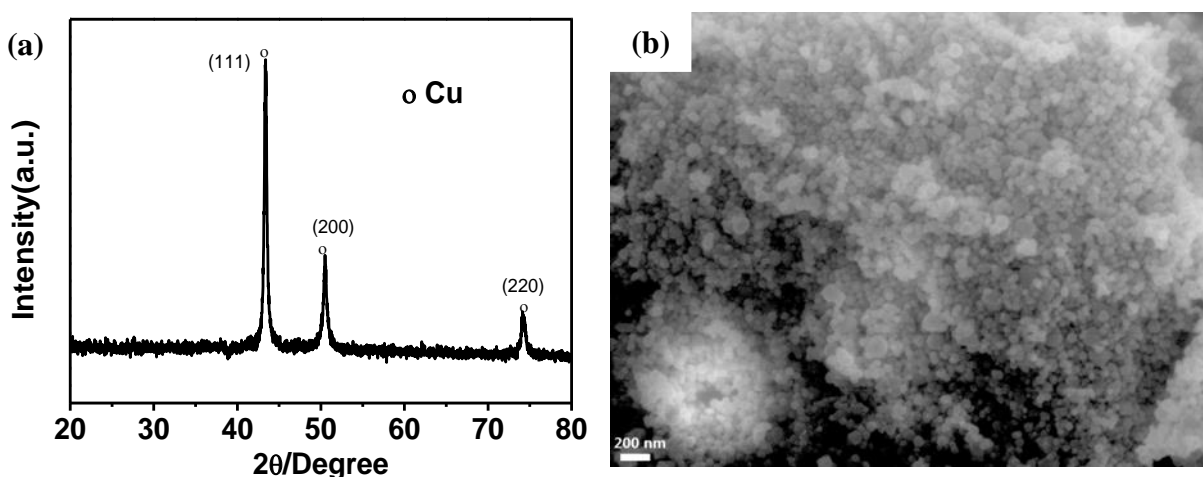


Figure 8.10. XRD and SEM images of samples prepared with different copper precursors. (a) XRD patterns; (b) CuBr; (c) CuCl₂; (d) CuF₂; (e) Cu(CH₃COO)₂; (f) Cu(acac)₂. All scale bars are 200 nm.

The effect of copper precursors was also studied (E7 group in Table 8.1). In addition to CuCl, three types of other copper precursors were chosen, including cuprous (I) bromide (CuBr), copper (II) halogenides (CuCl₂, CuBr₂, CuF₂), and organometallic copper acetate [Cu(ac)₂] and copper acetylacetonate [Cu(acac)₂]. The XRD pattern and morphology of each sample prepared from these precursors are shown in Figure 8.10. When CuCl was replaced by the similar CuBr, the product was a mixture of irregular big particles and small cubes [Figure 8.10(b)]. Its composition was also a mixture of Cu_{2-x}Te and Cu_{2.72}Te₂. These results are totally different from those obtained from CuCl precursor under the same conditions. When CuCl₂ and CuBr₂ were used as precursors, only CuCl₂ could yield irregular big particles made of Cu_{2-x}Te and Cu_{2.72}Te₂ [Figure 8.10(c)], and no product was obtained from CuBr₂ after the addition of TOPTe into its clear solution at 250 °C. CuF₂ could not be well dissolved in TOP below 200 °C, and the suspension became black and turbid above 220 °C. After purification of the black suspension, the XRD pattern and SEM image of the black precipitate prove that it consists of pure copper nanoparticles [Figure 8.11(a-b)]. This demonstrates the reducing capability of TOP, which has been utilized to prepare nanocatalysts in previous reports.^{365, 459, 460} After addition of TOPTe into the copper nanoparticles, the resultant product was pure irregular Cu_{2-x}Te nanoparticles [Figure 8.10(d)]. The different results obtained from cuprous or copper halogenides suggest the different reduction extent of the precursors and the different effects of halogen anions. The sample prepared from copper acetate also shows irregular particles, which were mainly made of Cu₇Te₅. The use of copper acetylacetonate resulted in a mixture of cubes and irregular nanoparticles, composed of pure Cu₇Te₅ [Figure 8.10(f)]. The exact Cu/Te ratios in these products were determined by ICP and are shown in

Table 8.2 (E7 group of samples). The Cu/Te ratio in the products prepared from CuBr (Sample E7-1) and CuCl₂ (Sample E7-2) precursors is around 1.70, which is close to that for the sample prepared from CuCl precursor and suggests similar reaction mechanisms for these three precursors. We speculate that these precursors first react with TOP to form a TOP-Cu complex at moderate temperature, and then react with TOPTe to form nanocubes under the assistance of TOP.⁴⁰² The TOP-Cu complex that is formed may stabilize the nanocube surface during growth, which also explains the requirement of excessive copper precursor (e.g. CuCl/TOPTe of 5) for the formation of nanocubes. The situation with CuCl₂ is more complex, as Cu²⁺ may be reduced to Cu⁺ first and then form the TOP-Cu complex.^{365, 459, 460} The reduction of copper (II) halcogenides by TOP is further demonstrated by the formation of pure Cu nanoparticles when CuF₂ was heated in TOP [as shown in Figure 8.11(a-b)]. The situation of Cu(CH₃COO)₂ (Sample E7-4) is more like that of CuCl₂, except for the different anions (i.e. CH₃COO⁻ vs Cl⁻). Compared with copper halogenides, Cu(acac)₂ (Sample E7-5) is easy to decompose at high temperature to form Cu or Cu₂O nanoparticles, which can react with TOPTe to form hollow or solid copper telluride nanoparticles. More investigations related to this precursor can be found in previous reports.^{222, 461}



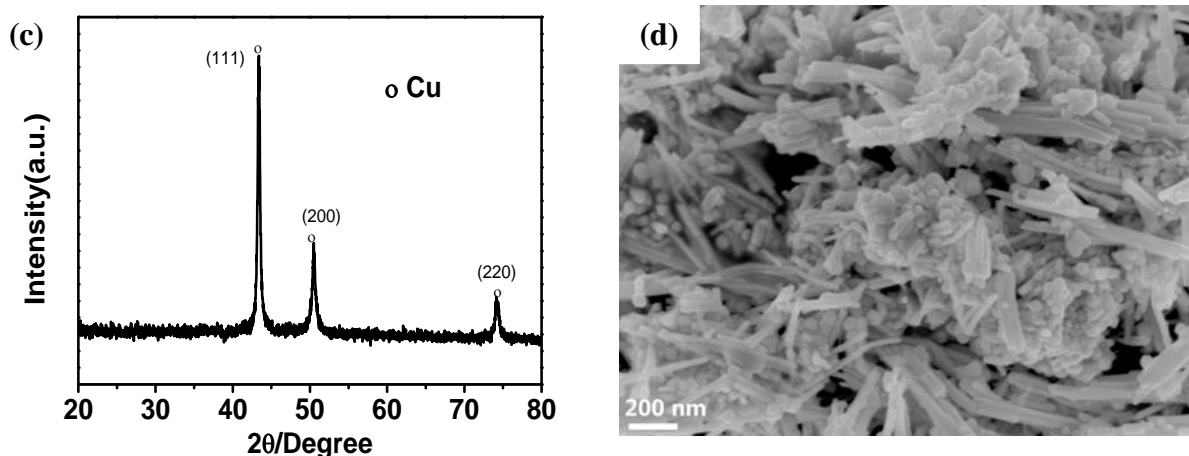


Figure 8.11. (a-b) XRD and SEM image of precipitate obtained by heating CuF_2 in TOP at 250 °C for 10 min. (c-d) XRD and SEM image of product obtained by heating CuCl in oleylamine at 250 °C for 10 min.

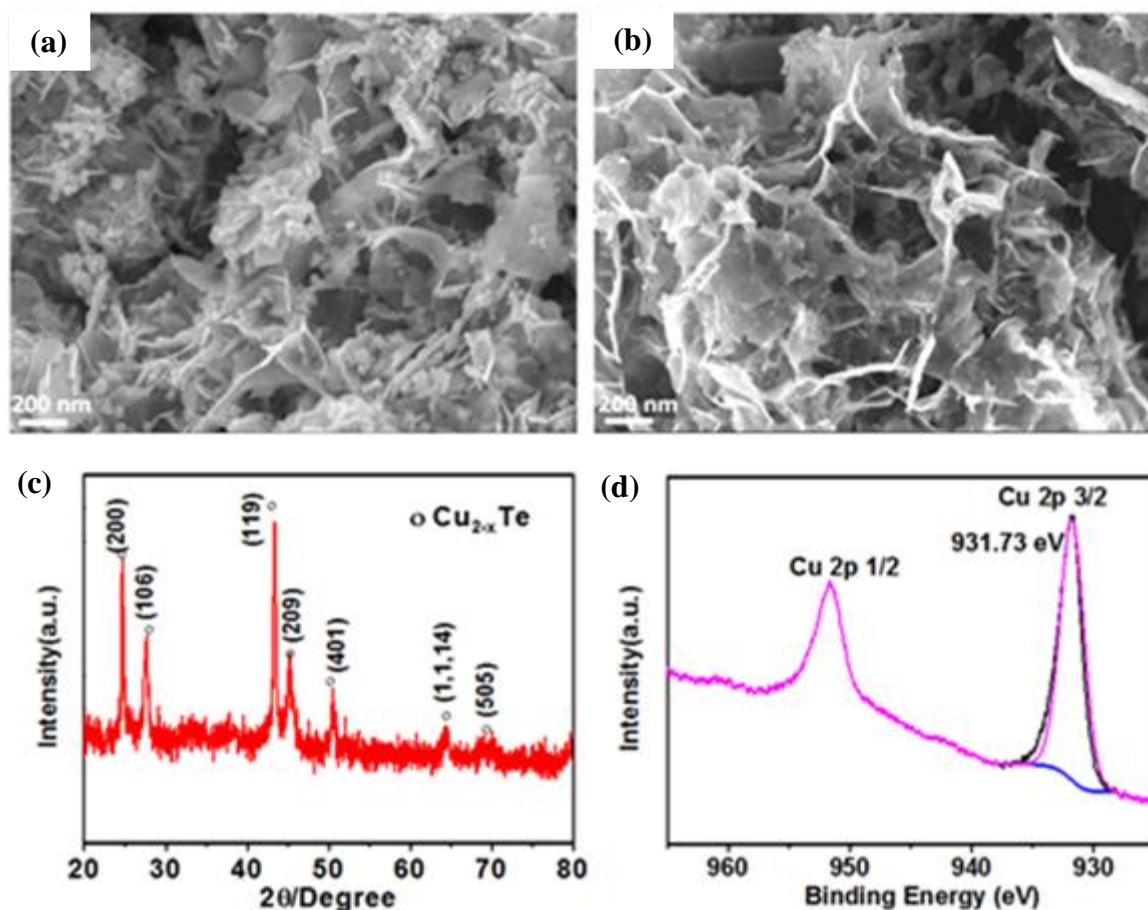


Figure 8.12. (a) SEM image of copper telluride nanosheets synthesized at 250 °C for 10 min with 0.02 M CuCl ; (b) SEM image of nanosheets synthesized at 230 °C for 10 min with 0.02 M CuCl .

M CuCl; (c) XRD pattern of nanosheets synthesized at 250 °C for 10 min with 0.05 M CuCl; (d) Cu 2p spectrum of copper telluride nanosheets synthesized at 250 °C for 10 min with 0.05 M CuCl.

8.3.2 Synthesis of Cu_{2-x}Te nanosheets.

The optimization of reaction parameters in the preparation of copper telluride nanocubes suggests that a reducing environment is necessary for the formation of single-phase product. Among the solvents investigated, only TOP and oleylamine have reducing capability. As demonstrated by Figure 8.12, Cu_{2-x}Te nanosheets can be prepared using 0.02 M CuCl and a CuCl/TOPTe ratio of 5 in oleylamine (Experiment E5-1 in Table 8.1). Further investigation shows that after CuCl was dissolved in oleylamine and heated to 250 °C for 10 min, the solution changed from green to yellow, then to brown, and finally to black. The black solution was cooled down and precipitated with ethanol to yield a black precipitate, which was identified as pure Cu nanoparticles and nanowires [Figure 8.11(c-d)]. After TOPTe was injected into the Cu-oleylamine solution, the copper nanoparticles and nanowires reacted with TOPTe to form Cu_{2-x}Te nanosheets. This means that oleylamine not only reduced CuCl to Cu at high temperature, but also served as a solvent and stabilizer during preparation.

The XPS spectrum of Cu 2p for this sample is shown in Figure 8.12(d). Two distinct peaks at 931.73 eV and 952.0 eV are assigned to Cu 2p_{3/2} and Cu 2p_{1/2}, respectively. The very weak, in fact negligible compared with the situation in Figure 8.1(d), the satellite peak at 942.5 eV means that the copper mainly exists as Cu^+ . The Te 3d core level spectrum in Figure 8.2(b) also confirms that no obvious oxidized product was present. The peak positions of Cu and Te are all consistent with those of Cu_{2-x}Te reported previously.^{222, 457, 458} The Cu/Te ratio was calculated to be 1.71 as shown in Table 7.2, i.e. the value of x is 0.29.

As shown in Figure 8.12(a), the product contains some nanoparticles. In order to obtain pure nanosheets, the reaction parameters were investigated one by one (E8, E9, and E10 groups in Table 8.1). In a similar way to the nanocubes prepared in TOP, the product varies case by case, which again demonstrates the complexity of copper tellurides. Figure 8.12(b) shows the nanosheets synthesized at lower temperature (i.e. 230 °C, Experiment E8-1 in Table 8.1). Although the nanoparticles in this product are reduced to some extent and they are hard to distinguish in the SEM image, they are clearly observed on the surfaces of the nanosheets under the TEM microscope [Figure 8.13(a)]. When the reaction temperature was increased to 270 °C (Experiment E8-2 in Table 8.1), the product had no nanosheets. There were only irregular large particles mixed with small ones [Figure 8.13(b)].

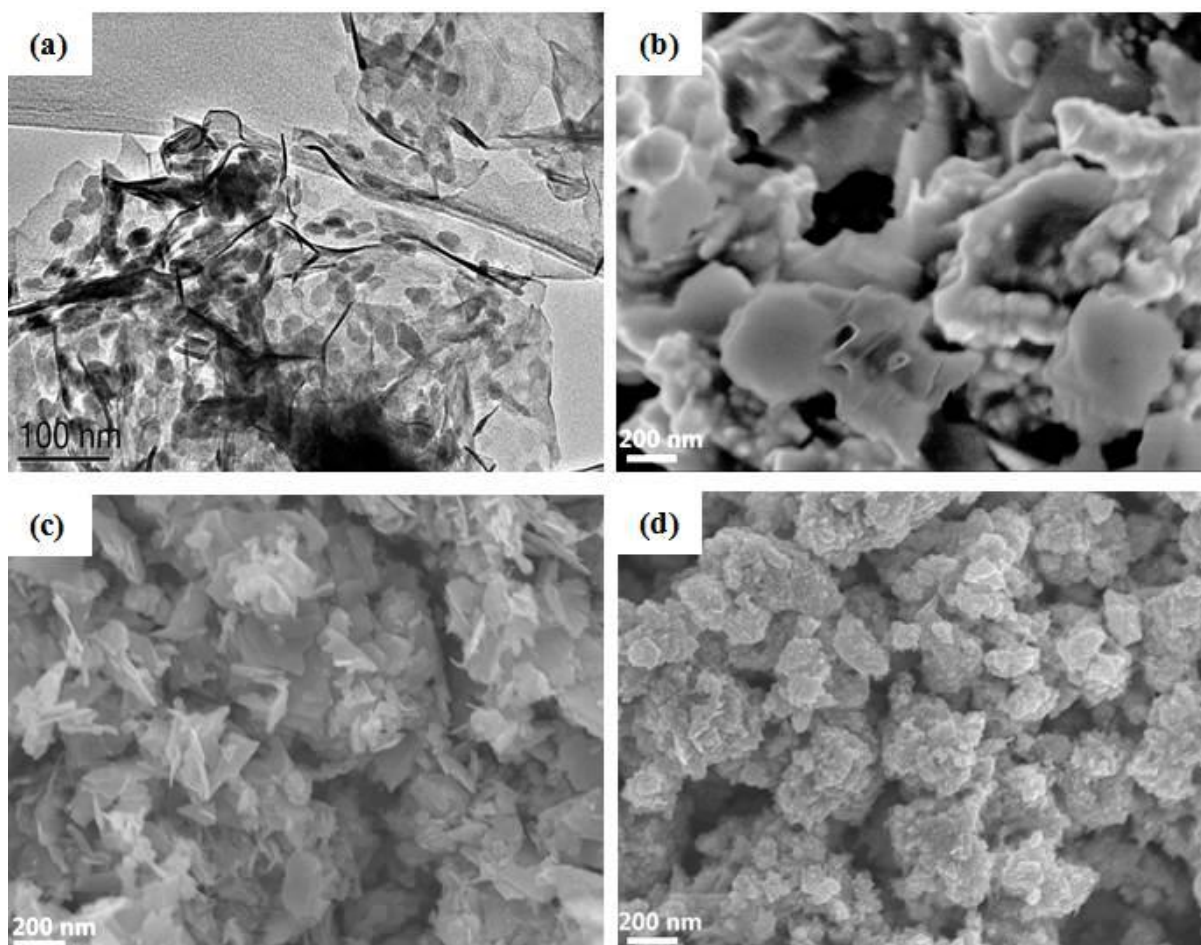


Figure 8.13. Different Cu_{2-x}Te sheet structure synthesized under different temperatures and CuCl concentrations. (a) TEM of sample synthesized with 0.02 M CuCl at 230 °C; (b) sample obtained from 0.02 M CuCl at 270 °C; (c) sample synthesized with 0.05 M CuCl at 250 °C; (d) sample synthesized with 0.005 M CuCl at 250 °C.

In addition to temperature, the formation of nanosheets is also influenced by the precursor concentration. Figure 8.13(c-d) shows the morphology of samples prepared with different CuCl concentrations. When the concentration of CuCl is decreased from 0.05 M to 0.005 M, the amount of nanoparticles obviously is increased (Experiments E9-1 and E9-2 in Table 8.1). The most suitable CuCl concentration for the formation of uniform nanosheets is therefore 0.05 M.

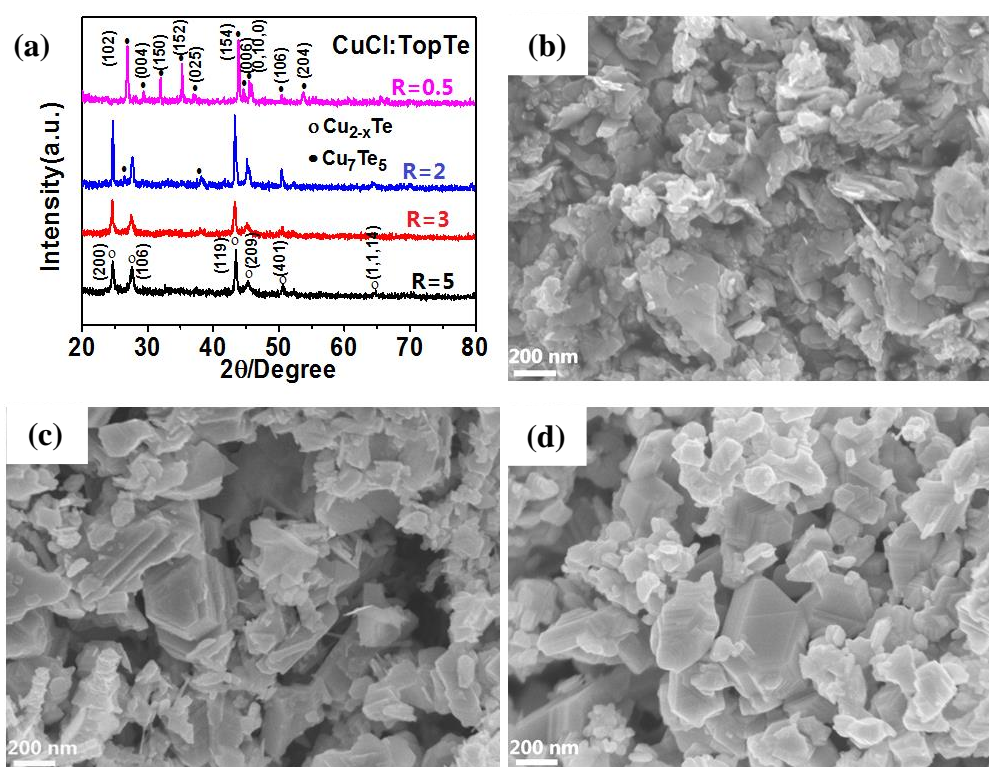


Figure 8.14. XRD patterns and SEM images of copper telluride nanostructures synthesized in pure oleylamine at 250°C for 10 min with different CuCl/TOPTe ratios (R): (a) XRD patterns; SEM images: (b) R = 3; (c) R = 2; (d) R = 0.5.

Figure 8.14 presents the morphology and crystal structures of samples synthesized from the same CuCl concentration (i.e. 0.05 M) with different CuCl/TOPTe ratios (R) (E10 group in Table 8.1). Similar to the case of the nanocubes, more CuCl promotes the formation of nanosheets. This supports the idea that the excess CuCl forms a complex with oleylamine to stabilize the nanosheets during growth. The sample morphology varied from irregular Cu_7Te_5 nanoparticles to sheet like Cu_{2-x}Te as R increased from 0.5 to 5. The minimum R for the formation of Cu_{2-x}Te nanosheets is 3, and the ideal ratio is 5.

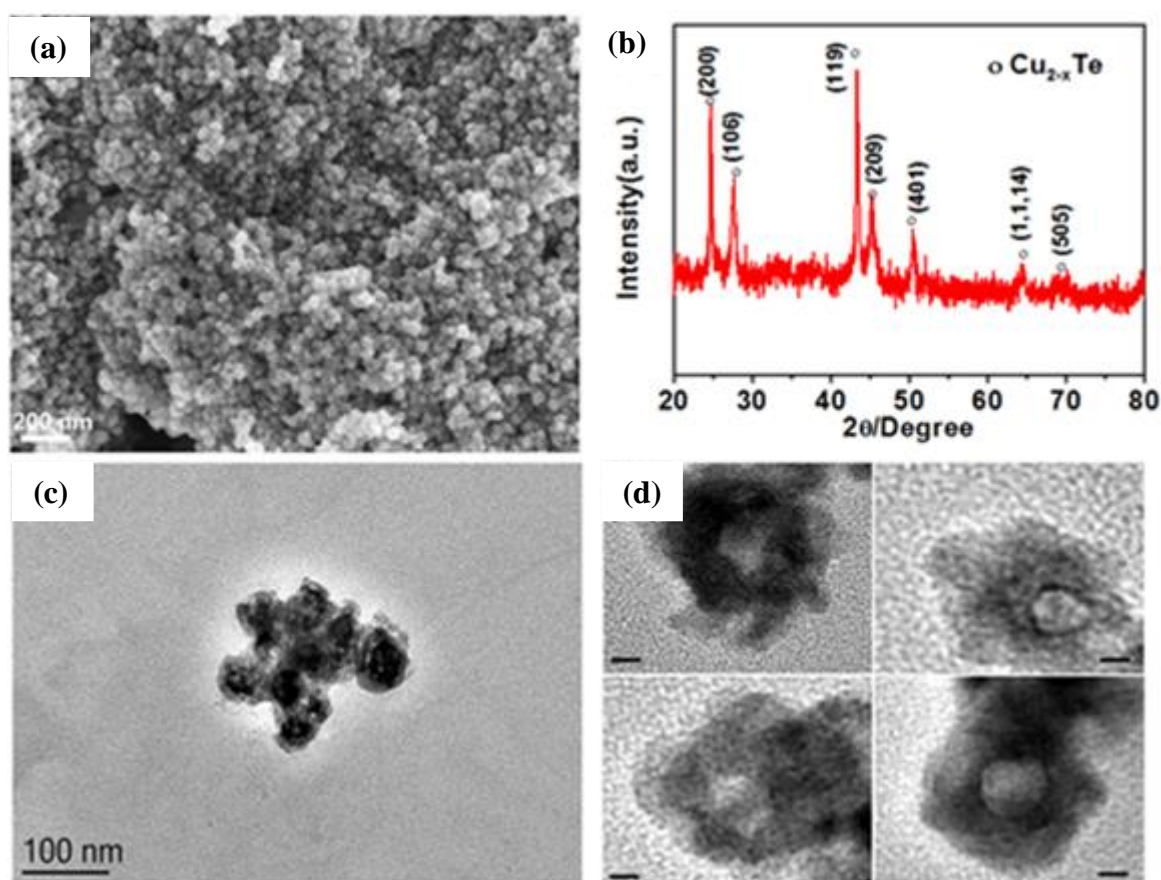


Figure 8.15. (a) SEM image, (b) XRD pattern, and (c-d) TEM images of hollow Cu_{2-x}Te nanoparticles synthesized by thermal decomposition of $\text{Cu}(\text{acac})_2$ in HDA. The scale bars in (d) are 10 nm.

As mentioned previously, copper chalcogenides have shown great potential in lithium ion batteries (LIBs) and sodium ion batteries (SIBs). We therefore tested the performance of the as-synthesized nanostructures as anodes in LIBs by using Cu_{2-x}Te nanosheets and $\text{Cu}_{1.67}\text{Te}$

nanocubes as examples. In order to demonstrate the effects of the nanostructured morphology on the performance of LIBs, we fabricated another reference electrode from hollow Cu_{2-x}Te nanoparticles (Figure 8.15), which were synthesized according to a previous report.²²² As shown in Figure 8.15, the synthesized nanoparticles are proven to be Cu_{2-x}Te with an average size around 40 nm. Both high and low magnification TEM images confirm their spherical and hollow structure. The Cu/Te ratio in the hollow Cu_{2-x}Te nanoparticles was calculated to be 1.69 (i.e. x value is 0.31) (Table 8.2).

8.3.3 Battery Performance of Cu_{2-x}Te As Anodes for the Lithium Ion Batteries.

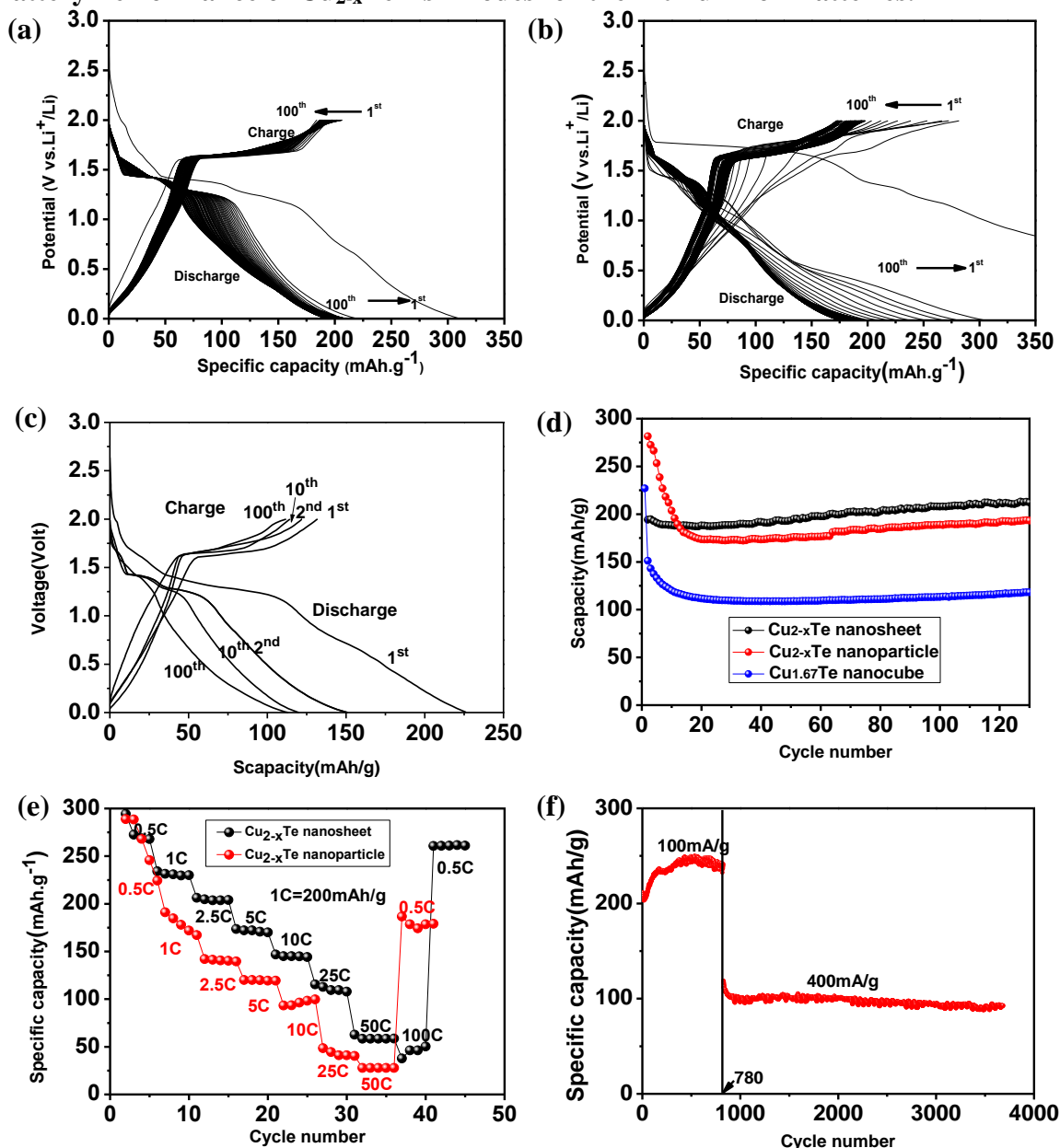


Figure 8.16. (a-c) Typical charge-discharge voltage profiles of the initial 100 cycles of the Li/LiPF₆/Cu_{2-x}Te batteries cycled at a current density of 0.5 C from 0 to 2 V. The anode electrodes are made from (a) nanosheets, (b) hollow nanoparticles, and (c) nanocubes, respectively; (d) cycling performance of cells from 0 to 2 V at the rate of 0.5 C; (e) charge-discharge curves of three cells at various current densities; (f) cycling performance of the Li/LiPF₆/Cu_{2-x}Te (nanosheet) battery between 0 and 2 V.

These three copper telluride nanostructures have similar Cu/Te ratios (i.e. Cu/Te ratios are 1.67, 1.71 and 1.69 for nanocubes, nanosheets and hollow nanoparticles, respectively), and the electrochemical performances of their electrodes are compared in Figure 8.16. Figure 8.16(a) presents the charge-discharge curves of electrode made from Cu_{2-x}Te nanosheets. There are two potential plateaus in the discharge curve, located at 1.4 and 1.3 V, respectively. Correspondingly, the charge curve shows one potential plateau at 1.6 V. After 100 cycles, the charge-discharge curves overlap well, suggesting that the Cu_{2-x}Te sheet-based electrode has good cycling stability. In comparison, the Cu_{2-x}Te hollow-particle based electrode was not stable in the first 10 cycles, although it became stable after that [Figure 8.16(b)]. The charge-discharge curves of electrode made from Cu_{1.67}Te nanocubes are shown in Figure 8.16(c), and the potential plateaus are almost the same as for the electrodes fabricated from Cu_{2-x}Te nanosheets and hollow nanoparticles, although its capacity is much lower than those of Cu_{2-x}Te cells made from nanosheets and hollow nanoparticles. Figure 8.16(d) shows the cycling performance of the three electrodes fabricated from copper telluride nanosheets, hollow nanoparticles, and nanocubes. Their theoretical capacities were calculated on the basis of Cu/Te ratios and listed in Table 8.3, which reached to 229.3 mAh/g, 226.9 mAh/g, and 228.1

mAh/g, respectively. Hence the composition of these three copper chalcogenides showed little influence on the capacity.

The above measured capacities of copper telluride electrodes are similar to those of electrodes made from copper sulfides or selenides.⁴⁵¹⁻⁴⁵⁴ Similar to other nanostructure based electrodes, their capacities drop in the first few cycles due to the irreversible absorption of Li ions on the surface, and the capacities of the nanoparticle and nanocube electrodes decrease much faster than that of the nanosheet electrode, i.e., the capacity of the nanoparticle electrode decreases from 282 mAh/g to 180 mAh/g after 20 cycles, and that for the nanocube electrode decreases from 220 mAh/g to 120 mAh/g after 10 cycles. In contrast, the capacity of the nanosheet electrode slightly decreases and then increases to 200 mAh/g as cycling proceeds. As illustrated by Figure 8.16(e), the Cu_{2-x}Te nanosheet electrode also has the best rate capability among the three cells. Even at a charge-discharge rate of 100 C (1 C = 200 mA/g), its discharge capacity was still 50 mAh/g, which is superior to the rate capability of the nanoparticle and nanocube electrodes.

Table 8.3. Copper deficiency (i.e. x values) and theoretical capacity^[a] of the three copper tellurides used as anodes of LIB.

Compound	Cu/Te	x value	Theoretical capacity (mAh/g)	Stable capacity ^[b] (mAh/g)
Cu _{1.67} Te nanocube	1.67:1	0.33	229.33	120
Cu _{2-x} Te nanosheet	1.71:1	0.29	226.86	200
Cu _{2-x} Te nanoparticle	1.69:1	0.31	228.09	180

[a] Theoretical capacity (C_t , mAh/g) was calculated by the following equation:

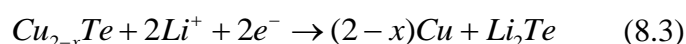
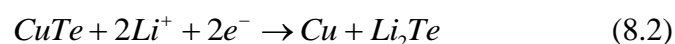
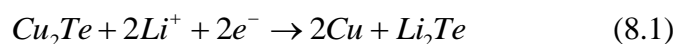
$$C_t = \frac{26800 \times n}{M}$$

In which n is the number that transferred during the electrochemical reaction; M is the molecular weight of the electrode material (g/mol).

[b] This referred to the capacity after 20 cycles at 100mA/g charge-discharge rate.

From the above data, it can be concluded that the Cu_{2-x}Te nanosheet electrode has the highest capacity and the best rate capability among the three types of electrodes, highlighting the importance of controlling nanostructure morphology. The excellent performance of the nanosheet electrode is attributed to the better electronic contact and uniformity of the nanosheets compared to the nanoparticles, as demonstrated for other two-dimensional (2D) electrodes.⁴⁶² To further study the stability of the nanosheet electrode, another cell was assembled and the charge-discharge current density of the battery was increased from 100 mA/g to 400 mA/g at the 780th cycle, leading to a decrease of capacity from 220 mAh/g to 113 mAh/g and then kept stable at around 90 mAh/g, even after 5000 cycles [Figure 8.16(f)]. This demonstrates the extremely high cycling stability of the nanosheet electrode.

The excellent cycling performance of copper telluride nanostructures as anode of LIBs is attributed to their variable compositions and structures. Our nanostructures have both Cu^+ and Cu^{2+} , and they have a hexagonal crystal structure whether they are Cu_2Te , CuTe , or Cu_{2-x}Te , in which the tellurium anions form a crystalline lattice and the copper cations are located in the sublattice. Replacement of copper ions with Li^+ cannot seriously change the volume of the unit cell, as the effective radii of Cu^+ (0.77 Å) and Cu^{2+} (0.73 Å) are similar to that of Li^+ (0.76 Å). The “displacement” reactions [Equation (8.1) and (8.2)] between Cu_2Te , CuTe , and Li_2Te in the cells cause no significant volume expansion, leading to the extremely high cycling stability of the cells. The overall reaction could be simplified as Equation (8.3).



Besides the cycle stability, another obvious merit of copper tellurides lay in its higher density and discharge voltage, which would lead to a high volumetric capacity.

8.4 Conclusions.

In summary, a simple hot-injection approach was developed to synthesize various copper telluride nanostructures. The influence of preparation parameters on the morphology, crystal structure, and composition has been systematically investigated. The results show that $\text{Cu}_{1.67}\text{Te}$ nanocubes can be obtained from CuCl precursor by using a high CuCl/TOPTe ratio (above 5) in TOP. Replacing TOP with oleylamine leads to Cu_{2-x}Te nanosheets. These copper telluride nanostructures have potential as anodes in rechargeable batteries due to their excellent cycling stability, as demonstrated by the LIB anodes made from Cu_{2-x}Te nanosheets, hollow Cu_{2-x}Te nanoparticles, and $\text{Cu}_{1.67}\text{Te}$ nanocubes, which have a specific capacity of 220 mAh/g, 180 mAh/g and 120 mAh/g, respectively. The Cu_{2-x}Te nanosheet cell could be charged-discharged over 5000 cycles, and its excellent cycling stability highlights its potential in long-life rechargeable batteries.

Chapter 9. General Conclusions and Outlook

9.1 General Conclusions.

In this doctoral work, three different synthetic routes on different nanostructured metal chalcogenides are developed. The influence of different synthetic parameters on the quality of final nanostructures is comprehensively investigated. Besides, their applications on thermoelectric, counter electrodes of quantum dot sensitized solar cells, and anode materials for lithium/sodium ion batteries are tested. Conclusions can be made as following:

(1) A robust and scalable aqueous method to the synthesis of different nanostructured thermoelectric metal chalcogenides is developed. The method includes reduction of chalcogen source and precipitation with metal ions. Benefit from the low solubility of metal chalcogenides in aqueous solution and the formation of H_2 bubble by hydrolyze of $NaBH_4$, uniform nanoparticles of Bi-, Pb-, Cu-, Ag-, Sn- chalcogenides ranging 10-20 nm can be obtained, plus nanorods of Bi_2S_3 with a diameter of 50-70 nm. This method is an environmental-friendly process for the preparation of low-cost metal chalcogenide nanomaterials for thermoelectric applications.

(2) The particle size and composition of metal chalcogenides could be easily tuned by the amount of reducing agent, the concentration of precursors, and the reduction time. With increasing precursor concentration and prolonging the reducing time of chalcogen source, the size of the final product can be increased. The amount of reduce agent plays significant role on the composition of product. The amount of acid and reaction speed plays significant role on crystallinity of bismuth chalcogenides.

(3) The resultant nanostructured metal chalcogenides are consolidated by spark plasma sintering technique. Lots of nanostructures can be preserved in these sintered bulk and no

composition changes are observed except significant improvement crystallinity of amorphous Bi_2Se_3 nanoparticles. Thermal stability of these four selenides are checked by thermal analyze. The results show obvious weight loss above 300-400 °C for Bi_2Se_3 and SnSe . No obvious weight loss can be observed on Ag_2Se and Cu_2Se nanobulk.

(4) The four selenides nanobulks are tested as potential thermoelectric materials. Compared with references, sintered Bi_2Se_3 and SnSe nanobulk show pronounced enhancement in the figure of merit values (ZTs) due to the presence of nanograins or nanopores, which can effectively decrease the thermal conductivity. However, excess amount of grain boundaries may also do harm to electrical conductivity, which leads to lower ZT on Cu_2Se and Ag_2Se nanobulks.

(5) Large-scale surfactant-free irregular CuAgSe nanoparticles were successfully synthesized via the reduction-precipitation aqueous method. Several groups of control experiment are conducted to investigate its mechanism. In the first steps, Selenium powder was reduced by NaBH_4 to form a Se precursor. Then the mixed solution of Cu^{2+} and Ag^+ ions is added into the Se precursor. Immediately, Cu^{2+} ions are reduced by excess NaBH_4 , Cu_2Se and Ag_2Se precipitates immediately, which then alloyed to form ternary CuAgSe .

(6) The resultant CuAgSe nanoparticles were sintered into pellets by an advanced SPS technique for thermoelectric investigation in the range of 3 K to 623 K. The results show an interesting temperature-dependent transport property accompanied by a phase transition, i.e. sintered CuAgSe nanoparticles exhibit metallic characteristics below 60 K, n-type semiconductor behavior in the range of 60 K to 480 K, and p-type semiconducting behavior above 480 K.

(7) The sintered CuAgSe pellet displays a ZT of 0.42 at 323 K and 0.9 at 623 K, and exhibits excellent cycling stability, the sample weight, composition, as well as morphology

did not change after 5 cycles of heating and cooling. The temperature-dependent n-p transition and the excellent stability of CuAgSe enable it to simultaneously serve as a promising n-type and promising p-type (at different temperatures) thermoelectric candidate for conversion of heat into electricity.

(8) Cu_2Te nanotubes and nanosheets are synthesized from Cu_2E ($\text{E} = \text{O}, \text{S}, \text{Se}$) via a simple anion exchange reaction in aqueous system at room temperature. Different from simple Kirkendall effect, the formation mechanism of nanosheets structure is ascribed to an exchange-peeling mechanism and the effect of unique crystal structure of Cu_2Te .

(9) The effect of reaction parameters on thickness, size of the Cu_2Te nanosheets are investigated using Cu_2Se nanoparticles as precursor. The results proved that with increasing of precursor concentrations or amount of NaBH_4 , the nanosheets became thicker, larger and much uniform; while the particles size of Cu_2Se precursor did not affect too much on quality of final product. And with increasing of stirring speed, length of Cu_2Te nanotubes decreased.

(10) Thus-formed Cu_2Te nanosheets, nanotubes and nanoparticles prepared by reduction-precipitation method are tested as counter electrodes in CdS/CdSe co-sensitized solar cells and show excellent catalytic activity towards the electrolyte compared with expensive Au counter electrodes. The performance of Cu_2Te strongly depends on its morphology, in which Cu_2Te nanosheets showed the maximum conversion efficiency of 5.35 % and Cu_2Te nanoparticles showed a value of 4.47 %. Considering their low cost and high catalytic activity, these Cu_2Te nanostructures have great potential in energy conversion.

(11) A $\text{Bi}_2\text{S}_3@\text{C}$ composite was fabricated by the aqueous reaction-precipitation method combined with ball milling.

(12) In this composite, Bi_2S_3 nanorods are first covered by an amorphous carbon layer and then wrapped with graphite nanoplates. The amorphous carbon layer significantly improved the electronic conductivity of Bi_2S_3 and prevented dissolution of Bi_2S_3 . The graphite nanoplates serve as both conductive layers and a buffer to alleviate the stress from volume expansion to avoid pulverization. Because the $\text{Bi}_2\text{S}_3@\text{C}$ composite possesses two active elements, Bi and S, and a good conductivity; it can deliver a reversible capacity as high as $550 \text{ mAh}\cdot\text{g}^{-1}$ for sodium storage. Besides, the $\text{Bi}_2\text{S}_3@\text{C}$ composite exhibits excellent cycling stability compared with Bi_2S_3 . Over 100 cycles, the $\text{Bi}_2\text{S}_3@\text{C}$ composite delivered $282 \text{ mAh}\cdot\text{g}^{-1}$, with 69% capacity retention compared with the second cycle.

(13) Moreover, the sodium storage mechanism of Bi_2S_3 is also well. The results demonstrate that the sodium ion storage mechanism is a substitution and insertion reaction, in which Bi_2S_3 reacts with Na to form Bi and Na_2S ; then Na is inserted into Bi layers to form 3 NaBi molecules. The low polarization, high density, and excellent cycling performance make $\text{Bi}_2\text{S}_3@\text{C}$ a promising anode candidate for sodium ion batteries.

(14) A simple hot injection approach was developed to synthesize various copper telluride nanostructures. $\text{Cu}_{1.67}\text{Te}$ nanocubes, Cu_{2-x}Te nanosheets and hollowed nanoparticles are fabricated by this method with different conditions.

(15) The influence of preparation parameters on the morphology, crystal structure, and composition has been systematically investigated. The results show that $\text{Cu}_{1.67}\text{Te}$ nanocubes can be obtained from CuCl precursor by using a high CuCl/TOPTe ratio (above 5) in TOP. Replacing TOP with oleylamine leads to Cu_{2-x}Te nanosheets.

(16) These copper telluride nanostructures including Cu_{2-x}Te nanosheets, hollow Cu_{2-x}Te nanoparticles, and $\text{Cu}_{1.67}\text{Te}$ nanocubes, are tested as anodes in lithium ion. They show a specific capacity of 220 mAh/g , 180 mAh/g and 120 mAh/g , respectively. The Cu_{2-x}Te

nanosheet cell could be charged-discharged over 5000 cycles without degradation.

9.2 Future work.

In general, although the synthesis, relevant chemicals-physical properties, and structures of nanostructured metal chalcogenides have been investigated for a long time, it is still one of the hottest materials, especially in the field of energy and environmental science. And, all the investigations and applications are based on their synthesis, although several new synthesis strategies are developed in this doctoral work, further improvements are still needed.

9.2.1 Future Work on Synthesis of Nanostructured Metal Chalcogenides.

In this doctoral work, an aqueous, low cost, scalable and efficient wet chemical synthetic route for different nanostructured metal chalcogenides has been developed. It is general, low cost and high efficiency method. Good size and composition control could be easily achieved by adjusting reaction parameters; however, morphology and reaction speed control is almost impossible as no any surfactants and templates are used. To overcome this drawback and preserve all the existed merits, the following work should be done:

- (1) It is possible to improve crystallinity of product by adjusting precipitation speed by adding pH control chemicals or by increasing reaction temperature.
- (2) Try to add small amount water soluble molecules as surfactants, such as polyvinylpyrrolidone (PVP), ethylenediaminetetraacetic acid (EDTA), mercaptoethanol (MCE), thioglycolic acid, etc. into the metal ions. For one thing, these surfactants can prevent aggregation of nanostructures, i.e. get mono-dispersed or smaller nanostructures. For another thing, it is possible to get nanostructures with different morphology. Thirdly, some components in these surfactants, such as thio- group may offer S dopants into the nanostructures.

(3) Having got two kinds of mono-dispersed nanostructures by surfactants with different charge types, it is possible to create new alloyed nanostructures under low temperature in large scale.

(4) Another important way to improve this aqueous method is by replacing water with other non-expensive organics, such as ethanol, ethylene glycol, etc.. For one thing, other metal chalcogenides which are easy to form metal hydroxides with water [i.e., $K_{sp}(\text{hydroxides}) < K_{sp}(\text{chalcogenides})$], may be fabricated, such as In- and Fe- chalcogenides. For another, the control over morphology may be achieved.

Based on the aqueous reduction-precipitation method and simple anion exchange reaction, Cu_2Te nanosheets and nanotubes can be fabricated. Further control over its properties may be achieved with employment following strategies:

(1) Although the transition mechanism has been developed, detailed transfer process from cubic Cu_2Se to hexagonal Cu_2Te including atom rearrangement and unit cell evolution is unclear. Ideal technique should be the liquid phase in-situ TEM.

(2) Usage of surfactants or other solvent may affect formation procedure of Cu_2Te nanosheets and thus may form different nanostructures, such as single atomic layer Cu_2Te .

(3) It is possible to seal the rolled nanotubes by surface modifications of the Cu_2Te nanosheets, which can be used to drug delivery or fabrication of composites.

As for the organic based hot injection method, although good control over size, morphology and composition could be easily achieved, its yield is too low and the cost is high, not mention the usage of harmful organics. Thus the possible of using solvothermal and replacing expensive high boiling point organics with other common solvents, such as low cost ethylene glycol, or other polyols will be tested. And at the same time, the reaction temperature can be

reduced.

9.2.2 Future Work on Applications of Nanostructured Metal Chalcogenides.

Based on the scalable aqueous synthetic route, thermoelectric application of these nanostructured metal chalcogenides can be achieved. Although significant decrease on thermal conductivity is observed in the sintered nanobulk, excess amount of boundaries sharply decrease electrical conductivity and lead to poor thermal stability. To further improvement of its performance, several works can be done:

(1) To eliminate the adverse effect of grain boundaries, surface modification on these nanostructures is needed. One thought is using inorganic nanocrystals with similar structures or low melting points to act as a kind of glue to increase bonding of nanostructures, which finally leads to increase of electrical conductivity. Another route is surface engineering to introduce other impurities to increase carrier concentrations.

(2) Instead of using single nanocrystals, combining these nanocrystals with other micro scale powders can form the full scale length phonon scattering while decrease the bad effect of boundaries. This could also increase thermal stability of the sintered bulk.

(3) As Bi_2Se_3 and SnSe show better performance than corresponding bulks, further improvement based on them will be done, such as introducing impurities via doping, increase preferential crystalline via heat treatment.

(4) The thermoelectric performance of CuAgSe are rarely reported, especially the effects of doping by different elements. And because it possesses layered orthorhombic structures, formation of single crystal is another possible way to enhance its thermoelectric performance.

Nanostructured Cu_2Te showed excellent electrocatalytic activity towards polysulfides electrolyte of quantum dot sensitized solar cells compared with expensive Au. Its cycle and

thermal stability would be further investigated. Besides, the counter electrodes performance of other analogous such as Cu_2S nanoparticles, Cu_2Se nanoparticles should be also investigated to compare with Cu_2Te nanosheets.

$\text{Bi}_2\text{S}_3@\text{C}$ composite showed superior cycle stability as well as reasonable high capacity as anode of sodium ion batteries or cathode of room temperature Na-S batteries. Further investigations should be focused on several directions.

(1) It has been shown that the coated carbon layer and plate like graphite plays important role in improving its performance compared with bare Bi_2S_3 , but it is difficult to get graphite nanoplates without presence of Bi_2S_3 . This reminds the effect of suitable nanostructures can promote peeling of layered structures, which needs further investigation.

(2) Other similar composites, such as SnS , Sb_2S_3 nanoparticles fabricated from the aqueous reduction-precipitation method are also worthy investigating.

(3) Despite the significant improvement effect of carbon layer, using chemical method to direct load metal chalcogenides nanostructures onto graphene or ball milled the nanostructures with graphite may become a general strategy to fabricate high performance anode materials with low cost.

Performance of Cu_2Te nanosheets synthesized from the hot injection method as anode of lithium ion batteries has been proved to showed excellent cycle stability due to the similar ion radius of Li^+ and Cu^+ ions. Other analogous, such as Cu_2S and Cu_2Se fabricated from the large scale aqueous method, as well as Cu_2Te nanosheets synthesized from the anion exchange reaction, should have similar cycle stability towards lithium ion batteries. Especially, Cu_2S and Cu_2Se are less toxic, much cheaper and show higher gravimetric specific capacity than Cu_2Te ; thus can yield better performance than Cu_2Te .

Reference

- [1]. S. L. Candelaria, Y. Shao, W. Zhou, X. Li, J. Xiao, J.-G. Zhang, Y. Wang, J. Liu, J. Li and G. Cao. *Nano Energy*, 1 (2012) 195-220.
- [2]. N. Fromer and M. Diallo. *Journal of Nanoparticle Research*, 15 (2013) 1-15.
- [3]. Y. X. Gan, B. J. Gan, E. Clark, L. Su and L. Zhang. *Materials Research Bulletin*, 47 (2012) 2380-2388.
- [4]. N. Linares, A. M. Silvestre-Albero, E. Serrano, J. Silvestre-Albero and J. Garcia-Martinez. *Chemical Society Reviews*, 43 (2014) 7681-7717.
- [5]. P. K. Nair, M. T. S. Nair, V. M. García, O. L. Arenas, A. C. Y. Peña, I. T. Ayala, O. Gomezdaza, A. Sánchez, J. Campos, H. Hu, R. Suárez and M. E. Rincón. *Solar Energy Materials and Solar Cells*, 52 (1998) 313-344.
- [6]. T. Wang, Z. Luo, C. Li and J. Gong. *Chemical Society Reviews*, 43 (2014) 7469-7484.
- [7]. H. Xia, M. Z. Hu, Y. S. Meng, J. Xie and X. Zhao. *Journal of Nanomaterials*, 2014 (2014) 2.
- [8]. G.-L. Xu, Q. Wang, J.-C. Fang, Y.-F. Xu, J.-T. Li, L. Huang and S.-G. Sun. *Journal of Materials Chemistry A*, 2 (2014) 19941-19962.
- [9]. M.-R. Gao, J. Jiang and S.-H. Yu. *Small*, 8 (2012) 13-27.
- [10]. R. S. Mane and C. D. Lokhande. *Materials Chemistry and Physics*, 65 (2000) 1-31.
- [11]. Y. Min, G. D. Moon, C.-E. Kim, J.-H. Lee, H. Yang, A. Soon and U. Jeong. *Journal of Materials Chemistry C*, 2 (2014) 6222-6248.
- [12]. H. Wang, Y. Liang, Y. Li and H. Dai. *Angewandte Chemie International Edition*, 50 (2011) 10969-10972.
- [13]. C. Zhao, D. Li and Y. Feng. *Journal of Materials Chemistry A*, 1 (2013) 5741-5746.
- [14]. Z. Chen, D. Higgins, A. Yu, L. Zhang and J. Zhang. *Energy & Environmental Science*, 4 (2011) 3167-3192.
- [15]. Y. Feng, A. Gago, L. Timperman and N. Alonso-Vante. *Electrochimica Acta*, 56 (2011) 1009-1022.
- [16]. F. Liu, J. Zhu, L. Hu, B. Zhang, J. Yao, M. K. Nazeeruddin, M. Gratzel and S. Dai. *Journal of Materials Chemistry A*, 3 (2015) 6315-6323.
- [17]. J.-H. Park, T. I. Lee, S.-H. Hwang, K.-J. Moon and J.-M. Myoung. *Progress in Photovoltaics: Research and Applications*, 23 (2015) 813-820.
- [18]. X. Yu, J. Zhu, F. Liu, J. Wei, L. Hu and S. Dai. *Science China Chemistry*, 56 (2013) 977-981.
- [19]. X. Yu, J. Zhu, Y. Zhang, J. Weng, L. Hu and S. Dai. *Chemical Communications*, 48 (2012) 3324-3326.
- [20]. D. Aldakov, A. Lefrancois and P. Reiss. *Journal of Materials Chemistry C*, 1 (2013) 3756-3776.
- [21]. S. Dolai, P. Dutta, B. B. Muhoberac, C. D. Irving and R. Sardar. *Chemistry of Materials*, 27 (2015) 1057-1070.
- [22]. S. D. Perera, H. Zhang, X. Ding, A. Nelson and R. D. Robinson. *Journal of Materials Chemistry C*, 3 (2015) 1044-1055.
- [23]. D. Chen, G. Ji, B. Ding, Y. Ma, B. Qu, W. Chen and J. Y. Lee. *Industrial & Engineering Chemistry Research*, 53 (2014) 17901-17908.
- [24]. L. Ji, Z. Lin, M. Alcoutlabi and X. Zhang. *Energy & Environmental Science*, 4 (2011) 2682-2699.
- [25]. P. Roy and S. K. Srivastava. *Journal of Materials Chemistry A*, 3 (2015) 2454-2484.
- [26]. C. Xia and H. N. Alshareef. *Chemistry of Materials*, 27 (2015) 4661-4668.
- [27]. G. A. Muller, J. B. Cook, H.-S. Kim, S. H. Tolbert and B. Dunn. *Nano Letters*, 15

- (2015) 1911-1917.
- [28]. K. Zhang, H. Chen, X. Wang, D. Guo, C. Hu, S. Wang, J. Sun and Q. Leng. *Journal of Power Sources*, 268 (2014) 522-532.
- [29]. C. Han, Z. Li and S. Dou. *Chinese Science Bulletin*, 59 (2014) 2073-2091.
- [30]. M. G. Kanatzidis. *Chemistry of Materials*, 22 (2010) 648-659.
- [31]. C. J. Vineis, A. Shakouri, A. Majumdar and M. G. Kanatzidis. *Advanced Materials*, 22 (2010) 3970-3980.
- [32]. A. D. LaLonde, Y. Pei, H. Wang and G. Jeffrey Snyder. *Materials Today*, 14 (2011) 526-532.
- [33]. K. Nielsch, J. Bachmann, J. Kimling and H. Böttner. *Advanced Energy Materials*, 1 (2011) 713-731.
- [34]. J. R. Sootsman, D. Y. Chung and M. G. Kanatzidis. *Angewandte Chemie International Edition*, 48 (2009) 8616-8639.
- [35]. C.-H. Lai, M.-Y. Lu and L.-J. Chen. *Journal of Materials Chemistry*, 22 (2012) 19-30.
- [36]. C. Burda, X. Chen, R. Narayanan and M. A. El-Sayed. *Chemical Reviews*, 105 (2005) 1025-1102.
- [37]. R. Liu, J. Duay and S. B. Lee. *Chemical Communications*, 47 (2011) 1384-1404.
- [38]. M. Bouroushian, *Electrochemistry of Metal Chalcogenides*, Springer Science&Buisness Media, Heidelberg, 2010.
- [39]. F. E. Haj Hassan and H. Akbarzadeh. *Computational Materials Science*, 35 (2006) 423-431.
- [40]. I. Khan, I. Ahmad, D. Zhang, H. A. Rahnamaye Aliabad and S. Jalali Asadabadi. *Journal of Physics and Chemistry of Solids*, 74 (2013) 181-188.
- [41]. V. Pandey, S. Gupta, D. S. Tomar and S. C. Goyal. *Phase Transitions*, 84 (2011) 624-638.
- [42]. K. Kurosaki, H. Matsumoto, A. Charoenphakdee, S. Yamanaka, M. Ishimaru and Y. Hirotsu. *Applied Physics Letters*, 93 (2008) 012101.
- [43]. M. Safdar, Z. Wang, M. Mirza, C. Jiang and J. He. *Journal of Materials Chemistry*, 22 (2012) 19228-19235.
- [44]. C.-H. Ho and Y.-C. Chen. *RSC Advances*, 3 (2013) 24896-24899.
- [45]. Y. Pei and D. T. Morelli. *Applied Physics Letters*, 94 (2009) 122112.
- [46]. B. Gürbulak, M. Şata, S. Dogan, S. Duman, A. Ashkhasi and E. F. Keskenler. *Physica E: Low-dimensional Systems and Nanostructures*, 64 (2014) 106-111.
- [47]. M. Isik and N. M. Gasanly. *Journal of Applied Physics*, 112 (2012) 083526.
- [48]. Y. P. M. Sadegh and A. Morsali. *Zeitschrift für anorganische und allgemeine Chemie*, 638 (2012) 451-454.
- [49]. K. Stöwe. *Journal of Solid State Chemistry*, 149 (2000) 123-132.
- [50]. G. Gomathi, S. Thirumaran and S. Ciattini. *Polyhedron*, 102 (2015) 424-433.
- [51]. S. V. Borisov, S. A. Magarill and N. V. Pervukhina. *Journal of Structural Chemistry*, 54 (2013) 963-967.
- [52]. J.-S. Rhyee, K. H. Lee, S. M. Lee, E. Cho, S. I. Kim, E. Lee, Y. S. Kwon, J. H. Shim and G. Kotliar. *Nature*, 459 (2009) 965-968.
- [53]. J.-S. Rhyee and J. Kim. *Materials*, 8 (2015) 1283.
- [54]. C.-Y. Lu, J. A. Adams, Q. Yu, T. Ohta, M. A. Olmstead and F. S. Ohuchi. *Physical Review B*, 78 (2008) 075321.
- [55]. S. Morley, M. von der Emde, D. R. T. Zahn, V. Offermann, T. L. Ng, N. Maung, A. C. Wright, G. H. Fan, I. B. Poole and J. O. Williams. *Journal of Applied Physics*, 79 (1996) 3196-3199.
- [56]. J.-S. Rhyee, E. Cho, K. H. Lee, S. I. Kim, E. S. Lee, S. M. Lee and Y. S. Kwon. *Journal of Applied Physics*, 105 (2009) 053712.

- [57]. J.-S. Rhyee, E. Cho, K. H. Lee, S. M. Lee, S. I. Kim, H.-S. Kim, Y. S. Kwon and S. J. Kim. *Applied Physics Letters*, 95 (2009) 212106.
- [58]. N. Barreau, S. Marsillac, D. Albertini and J. C. Bernede. *Thin Solid Films*, 403–404 (2002) 331-334.
- [59]. M. A. Mughal, R. Engelken and R. Sharma. *Solar Energy*, 120 (2015) 131-146.
- [60]. J. Duan, Q. Tang, B. He and L. Yu. *Electrochimica Acta*, 139 (2014) 381-385.
- [61]. A. A. A. Darwish, T. A. Hanafy, A. A. Attia, D. M. Habashy, M. Y. El-Bakry and M. M. El-Nahass. *Superlattices and Microstructures*, 83 (2015) 299-309.
- [62]. Z. Wang, M. Safdar, C. Jiang and J. He. *Nano Letters*, 12 (2012) 4715-4721.
- [63]. A. Rabkin, S. Samuha, R. E. Abutbul, V. Ezersky, L. Meshi and Y. Golan. *Nano Letters*, 15 (2015) 2174-2179.
- [64]. Q. Wang, S.-Z. Kang, X. Li, Y.-W. Yang, L. Qin and J. Mu. *Journal of Alloys and Compounds*, 631 (2015) 21-25.
- [65]. E. Güneri, F. Göde, B. Boyarbay and C. Gümüş. *Materials Research Bulletin*, 47 (2012) 3738-3742.
- [66]. R. Fei, W. Li, J. Li and L. Yang. *Applied Physics Letters*, 107 (2015) 173104.
- [67]. L.-D. Zhao, S.-H. Lo, Y. Zhang, H. Sun, G. Tan, C. Uher, C. Wolverton, V. P. Dravid and M. G. Kanatzidis. *Nature*, 508 (2014) 373-377.
- [68]. K. Biswas, J. He, I. D. Blum, C.-I. Wu, T. P. Hogan, D. N. Seidman, V. P. Dravid and M. G. Kanatzidis. *Nature*, 489 (2012) 414-418.
- [69]. C.-C. Huang, Y.-J. Lin, C.-J. Liu and Y.-W. Yang. *Microelectronic Engineering*, 110 (2013) 21-24.
- [70]. Y. Jia, F. Yang, F. Cai, C. Cheng and Y. Zhao. *Electronic Materials Letters*, 9 (2013) 287-291.
- [71]. H.-C. Tao, X.-L. Yang, L.-L. Zhang and S.-B. Ni. *Journal of Electroanalytical Chemistry*, 728 (2014) 134-139.
- [72]. J. Cai, Z. Li and P. K. Shen. *ACS Applied Materials & Interfaces*, 4 (2012) 4093-4098.
- [73]. R. Geethu, R. Jacob, T. Shripathi, G. S. Okram, V. Ganesan, S. Tripathi, A. Fatima, P. V. Sreenivasan, K. S. Urmila, B. Pradeep and R. R. Philip. *Applied Surface Science*, 258 (2012) 6257-6260.
- [74]. Y. Bai, X. Zong, H. Yu, Z.-G. Chen and L. Wang. *Chemistry – A European Journal*, 20 (2014) 8670-8676.
- [75]. P. S. Salmon. *Journal of Non-Crystalline Solids*, 353 (2007) 2959-2974.
- [76]. R. Golovchak, O. Shpotyuk, S. Kozyukhin, A. Kovalskiy, A. C. Miller and H. Jain. *Journal of Applied Physics*, 105 (2009) 103704.
- [77]. K. Cao, D. Ferizovic and M. Muñoz. *Journal of Applied Physics*, 104 (2008) 123511.
- [78]. A. H. Moharram and F. M. Abdel-Rahim. *Vacuum*, 72 (2003) 113-121.
- [79]. S. Mushtaq, B. Ismail, M. Aurang Zeb, N. J. Suthan Kissinger and A. Zeb. *Journal of Alloys and Compounds*, 632 (2015) 723-728.
- [80]. K. C. Godel, Y. C. Choi, B. Roose, A. Sadhanala, H. J. Snaith, S. I. Seok, U. Steiner and S. K. Pathak. *Chemical Communications*, 51 (2015) 8640-8643.
- [81]. Y. Zhou, L. Wang, S. Chen, S. Qin, X. Liu, J. Chen, D.-J. Xue, M. Luo, Y. Cao, Y. Cheng, E. H. Sargent and J. Tang. *Nat Photon*, 9 (2015) 409-415.
- [82]. Z.-H. Ge, L.-D. Zhao, D. Wu, X. Liu, B.-P. Zhang, J.-F. Li and J. He. *Materials Today*, DOI: <http://dx.doi.org/10.1016/j.mattod.2015.10.004>.
- [83]. Q. Yang, L. Chen, C. Hu, S. Wang, J. Zhang and W. Wu. *Journal of Alloys and Compounds*, 612 (2014) 301-305.
- [84]. H. Koc, H. Ozisik, E. Deligöz, A. Mamedov and E. Ozbay. *Journal of Molecular Modeling*, 20 (2014) 1-12.
- [85]. Y. D. Glinka, S. Babakiray and D. Lederman. *Journal of Applied Physics*, 118 (2015)

- 135713.
- [86]. Z. Wang, T. Ye and R. G. Mani. *Applied Physics Letters*, 107 (2015) 172103.
- [87]. M. Li, C.-Z. Chang, L. Wu, J. Tao, W. Zhao, M. H. W. Chan, J. S. Moodera, J. Li and Y. Zhu. *Physical Review Letters*, 114 (2015) 146802.
- [88]. B. Poudel, Q. Hao, Y. Ma, Y. Lan, A. Minnich, B. Yu, X. Yan, D. Wang, A. Muto, D. Vashaee, X. Chen, J. Liu, M. S. Dresselhaus, G. Chen and Z. Ren. *Science*, 320 (2008) 634-638.
- [89]. J. Gopalakrishnan and K. S. Nanjundaswamy. *Bulletin of Materials Science*, 5 (1983) 287-306.
- [90]. A. Simon. *Angewandte Chemie International Edition in English*, 20 (1981) 1-22.
- [91]. M. Bouroushian, *Electrochemistry of Metal Chalcogenides*, Springer Science&Business Media, Heidelberg, 2010.
- [92]. K. Fan, C. Liao, R. Xu, H. Zhang, Y. Cui and J. Zhang. *Chemical Physics Letters*, 633 (2015) 1-5.
- [93]. J. Díaz-Reyes, R. S. Castillo-Ojeda, R. Sánchez-Espíndola, M. Galván-Arellano and O. Zaca-Morán. *Current Applied Physics*, 15 (2015) 103-109.
- [94]. S. Zhou, Y. Li, Z. Chen, X. Xia Li, N. Chen and G. Du. *Ceramics International*, 39 (2013) 6763-6768.
- [95]. K. Gong and D. F. Kelley. *The Journal of Physical Chemistry Letters*, 6 (2015) 1559-1562.
- [96]. M. Cardona, R. K. Kremer, R. Lauck, G. Siegle, A. Muñoz and A. H. Romero. *Physical Review B*, 80 (2009) 195204.
- [97]. Y. Gui, L. Qian and X. Qian. *Materials Chemistry and Physics*, 125 (2011) 698-703.
- [98]. C. E. M. Campos. *Journal of Nano Research*, 29 (2014) 35-39.
- [99]. U. Norio, T. Madoka, Y. Shota, T. Masatoshi, T. Kazuyasu, F. Takenori, T. Ryo, M. Nobuaki and I. Shin-Ichi. *Japanese Journal of Applied Physics*, 51 (2012) 053001.
- [100]. M. S. Whittingham. *Progress in Solid State Chemistry*, 12 (1978) 41-99.
- [101]. S. Sharma, S. Auluck and M. A. Khan. *Pramana*, 54 (2000) 431-440.
- [102]. F. Güller, C. Helman and A. M. Llois. *Physica B: Condensed Matter*, 407 (2012) 3188-3191.
- [103]. C. Ataca, H. Şahin and S. Ciraci. *The Journal of Physical Chemistry C*, 116 (2012) 8983-8999.
- [104]. L.-Y. Gan, Q. Zhang, Y.-J. Zhao, Y. Cheng and U. Schwingenschlögl. *Scientific Reports*, 4 (2014) 6691.
- [105]. H. Wang, H. Yuan, S. Sae Hong, Y. Li and Y. Cui. *Chemical Society Reviews*, 44 (2015) 2664-2680.
- [106]. M. Acerce, D. Voiry and M. Chhowalla. *Nat Nano*, 10 (2015) 313-318.
- [107]. L. M. Xie. *Nanoscale*, 7 (2015) 18392-18401.
- [108]. A. B. Kaul. *Journal of Materials Research*, 29 (2014) 348-361.
- [109]. X. Li and H. Zhu. *Journal of Materiomics*, 1 (2015) 33-44.
- [110]. T. Heine. *Accounts of Chemical Research*, 48 (2015) 65-72.
- [111]. F. Xia, H. Wang, D. Xiao, M. Dubey and A. Ramasubramaniam. *Nat Photon*, 8 (2014) 899-907.
- [112]. S. Han, R. Bhatia and S.-W. Kim. *Nano Convergence*, 2 (2015) 17.
- [113]. P. Miró, J. H. Han, J. Cheon and T. Heine. *Angewandte Chemie International Edition*, 53 (2014) 12624-12628.
- [114]. F. Jellinek. *Reactivity of Solids*, 5 (1988) 323-339.
- [115]. L. Zhu, B. Richardson, J. Tanumihardja and Q. Yu. *CrystEngComm*, 14 (2012) 4188-4195.
- [116]. P. Day, N. S. Hush and R. J. H. Clark. *Philosophical Transactions of the Royal Society*

- of London A: Mathematical, Physical and Engineering Sciences, 366 (2008) 5-14.
- [117]. İ. A. Kariper. Progress in Natural Science: Materials International, 24 (2014) 663-670.
- [118]. Y. M. Goryachev and T. G. Kutsenok. Soviet Powder Metallurgy and Metal Ceramics, 8 (1969) 386-388.
- [119]. F. M. Ryan, I. N. Greenberg, F. L. Carter and R. C. Miller. Journal of Applied Physics, 33 (1962) 864-868.
- [120]. L. Chen, S.-Q. Xia and J. D. Corbett. Inorganic Chemistry, 44 (2005) 3057-3062.
- [121]. H. Cordes and R. Schmid-Fetzer. Journal of Alloys and Compounds, 216 (1995) 197-206.
- [122]. B. Harbrecht, M. Conrad, T. Degen and R. Herberitz. Journal of Alloys and Compounds, 255 (1997) 178-182.
- [123]. T. Hughbanks. Journal of Alloys and Compounds, 229 (1995) 40-53.
- [124]. C. S. Rout, B.-H. Kim, X. Xu, J. Yang, H. Y. Jeong, D. Odkhuu, N. Park, J. Cho and H. S. Shin. Journal of the American Chemical Society, 135 (2013) 8720-8725.
- [125]. I. Tsubokawa. Journal of the Physical Society of Japan, 14 (1959) 196-198.
- [126]. J. R. Alain Meerschaut, *Crystal Chemistry and Properties of Materials with Quasi-One-Dimensional Structures*, D. Reidel Publishing Company, 1987.
- [127]. J. Rouxel. Accounts of Chemical Research, 25 (1992) 328-336.
- [128]. Y. Zhang and X. Wu. Physics Letters A, 377 (2013) 3154-3157.
- [129]. T. Klimczuk, K. Baroudi, J. W. Krizan, A. L. Kozub and R. J. Cava. Journal of Alloys and Compounds, 649 (2015) 906-909.
- [130]. A. Prodan, V. Marinković, F. W. Boswell, J. C. Bennett and M. Remškar. Journal of Alloys and Compounds, 219 (1995) 69-72.
- [131]. Y. Adachi, K. Izaki, K. Koike, H. Morita, T. Kaneko, H. Kimura and A. Inoue. Journal of Magnetism and Magnetic Materials, 310 (2007) 1849-1850.
- [132]. S. W. W. Young D. J., Kirkaldy J. S. Journal of The Electrochemical Society, 120 (1973) 1221-1224.
- [133]. Y. Adachi, M. Yuzuri, T. Kaneko, S. Abe and H. Yoshida. Journal of the Physical Society of Japan, 63 (1994) 369-370.
- [134]. M. Yuzuri and R. Omi. Journal of Magnetism and Magnetic Materials, 90-91 (1990) 155-156.
- [135]. A. Maignan, Y. Bréard, E. Guilmeau and F. Gascoin. Journal of Applied Physics, 112 (2012) 013716.
- [136]. Q. Li, E. C. Walter, W. E. van der Veer, B. J. Murray, J. T. Newberg, E. W. Bohannon, J. A. Switzer, J. C. Hemminger and R. M. Penner. The Journal of Physical Chemistry B, 109 (2005) 3169-3182.
- [137]. W. Xie, S. Populoh, K. Gałazka, X. Xiao, L. Sagarna, Y. Liu, M. Trottmann, J. He and A. Weidenkaff. Journal of Applied Physics, 115 (2014) 103707.
- [138]. R. Masrour, L. Bahmad, E. K. Hlil, M. Hamedoun and A. Benyoussef. Journal of Superconductivity and Novel Magnetism, 27 (2014) 2311-2315.
- [139]. A. Tubtimtae, T. Hongto, K. Hongsith and S. Choopun. Superlattices and Microstructures, 66 (2014) 96-104.
- [140]. R. C. Roundy and M. E. Raikh. Physical Review B, 91 (2015) 045202.
- [141]. W. R. Cook. Journal of the American Ceramic Society, 51 (1968) 518-520.
- [142]. H. J. Lamfers, A. Meetsma, G. A. Wiegers and J. L. de Boer. Journal of Alloys and Compounds, 241 (1996) 34-39.
- [143]. P. F. Weck, E. Kim and K. R. Czerwinski. Dalton Transactions, 42 (2013) 15288-15295.
- [144]. Z. G. Yu, Y. Cai and Y.-W. Zhang. Scientific Reports, 5 (2015) 13783.
- [145]. S. Yang, C. Wang, H. Sahin, H. Chen, Y. Li, S.-S. Li, A. Suslu, F. M. Peeters, Q. Liu, J.

- Li and S. Tongay. *Nano Letters*, 15 (2015) 1660-1666.
- [146]. F. R. Livens, M. J. Jones, A. J. Hynes, J. M. Charnock, J. F. W. Mosselmans, C. Hennig, H. Steele, D. Collison, D. J. Vaughan, R. A. D. Patrick, W. A. Reed and L. N. Moyes. *Journal of Environmental Radioactivity*, 74 (2004) 211-219.
- [147]. D. E. Schwarz, A. I. Frenkel, R. G. Nuzzo, T. B. Rauchfuss and A. Vairavamurthy. *Chemistry of Materials*, 16 (2004) 151-158.
- [148]. C. Sepúlveda, R. García, P. Reyes, I. T. Ghampson, J. L. G. Fierro, D. Laurenti, M. Vrinat and N. Escalona. *Applied Catalysis A: General*, 475 (2014) 427-437.
- [149]. E. Zhang, Y. Jin, X. Yuan, W. Wang, C. Zhang, L. Tang, S. Liu, P. Zhou, W. Hu and F. Xiu. *Advanced Functional Materials*, 25 (2015) 4076-4082.
- [150]. Y.-C. Lin, H.-P. Komsa, C.-H. Yeh, T. Björkman, Z.-Y. Liang, C.-H. Ho, Y.-S. Huang, P.-W. Chiu, A. V. Krasheninnikov and K. Suenaga. *ACS Nano*, 9 (2015) 11249-11257.
- [151]. F. Aramu and P. Manca. *Il Nuovo Cimento (1955-1965)*, 33 (1964) 1025-1030.
- [152]. A. Ciechan, M. J. Winiarski and M. Samsel-Czekała. *Journal of Alloys and Compounds*, 630 (2015) 100-105.
- [153]. Q. Zheng, X. Cheng and H. Li. *Catalysts*, 5 (2015) 1079.
- [154]. S. Huang, Q. He, W. Chen, J. Zai, Q. Qiao and X. Qian. *Nano Energy*, 15 (2015) 205-215.
- [155]. S. S. Zhang and D. T. Tran. *Electrochimica Acta*, 176 (2015) 784-789.
- [156]. C. Uhlig, E. Guenes, A. Schulze, M. Elm, P. Klar and S. Schlecht. *Journal of Electronic Materials*, 43 (2014) 2362-2370.
- [157]. M. Mousavi-Kamazani, M. Salavati-Niasari, M. Goudarzi and A. Gharehbaei. *Journal of Inorganic and Organometallic Polymers and Materials*, DOI: 10.1007/s10904-015-0300-8(2015) 1-5.
- [158]. S. Dong, S. Wang, J. Guan, S. Li, Z. Lan, C. Chen, C. Shang, L. Zhang, X. Wang, L. Gu, G. Cui and L. Chen. *The Journal of Physical Chemistry Letters*, 5 (2014) 615-621.
- [159]. T. R. Yang, Y.-S. Huang, Y. K. Chyan and J. D. Chang. *Czechoslovak Journal of Physics*, 46 (1996) 2541-2542.
- [160]. T. Schwarzlose, S. Fiechter and W. Jaegermann. *Berichte der Bunsengesellschaft für physikalische Chemie*, 96 (1992) 887-893.
- [161]. V. K. J. Sandio Dey. *Platinum Metals Review*, 48 (2004) 16-29.
- [162]. X. Jiang, Y. Xie, J. Lu, W. He, L. Zhu and Y. Qian. *Journal of Materials Chemistry*, 10 (2000) 2193-2196.
- [163]. R. Blachnik, M. Lasocka and U. Walbrecht. *Journal of Solid State Chemistry*, 48 (1983) 431-438.
- [164]. D. J. Chakrabarti and D. E. Laughlin. *Bulletin of Alloy Phase Diagrams*, 4 (1983) 254-271.
- [165]. T. Ohtani, M. Motoki, K. Koh and K. Ohshima. *Materials Research Bulletin*, 30 (1995) 1495-1504.
- [166]. M. K. Balapanov, R. A. Yakshibaev and U. K. Mukhamed'yanov. *Physics of the Solid State*, 45 (2003) 634-638.
- [167]. H. Liu, X. Shi, F. Xu, L. Zhang, W. Zhang, L. Chen, Q. Li, C. Uher, T. Day and G. J. Snyder. *Nat Mater*, 11 (2012) 422-425.
- [168]. M. D. Lubomir GULAY, Oksana STROK, Adam PIETRASZKO. *Chemistry of Metals and Alloys*, 4 (2011) 200-205.
- [169]. Y. Zhao and C. Burda. *Energy & Environmental Science*, 5 (2012) 5564-5576.
- [170]. M. Afzaal and P. O'Brien. *Journal of Materials Chemistry*, 16 (2006) 1597-1602.
- [171]. S. Mirov, V. Fedorov, I. Moskalev, M. Mirov and D. Martyshkin. *Journal of Luminescence*, 133 (2013) 268-275.
- [172]. D. Xu, T. Biegala, M. Carmody, J. W. Garland, C. Grein and S. Sivananthan. *Applied*

- Physics Letters, 96 (2010) 073508.
- [173]. J. J. Loferski. *Journal of Applied Physics*, 27 (1956) 777-784.
- [174]. A. M. Glazer and K. Stadnicka. *Journal of Applied Crystallography*, 19 (1986) 108-122.
- [175]. B. A. Lombos, E. Y. M. Lee, A. L. Kipling and R. W. Krawczyniuk. *Journal of Physics and Chemistry of Solids*, 36 (1975) 1193-1198.
- [176]. S. H. Wei and A. Zunger. *Physical Review B*, 37 (1988) 8958-8981.
- [177]. M.-R. Gao, Y.-F. Xu, J. Jiang and S.-H. Yu. *Chemical Society Reviews*, 42 (2013) 2986-3017.
- [178]. A. Kanatzia, C. Papageorgiou, C. Lioutas and T. Kyratsi. *Journal of Electronic Materials*, 42 (2013) 1652-1660.
- [179]. J.-J. Shen, T.-J. Zhu, X.-B. Zhao, S.-N. Zhang, S.-H. Yang and Z.-Z. Yin. *Energy & Environmental Science*, 3 (2010) 1519-1523.
- [180]. L.-l. Zhao, X.-l. Wang, J.-y. Wang, Z.-x. Cheng, S.-x. Dou, J. Wang and L.-q. Liu. *Scientific Reports*, 5 (2015) 7671.
- [181]. K. H. L. Sang Il Kim, Hyeon A. Mun, Hyun Sik Kim, Sung Woo Hwang, Jong Wook Roh, Dae Jin Yang, Weon Ho Shin, Xiang Shu Li, Young Hee Lee, G. Jeffrey Snyder, Sung Wng Kim. *Science*, 348 (2015) 109-114.
- [182]. R. Venkatasubramanian, E. Siivola, T. Colpitts and B. O'Quinn. *Nature*, 413 (2001) 597-602.
- [183]. E. Yu, S.-C. Kim, H. J. Lee, K. H. Oh and M.-W. Moon. *Scientific Reports*, 5 (2015) 9362.
- [184]. J. Zhou, Q. Zeng, D. Lv, L. Sun, L. Niu, W. Fu, F. Liu, Z. Shen, C. Jin and Z. Liu. *Nano Letters*, 15 (2015) 6400-6405.
- [185]. I. Chuprakov, S. and K. Dahmen, H. J. *Phys. IV France*, 09 (1999) Pr8-313-Pr318-319.
- [186]. S. Chen, K. Cai and S. Shen. *Journal of Electronic Materials*, DOI: 10.1007/s11664-015-4058-0(2015) 1-8.
- [187]. W.-T. Yao and S.-H. Yu. *Advanced Functional Materials*, 18 (2008) 3357-3366.
- [188]. K. B. Tang, Y. T. Qian, J. H. Zeng and X. G. Yang. *Advanced Materials*, 15 (2003) 448-450.
- [189]. M. K. Devaraju and I. Honma. *Advanced Energy Materials*, 2 (2012) 284-297.
- [190]. H.-W. Liang, Q.-F. Guan, L.-F. Chen, Z. Zhu, W.-J. Zhang and S.-H. Yu. *Angewandte Chemie International Edition*, 51 (2012) 5101-5105.
- [191]. H. Liu, B. Zhang, H. Shi, Y. Tang, K. Jiao and X. Fu. *Journal of Materials Chemistry*, 18 (2008) 2573-2580.
- [192]. Z. Zhuang, Q. Peng, J. Zhuang, X. Wang and Y. Li. *Chemistry – A European Journal*, 12 (2006) 211-217.
- [193]. J. Fu, S. Song, X. Zhang, F. Cao, L. Zhou, X. Li and H. Zhang. *CrystEngComm*, 14 (2012) 2159-2165.
- [194]. W. Shi, J. Yu, H. Wang and H. Zhang. *Journal of the American Chemical Society*, 128 (2006) 16490-16491.
- [195]. L.-Y. Chen, Z.-D. Zhang and W.-Z. Wang. *The Journal of Physical Chemistry C*, 112 (2008) 4117-4123.
- [196]. A. Qin, Y. Fang, P. Tao, J. Zhang and C. Su. *Inorganic Chemistry*, 46 (2007) 7403-7409.
- [197]. Q. Peng, Y. Dong and Y. Li. *Angewandte Chemie International Edition*, 42 (2003) 3027-3030.
- [198]. L. Ye, W. Guo, Y. Yang, Y. Du and Y. Xie. *Chemistry of Materials*, 19 (2007) 6331-6337.
- [199]. Q. Lu, F. Gao and D. Zhao. *Nano Letters*, 2 (2002) 725-728.

- [200]. J.-L. Mi, N. Lock, T. Sun, M. Christensen, M. Søndergaard, P. Hald, H. H. Hng, J. Ma and B. B. Iversen. *ACS Nano*, 4 (2010) 2523-2530.
- [201]. Y. Zhao, Y. Xie, J.-S. Jie, C.-Y. Wu and S. Yan. *Journal of Materials Chemistry*, 19 (2009) 3378-3383.
- [202]. J. Qian, G. Cui, M. Jing, Y. Wang, M. Zhang and J. Yang. *International Journal of Photoenergy*, 2012 (2012) 6.
- [203]. P. Liu, H. Zhang, H. Liu, Y. Wang, X. Yao, G. Zhu, S. Zhang and H. Zhao. *Journal of the American Chemical Society*, 133 (2011) 19032-19035.
- [204]. H. Zhao, Y. Shen, S. Zhang and H. Zhang. *Langmuir*, 25 (2009) 11032-11037.
- [205]. H. Zhang, Y. Li, P. Liu, Y. Li, D. Yang, H. Yang and H. Zhao. *Chemistry – A European Journal*, 18 (2012) 5165-5169.
- [206]. H. K. Sridhar Komarneni. *Pure Applied Chemistry*, 74 (2002) 1537-1543.
- [207]. Z. He, S. H. Yu, X. Zhou, X. Li and J. Qu. *Advanced Functional Materials*, 16 (2006) 1105-1111.
- [208]. S. Novaconi, P. Vlazan, I. Malaescu, I. Badea, I. Grozescu and P. Sfirloaga. *Central European Journal of Chemistry*, 11 (2013) 1599-1605.
- [209]. V. K. Ivanov, A. E. Baranchikov, A. S. Vanetsev, A. S. Shaporev, O. S. Polezhaeva, Y. D. Tret'yakov, P. P. Fedorov and V. V. Osiko. *Russian Journal of Inorganic Chemistry*, 52 (2007) 1321-1327.
- [210]. S.-L. Yang, H.-B. Yao, M.-R. Gao and S.-H. Yu. *CrystEngComm*, 11 (2009) 1383-1390.
- [211]. M.-R. Gao, Z.-Y. Lin, J. Jiang, H.-B. Yao, Y.-M. Lu, Q. Gao, W.-T. Yao and S.-H. Yu. *Chemistry – A European Journal*, 17 (2011) 5068-5075.
- [212]. C. B. Murray, D. J. Norris and M. G. Bawendi. *Journal of the American Chemical Society*, 115 (1993) 8706-8715.
- [213]. J. Park, J. Joo, S. G. Kwon, Y. Jang and T. Hyeon. *Angewandte Chemie International Edition*, 46 (2007) 4630-4660.
- [214]. K.-S. Cho, D. V. Talapin, W. Gaschler and C. B. Murray. *Journal of the American Chemical Society*, 127 (2005) 7140-7147.
- [215]. A. Sahu, L. Qi, M. S. Kang, D. Deng and D. J. Norris. *Journal of the American Chemical Society*, 133 (2011) 6509-6512.
- [216]. V. Chikan and D. F. Kelley. *Nano Letters*, 2 (2002) 141-145.
- [217]. W. Lu, Y. Ding, Y. Chen, Z. L. Wang and J. Fang. *Journal of the American Chemical Society*, 127 (2005) 10112-10116.
- [218]. K. D. Oyler, X. Ke, I. T. Sines, P. Schiffer and R. E. Schaak. *Chemistry of Materials*, 21 (2009) 3655-3661.
- [219]. J. H. Yu, J. Joo, H. M. Park, S.-I. Baik, Y. W. Kim, S. C. Kim and T. Hyeon. *Journal of the American Chemical Society*, 127 (2005) 5662-5670.
- [220]. L. Chen, H. Zhan, X. Yang, Z. Sun, J. Zhang, D. Xu, C. Liang, M. Wu and J. Fang. *CrystEngComm*, 12 (2010) 4386-4391.
- [221]. M. Ibáñez, R. Zamani, S. Gorsse, J. Fan, S. Ortega, D. Cadavid, J. R. Morante, J. Arbiol and A. Cabot. *ACS Nano*, 7 (2013) 2573-2586.
- [222]. G. Xiao, Y. Zeng, Y. Jiang, J. Ning, W. Zheng, B. Liu, X. Chen, G. Zou and B. Zou. *Small*, 9 (2013) 793-799.
- [223]. Y. Min, G. Park, B. Kim, A. Giri, J. Zeng, J. W. Roh, S. I. Kim, K. H. Lee and U. Jeong. *ACS Nano*, 9 (2015) 6843-6853.
- [224]. R. Malakooti, L. Cademartiri, Y. Akçakir, S. Petrov, A. Migliori and G. A. Ozin. *Advanced Materials*, 18 (2006) 2189-2194.
- [225]. I. T. Sines, R. Misra, P. Schiffer and R. E. Schaak. *Angewandte Chemie International Edition*, 49 (2010) 4638-4640.

- [226]. D. D. Vaughn, S.-I. In and R. E. Schaak. *ACS Nano*, 5 (2011) 8852-8860.
- [227]. D. D. Vaughn, O. D. Hentz, S. Chen, D. Wang and R. E. Schaak. *Chemical Communications*, 48 (2012) 5608-5610.
- [228]. D. Wang, C. Hao, W. Zheng, Q. Peng, T. Wang, Z. Liao, D. Yu and Y. Li. *Advanced Materials*, 20 (2008) 2628-2632.
- [229]. K. H. Park, J. Choi, H. J. Kim, J. B. Lee and S. U. Son. *Chemistry of Materials*, 19 (2007) 3861-3863.
- [230]. F. Ye, C. Wang, G. Du, X. Chen, Y. Zhong and J. Z. Jiang. *Journal of Materials Chemistry*, 21 (2011) 17063-17065.
- [231]. H. Zhang, G. Long, D. Li, R. Sabirianov and H. Zeng. *Chemistry of Materials*, 23 (2011) 3769-3774.
- [232]. C. Wang, D. Zhang, L. Xu, Y. Jiang, F. Dong, B. Yang, K. Yu and Q. Lin. *Angewandte Chemie International Edition*, 50 (2011) 7587-7591.
- [233]. H. Shen, H. Wang, H. Yuan, L. Ma and L. S. Li. *CrystEngComm*, 14 (2012) 555-560.
- [234]. Y. Zhao, Y. Zhang, H. Zhu, G. C. Hadjipanayis and J. Q. Xiao. *Journal of the American Chemical Society*, 126 (2004) 6874-6875.
- [235]. Y. Xu, N. Al-Salim, C. W. Bumby and R. D. Tilley. *Journal of the American Chemical Society*, 131 (2009) 15990-15991.
- [236]. V. V. Singh, G. K. Rao, A. Kumar and A. K. Singh. *Dalton Transactions*, 41 (2012) 1142-1145.
- [237]. M. D. Regulacio, K. Bussmann, B. Lewis and S. L. Stoll. *Journal of the American Chemical Society*, 128 (2006) 11173-11179.
- [238]. Y. Du, B. Xu, T. Fu, M. Cai, F. Li, Y. Zhang and Q. Wang. *Journal of the American Chemical Society*, 132 (2010) 1470-1471.
- [239]. Z. Zhang, W. P. Lim, C. T. Wong, H. Xu, F. Yin and W. S. Chin. *Nanomaterials*, 2 (2012) 113.
- [240]. P. V. Vanitha and P. O'Brien. *Journal of the American Chemical Society*, 130 (2008) 17256-17257.
- [241]. W. Maneprakorn, M. A. Malik and P. O'Brien. *Journal of Materials Chemistry*, 20 (2010) 2329-2335.
- [242]. J.-w. Seo, J.-t. Jang, S.-w. Park, C. Kim, B. Park and J. Cheon. *Advanced Materials*, 20 (2008) 4269-4273.
- [243]. Y. Zhang, Y. Du, H. Xu and Q. Wang. *CrystEngComm*, 12 (2010) 3658-3663.
- [244]. S. Schulz, S. Heimann, J. Friedrich, M. Engenhorst, G. Schierning and W. Assenmacher. *Chemistry of Materials*, 24 (2012) 2228-2234.
- [245]. C. Altavilla, M. Sarno and P. Ciambelli. *Chemistry of Materials*, 23 (2011) 3879-3885.
- [246]. A. Ghezelbash, M. B. Sigman and B. A. Korgel. *Nano Letters*, 4 (2004) 537-542.
- [247]. M. Nath, A. Choudhury and C. N. R. Rao. *Chemical Communications*, DOI: 10.1039/B412056F(2004) 2698-2699.
- [248]. H.-W. Chang, B. Sarkar and C. W. Liu. *Crystal Growth & Design*, 7 (2007) 2691-2695.
- [249]. M. A. Malik, M. Y. Wani and M. A. Hashim. *Arabian Journal of Chemistry*, 5 (2012) 397-417.
- [250]. M. Schwarze, T. Pogrzeba, I. Volovych and R. Schomacker. *Catalysis Science & Technology*, 5 (2015) 24-33.
- [251]. J. Xu, A. Yin, J. Zhao, D. Li and W. Hou. *The Journal of Physical Chemistry B*, 117 (2013) 450-456.
- [252]. X. Q. Chen, Z. Li, Y. Bai, Q. Sun, L. Z. Wang and S. X. Dou. *Chemistry – A European Journal*, 21 (2015) 1055-1063.
- [253]. X. Wang, J. Zhuang, Q. Peng and Y. Li. *Nature*, 437 (2005) 121-124.

- [254]. G. F. Walker. *Nature*, 187 (1960) 312-313.
- [255]. G. Z. Magda, J. Petó, G. Dobrik, C. Hwang, L. P. Biró and L. Tapasztó. *Scientific Reports*, 5 (2015) 14714.
- [256]. J. Feng, X. Sun, C. Wu, L. Peng, C. Lin, S. Hu, J. Yang and Y. Xie. *Journal of the American Chemical Society*, 133 (2011) 17832-17838.
- [257]. T. Sasaki, M. Watanabe, H. Hashizume, H. Yamada and H. Nakazawa. *Journal of the American Chemical Society*, 118 (1996) 8329-8335.
- [258]. D. Golberg. *Nat Nano*, 6 (2011) 200-201.
- [259]. M. B. Dines. *Journal of Chemical Education*, 51 (1974) 221.
- [260]. H. S. S. Ramakrishna Matte, A. Gomathi, A. K. Manna, D. J. Late, R. Datta, S. K. Pati and C. N. R. Rao. *Angewandte Chemie International Edition*, 49 (2010) 4059-4062.
- [261]. Z. Zeng, Z. Yin, X. Huang, H. Li, Q. He, G. Lu, F. Boey and H. Zhang. *Angewandte Chemie International Edition*, 50 (2011) 11093-11097.
- [262]. P. Puneet, R. Podila, M. Karakaya, S. Zhu, J. He, T. M. Tritt, M. S. Dresselhaus and A. M. Rao. *Scientific Reports*, 3 (2013) 3212.
- [263]. G. Eda, H. Yamaguchi, D. Voiry, T. Fujita, M. Chen and M. Chhowalla. *Nano Letters*, 11 (2011) 5111-5116.
- [264]. J. Zheng, H. Zhang, S. Dong, Y. Liu, C. Tai Nai, H. Suk Shin, H. Young Jeong, B. Liu and K. Ping Loh. *Nat Commun*, 5 (2014).
- [265]. J. N. Coleman, M. Lotya, A. O'Neill, S. D. Bergin, P. J. King, U. Khan, K. Young, A. Gaucher, S. De, R. J. Smith, I. V. Shvets, S. K. Arora, G. Stanton, H.-Y. Kim, K. Lee, G. T. Kim, G. S. Duesberg, T. Hallam, J. J. Boland, J. J. Wang, J. F. Donegan, J. C. Grunlan, G. Moriarty, A. Shmeliov, R. J. Nicholls, J. M. Perkins, E. M. Grieveson, K. Theuwissen, D. W. McComb, P. D. Nellist and V. Nicolosi. *Science*, 331 (2011) 568-571.
- [266]. Z. Ding, S. K. Bux, D. J. King, F. L. Chang, T.-H. Chen, S.-C. Huang and R. B. Kaner. *Journal of Materials Chemistry*, 19 (2009) 2588-2592.
- [267]. L. N. Maskaveva, Z. I. Smirnova and V. F. Markov. *Russian Chemical Bulletin*, 63 (2014) 1515-1522.
- [268]. G. D. Moon, S. Ko, Y. Min, J. Zeng, Y. Xia and U. Jeong. *Nano Today*, 6 (2011) 186-203.
- [269]. D. H. Son, S. M. Hughes, Y. Yin and A. Paul Alivisatos. *Science*, 306 (2004) 1009-1012.
- [270]. G. D. Moon, S. Ko, Y. Xia and U. Jeong. *ACS Nano*, 4 (2010) 2307-2319.
- [271]. M. Pang and H. C. Zeng. *Langmuir*, 26 (2010) 5963-5970.
- [272]. H. Cao, X. Qian, C. Wang, X. Ma, J. Yin and Z. Zhu. *Journal of the American Chemical Society*, 127 (2005) 16024-16025.
- [273]. I. T. Sines, D. D. Vaughn, A. J. Biacchi, C. E. Kingsley, E. J. Popczun and R. E. Schaak. *Chemistry of Materials*, 24 (2012) 3088-3093.
- [274]. B. Sadtler, D. O. Demchenko, H. Zheng, S. M. Hughes, M. G. Merkle, U. Dahmen, L.-W. Wang and A. P. Alivisatos. *Journal of the American Chemical Society*, 131 (2009) 5285-5293.
- [275]. S. E. Wark, C.-H. Hsia and D. H. Son. *Journal of the American Chemical Society*, 130 (2008) 9550-9555.
- [276]. C. Yan and D. Xue. *The Journal of Physical Chemistry B*, 110 (2006) 25850-25855.
- [277]. Y. Yin, R. M. Rioux, C. K. Erdonmez, S. Hughes, G. A. Somorjai and A. P. Alivisatos. *Science*, 304 (2004) 711-714.
- [278]. Y. Yin, C. K. Erdonmez, A. Cabot, S. Hughes and A. P. Alivisatos. *Advanced Functional Materials*, 16 (2006) 1389-1399.
- [279]. P. H. C. Camargo, Z. Peng, X. Lu, H. Yang and Y. Xia. *Journal of Materials Chemistry*,

- 19 (2009) 1024-1030.
- [280]. G. Zhang, Q. Yu, Z. Yao and X. Li. *Chemical Communications*, DOI: 10.1039/B822595H(2009) 2317-2319.
- [281]. A. Cabot, R. K. Smith, Y. Yin, H. Zheng, B. M. Reinhard, H. Liu and A. P. Alivisatos. *ACS Nano*, 2 (2008) 1452-1458.
- [282]. K. Wang, H.-W. Liang, W.-T. Yao and S.-H. Yu. *Journal of Materials Chemistry*, 21 (2011) 15057-15062.
- [283]. G. Zhang, B. Kirk, L. A. Jauregui, H. Yang, X. Xu, Y. P. Chen and Y. Wu. *Nano Letters*, 12 (2012) 56-60.
- [284]. B. Gates, Y. Wu, Y. Yin, P. Yang and Y. Xia. *Journal of the American Chemical Society*, 123 (2001) 11500-11501.
- [285]. Y. Shi, J. Chen and P. Shen. *Journal of Alloys and Compounds*, 441 (2007) 337-343.
- [286]. H.-S. Shim, V. R. Shinde, J. W. Kim, T. P. Gujar, O.-S. Joo, H. J. Kim and W. B. Kim. *Chemistry of Materials*, 21 (2009) 1875-1883.
- [287]. J. Park, H. Zheng, Y.-w. Jun and A. P. Alivisatos. *Journal of the American Chemical Society*, 131 (2009) 13943-13945.
- [288]. G. She, X. Zhang, W. Shi, Y. Cai, N. Wang, P. Liu and D. Chen. *Crystal Growth & Design*, 8 (2008) 1789-1791.
- [289]. D. Pinisetty, D. Davis, E. J. Podlaha-Murphy, M. C. Murphy, A. B. Karki, D. P. Young and R. V. Devireddy. *Acta Materialia*, 59 (2011) 2455-2461.
- [290]. N. Han, S. I. Kim, J.-D. Yang, K. Lee, H. Sohn, H.-M. So, C. W. Ahn and K.-H. Yoo. *Advanced Materials*, 23 (2011) 1871-1875.
- [291]. Y. Chen, C. Davoisne, J.-M. Tarascon and C. Guery. *Journal of Materials Chemistry*, 22 (2012) 5295-5299.
- [292]. S. Murugesan, P. Kearns and K. J. Stevenson. *Langmuir*, 28 (2012) 5513-5517.
- [293]. S. Li, M. S. Toprak, H. M. A. Soliman, J. Zhou, M. Muhammed, D. Platzek and E. Müller. *Chemistry of Materials*, 18 (2006) 3627-3633.
- [294]. F. Ozel, M. Kus, A. Yar, E. Arkan, M. Can, A. Aljabour, N. Varal and M. Ersoz. *Journal of Materials Science*, 50 (2015) 777-783.
- [295]. K.-J. Lee, H. Song, Y.-I. Lee, H. Jung, M. Zhang, Y.-H. Choa and N. V. Myung. *Chemical Communications*, 47 (2011) 9107-9109.
- [296]. C. S. Reddy, A. Zak and E. Zussman. *Journal of Materials Chemistry*, 21 (2011) 16086-16093.
- [297]. G. Yang, W. Yan, Q. Zhang, S. Shen and S. Ding. *Nanoscale*, 5 (2013) 12432-12439.
- [298]. A. P. Gonçalves and C. Godart. *The European Physical Journal B*, 87 (2014) 1-29.
- [299]. T. Kuroki, K. Kabeya, K. Makino, T. Kajihara, H. Kaibe, H. Hachiuma, H. Matsuno and A. Fujibayashi. *Journal of Electronic Materials*, 43 (2014) 2405-2410.
- [300]. T. C. Harman, P. J. Taylor, M. P. Walsh and B. E. LaForge. *Science*, 297 (2002) 2229-2232.
- [301]. C. Wan, X. Gu, F. Dang, T. Itoh, Y. Wang, H. Sasaki, M. Kondo, K. Koga, K. Yabuki, G. J. Snyder, R. Yang and K. Koumoto. *Nat Mater*, 14 (2015) 622-627.
- [302]. W. Mi, P. Qiu, T. Zhang, Y. Lv, X. Shi and L. Chen. *Applied Physics Letters*, 104 (2014) 133903.
- [303]. G. G. Yadav, J. A. Susoreny, G. Zhang, H. Yang and Y. Wu. *Nanoscale*, 3 (2011) 3555-3562.
- [304]. S. LeBlanc, S. K. Yee, M. L. Scullin, C. Dames and K. E. Goodson. *Renewable and Sustainable Energy Reviews*, 32 (2014) 313-327.
- [305]. H. K. Jun, M. A. Careem and A. K. Arof. *Renewable and Sustainable Energy Reviews*, 22 (2013) 148-167.
- [306]. W. Shockley and H. J. Queisser. *Journal of Applied Physics*, 32 (1961) 510-519.

- [307]. Z. Yang, C.-Y. Chen, P. Roy and H.-T. Chang. *Chemical Communications*, 47 (2011) 9561-9571.
- [308]. M. Kouhnavard, S. Ikeda, N. A. Ludin, N. B. Ahmad Khairudin, B. V. Ghaffari, M. A. Mat-Teridi, M. A. Ibrahim, S. Sepeai and K. Sopian. *Renewable and Sustainable Energy Reviews*, 37 (2014) 397-407.
- [309]. J. Jiao, Z.-J. Zhou, W.-H. Zhou and S.-X. Wu. *Materials Science in Semiconductor Processing*, 16 (2013) 435-440.
- [310]. X.-Y. Yu, B.-X. Lei, D.-B. Kuang and C.-Y. Su. *Journal of Materials Chemistry*, 22 (2012) 12058-12063.
- [311]. S. W. Jung, J.-H. Kim, H. Kim, C.-J. Choi and K.-S. Ahn. *Current Applied Physics*, 12 (2012) 1459-1464.
- [312]. X. Hu, Q. Zhang, X. Huang, D. Li, Y. Luo and Q. Meng. *Journal of Materials Chemistry*, 21 (2011) 15903-15905.
- [313]. P. K. Santra and P. V. Kamat. *Journal of the American Chemical Society*, 134 (2012) 2508-2511.
- [314]. M. Venkata-Haritha, C. V.V.M. Gopi, C. V. Thulasi-Varma, S.-K. Kim and H.-J. Kim. *Journal of Photochemistry and Photobiology A: Chemistry*, 315 (2016) 34-41.
- [315]. G. Sixto, M.-S. Iván, M. Lorena, G. Nestor, L.-V. Teresa, G. Roberto, J. D. Lina, S. Qing, T. Taro and B. Juan. *Nanotechnology*, 20 (2009) 295204.
- [316]. Y. Liao, J. Zhang, W. Liu, W. Que, X. Yin, D. Zhang, L. Tang, W. He, Z. Zhong and H. Zhang. *Nano Energy*, 11 (2015) 88-95.
- [317]. K. Meng, G. Chen and K. R. Thampi. *Journal of Materials Chemistry A*, 3 (2015) 23074-23089.
- [318]. H. Jun, M. Careem and A. Arof. *Nanoscale Research Letters*, 9 (2014) 1-7.
- [319]. H.-J. Kim, S.-W. Kim, C. V. V. M. Gopi, S.-K. Kim, S. S. Rao and M.-S. Jeong. *Journal of Power Sources*, 268 (2014) 163-170.
- [320]. W. Chen, M. Wang, T. Qian, H. Cao, S. Huang, Q. He, N. Liang, C. Wang and J. Zai. *Nano Energy*, 12 (2015) 186-196.
- [321]. C. V. V. M. Gopi, M. Venkata-Haritha, S. Ravi, C. V. Thulasi-Varma, S.-K. Kim and H.-J. Kim. *Journal of Materials Chemistry C*, 3 (2015) 12514-12528.
- [322]. J.-L. Yue, Q. Sun and Z.-W. Fu. *Chemical Communications*, 49 (2013) 5868-5870.
- [323]. X. Rui, H. Tan and Q. Yan. *Nanoscale*, 6 (2014) 9889-9924.
- [324]. C. Bommier and X. Ji. *Israel Journal of Chemistry*, 55 (2015) 486-507.
- [325]. L. Li, M. Caban-Acevedo, S. N. Girard and S. Jin. *Nanoscale*, 6 (2014) 2112-2118.
- [326]. B. Qu, C. Ma, G. Ji, C. Xu, J. Xu, Y. S. Meng, T. Wang and J. Y. Lee. *Advanced Materials*, 26 (2014) 3854-3859.
- [327]. L. L. Baranowski, G. J. Snyder and E. S. Toberer. *Energy & Environmental Science*, 5 (2012) 9055-9067.
- [328]. D. Kraemer, B. Poudel, H.-P. Feng, J. C. Caylor, B. Yu, X. Yan, Y. Ma, X. Wang, D. Wang, A. Muto, K. McEnaney, M. Chiesa, Z. Ren and G. Chen. *Nat Mater*, 10 (2011) 532-538.
- [329]. W.-S. Liu, Q. Zhang, Y. Lan, S. Chen, X. Yan, Q. Zhang, H. Wang, D. Wang, G. Chen and Z. Ren. *Advanced Energy Materials*, 1 (2011) 577-587.
- [330]. T. Hogan, A. Downey, J. Short, J. D'Angelo, C.-I. Wu, E. Quarez, J. Androulakis, P. F. P. Poudeu, J. Sootsman, D.-Y. Chung, M. G. Kanatzidis, S. D. Mahanti, E. Timm, H. Schock, F. Ren, J. Johnson and E. Case. *Journal of Electronic Materials*, 36 (2007) 704-710.
- [331]. J. P. Heremans, V. Jovovic, E. S. Toberer, A. Saramat, K. Kurosaki, A. Charoenphakdee, S. Yamanaka and G. J. Snyder. *Science*, 321 (2008) 554-557.
- [332]. K. F. Hsu, S. Loo, F. Guo, W. Chen, J. S. Dyck, C. Uher, T. Hogan, E. K.

- Polychroniadis and M. G. Kanatzidis. *Science*, 303 (2004) 818-821.
- [333]. R. J. Mehta, Y. Zhang, C. Karthik, B. Singh, R. W. Siegel, T. Borca-Tasciuc and G. Ramanath. *Nat Mater*, 11 (2012) 233-240.
- [334]. M. Scheele, N. Oeschler, K. Meier, A. Kornowski, C. Klinke and H. Weller. *Advanced Functional Materials*, 19 (2009) 3476-3483.
- [335]. H. Liu, X. Yuan, P. Lu, X. Shi, F. Xu, Y. He, Y. Tang, S. Bai, W. Zhang, L. Chen, Y. Lin, L. Shi, H. Lin, X. Gao, X. Zhang, H. Chi and C. Uher. *Advanced Materials*, 25 (2013) 6607-6612.
- [336]. Z.-H. Ge, B.-P. Zhang, Y.-X. Chen, Z.-X. Yu, Y. Liu and J.-F. Li. *Chemical Communications*, 47 (2011) 12697-12699.
- [337]. P. Pichanusakorn and P. Bandaru. *Materials Science and Engineering: R: Reports*, 67 (2010) 19-63.
- [338]. A. Shakouri. *Annual Review of Materials Research*, 41 (2011) 399-431.
- [339]. S. A. Humphry-Baker and C. A. Schuh. *Acta Materialia*, 75 (2014) 167-179.
- [340]. M. V. Kovalenko, W. Heiss, E. V. Shevchenko, J.-S. Lee, H. Schwinghammer, A. P. Alivisatos and D. V. Talapin. *Journal of the American Chemical Society*, 129 (2007) 11354-11355.
- [341]. H. Yang, S. W. Finefrock, J. D. Albarracin Caballero and Y. Wu. *Journal of the American Chemical Society*, 136 (2014) 10242-10245.
- [342]. D. Li, Z. Zheng, Y. Lei, S. Ge, Y. Zhang, Y. Zhang, K. W. Wong, F. Yang and W. M. Lau. *CrystEngComm*, 12 (2010) 1856-1861.
- [343]. W. Yao, S. H. Yu, X. Y. Huang, J. Jiang, L. Q. Zhao, L. Pan and J. Li. *Advanced Materials*, 17 (2005) 2799-2802.
- [344]. M. Saranya, C. Santhosh, R. Ramachandran and A. Nirmala Grace. *Journal of Nanotechnology*, 2014 (2014) 8.
- [345]. X. Meng, G. Tian, Y. Chen, Y. Qu, J. Zhou, K. Pan, W. Zhou, G. Zhang and H. Fu. *RSC Advances*, 2 (2012) 2875-2881.
- [346]. Q.-m. Liu, D.-b. Zhou, Y. Yamamoto, R. Ichino and M. Okido. *Transactions of Nonferrous Metals Society of China*, 22 (2012) 117-123.
- [347]. M. Zong, Y. Huang, H. Wu, Y. Zhao, P. Liu and L. Wang. *Materials Letters*, 109 (2013) 112-115.
- [348]. D. Dodoo-Arhin, M. Leoni, P. Scardi, E. Garnier and A. Mittiga. *Materials Chemistry and Physics*, 122 (2010) 602-608.
- [349]. Z. Li, A. J. Du, Q. Sun, M. Aljada, L. N. Cheng, M. J. Riley, Z. H. Zhu, Z. X. Cheng, X. L. Wang, J. Hall, E. Krausz, S. Z. Qiao, S. C. Smith and G. Q. Lu. *Chemical Communications*, 47 (2011) 11894-11896.
- [350]. P. E. Larson. *Journal of Electron Spectroscopy and Related Phenomena*, 4 (1974) 213-218.
- [351]. C. Han, Z. Li, W.-j. Li, S.-l. Chou and S.-x. Dou. *Journal of Materials Chemistry A*, 2 (2014) 11683-11690.
- [352]. K. Laajalehto, I. Kartio and P. Nowak. *Applied Surface Science*, 81 (1994) 11-15.
- [353]. P. K. Khanna, N. Singh, S. Charan, A. K. Viswanath and K. R. Patil. *Materials Research Bulletin*, 42 (2007) 1414-1421.
- [354]. T. S. Zyubina, V. S. Neudachina, L. V. Yashina and V. I. Shtanov. *Surface Science*, 574 (2005) 52-64.
- [355]. S. Warule, R. Kashid, D. Shinde, N. Chaudhari, B. Kale and M. More. *Journal of Nanoparticle Research*, 14 (2012) 1-13.
- [356]. T. Wei, Y. Zhang, W. Dong, C. Huang, Y. Sun, X. Chen and N. Dai. *physica status solidi (a)*, 210 (2013) 1909-1913.
- [357]. B. Zhou, Y. Zhao, L. Pu and J.-J. Zhu. *Materials Chemistry and Physics*, 96 (2006)

- 192-196.
- [358]. L. Zhao, F. Tao, Z. Quan, X. Zhou, Y. Yuan and J. Hu. *Materials Letters*, 68 (2012) 28-31.
- [359]. D. Sakurai, J. J. Molino Cornejo, H. Daiguji and F. Takemura. *Journal of Materials Chemistry A*, 1 (2013) 14562-14568.
- [360]. S. Wu, K. Huang, E. Shi, W. Xu, Y. Fang, Y. Yang and A. Cao. *ACS Nano*, 8 (2014) 3522-3530.
- [361]. Y. Wang, D. Huang, X. Zhu, Y. Ma, H. Geng, Y. Wang, G. Yin, D. He, Z. Yang and N. Hu. *Nanoscale Research Letters*, 9 (2014) 1-8.
- [362]. R. B. Schwarz and W. L. Johnson. *Physical Review Letters*, 51 (1983) 415-418.
- [363]. S. Jiang, Y. Chen, H. Pan, Y.-J. Zhang and R. Tang. *Physical Chemistry Chemical Physics*, 15 (2013) 12530-12533.
- [364]. J. Nai, S. Wang, Y. Bai and L. Guo. *Small*, 9 (2013) 3147-3152.
- [365]. Z. Li, A. Kornowski, A. Myalitsin and A. Mews. *Small*, 4 (2008) 1698-1702.
- [366]. X. H. Liao, H. Wang, J. J. Zhu and H. Y. Chen. *Materials Research Bulletin*, 36 (2001) 2339-2346.
- [367]. M. P. Deshpande, P. N. Sakariya, S. V. Bhatt, N. Garg, K. Patel and S. H. Chaki. *Materials Science in Semiconductor Processing*, 21 (2014) 180-185.
- [368]. C.-H. Yang, W.-T. Wang, A. Grumezescu, K.-S. Huang and Y.-S. Lin. *Nanoscale Research Letters*, 9 (2014) 277.
- [369]. K. Liu, J. Wang, H. Liu and D. Xiang. *Rare Metals*, 28 (2009) 112-116.
- [370]. H. Fan, S. Zhang, P. Ju, H. Su and S. Ai. *Electrochimica Acta*, 64 (2012) 171-176.
- [371]. K. Tezuka, S. Kase and Y. J. Shan. *Journal of Asian Ceramic Societies*, 2 (2014) 366-370.
- [372]. K. Ananthi, K. Thilakavathy, N. Muthukumarasamy, S. Dhanapandian and K. R. Murali. *Journal of Materials Science: Materials in Electronics*, 23 (2012) 1338-1341.
- [373]. W. Wang, Y. Geng, Y. Qian, M. Ji and Y. Xie. *Materials Research Bulletin*, 34 (1999) 877-882.
- [374]. H. Li, Y. Yu and G. Li. *Journal of Applied Physics*, 115 (2014) 124316.
- [375]. Z. Zhang, J. K. Yee, P. A. Sharma, N. Yang and E. J. Lavernia. *Journal of Materials Research*, 28 (2013) 1853-1861.
- [376]. J. de Boor, D. S. Kim, X. Ao, M. Becker, N. F. Hinsche, I. Mertig, P. Zahn and V. Schmidt. *Applied Physics A*, 107 (2012) 789-794.
- [377]. J.-F. Li, W.-S. Liu, L.-D. Zhao and M. Zhou. *NPG Asia Mater*, 2 (2010) 152-158.
- [378]. Z.-G. Chen, G. Han, L. Yang, L. Cheng and J. Zou. *Progress in Natural Science: Materials International*, 22 (2012) 535-549.
- [379]. H. Alam and S. Ramakrishna. *Nano Energy*, 2 (2013) 190-212.
- [380]. K. Kadel, L. Kumari, W. Li, J. Huang and P. Provencio. *Nanoscale Res Lett*, 6 (2011) 57.
- [381]. L. E. Bell. *Science*, 321 (2008) 1457-1461.
- [382]. G. A. Slack, in *Solid State Physics*, eds. F. S. Henry Ehrenreich and T. David, Academic Press, 1979, vol. Volume 34, pp. 1-71.
- [383]. A. J. Hong, L. Li, H. X. Zhu, X. H. Zhou, Q. Y. He, W. S. Liu, Z. B. Yan, J. M. Liu and Z. F. Ren. *Solid State Ionics*, 261 (2014) 21-25.
- [384]. S. Ishiwata, Y. Shiomi, J. S. Lee, M. S. Bahramy, T. Suzuki, M. Uchida, R. Arita, Y. Taguchi and Y. Tokura. *Nat Mater*, 12 (2013) 512-517.
- [385]. C. Fang, S. Zhang, P. Zuo, W. Wei, B. Jin, J. Wu and Y. Tian. *Journal of Crystal Growth*, 311 (2009) 2345-2351.
- [386]. Y. Gao, Z. Zheng, Y. Tian, Y. Zhang and Y. Zhang. *European Journal of Inorganic Chemistry*, 2011 (2011) 4198-4203.

- [387]. J. P. Perdew, K. Burke and M. Ernzerhof. *Physical Review Letters*, 77 (1996) 3865-3868.
- [388]. B. Delley. *The Journal of Chemical Physics*, 92 (1990) 508-517.
- [389]. B. Delley. *The Journal of Chemical Physics*, 113 (2000) 7756-7764.
- [390]. Q. Sun, Z. Li, D. J. Searles, Y. Chen, G. Lu and A. Du. *Journal of the American Chemical Society*, 135 (2013) 8246-8253.
- [391]. G. K. C. A. J. Frueh, Ch. Knight. *Zeitschrift für Kristallographie*, 108 (1957) 389-396.
- [392]. G. N. A. N. N. Bikkulova, A.N.Skomorokhov, E.L.Yadrov-skii, A. I.Beskrovnyi, Y.M.Stepanov. *Bulletin of the Russian Academy of Sciences: Physics*, 70 (2006) 641-643.
- [393]. Y. S. S. Ishiwata, J.S.Lee, et al. *Nature Materials*, 12 (2013) 512-517.
- [394]. L. L. A. J. Hong, H. X. Zhu, et al. *Solid State Ionics*, 261 (2014) 21-25.
- [395]. H. C. Chou, A. Rohatgi, E. W. Thomas, S. Kamra and A. K. Bhat. *Journal of The Electrochemical Society*, 142 (1995) 254-259.
- [396]. B. E. McCandless, S. S. Hegedus, R. W. Birkmire and D. Cunningham. *Thin Solid Films*, 431-432 (2003) 249-256.
- [397]. X. Wu, J. Zhou, A. Duda, Y. Yan, G. Teeter, S. Asher, W. K. Metzger, S. Demtsu, S.-H. Wei and R. Noufi. *Thin Solid Films*, 515 (2007) 5798-5803.
- [398]. J. H. Yun, K. H. Kim, D. Y. Lee and B. T. Ahn. *Solar Energy Materials and Solar Cells*, 75 (2003) 203-210.
- [399]. J. Zhou, X. Wu, A. Duda, G. Teeter and S. H. Demtsu. *Thin Solid Films*, 515 (2007) 7364-7369.
- [400]. C. M. Hessel, V. P. Pattani, M. Rasch, M. G. Panthani, B. Koo, J. W. Tunnell and B. A. Korgel. *Nano Letters*, 11 (2011) 2560-2566.
- [401]. P. Kumar and K. Singh. *Crystal Growth & Design*, 9 (2009) 3089-3094.
- [402]. W. Li, R. Zamani, P. Rivera Gil, B. Pelaz, M. Ibáñez, D. Cadavid, A. Shavel, R. A. Alvarez-Puebla, W. J. Parak, J. Arbiol and A. Cabot. *Journal of the American Chemical Society*, 135 (2013) 7098-7101.
- [403]. Q. Tian, F. Jiang, R. Zou, Q. Liu, Z. Chen, M. Zhu, S. Yang, J. Wang, J. Wang and J. Hu. *ACS Nano*, 5 (2011) 9761-9771.
- [404]. S. Ballikaya, H. Chi, J. R. Salvador and C. Uher. *Journal of Materials Chemistry A*, 1 (2013) 12478-12484.
- [405]. Y. He, P. Lu, X. Shi, F. Xu, T. Zhang, G. J. Snyder, C. Uher and L. Chen. *Advanced Materials*, 27 (2015) 3639-3644.
- [406]. H. Choi, C. Nahm, J. Kim, C. Kim, S. Kang, T. Hwang and B. Park. *Current Applied Physics*, 13, Supplement 2 (2013) S2-S13.
- [407]. H.-X. Mai, Y.-W. Zhang, L.-D. Sun and C.-H. Yan. *Chemistry of Materials*, 19 (2007) 4514-4522.
- [408]. X. Wu, Y. Yu, Y. Liu, Y. Xu, C. Liu and B. Zhang. *Angewandte Chemie International Edition*, 51 (2012) 3211-3215.
- [409]. B. D. Anderson and J. B. Tracy. *Nanoscale*, 6 (2014) 12195-12216.
- [410]. B. J. Beberwyck and A. P. Alivisatos. *Journal of the American Chemical Society*, 134 (2012) 19977-19980.
- [411]. M. A. Hossain, J. R. Jennings, C. Shen, J. H. Pan, Z. Y. Koh, N. Mathews and Q. Wang. *Journal of Materials Chemistry*, 22 (2012) 16235-16242.
- [412]. H. K. Jun, M. A. Careem and A. K. Arof. *Renewable and Sustainable Energy Reviews*, 22 (2013) 148-167.
- [413]. Y.-L. Lee and Y.-S. Lo. *Advanced Functional Materials*, 19 (2009) 604-609.
- [414]. Z. Pan, I. Mora-Seró, Q. Shen, H. Zhang, Y. Li, K. Zhao, J. Wang, X. Zhong and J. Bisquert. *Journal of the American Chemical Society*, 136 (2014) 9203-9210.

- [415]. X. Z. Yang Bai, Hua Yu, Zhigang Chen, Lianzhou Wang. *Chemistry-A European Journal*, 20 (2014) 8670-8676.
- [416]. X. Zhang, Z. Xiaolong, L. Yu, L. Yibing and W. Jihuai. *Journal of materials science. Materials in electronics*, 26 (2015) 693-699.
- [417]. Y. Bai, C. Han, X. Chen, H. Yu, X. Zong, Z. Li and L. Wang. *Nano Energy*, 13 (2015) 609-619.
- [418]. A. D. Savariraj, K. K. Viswanathan and K. Prabakar. *Electrochimica Acta*, 149 (2014) 364-369.
- [419]. F. Wang, H. Dong, J. Pan, J. Li, Q. Li and D. Xu. *The Journal of Physical Chemistry C*, 118 (2014) 19589-19598.
- [420]. M. Ye, C. Chen, N. Zhang, X. Wen, W. Guo and C. Lin. *Advanced Energy Materials*, 4 (2014) n/a-n/a.
- [421]. K. Zhao, Z. Pan, I. Mora-Seró, E. Cánovas, H. Wang, Y. Song, X. Gong, J. Wang, M. Bonn, J. Bisquert and X. Zhong. *Journal of the American Chemical Society*, 137 (2015) 5602-5609.
- [422]. Q. Zhang, X. Guo, X. Huang, S. Huang, D. Li, Y. Luo, Q. Shen, T. Toyoda and Q. Meng. *Physical Chemistry Chemical Physics*, 13 (2011) 4659-4667.
- [423]. J. B. Rivest and P. K. Jain. *Chemical Society Reviews*, 42 (2013) 89-96.
- [424]. C. Han, Z. Li, G. Q. Lu and S. Xue Dou. *Nano Energy*, 15 (2015) 193-204.
- [425]. Q. L. Jining Gao, Huabo Zhao, Lianshan Li, Chunling Liu, Qihuang Gong, Limin Qi. *Chem. Mater.*, 20 (2008) 6263-6269.
- [426]. C.-H. Kuo, Y.-T. Chu, Y.-F. Song and M. H. Huang. *Advanced Functional Materials*, 21 (2011) 792-797.
- [427]. X. Xia, C. Zhu, J. Luo, Z. Zeng, C. Guan, C. F. Ng, H. Zhang and H. J. Fan. *Small*, 10 (2014) 766-773.
- [428]. H. Fujihara, M. Yabe and N. Furukawa. *Journal of the Chemical Society, Perkin Transactions 1*, DOI: 10.1039/P19960001783(1996) 1783-1785.
- [429]. D. L. Klayman and T. S. Griffin. *Journal of the American Chemical Society*, 95 (1973) 197-199.
- [430]. R. H. Wood. *Journal of the American Chemical Society*, 80 (1958) 1559-1562.
- [431]. H. Y. Yang Bai, Zhen Li, Rose Amal, Gao Qing (Max) Lu, Lian Zhou Wang. *Advanced Materials*, 24 (2012) 5850-5856.
- [432]. B. Dunn, H. Kamath and J.-M. Tarascon. *Science*, 334 (2011) 928-935.
- [433]. J. B. Goodenough and K.-S. Park. *Journal of the American Chemical Society*, 135 (2013) 1167-1176.
- [434]. Z. Yang, J. Zhang, M. C. W. Kintner-Meyer, X. Lu, D. Choi, J. P. Lemmon and J. Liu. *Chemical Reviews*, 111 (2011) 3577-3613.
- [435]. K. B. Hueso, M. Armand and T. Rojo. *Energy & Environmental Science*, 6 (2013) 734-749.
- [436]. X. Lu, B. W. Kirby, W. Xu, G. Li, J. Y. Kim, J. P. Lemmon, V. L. Sprenkle and Z. Yang. *Energy & Environmental Science*, 6 (2013) 299-306.
- [437]. Z. Wen, Y. Hu, X. Wu, J. Han and Z. Gu. *Advanced Functional Materials*, 23 (2013) 1005-1018.
- [438]. W. Li, S.-L. Chou, J.-Z. Wang, J. H. Kim, H.-K. Liu and S.-X. Dou. *Advanced Materials*, 26 (2014) 4037-4042.
- [439]. J. Qian, Y. Xiong, Y. Cao, X. Ai and H. Yang. *Nano Letters*, 14 (2014) 1865-1869.
- [440]. D. Y. W. Yu, P. V. Prikhodchenko, C. W. Mason, S. K. Batabyal, J. Gun, S. Sladkevich, A. G. Medvedev and O. Lev. *Nat Commun*, 4 (2013).
- [441]. L. Ji, M. Gu, Y. Shao, X. Li, M. H. Engelhard, B. W. Arey, W. Wang, Z. Nie, J. Xiao, C. Wang, J.-G. Zhang and J. Liu. *Advanced Materials*, 26 (2014) 2901-2908.

- [442]. J.-S. Kim, H.-J. Ahn, H.-S. Ryu, D.-J. Kim, G.-B. Cho, K.-W. Kim, T.-H. Nam and J. H. Ahn. *Journal of Power Sources*, 178 (2008) 852-856.
- [443]. D. Su, S. Dou and G. Wang. *Nano Energy*, 12 (2015) 88-95.
- [444]. H. Fei, Z. Feng and X. Liu. *Ionics*, 21 (2015) 1967-1972.
- [445]. Y. Zhao, D. Gao, J. Ni, L. Gao, J. Yang and Y. Li. *Nano Research*, 7 (2014) 765-773.
- [446]. I.-Y. Jeon, H.-J. Choi, S.-M. Jung, J.-M. Seo, M.-J. Kim, L. Dai and J.-B. Baek. *Journal of the American Chemical Society*, 135 (2013) 1386-1393.
- [447]. T. H. Hwang, D. S. Jung, J.-S. Kim, B. G. Kim and J. W. Choi. *Nano Letters*, 13 (2013) 4532-4538.
- [448]. W.-J. Li, S.-L. Chou, J.-Z. Wang, H.-K. Liu and S.-X. Dou. *Chemical Communications*, 51 (2015) 3682-3685.
- [449]. S. Xin, Y.-X. Yin, Y.-G. Guo and L.-J. Wan. *Advanced Materials*, 26 (2014) 1261-1265.
- [450]. Y.-X. Wang, S.-L. Chou, H.-K. Liu and S.-X. Dou. *Carbon*, 57 (2013) 202-208.
- [451]. F. Bonino, S. Morzilli and B. Scrosati. *Journal of Power Sources*, 14 (1985) 65-69.
- [452]. T. B. Kim, J. W. Choi, H. S. Ryu, G. B. Cho, K. W. Kim, J. H. Ahn, K. K. Cho and H. J. Ahn. *Journal of Power Sources*, 174 (2007) 1275-1278.
- [453]. S. Ni, T. Li and X. Yang. *Thin Solid Films*, 520 (2012) 6705-6708.
- [454]. M.-Z. Xue, Y.-N. Zhou, B. Zhang, L. Yu, H. Zhang and Z.-W. Fu. *Journal of The Electrochemical Society*, 153 (2006) A2262-A2268.
- [455]. C.-C. Lin, W.-F. Lee, M.-Y. Lu, S.-Y. Chen, M.-H. Hung, T.-C. Chan, H.-W. Tsai, Y.-L. Chueh and L.-J. Chen. *Journal of Materials Chemistry*, 22 (2012) 7098-7103.
- [456]. Q. Wang, G. Chen, D. Chen and R. Jin. *CrystEngComm*, 14 (2012) 6962-6973.
- [457]. E. P. Domashevskaya, V. V. Gorbachev, V. A. Terekhov, V. M. Kashkarov, E. V. Panfilova and A. V. Shchukarev. *Journal of Electron Spectroscopy and Related Phenomena*, 114-116 (2001) 901-908.
- [458]. Y. Zhang, Z.-P. Qiao and X.-M. Chen. *Journal of Materials Chemistry*, 12 (2002) 2747-2748.
- [459]. Z. Li, Ö. Kurtulus, N. Fu, Z. Wang, A. Kornowski, U. Pietsch and A. Mews. *Advanced Functional Materials*, 19 (2009) 3650-3661.
- [460]. Z. Li, L. Cheng, Q. Sun, Z. Zhu, M. J. Riley, M. Aljada, Z. Cheng, X. Wang, G. R. Hanson, S. Qiao, S. C. Smith and G. Q. Lu. *Angewandte Chemie International Edition*, 49 (2010) 2777-2781.
- [461]. H.-J. Yang, C.-Y. Chen, F.-W. Yuan and H.-Y. Tuan. *The Journal of Physical Chemistry C*, 117 (2013) 21955-21964.
- [462]. P. L. Taberna, S. Mitra, P. Poizot, P. Simon and J. M. Tarascon. *Nature Materials*, 5 (2006) 567-573.

Appendix

Appendix A: List of Publications.

- [1] **Chao Han**, Qiao Sun, Zhenxiang Cheng, Jianli Wang, Zhen Li, Gaoqing Lu, Shixue Dou. Ambient Scalable Synthesis of Surfactant-free Thermoelectric CuAgSe Nanoparticles with Reversible Metallic-n-p Conductivity Transition. **Journal of the American Chemical Society**, 2014, 136, 17626-176533. (IF: 11.4)
- [2] **Chao Han**, Zhen Li, Gaoqing Lu, Shixue Dou. Robust Scalable Synthesis of Surfactant-free Thermoelectric Metal Chalcogenide Nanostructures. **Nano Energy**, 2015, 15, 193-204. (IF: 10.2)
- [3] **Chao Han**, Zhen Li, Weijie Li, Shulei Chou, Shixue Dou. Controlled Synthesis of Copper Tellurides Nanostructures for Long-cycling Anodes in Lithium Ion Batteries. **Journal of Materials Chemistry A**, 2014, 30, 11683-11690. (IF:7.3)
- [4] **Chao Han**, Zhen Li, Shixue Dou. Recent Progress in Thermoelectricity Materials. **Chinese Science Bulletin**, 2014, 59(18), 2073-2091. (IF: 1.4)
- [5] **Chao Han**, Yang Bai, Qiao Sun, Zhen Li, Shaohua Zhang, Lianzhou Wang, Shixue Dou. Aqueous Synthesis for Cu₂Te Nanotube and Nanosheet via Fast Anion Exchange and Their Applications as Counter Electrodes for CdS/CdSe Co-sensitized Solar Cell. (**Advanced Science**, DOI: 10.1002/advs.201500350)
- [6] **Chao Han**, Zhen Li, Shixue Dou. New Strategies to Enhance Thermoelectric Performance of Metal Chalcogenides. (**Advanced Energy Materials**, submitted).
- [7] Yang Bai, **Chao Han**, Xinqi Chen, Hua Yu, Xu Zong, Zhen Li, Lianzhou Wang. Boosting the Efficiency of Quantum Dot Sensitized Solar Cells up to 7.11% Through Simultaneous

Engineering of Photocathode and Photoanode. **Nano Energy, 2015, 13, 609-619. (IF: 10.2)**

[8] Wei-Jie Li, **Chao Han**, Shu-Lei Chou, Jia-Zhao Wang, Zhen Li, Yong-Mook Kang, Hua-Kun Liu and Shi-Xue Dou. Graphite Nanoplate Coated Bi₂S₃ Composite with High Volume Energy Density and Excellent Cycle Life for Room-temperature Sodium-sulfide Batteries. **Chemistry-A European Journal, 2015, 21, 1-9. (IF=5.7)**

[9] Jinyan Xiong, Zhen Li, **Chao Han**, Weijie Li, Jun Chen, Shulei Chou, and Shixue Dou, Ambient Synthesis of a Multifunctional 1D/2D Hierarchical Ag-Ag₂S Nanowire/Nanosheet Heterostructure with Diverse Applications. **CrystEngComm, 2015, DOI: 10.1039/C5CE02134K. (IF=4.0)**

[10] Jinyan Xiong, **Chao Han**, Zhen Li, Shixue Dou. Effects of Nanostructure on Clean Energy: Big Solutions Gained from Small Features. **Chinese Science Bulletin, 2015, DOI: 10.1007/s11434-015-0972-z. (IF: 1.4)**

[11] **International patent: Chao Han**, Zhen Li, Shixue Dou. Aqueous-based Method of Preparing Metal Chalcogenide Nanomaterials (**Being processed**).

Appendix B: Oral Presentation and Poster on Conference.

1. The 2nd Baosteel-Australia Joint Research and Development Center (BAJC) Annual Project Review.

Time: Feb 2-4, 2015.

Place: Sydney, Australia.

Form: Oral Presentation.

Title: Waste Heat Recovery from Steelworks using Advanced Thermoelectric Materials and Generator Technology.

2. Nanotech France 2015 -International Conference & Exhibition.

Time: Jun 15 - 17, 2015.

Place: Paris, France.

Form: Oral Presentation.

Title: Ambient and Scalable Synthesis of Nanostructured Metal Chalcogenides Aimed on Thermoelectric Application.

3. The 5th Australia-China Symposium for Materials Science.

Time: July 21 - 23, 2014.

Place: Wollongong, Australia.

Form: Poster.

Title: Controlled Synthesis of Nanostructured Copper Tellurides and their Applications as Anode of LIBs with Ultra-stable Cycle Performance.

Appendix C: Received Awards.

1. International Postgraduate Tuition Award (IPTA), 2011-2014, University of Wollongong;
2. Chinese Government Scholarship, 2011-2014, China Scholarship Council;
3. Excellent Research Top-Up Award, 2014-2015, University of Wollongong;
4. Student Travel Grant to Attend International Conference, 2015, University of Wollongong.
5. Best Paper Awards of ISEM, 2015, University of Wollongong.